UNIVERSITY OF OSLO

MASTERS THESIS

# A Statistical Analysis of Strong Gravitational Lensing in Planck Sunyaev-Zel'dovich Selected Galaxy Clusters


*Author:*
Evan Benjamin
Edmund MARKEL

*Supervisor:*
Håkon DAHLE


*A thesis submitted in fulfillment of the requirements for the degree of Master of Science*

*in the*


Cosmology and Extragalactic Astronomy Group
Institute of Theoretical Astrophysics

UiO : Universitetet i Oslo


"*These are projections surprised in transparence, by the light of tenderness, of things that dream and talk in their sleep.*"

Tristan Tzara

UNIVERSITY OF OSLO

# *Abstract*

Institute of Theoretical Astrophysics

Master of Science

**A Statistical Analysis of Strong Gravitational Lensing in Planck Sunyaev-Zel'dovich Selected Galaxy Clusters**

by Evan Benjamin Edmund MARKEL

The Planck Sunyaev-Zeldovich Cluster catalogue provides an all-sky set of SZ detected galaxy clusters, which is the first of its kind. SZ signals are independent of redshift which allows a greater volume of space to be surveyed, compared to luminosity dependent X-ray and optical surveys. The statistical analysis of strong gravitational lensing from a complete and well defined set selection provides an opportunity for studying the largest structure in the universe and addresses issues raised in previous lensing cluster analysis. Previous cluster statistics have shown an over-abundance of arc detections relative to cosmological theory, which may be due to biases in cluster detection methods. Optical cluster surveys do not probe deep enough, X-ray surveys are biased towards less dense and massive cluster profiles, and both suffer from a lack of a statistically significant sample set. The two year Planck mission has produced a large SZ selected cluster set, from which 147 clusters with signal-to-noise ratios $\geq$ 6.0 and redshifts ranging from $0.14 \leq z \geq 1.8$, are analyzed for detections of strongly lensed arcs. 72 lensing clusters with 214 total arcs were analyzed for comparison to theory and previous arc catalogues in terms of Einstein radii, arc orientations, length to width ratios, magnitudes, surface brightnesses, and arc frequency.

# *Acknowledgements*

I want to thank my advisor, Håkon Dahle, for developing the ideas for this project as well as for the many hours of instruction and aid in the research process. Thanks to Benjamin Racine and Max Groenke for their technical assistance, as well as the other students for their camaraderie. Thank you to my family for all their support during my time in Norway. I'd also like to thank all my friends, near and far, for their help and encouragement throughout this whole process.

# Contents

# List of Figures

# List of Tables

# Physical Constants

| | |
|---|---|
| Speed of Light | $c_0 = 2.997\,924\,58 \times 10^8\ \mathrm{m\,s^{-1}}$ (exact) |
| Boltzmann Constant | $k_B = 1.380\,648\,52 \times 10^{-23}\ m^2 kg s^{-2} K^{-1}$ (exact) |
| Solar Mass | $M_{sun} = 1.989 \times 10^{31}\ kg$ (exact) |
| Gravitational Constant | $\mathrm{G} = 6.674\,08 \times 10^{-11}\ \mathrm{m^3 kg^{-1} s^{-2}}$ (exact) |
| Thomson cross section | $\sigma_T = 6.652\,458\,734 \times 10^{-29}\ \mathrm{m^2}$ (exact) |
| Mass of electron | $m_e = 9.109\,38 \times 10^{-31}\ \mathrm{kg}$ (exact) |
| Hubble constant | $H_0 = 74.3\ \mathrm{kms^{-1}Mpc^{-1}}$ |

# Chapter 1

# The Physics of Galaxy Clusters and Cosmology

## 1.1 Project Introduction

With theoretical underpinnings dating back to Isaac Newton, refined through General Relativity by Albert Einstein, and discovered on the extra-galactic scale only decades ago, gravitational lensing has become an independent astrophysical tool that can be deployed in conjunction with the most modern observational techniques to measure structure in the universe on the largest scales and aid in the determination of cosmological parameters. The magnified lenses also conserve the surface brightness of the background sources. The magnification effect can be almost $\geq 100$ times than the source so the lenses can allow observations of objects that would otherwise be too faint to see. Gravitational lensing is most generally an optical effect in which a background source's emitted light is bent around massive foreground objects in the line of sight of an observer. The more massive the lensing intermediary, the greater the light is distorted. Lensing is broadly categorized into microlensing, weak lensing, and strong lensing. Microlensing and weak lensing are subject to different methods of analysis, and their explanations are left to other sources. The most massive lenses create the greatest distortion, so it's no surprise that strong lensing is closely linked to the observational analysis of galaxy clusters.

The all sky Planck survey gives us a variety of accurate observational parameters from which this project has compiled a well-defined set of 147 galaxy clusters. The sample is large enough to address the so called arc statistics problem, in which more strong lenses have been observed than were predicted by cosmological models.

### 1.1.1 Motivation: Arc Statistics Problem

Gravitational lensing surveys over the last couple of decades are at odds with theoretical predictions. The first strong lensing surveys exhibited

almost an order of magnitude higher frequency of lensing than should have occurred based on the standard $\Lambda CDM$ model (Meneghetti et al 2013). Two possible reasons for this is the selection criteria for sampling galaxy clusters. Most previous optical surveys do not contain a dataset for enough of the sky or for the distances needed for a large sample set. X-ray selected clusters tend to pick out the clusters with the highest cluster center X-ray luminosities, which tend to be more massive and dense than an ideal sample set. Another reason is our understanding of mass distribution within clusters. More complicated cluster mass profiles will produce more arcs than spherical models, which when utilized in simulations, may bring the predictions closer to observations. With an all sky cluster catalogue produced by the Planck satellite, we can conduct a lensing analysis of a large, well-defined cluster set that will help test the hypothesis that the arc statistics problem arises from insufficiencies in the cluster sampling.

## 1.2 Galaxy Clusters

Rich galaxy clusters and superclusters are the most massive gravitationally bound objects in the known universe, and, because of this, they are able to give great insight into the development of cosmic structure from early times until the present observable positions. As the largest overdense regions in the universe that have undergone gravitational collapse, knowing their properties in turn helps cosmologists to directly constrain the cosmic parameters that are necessary to model and understand the primordial perturbations that evolved into the overdense regions and voids of large scale structure.

Clusters of galaxies can have between fifty and thousands of member galaxies. Cluster structure is broadly comprised of the galaxies themselves, large volumes of superheated electron gas, $T \approx 10^7 K$, between the galaxies all orbiting a dense central core, and dark matter, which comprises 85% of the cluster mass and creates the gravitational potential in which the baryonic matter resides. The hot, dense cluster core is the most detectable signature of a cluster's existence through optical and X-ray observations. Since the strong lensing strength is a function only of gravity and geometry, analyzing lensing features can be combined with other mass detection phenomena to discover and classify dark matter distribution in large scale structure.

One such dark matter issue is the cusp/core problem for cold dark matter (CDM), which gravitational lensing observations can help to resolve. The problem is that the central regions of galaxies have been observed to have a flat, or core, profile, while most CDM simulations predict a cuspy profile at the center of dark matter halos, where the density should increase sharply according to power law distributions.

### 1.2.1 Mass Distribution

In a gravitationally bound system, such as galaxies, clusters and superclusters of galaxies, the members reach a dynamic equilibrium state after a period of time depending on the scale of the system. In observational mass determinations of these systems, the velocity dispersion of the bound members and the thermodynamic physics derived virial theorem can be utilized for mass estimates. The virial theorem relates the total kinetic energy $T$ to the bound potential energy $U$ as follows:

$$T = \frac{1}{2}|U| \tag{1.1}$$

Spectroscopic measurements of the radial velocity dispersion, $\langle v_r \rangle$, of the bound members along the line of sight and their the average separation, $R_{avg}$, within the system allows us to determine the mass:

$$M = \frac{3\langle v_r \rangle R_{avg}}{G} \tag{1.2}$$

Many cluster masses, on the order of magnitude of $10^{14}-10^{15}$ solar masses, have been measured in this fashion. In this study, we will be able to compare this method with gravitational lensing and the Sunyaev-Zel'dovich effect mass estimations.

### 1.2.2 Intra-cluster Medium

Large, dense galaxy clusters are detectable by the hot ionized gas (~$10^7 K$) that lies in the intra-cluster medium (ICM) between its galactic members. Photon emissions from this gas are essential to discovering galaxy clusters and distinguishing them from unconnected galaxies along similar lines of sight, along with velocity dispersions, and observed redshift.

## 1.3 The Cosmic Microwave Background and the Sunyaev-Zel'dovich Effect

Scaling up from galaxy clusters, we reach the realm of cosmology. Understanding observational phenomena of cosmology will provide a framework for understanding gravitational lensing and the impact of its analysis.

### 1.3.1 Cosmic Microwave Background

The CMB is the oldest light in the universe as it was emitted during the Cosmological epoch of recombination when matter and radiation decoupled rendering the universe transparent. The radiation has an average temperature of roughly 2.7K but the anisotropies found in the radiation distribution correspond to the primordial matter density fluctuations of the plasmic universe. Mapping and modeling the anisotropies to constrain cosmological parameters is a primary goal of the Planck mission from which this project originates.

This is studied extensively elsewhere, and this lensing study focuses on secondary information observable through measuring the ubiquitous CMB. A small shift in the CMB intensity spectrum for certain wavelengths, theorized by Sunyaev and Zel'dovich in 1969, was predicted to be a signature of galaxy clusters in the direction of the spectral shift.

The Sunyaev-Zel'dovich effect provides us with a fairly new observational tool to calculate cluster detections in an unbiased sampling that will be important for utilizing cluster strong lensing for cosmology. The Sunayev-Zel'dovich effect involves the interaction of CMB radiation and the very hot intergalactic gas that resides within clusters of galaxies. The electrons of the hot intra-cluster gas can alter the wavelengths of the cosmic microwave background radiation via Compton scattering and inverse Compton scattering. So, photons entering the ICM will randomly be scattered with an increase in energy (decrease in wavelength), scattered with a decrease in energy (increase in wavelength), or will pass through unperturbed.

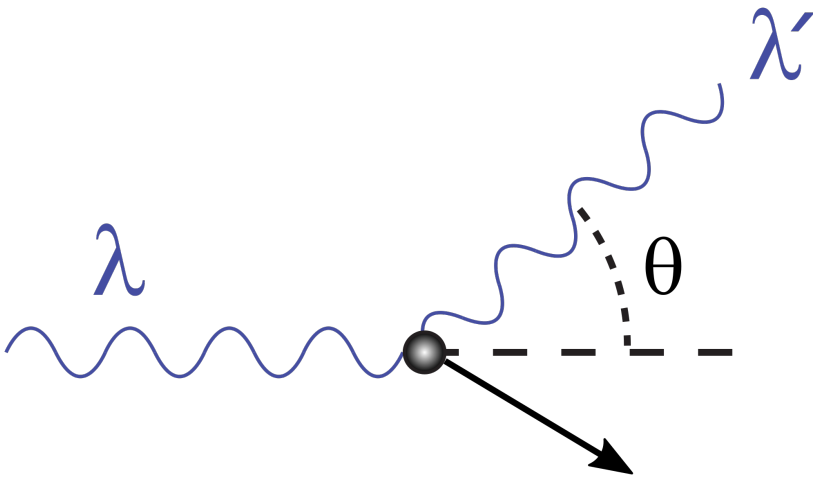


FIGURE 1.1: An illustration of Compton scattering of a CMB photon interaction with a high energy electron in the hot intracluster medium.

Although both scatterings occur, the second order approximation of the scattering yields an overall increase in energy levels, so the overall detectable effect on the CMB radiation is the inverse Compton scattering.

Along our line of sight, we see a relatively homogeneous average CMB photon frequency of 218 GHz, the exact frequency at which the SZ effect disappears (Planck Collaboration 2013). In the direction of a galaxy cluster, there will be a decrease in population of these unperturbed CMB photons as they are scattered out of our path. There will also be CMB photons that are scattered into our line of sight and these will show an overall increase in energy. An observer will then able to find the locations on the sky of galaxy clusters by detecting areas where there are greater concentrations of CMB photons with frequencies greater than 218 GHz and deficits of CMB photons of lower frequencies. So an observer can view locally hot (cold) (~1$mK$) (Carlstrom et al 2002) regions where frequencies are higher (lower) than 218 GHz as candidate galaxy clusters. This effect is due solely to the physics of Compton scattering: the CMB photons are given a boost from the much hotter electrons thereby shifting lower energy photons to a higher part of the spectrum.

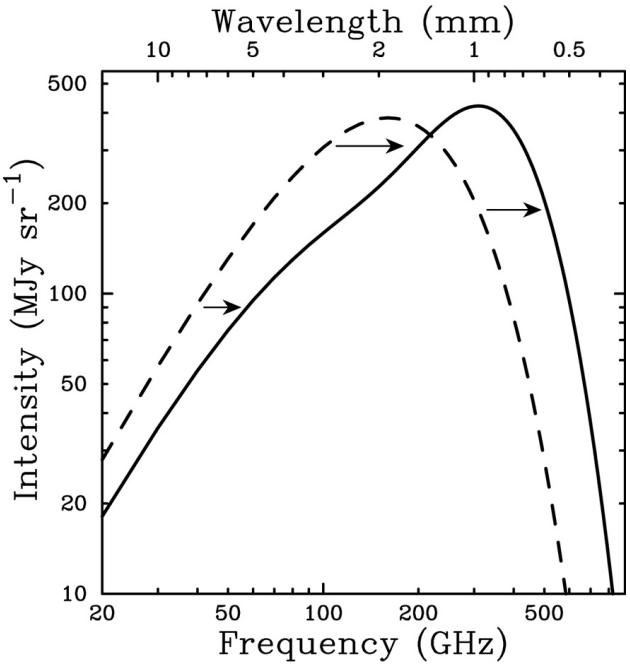


FIGURE 1.2: The spectral boost of the CMB intensity due to the observable SZ effects shown above for a supermassive cluster (Carlstrom et al 2002).

It's worth mentioning that there are two kinds of SZ interactions that the passing photons can have with the free electrons of the ICM. The aforementioned effect of the CMB photons randomly interacting with the free electrons is referred to as the thermal SZ effect and the photons are altered as above. There is also a kinematic SZ effect which is Compton scattering due to the overall motion of the cluster.

### 1.3.2 Thermal SZ Effect and Compton Parameter y

Let's examine the thermal SZ effect more formally. We want to measure the differential between the Compton scattered photons and the unperturbed CMB photons. The energy boost for a single scattering is given by:

$$\Delta E = \frac{k_B T_e}{m_e c^2} \tag{1.3}$$

where $T_e$ is the electron temperature (approximately isothermal in gas region) and $m_e c^2$ is the electron rest mass. In order to measure the amplitude of the spectral shift, we have to integrate along the line of sight and account for the surface area of the cluster. Let's introduce this amplitude as the Compton parameter, $y$, which will be an important observed quantity in Chapter 2. Integrating $\Delta E$ along the sight, we define the Compton parameter as a pressure integral:

$$y = \int \sigma_T n_e \frac{k_B T_{elec}}{m_{elec} c^2} dl \tag{1.4}$$

where $\sigma_T$ is the Thomson cross section and $n_e$ is the electron density of the ICM. For an isothermal cluster, the line of sight integral is equivalent to the optical depth $\tau_e$ of the electron gas. Sunyaev-Zel'dovich showed in their 1972 paper that the change in intensity due to the thermal SZ effect is given by the Kompaneets equation and then the spectral distribution is defined as follows:

$$\Delta I_\nu = I_\nu \cdot y \cdot f(x), f(x) = \frac{x e^x}{e^x - 1} \left[ x \left( \frac{e^x + 1}{e^x - 1} \right) - 4 \right] \tag{1.5}$$

where x is defined as a dimensionless frequency $x \equiv \frac{h\nu}{k_B T_{CMB}}$. The spectral distribution of the thermal SZ effect then looks like this:

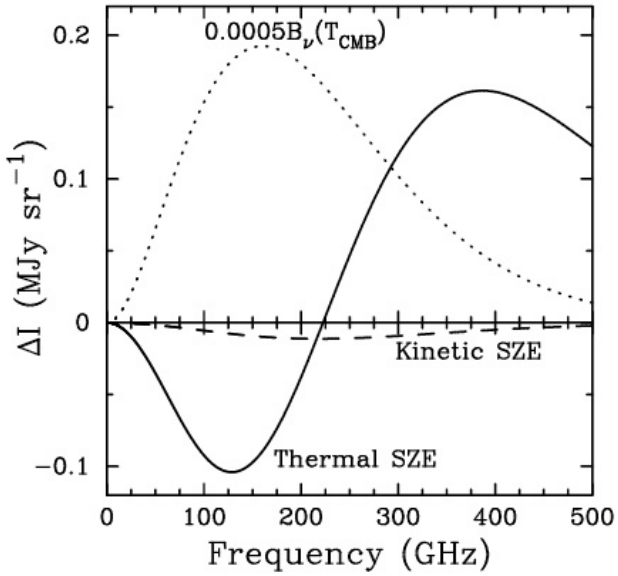


FIGURE 1.3: The intensity of the CMB photons is reduced from its re-scaled unperturbed intensity (dotted line) for low frequencies, unchanged for $\nu = 218GHz$, and increased for higher frequencies. The kinematic SZ effect is also shown. It is a much smaller effect that is washed out in most cases by the CMB anisotropy spectrum (Carlstrom et al 2002).

### 1.3.3 Kinematic SZ Effect

The thermal SZ effect is viewed with respect to the cluster at rest relative to the frame of the CMB photons. In reality there is a Doppler effect between the ICM and CMB photons, which we can measure along our line of sight as the peculiar velocity $v_r$. The relative temperature boost of the CMB photon from this effect is given by:

$$\frac{\delta T}{T} = -\frac{v_r}{c}\tau \tag{1.6}$$

where $\tau$ is the optical depth as before. So, if a cluster is moving towards (away from) the observer then the $v_r$ is negative (positive), and the boost given to the CMB photons by the kinematic SZ effect is positive (negative). These relative temperature boosts are not enough on their own to distinguish the effect from the CMB anisotropies so, unlike the thermal SZ effect, the kinematic SZ effect is mostly washed out by the CMB anisotropic spectrum.

In terms of large scale cosmological structure, the SZ effect works uniquely for galaxy clusters. An all sky survey of the SZ effect will accurately pick out clusters as the the intergalactic gas does not exist in the large dense quantities needed to produce the SZ effect in other regions. Also, the distance to the clusters can be determined through this effect independently

from the cosmic distance ladder methods as the effect is a primary measurement from the intracluster gas itself.

### 1.3.4 X-ray versus SZ Observations

X-rays are emitted as Bremsstrahlung from the same ICM source as the SZ, and their observed properties tell us about the size of the cluster. However the X-rays are emitted more strongly from more dense regions near the cluster centers X-ray emissivity $\propto n)e^2$. X-ray flux falls off as the luminosity distance$^2$, whereas the thermal SZ effect is independent of redshift-an observational advantage. The surface brightness of X-ray detections scales as $S_X \propto (1+z)^{-4}$ and the SZ effect is only caused by a spectral distortion in the CMB photon distribution.

There are issues in existing observations on two fronts: identifying clusters for a volume of detectable space and measuring the mass distribution within the detected cluster.

## 1.4 Strong Gravitational Lensing as Cosmological Tool

This chapter has presented an overview of the composition of galaxy clusters and the decades old theoretical SZ detection technique that has very recently become a groundbreaking observational reality. We'll turn now to the phenomena specifically under study in this thesis.

The most massive galaxy clusters have the highest angular lensing cross section on the sky where the mass is dense enough to bend the light of objects lying behind it. Einstein correctly predicted that our sun bends the light of stars lying nearly directly behind by twice the amount of deflection that Newtonian theory allows. There are other examples of multiple images and microlensing closer to Earth, however these are quite rare as the lensing cross section is so small for these lenses orders of magnitude smaller than galaxy clusters. To get the lensing effects needed to produce strong lenses, you need the most massive objects in the universe.

The more massive the cluster, the greater its lensing potential is. Since we are talking about the very tail end of the most massive cosmological structures, the number density of supermassive clusters is quite small. That means these objects are spread out along the sky as well as having large variation in redshift. So a search for lensing clusters is greatly aided by the redshift independent SZ signature. The rarity of the most massive clusters also necessitates a whole sky survey with high redshift depth for detecting a significant number of potential massive lens clusters.

### 1.4.1 Lens Optics

The optical magnification of a background galaxy by a cluster is determined by the cluster mass distribution, which is a complicated thing! Following is the presentation of a simple approximation of the cluster mass profile to be utilized in the arc statistics analysis in Chapter 5.

#### Arc Orientation, Caustic Lines, and Critical Curves

Arc statistics aid in the prediction of cluster mass distributions and core profiles. In practice, the cluster is not spherical and certainly not point-like. The position and orientation of lenses determine the position of sources relative to the cluster along the line of sight. Still approximating the cluster mass as a single lens, we can define the *caustic line* as the ideal position of the source that would be infinitely magnified along the *caustic line* to the observer The source's proximity to the caustic affects will determine the placement and strength of the lensed images in the cluster plane relative to the observer.

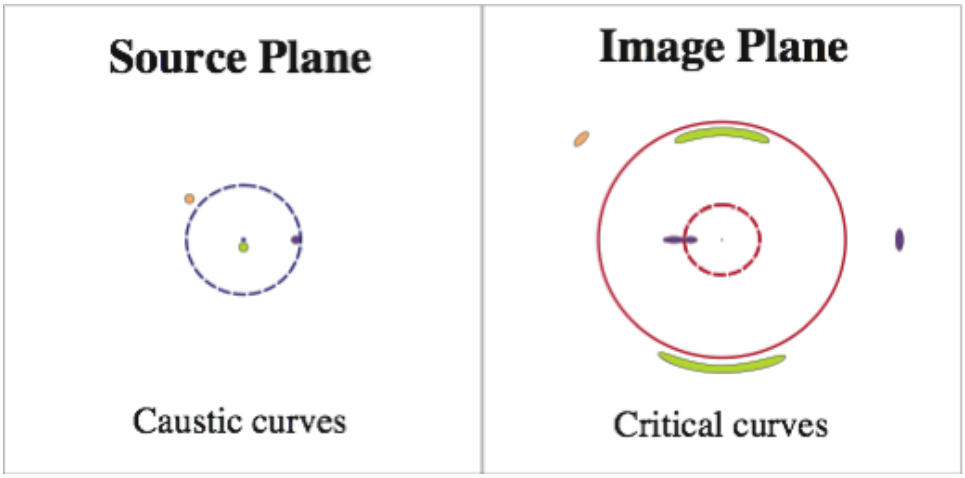


FIGURE 1.4: A drawing showing the caustic curves and source object locations on the left and the magnified images on the right for a spherically symmetric massively extended object. This is the simplest approximation of a galaxy cluster's radial mass distribution (Kitching 2010).

The position and orientation of arcs in a cluster help determine the overall mass distribution, and radially oriented arcs especially, aid in the estimation of the core density profile at the cluster's center (Oguri 2002).

Defining the critical curve of a cluster based on the Einstein radius allows the cluster mass estimation to be quickly calculated. The mass contained

within the critical curve for tangentially oriented arcs, symmetrically approximated as $\Theta_T$, of the cluster is given by:

$$M(\Theta_E^t) = \frac{c^2}{4G} \cdot \frac{D_{OL} D_{OS}{}^2}{D_{LS}} \Theta_T^2 \tag{1.7}$$

With the distances in this equation illustrated in Figure 1.5. Thus determining the Einstein radius for tangential arcs in the set can be used to calculate the cluster masses, separately from X-ray observations or the SZ effect.

**Determination of the Einstein Radius of a Cluster**

The Einstein Radius, $\Theta_E$, of a gravitational lens is the angular distance separating the lensing mass center and the lensed image in the case of an Einstein ring. The Einstein ring occurs in the case of perfect alignment between the observer, single lens with radially symmetric projected mass distribution, and distant background source. In the case of a point source, a star, and a foreground, lens, the deflection angle, $\alpha$ can be calculated. This relation was one of the results of General Relativity:

$$\alpha = \frac{4GM}{rc^2} \tag{1.8}$$

where $r$ is the impact parameter of the lens.

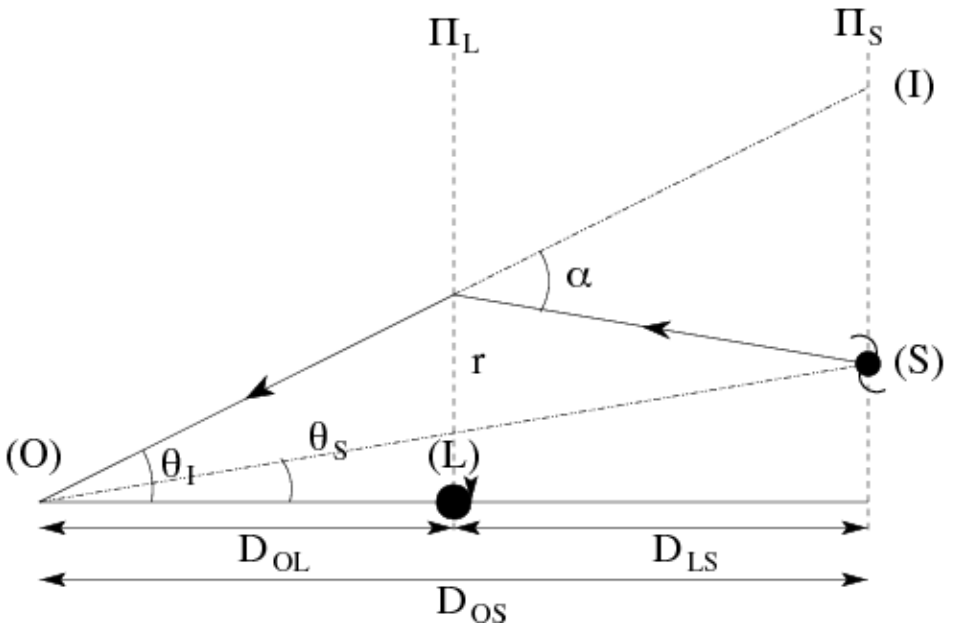


FIGURE 1.5: The cluster lens (L) lies between the observer (O) and the source galaxy (S).

And the observed angular displacement is related to the Einstein radius by:

$$\Theta_E = \frac{r}{D_{OL}} \tag{1.9}$$

Then the Einstein radius can be calculated in the trigonometric limit of small angles,

$$\Theta_E = \alpha \, (D_{LS}/D_{OS}) \tag{1.10}$$

Substituting in $\alpha$ and the relation between $\Theta_E$ and $r$,

$$\Theta_E^2 = \frac{4GM}{c^2}\left(\frac{D_{LS}}{D_{OS}D_{OL}}\right) \tag{1.11}$$

In the case of an extended source, in this perfect alignment, Einstein rings are visible. The radial distance from the center of the lens to the appearance of an Einstein ring exhibits the lensing strength and, since this is solely determined by the lens' gravity, its mass; also, again, the distance between the source and the lens as in the equation above.

If a cluster has a radially symmetric mass distribution, a singular isothermal sphere (SIS) describes the distribution as follows:

$$\rho = \frac{\sigma_V^2}{2\pi G}\frac{1}{r^2} \tag{1.12}$$

where $\rho$ is the mass density, r is the radius of the SIS, and $\sigma_V^2$ is the velocity dispersion of the cluster members. For the cluster mass distribution approximation of the SIS, the circle at this radius is the critical line, where tangentially oriented lensed images of a background source will appear. The lensing equation treating the cluster as a single optical lensing source remains the same as in the previous case.

From the Einstein radius, the lensing cross section of the cluster is a simple geometrical area in the SIS approximation:

$$\sigma_{lens} = \pi {\Theta_E}^2 \tag{1.13}$$

While this is a huge oversimplification of cluster mass distributions, it is still a powerful tool for expressing the lensing strength of the large cluster set in this study utilizing the observed arc separations from the cluster centers as a determinate of $\Theta_E$. See Chapter 5 for analysis.

#### Lensing for Extended Asymmetrical Objects

Actual galaxy cluster mass distributions are much more complicated than the above example. Accruing the orientation of the individual arc segments helps constrain the cluster density profile and the ratio of radial to

tangential arcs in a statistical survey aids in observing large scale structure.

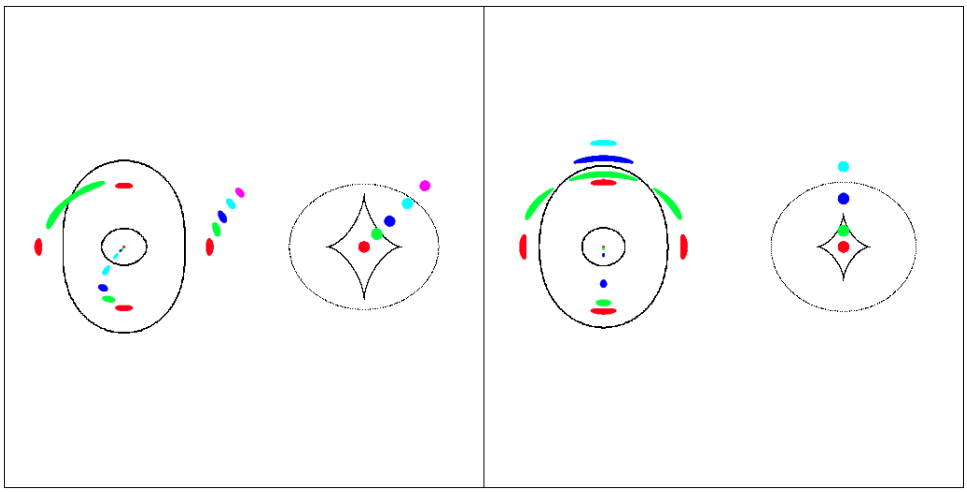

FIGURE 1.6: For an elliptical lens, the caustic curves are in the more complicated fold pattern as seen here. The observable cluster with critical curves are shown on the left while the source location relative to the caustic and critical curves are shown on the right hand side in each panel.

The statistics of arc orientation influencing the density profile of galaxy clusters can directly address the cusp-core density problem for cold dark matter.

# Chapter 2

# Galaxy Cluster Surveys and Arc Surveys

The most massive rich galaxy clusters are the most likely to be gravitational lenses and the most massive clusters are only found comprehensively through large volume surveys, where the whole sky is surveyed for a high redshift range. This chapter outlines the previous all sky cluster surveys and arc surveys of known cluster sets from optical, X-ray, and Sunyaev-Zel'dovich detections. The Planck mission will also be analyzed as well as the considerations taken into account for developing the strong lensing analysis set of 147 clusters that have been analyzed for this thesis.

## 2.1 Previous Cluster Surveys and the Need for Better Cluster Set Selection

A quick look at previous work done in selecting galaxy cluster surveys.

### 2.1.1 Optical Cluster Surveys

The Abell catalogue (Abell 1958) of rich clusters of galaxies originally published in 1958 that was based on photographic plates and a visual examination of Palomar Observatory Sky Survey. The catalogue has been expanded with observations from the sourthern sky and now contains 4,073 rich clusters with redshift $z \leq 0.2$ in an all sky survey (Abell, Corwin, Olowin 1989). Many clusters studied here are best known through their Abell nomenclature and have been studied in detail by the Hubble telescope.

#### Sloan Digital Sky Survey and Sloan Bright Arcs Survey

The SDSS contains multiband images for 1/3 of the sky and is one of the largest resources for optically selected clusters with 132,684 clusters (Wen et al 2012).

### 2.1.2 Optical Arc Surveys

#### Sloan Bright Arcs Survey

The Sloan Bright Arcs Survey (SBAS) based on the Sloan Digital Sky Survey (SDSS) catalog selected arc candidates based on their blueness. The cluster galaxies contained $gri$ band imaging and the blue objects were defined as $g$ - $r \leq 1$ or $r$ - $i \leq 1$.

#### Sloan Giant Arc Survey

This was the largest arc survey before availability of all sky SZ cluster data. There are published studies of the arc statistics and spectroscopy for 26 strong lensing galaxy clusters (Bayliss et al 2011).

### 2.1.3 X-ray Cluster Surveys

X-ray astronomy effectively began with the UHURU satellite, launched in 1970, followed by the Einstein satellite in 1982. The first satellite provided entries into many X-ray catalogues and many have since been updated and populated by the Roentgen Satellite (ROSAT) All Sky Survey (RASS). The ROSAT Bright Source Catalogue (BSC) (Voges et al 1999) covers 92% of the sky and contains 8,547 sources, and the ROSAT Faint Source Catalogue (FSC) (Voges et al 2000) contain 105,924 sources. The Bright Cluster Survey (BCS) (Ebeling et al 1998) contain the confirmed galaxy clusters from the larger set and have contributed to many X-ray surveys of rich clusters and lensing analysis.

#### LoCuSS Survey

Local Cluster substructure survey detailed by Smith et al 2005.This survey selected selected 165 clusters between $0.15 < z < 0.30$ utilizing the X-ray brightness emitted (Richard et al 2010).

### 2.1.4 X-Ray Arc Surveys

#### MAssive Cluster Survey (MACS

The MACS survey is an all sky catalogue (excepting the sky region of the Galactic plane) of the brightest X-ray emitting clusters with $z > 0.3$ (Ebeling, Edge, and Henry 2001). The survey is based on observations from the Rosat All Sky Catalogue.

**CLASH Survey**

The Cluster Lensing and Supernova survey with Hubble (CLASH) (Postman et al 2012) was an HST program that focused on analyzing the mass distributions and lensing cross sections of 20 X-ray selected galaxy clusters and 5 additional lensing-selected clusters. The additional clusters were chosen based on Einstein radii that were known to be larger than 35 arcseconds in order to find highly magnified arcs with source redshifts greater than 7, which are some of the most distant galaxies ever observed.

The mission measured each cluster in 16 broadband filters for 20 earth orbits each utilizing the Wide Field Camera 3 Instrument (WFC3/UVIS, WFC3/IR) and the Advanced Camera for Surveys instrument (ACS/WFC). Archival HST cluster images were also used for the combined cluster image analysis. The high number of filters allowed the redshifts of cluster members and many faint lensed sources to be calculated through photometry. This represents a new accuracy in determining the galactic distances in and behind the CLASH clusters, and these redshifts have been utilized in my analysis as much as possible. The CLASH survey is one of the most detailed cluster surveys and the most recently published at the time of this project.

### 2.1.5 Issues with Existing Cluster Sets

Optically selected clusters for lensing analysis are often biased towards clusters that have been previously studied in good detail and are at lower redshifts than X-ray selected. For statistical sets drawing from the Einstein Medium Sensitivity Survey (EMSS) for X-ray detected clusters, and the Sloan Digital Sky Survey (SDSS) for optically selected clusters, the literature has shown that there are fundamental differences in the lensing ratios of both sets of clusters. X-ray selected clusters tend to favor clusters which exhibit lensing. X-ray selected clusters such as the MACS survey show 5-10 times richer lenses detections than the optically selected Red Sequence Cluster Survey (RCS) lensing clusters (Horesh et al 2010). Many singularly analyzed clusters exhibited interesting opportunities such as large numbers of galaxies within the cluster and interesting gravitational lensing features. A cluster having these properties means higher densities and complicated morphologies that bias towards greater lensing numbers compared to a randomly selected cluster set. While it is useful to include these data in survey sets where observation time is a scarce commodity, their inclusion works against the need to solve the overabundance of observed arcs compared to theoretical cosmological predictions.

X-ray selected clusters have a different selection bias compared to optically selected clusters because of the nature of clusters that emit strong X-ray radiation. Meneghetti et al 2010 showed that the strongest lenses have higher luminosities in the X-ray regime than the average cluster. Hence,

more arcs are also seen in the X-ray cluster sets than would theoretically be seen in a neutrally selected cluster set.

To illustrate the difference in cluster selection techniques, here is an example from the Planck collaboration which shows the well known Coma cluster, Abell 1656, which shows the SZ signal compared to the ROSAT X-ray image.

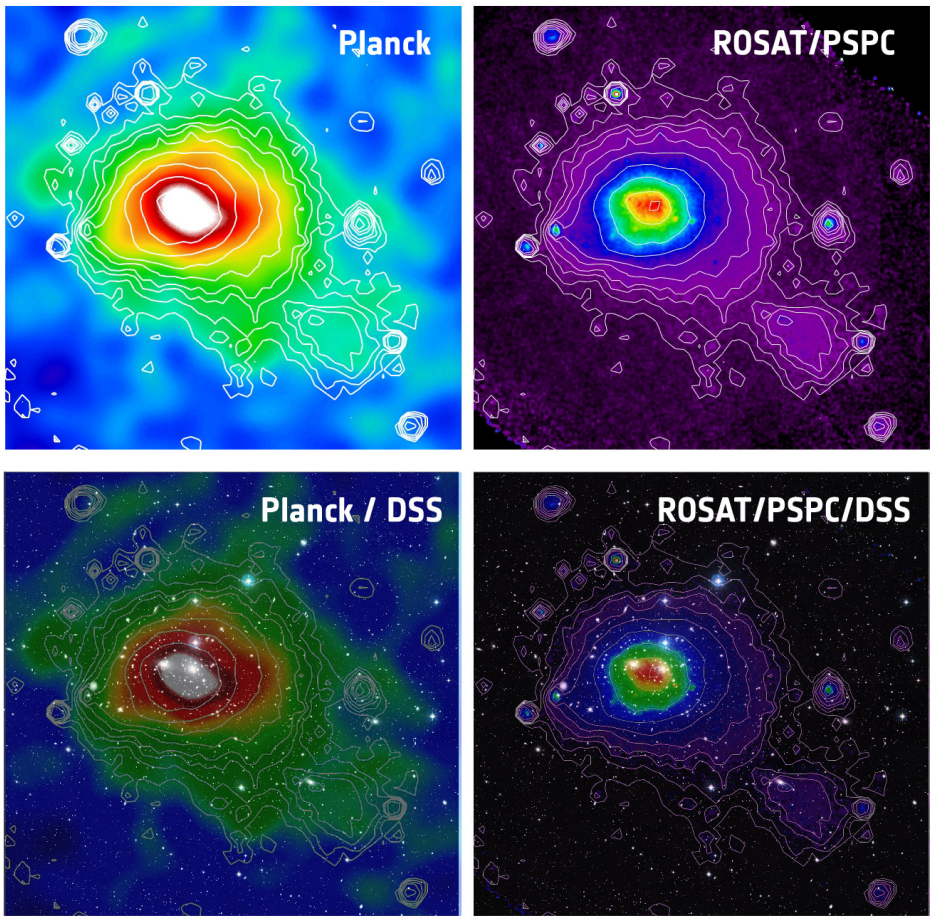


FIGURE 2.1: The top left shows the Planck SZ detection and the top right shows the ROSAT X-ray image. The bottom images show the above signals overlaid with optical images (Planck Collaboration 2010).

Details about the supercluster structure are best informed when comparing the two detections. Details of the overall structure is lost when viewed individually, and the narrow structure of the X-ray detection illustrates how this method can miss more relaxed cluster structure. And the tidal forces of merging clusters can provide better lensing opportunities that may be missed through optical or X-ray all sky surveys.

## 2.2 Sunyaev-Zel'dovich Cluster Surveys

Many of the optical and X-ray biases are avoided by SZ selected clusters. Like cluster X-ray detections, the intra-cluster medium is repsonsible for producing the SZ effect, as Chapter 1 explained is the reverse Compton scattering of CMB photons transiting through the cluster's ionized gas.

### 2.2.1 Ground Based Sunyaev-Zel'dovich Surveys

Over the past three decades there has been much development in observations of the SZ effect. There are currently two active ground based SZ surveys that are conducting high resolution sky surveys from the Southern hemisphere. They also are working with the Planck mission to help validate SZ detected cluster candidates.

#### Atacama Cosmology Telescope (ACT)

The Chilean desert based telescope is measuring the 1D thermal SZ effect on CMB photons in the frequency range of 148 GHz for one section of the sky measuring in the hundreds of degrees. For this frequency, the SZ effect reduces the temperature in the detected cluster region. From this analysis, the goal is to calculate the present a sensitive probe of the amplitude of the matter density perturbations, $\sigma_8$.

#### South Pole Telescope(SPT)

Working in conjunction with ACT, the SPT also is measuring the thermal SZ effect in 150, 219, and 274 GHz bands, detecting the two thermal SZ effects and comparing against the middle frequency, in which no SZ signal should be detected. ACT and SPT have identified 23 SZ selected clusters, of which 6 have strong lensing arcs (Meneghetti et al 2011).

## 2.3 Planck Mission and its Sunyaev-Zel'dovich Cluster Sets

The mission released three sets of SZ selected clusters, ESZ, PSZ1, and PSZ2. The data used in this study utilized the 2013 PSZ1 cluster set as the latest (2015) was not complete during the analysis period of the project. Follow up observations for validation of candidate clusters were conducted at the Nordic Optical Observatory soon after the PSZ1 catalog release in 2014. However, cluster masses and redshifts for the cluster used at the

time of publication have been updated with the updated PSZ1 values informed by the extended observation period in which PSZ2 was developed.

### 2.3.1 SZ Project Overview and Instrumentation

The Planck satellite was launched in May 2009 and measure the anisotropic temperature variations of the CMB radiation until October 2013. The satellite collected full sky CMB detections twice each year during this time. However the mission masked our own Galactic plane to minimize contamination from the foreground stars and dust. The mask removed 16.3% of the all sky survey. The satellite collected data from 9 frequencies split among two instruments. The Low Frequency Instrument (LFI) is comprised of pseudo-correlation radiometers centered at 30, 44, and 70 GHz bands, and the High Freqency Instrument (HFI) is comprised of bolometers with frequencies centered at 100, 143, 217, 353, 545, and 857 GHz. The final data release of Planck included measurements in all frequencies of the CMB temperature and the lowest 7 frequencies also measured the CMB polarization

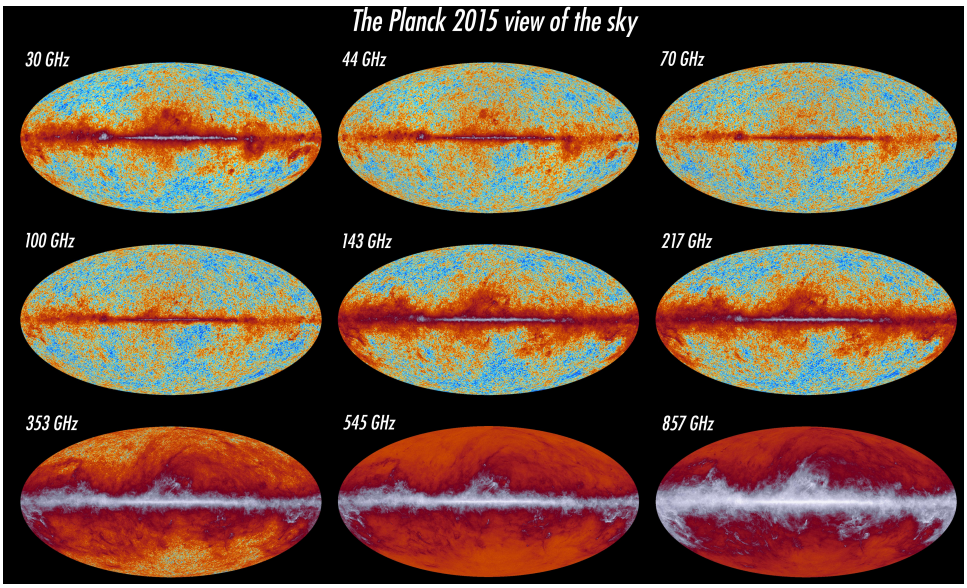


FIGURE 2.2: All Bands map of the Planck CMB anisotropies. Planck collaboration 2015.

The 2015 Planck released an all sky thermal SZ map with a Gaussian reconstruction of the thermal SZ effect for the masked region. Dust and foreground source contamination were also carefully extracted from the data to diminish false SZ Compton scattering effect identifications. It's worth repeating from Chapter 1 that CMB photons are not affected by SZ at around 217 GHz so this is an important channel for testing the likelihood of true cluster detections versus other sources such as galactic dust or cold spots. If we see a greater intensity of CMB photons in the 353, 545,

and 857 GHz channels, a lower intensity of CMB photons in the 100 and 143 GHz bands, and no change in the 217 GHz band, then the true detection likelihood is high. While the temperature and polarization of the CMB is the primary mission of Planck, the frequency design of its High Frequency Instrument is strongly influenced by the opportunity to develop the high signal to noise full sky SZ map seen below.

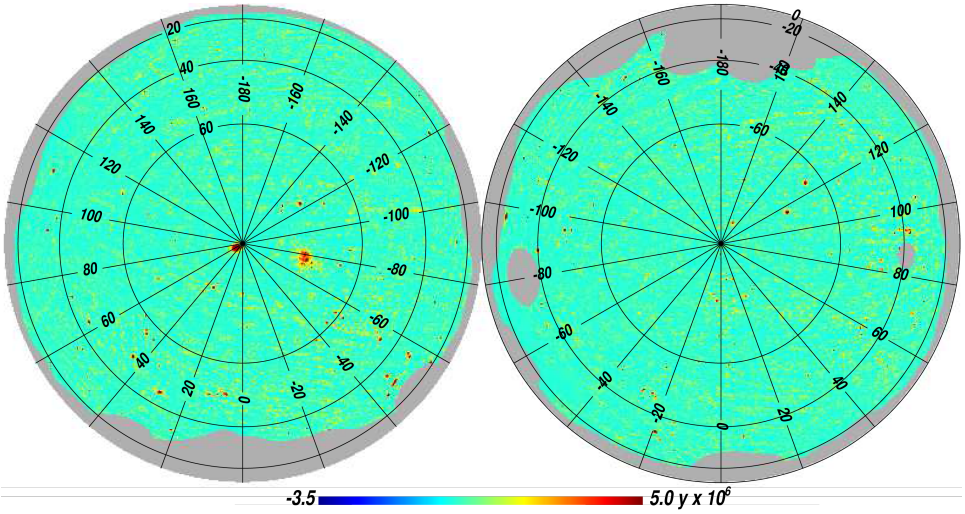


FIGURE 2.3: 2015 Release of the Planck SZ all sky map by Planck collaboration.

The detection algorithms for the SZ effect on Planck are divided into two classes: direction detection, which involves signals sourced directly from the individual frequency band channels, and indirect detection, where algorithms separate various components within the channels and reconstruct.

### 2.3.2 Early Planck SZ Set

The first Planck release involved a blind cluster set selection based solely on the direct detection algorithm of the SZ signal collected over 10 months of operation. Only the HFI was used for this set selection and the set (ESZ) is comprised of 189 cluster candidates with signal-to-noise ratios (SNR) ranging from $6 < SNR < 29$. Most cluster candidates were not at high redshifts, with 86% of the ESZ set having $z < 0.3$. Of the 189, 20 were determined to be newly discovered galaxy cluster candidates and all were estimated for the integrated Compton parameter Y.

The sample set began with 1000 blindly selected candidates with $SNR > 4.0$ and galactic latitudes 14 degrees away from the galactic plane. The raw list is then subjected to three levels of scrutiny: Planck's primary direct detection algorithm-Matched Multi-filter (MMF3), rejecting candidates with rising energy spectra in the 857 GHz band, and rejecting SZ detections with 7 arcminutes of known galactic sources or algorithmically detected galactic cold clumps. This cuts the candidate set down to

770 members. However, the MMF3 detection algorithm has modeled the likelihood of false detections at $SNR > 4.0$ at 30%.

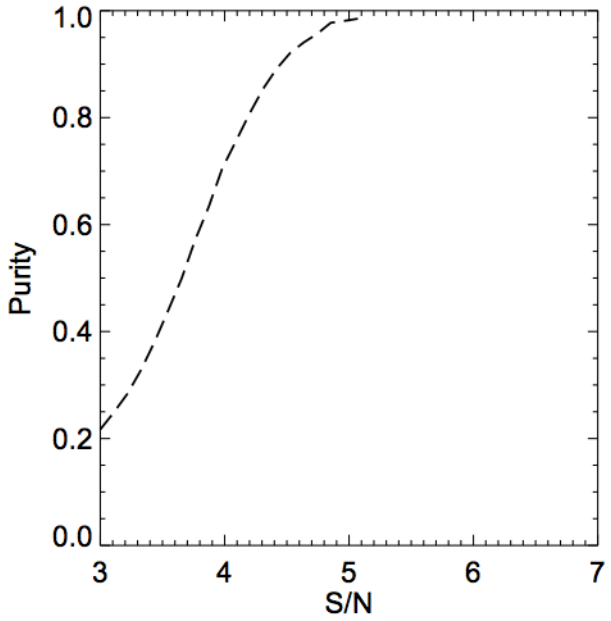


FIGURE 2.4: The likelihood of SZ detections being true for given SNR. Planck collaboration 2013.

The purity is near 1.0 for $SNR > 6.0$ and the cut is made here for the early sample in order to present a clean sample set. The next sets, with longer observation periods, lowered this threshold. This leaves 201 candidates remaining, and the number is reduced to 190 when the catalog is then cross-compared with the X-ray cluster detections from the XMM-Newton ESA science mission utilizing the European Northern and Southern Observatories (ENO and ESO). The 11 removed through this independently collected data were then confirmed to be false foreground dust detections.

The candidate clusters were also compared to the existing Meta-Catalog of X-ray detected Clusters of galaxies (MCXC) for X-ray detections and the XMM-Newton ESA mission coordinated an X-ray confirmation study for 21 of the cluster candidates. The set was also compared to the optically selected Abell and Zwicky cluster catalogs, and ESZ was also compared to all known SZ detected clusters including those newly found at ACT and SPT in 2010. These comparisons and follow up studies confirmed all but 9 candidates as actual clusters. One of the 9 was eventually rejected to give the 189 cluster candidates with high probabilities of being actual clusters.

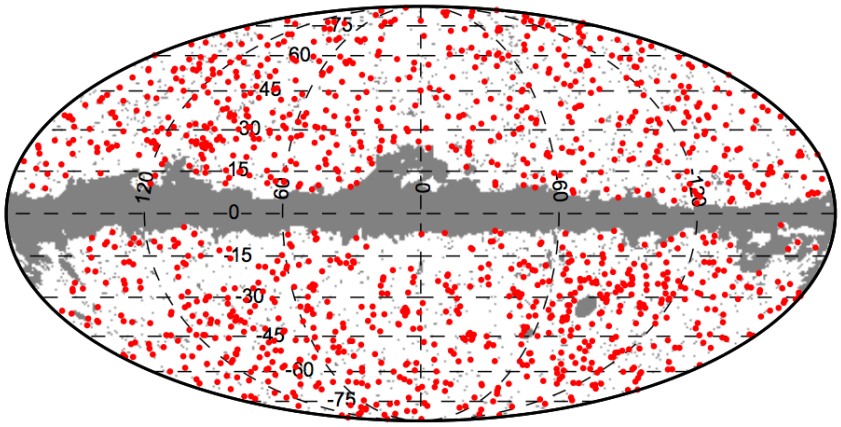


FIGURE 2.5: A masked all sky map of the 1227 candidate clusters of the entire PSZ1 catalog.

### 2.3.3 Planck 2013 SZ Set 1

After surveying the sky for 15.5 months, the Planck mission compiled the data for the PSZ1 catalog, which is 6 times larger than ESZ with 1227 blindly detected entries.

A good illustration of the multiband detection of the PSZ1 cluster set is shown below. All 9 bands are represented for each of the four cluster reliability classes shown from left to right: confirmed cluster, high reliability candidate, probable cluster candidate, and most uncertainty in the 1227 candidate survey.

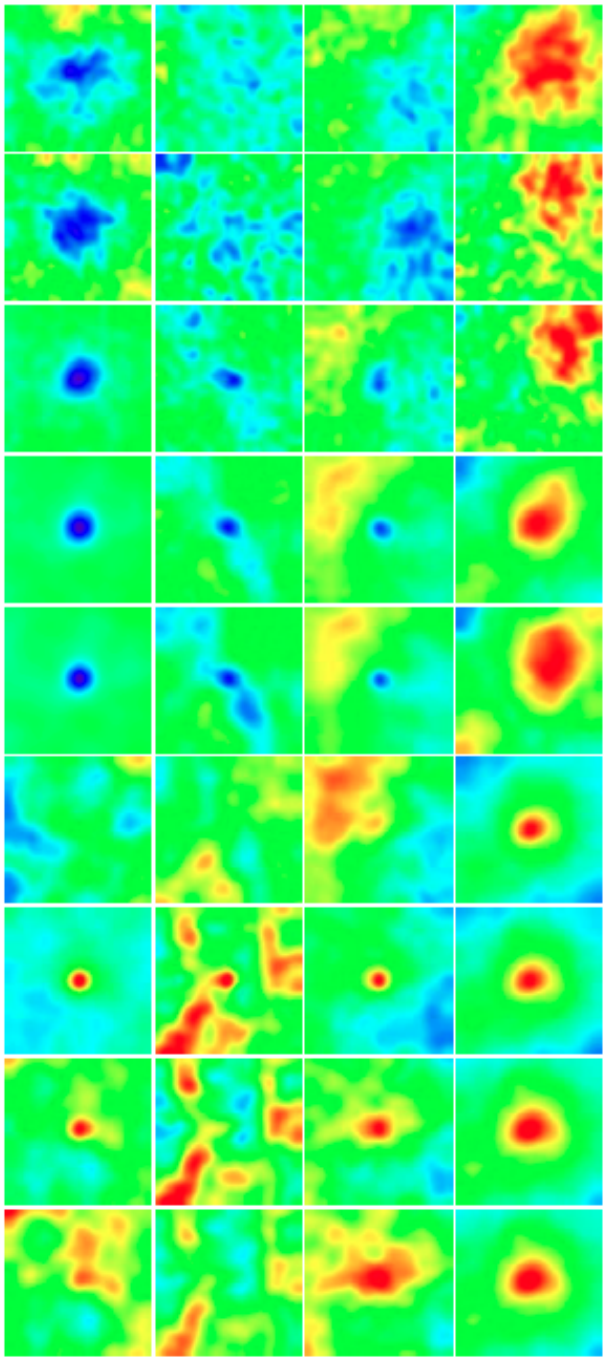

FIGURE 2.6: The bands from top to bottom are in ascension of frequency. Note for the left column representing the sure detection, the 5 lowest bands show the cold detection (decrease in CMB photon intensity), the sixth band (217GHz) shows no SZ signal at all, and the bottom 3 bands show the hot or intensity increase expected from the SZ effect. Planck collaboration 2015.

### Catalog Parameters and Selection Criteria

The 6 channels on the HFI are used to produce the PSZ1 catalog. While 5 different combinations of channels were evaluated for breadth of detection and strength of signal, the Planck mission found that the 6 bands of 100-857 GHz produced the strongest signal to noise ratio. Several masks were employed on top of the raw data to eliminate detections erroneously ascribed to easily detectable foreground sources.

A point source mask collected detections from across all 6 frequency bands were point detections had a $SNR > 10$ and a 1.28 FWHM, corresponding to 3 times the beam width. Radio contamination is a concern but the point emissions are well concentrated so not much radio source leaks outside the mask boundary. The mask was then widened to 5 times the beam width at the point sources to avoid false detections at the point boundaries within the mask and the total area of the mask was 2.9%.

The direct detection algorithm involves the same triple screening methodology as described for the ESZ cluster set above. The clusters are themselves detected based on a standard Navarro-Frenk-White (NFW) profile using pressures measured from baseline X-ray model utilizing observations from REXCESS and parametrized by Arnaud et al 2010. The clusters are measured in the following units: $R_{500}$ represents the radius from the cluster center out to the point where the average density inside the sphere is 500 times the critical density $\rho_c$ where

$$\rho_c = \frac{3H^2}{8\pi G} \tag{2.1}$$

from the Friedmann equations for a flat universe. And $M_500$ is the mass contained within this sphere. $M_500$ will often be used in this study to analyze the cluster set. $Y_{500}$ represents the SZ flux within this radius, where Y is the same Compton parameter derived in Chapter 1. The angular cluster scale parameter $\Theta_{500}$ was also used. The cluster quantities are calculated using standard $\Lambda CDM$ cosmology: $H0 = 70 kms^{-1}Mpc^{-1}$, $\Omega_m = 0.3$, an $\Omega_\Lambda = 0.7$.

A galactic source mask similar to the ESZ mask was developed that covered 15% of the sky, and combined with the point source mask, the conjoined mask for PSZ1 yields 16.3% total sky masking. The screened SZ detected clusters with $SNR > 4.5$ are then tested further for false detections.

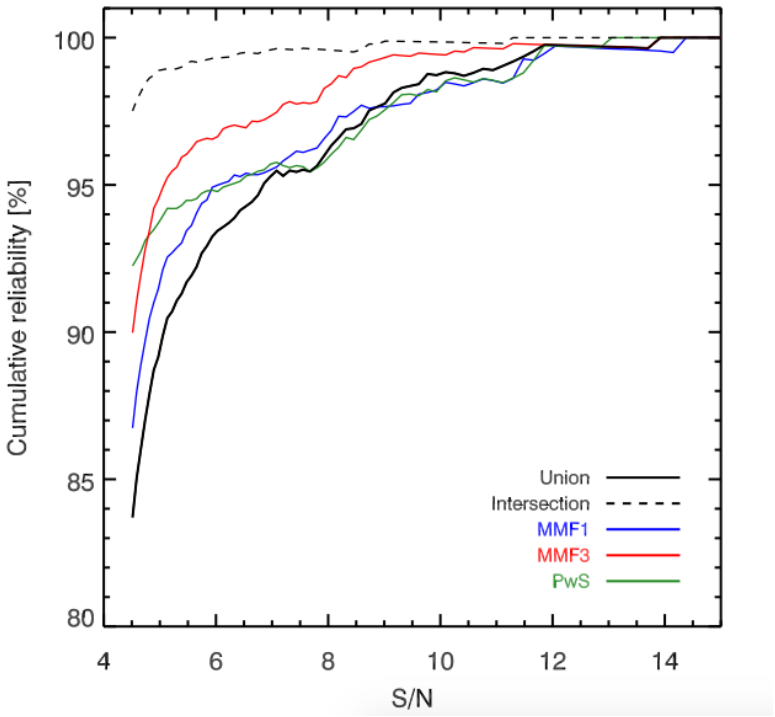


FIGURE 2.7: Showing the likelihood of a detected SZ signal to represent an actual cluster in the PSZ1 catalog. Each of the 3 detection algorithms were computed separately and shown here in color.

Candidate clusters with $SNR > 6.0$ have a very high probability of representing real clusters and were thus chosen for representation in this study in order to ensure a high probability of surveying real clusters for strong lensing. For the clusters under analysis in this project, the relation between signal to noise and $M_{500}$ is demonstrated below

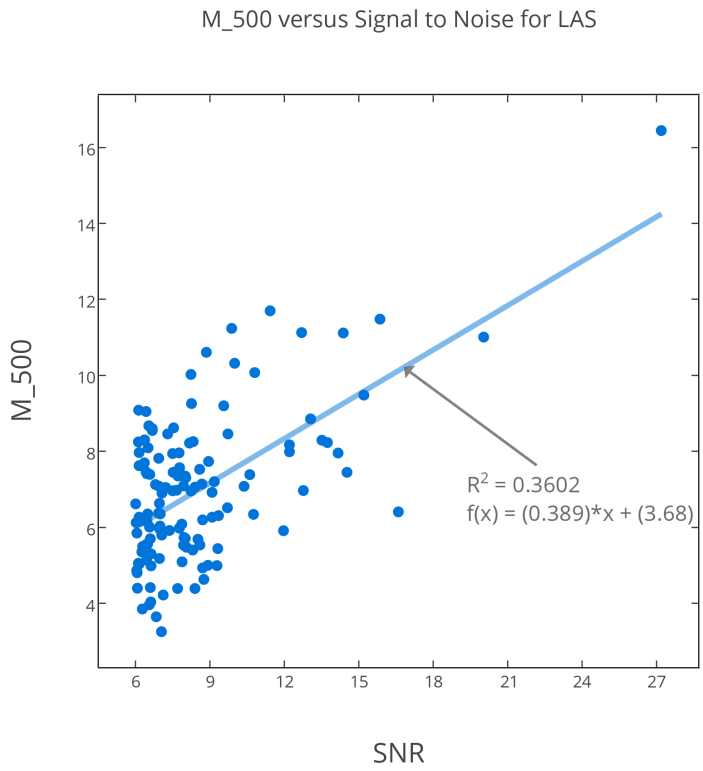


FIGURE 2.8: There is a correlation betweeen signal to noise and SZ mass but only a 36% match to the linear fit.

In Chapter 5 we will look at the clusters as functions of both related parameters.

### Validation

The Planck mission also pursued X-ray (ROSAT All Sky Survey, and MCXC/XMM-Newton follow-up validation survey), infrared (Wide-field Infrared Survey), optical (Sloan Digital Sky Survey, Abell, and Zwicky), and previous SZ surveys (ACT and SPT) to cross validate of cluster candidates similar to the work done for the ESZ release. Since the SZ signal is observed from a wider cluster area on the sky than X-ray or optical studies, Planck searched these cluster sets within 5 arcminutes of their position estimates to ensure there was extremely little chance of failing to validate a cluster candidate due to positional error. The results of this external validation yielded 683 confirmed as previously known clusters, 178 confirmed via follow-up observations, and 366 are given candidate status with three tiers of actual cluster likelihood. Of the still candidate clusters, 54 are highly likely to be clusters, 170 are probably, and 142 are in the least likely tier.

| Category | $N$ | Catalogue, telescope, or reliability |
|---|---|---|
| Previously known . . . . . | 683 | 472 X-ray: MCXC meta-catalogue<br>182 Optical: Abell, Zwicky, SDSS catalogues<br>16 SZ: SPT, ACT<br>13 Misc: NED or SIMBAD |
| New confirmed . . . . . | 178 | Follow-up, archival data, SDSS survey |
| New candidate . . . . . | 366 | 54 High reliability<br>170 Medium reliability<br>142 Low reliability |
| **Total *Planck* SZ catalogue . . . . .** | **1227** | |

FIGURE 2.9: Planck external validation status as of the initial publication of PSZ1.

After the external validation, 70.6% of the 1227 cluster candidates had been confirmed as definite clusters. The percentage rises to 73% when the set only includes $SNR > 6.0$. Also, 813 of the 1227 clusters in PSZ1 contained quantities for redshift and mass $M_{500}$.

### 2.3.4 Planck 2015 SZ Set 2

The final Planck release (PSZ2) represents the SZ cluster detections spanning the full 29 months of observation, almost twice as long as PSZ1.There are roughly 1600 cluster candidate members in this set with $SNR \geq 4.5$. The longer observation period allowed higher cluster counts and thus improvement on the calculations of the SNR and redshift values for the cluster candidates as these are shown to be dependent on the cluster counts in Planck Collaboration XX 2014. This leads to 439 of the candidate list containing $SNR > 6.0$, which is more than twice the number of similar cluster candidates in PSZ1. A further 86 clusters were upgraded from candidate to confirmed status, and the overall purity of the original PSZ1 catalog was upgraded to 94%.

My analysis is based on the original PSZ1 and utilizing the new $SNR$ values would have changed the set selection during a period of ongoing observational verification of cluster candidacy. The release of PSZ2 did not change the cluster candidate members of my analysis, however redshift and mass values for the PSZ1 candidates were updated as the Planck collaboration updated their PSZ1 databases. At the time of analysis, 13 cluster redshifts for cluster candidates in PSZ1 that were lacking redshifts and mass calculations were updated with the newest data release and have been included in my survey set and subsequent lensing analysis.

## 2.4 PSZ1 Cluster Set Selected for Analysis

The 1227 PSZ1 galaxy clusters identified have been further reduced based on several parameters to ensure a high reliability of cluster candidacy. Through 3 more stringent selection criteria than the PSZ1 catalog, my

analysis set for strong lenses narrows to 147 lensing cluster candidates. The entire lensing analysis set is located in Appendix G.

Of the 147, image data was available for 124 confirmed clusters and 1 cluster candidate, PSZ1 G206.64-21.17, imaged with the Subaru telescope, which registered as a possible false cluster detection due to galactic dust. There was no obvious cluster near the PSZ1 position on the sky.

#### Signal to Noise Ratio

The first selection criteria is a cut in the signal to noise ratio. The set includes all SZ cluster candidates with $SNR > 4.5$, and the cut made for analysis is $SNR > 6.0$. See 2.7 for plot showing the purity increase. This cut brings the PSZ1 selection down to 377 cluster candidates. The signal to noise cut is not just about the reliability of the cluster candidates. As the SZ effect is stronger with more massive clusters, a higher SNR for a detection corresponds to a more massive cluster. More massive clusters will have larger lensing cross sections and often more complicated mass distributions, both of which increase the likelihood that the cluster is a lens.

#### Declination

The research included in this thesis involves observational follow-ups for PSZ1 designated cluster candidates independently of the Planck mission and observations were conducted at the Nordic Optical Telescope in La Palma, The Subarau Telescope in Hawaii, and the Canada-France-Hawaii Telescope in Hawaii as well. To improve the candidate purity, a cut in the declination of cluster positions was made at $DEC > -15$. The reduced PSZ1 now numbered 212 cluster candidate members. This was made to narrow the region of the sky observed to that which is best observable from the Northern hemisphere.

#### Cluster Redshift

Clusters with low redshifts are inefficient lenses, so another a cut was made with regards to the minimum redshift was raised to $z > 0.15$. 4 clusters with redshifts ranging from $[0.124, 0.147]$ were still included as they were known to have observational data or were known to be strong lensing candidates for other reasons, such as the CLASH HST study surveyed in great detail several of the lenses included in the final list at low redshifts. 3 other clusters had redshifts lower than 0.15 that were re-evaluated during the PSZ1 cluster values update. For clusters at this redshift that are lensing candidates, there was a good availability of images available for inclusion. With this final cut, the PSZ1 cluster survey subset, or Lensing Analysis Set, (LAS) used in this analysis numbered 147.

Of the 147 clusters in the LAS, 130 have cluster redshifts and 127 have $M_{500}$ quantities from the updated PSZ1 catalogue.

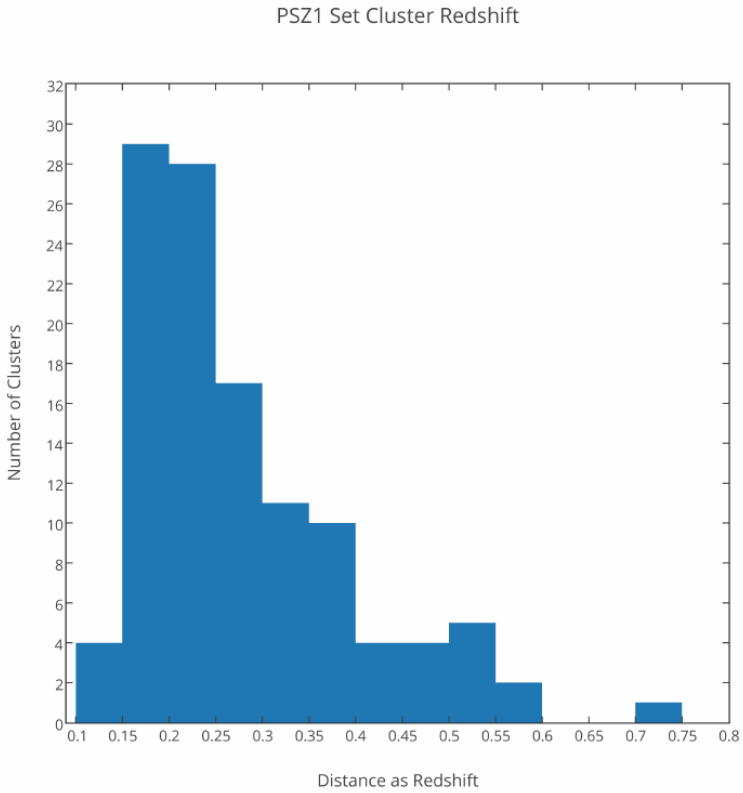


FIGURE 2.10: Redshifts for all the clusters in the LAS. The median redshift for all set clusters is 0.25

The clusters were analyzed for strong lensing candidates and the methodology and toolkit used for this process in detailed in Chapter 3.

# Chapter 3

# Methods for Analyzing Strong Lensing Image Data

With the understanding of our galaxy cluster survey set selection, the task at hand is to compile the relevant space and ground based images of the clusters and then analyze them for strong lenses. This chapter goes through the methods and computational tools to derive the statistics for the FITS images of the observed lensing clusters.

## 3.1 Analytic Features Needed for a Rigorous Analysis of Strong Lenses

While numerous theoretical tools exist for modeling foreground mass distribution and predicting the placement and appearance of arcs in images, much of the detection of lensed objects still relies most heavily on visual determinations.

### 3.1.1 Photometry and Astrometry

The photometric features needed to develop a strong catalogue of strongly lensed objects include the radial distance of the object to the brightest cluster galaxy (BCG), the length to width ratio of the lensed galaxies, the ratio of tangential to radial arcs relative to the BCG or mass center, the flux of the arcs, the brightness magnitude of the arcs, the surface brightness, and photometric features of the foreground galaxy clusters.

This section goes over the methods I used to calculate the statistics for the clusters. The starting point is a calibrated FITS image file. The FITS files were then analyzed using software including IDL, Matlab, Python, SExtractor, Imcat, IRAF program package, and SAOImage ds9.

### SExtractor Overview

SExtractor provides the photometric analysis for most of the PSZ1 cluster set analyzed in this thesis. The software develops a photometric catologue of astronomical objects through analyzing a FITS image. Through a variety of user-selected input parameters, SExtractor does a good job of deblending oversaturated features and distinguishing background source photometrics from foreground stars. It's worth mentioning that SExtractor was primarily designed for deriving photometry of galaxies and distinguishing these extended objects from foreground stars. There are some issues with the detection of objects with low surface brightness. The complicated morphology of giant arcs presents some challenges for detection and derivation of photometry but most are solvable through techniques outlined in this chapter. Chapter 6 will compare the results of SExtractor with other algorithms and ideas from published works.

### SExtractor: Deblending Objects in FITS images and Extracting Magnitude

The astrometrical magnitude is a logarithmic measure of an object's brightness for a given wavelength or image band filter. Astronomical magnitudes are generally either measures of an object's apparent or absolute magnitude. The apparent magnitude measures the observed brightness of an object compared to a set reference point whose magnitude serves as a baseline. The measured object's magnitude can be derived as such:

$$m_{object} - m_{reference} = -2.5log\left(\frac{B_{object}}{B_{reference}}\right) \tag{3.1}$$

where I refers to the object's brightness. The second category of magnitudes is absolute, which normalizes apparent magnitude for real distances. The perceived brightness of an object located at a fixed distance D is then calculated from the apparent magnitude $m$:

$$M_{AB} = m - log(D) + 5.0 \tag{3.2}$$

which is derived from the fact that the luminosity L of an object falls off at a rate of the square of the distance, so the brightness $\propto \frac{L}{D^2}$. All the magnitudes presented in this study are absolute.

There are four different viable options within SExtractor for calculating the magnitude of the astrophysical objects. The first two are isophotal and corrected isophotal magnitudes. The threshold is the lowest isophote, or connected region sharing the same light intensity. The isophotal magnitude simply sums up the magnitudes for regions above the detection threshold, which is inputted in the $.sex$ text file by the user. The value

was always between 1.5 and 2 $\sigma$ in $MAG/arcsec^2$ above the background noise of the image. For space based images, the number of connected pixels tended to be 9 connected pixels, while ground based images had a lower detection threshold. Because ground based images could be much noisier, SExtractor had to be re-rerun with 5 and sometimes only 3 connected pixels above the analysis threshold. The corrected isophotal magnitude makes a Gaussian correction from this simple pixelated shape by assuming spherical symmetry. This correction would work decently for point-like objects (stars), but the Gaussian shape does not work well with extended objects like non-spherical galaxies-and worse on extended arcs. The first two magnitudes are shown in the two left images below. The aperture and auto magnitudes will be considered next.

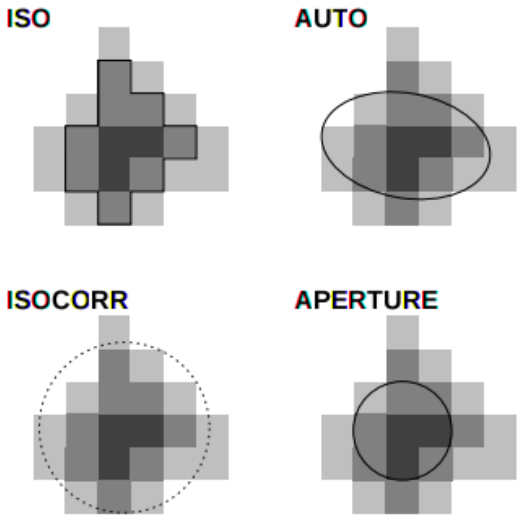


FIGURE 3.1: Different magnitude apertures in SExtractor shown on an example object detected above the minimum threshold.

The aperture magnitude is a more sophisticated photometric tool than the isophotal ones, but still employs circular apertures. These apertures are based on user-inputted values specific to the telescope's instrument. This would be a strong fit for foreground objects in an image but not so much for the magnitudes of extended arcs. The aperture magnitude is most useful for the development of color images from multiple bands. With a heterogeneous data set, the aperture inputs are color coordinated by SExtractor, allowing the difference image between two bands to be accurately represented and color calibrated.

The auto-magnitude uses an elliptical aperture based on the Kron radius of an ellipse. The Kron radius is given by:

$$\frac{\sum_i r_i I(r_i)}{\sum i I(r_i)} \tag{3.3}$$

where the sum over i indicates all the pixels in the object and the radius of the ellipse is given by the standard a and b axes, and $r_i$ is given by:

$$r_i^2 = cxx(x_i - x)^2 + cyy(y_i - y)^2 + cxx(x_i - x)(y_i - y) \tag{3.4}$$

where x and y are the SExtractor computed ellipse centers. This elliptical aperture is much more accurate than the previous three circular options and is the metric of choice for extracting the magnitudes of the arcs in this study. The check image file is a way to test your input parameters for a given image. Here, a strong arc detected in MOSCA 685[1] g band image taken at the Nordic Optical Telescope. The image is shown with the Kron ellipses drawn around the objects. This is a good way to check your deblending thresholds and minimum pixel area. The Sextracted magnitude area for Arc C is drawn on the image.

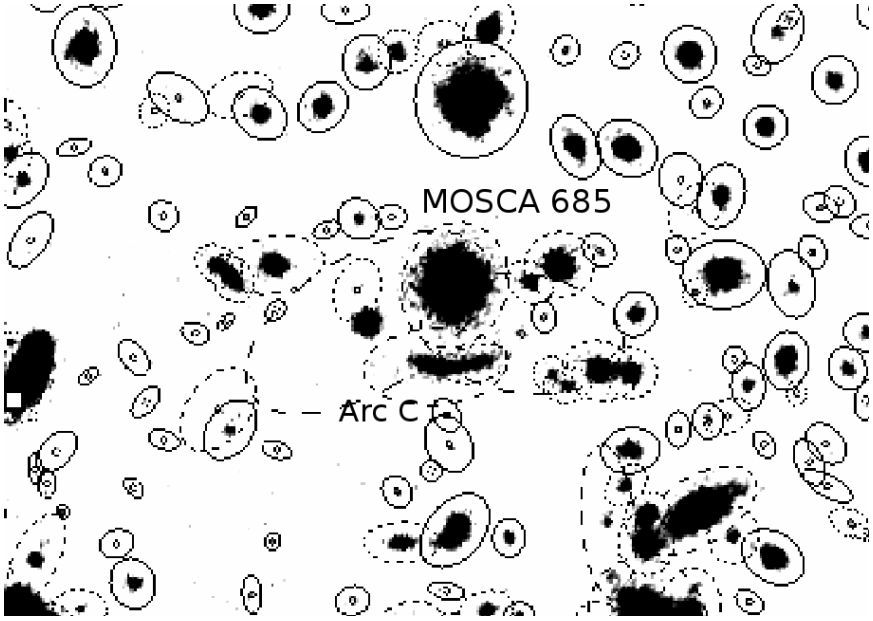


FIGURE 3.2: The aperture check image file shows whether or not the perceived arc is grouped as a single object or multiple. Also, if the calculated area overlaps too much with other objects–most commonly a bright central foreground cluster galaxy. Here the bright foreground galaxy overlaps the integrated flux ellipsoid for Arc C. The absolute magnitude for Arc C is 18.67.

For arcs located very close to the cluster center, removal of foreground galaxies is needed using programs such as GALFIT. The next section explains the galaxy removal process for cases such as for MOSCA 685.

[1] 685 refers to a preliminary identification system. For some clusters, the preliminary nomenclature is used. Appendix D contains images for all NOT clusters that include the NOT nomenclature and sometimes more familiar previous catalogue names, as well as the PSZ1 cluster name.

**Utilizing GALFIT for better Photometry**

Most radial arcs lie close to a bright lensing galaxy and removal of the central galaxy is sometimes necessary to get the brightness magnitude of the arcs with as little as possible saturation from nearby sources. The foreground galaxy morphology is best fit with a Sersic profile in GALFIT (Peng et al 2010). As explained in the GALFIT manual, the Sersic intensity profile (Sersic 1968) is defined by:

$$I(R) = I_e e^{-b_n\left[\left(\frac{R}{R_E}\right)^{1/n}-1\right]} \tag{3.5}$$

where $I_e$ is the intensity at the half light radius $R_e$ which encloses half of all the object's flux. $n$ is an index value that changes the shape of the curve. The classic Sersic profile is called de Vaucouleurs profile sets $n = 4$. This was based on observations of many galaxy shapes and is the value I choose to use in this analysis.

The magnitude from the original SExtractor run needs to be input to GALFIT. This can be calculated using the image's zero point magnitude and the exposure time of the image or set of images if the total image is comprised of dithered and stacked images.

$$m_{tot} = -2.5 log_{10}\left(\frac{F_{tot}}{EXPTIME}\right) + MAGZPT \tag{3.6}$$

Let's revisit the MOSCA g band image from the previous section on SExtractor. As shown in figure 3.2, the SExtracted Kron ellipse for the lensing galaxy overlapped with Arc C and needed further deblending. The g band image was run through GALFIT to remove this galaxy. A Sersic profile with a half light radius $R_e = 5.1$ and a Sersic index $n = 4$. GALFIT needs an input file with the Sersic parameters as well as the exposure time, plate scale, and photometric zero point magnitude from the header of the original FITS file. The input file also needs photometric and geometric information available from the SExtractor catalogue. This includes pixel position, axis ratio ($b/a$), axial position angle, and integrated magnitude.

The outputted image from GALFIT is then again SExtracted and the catalogue is re-analyzed as seen below:

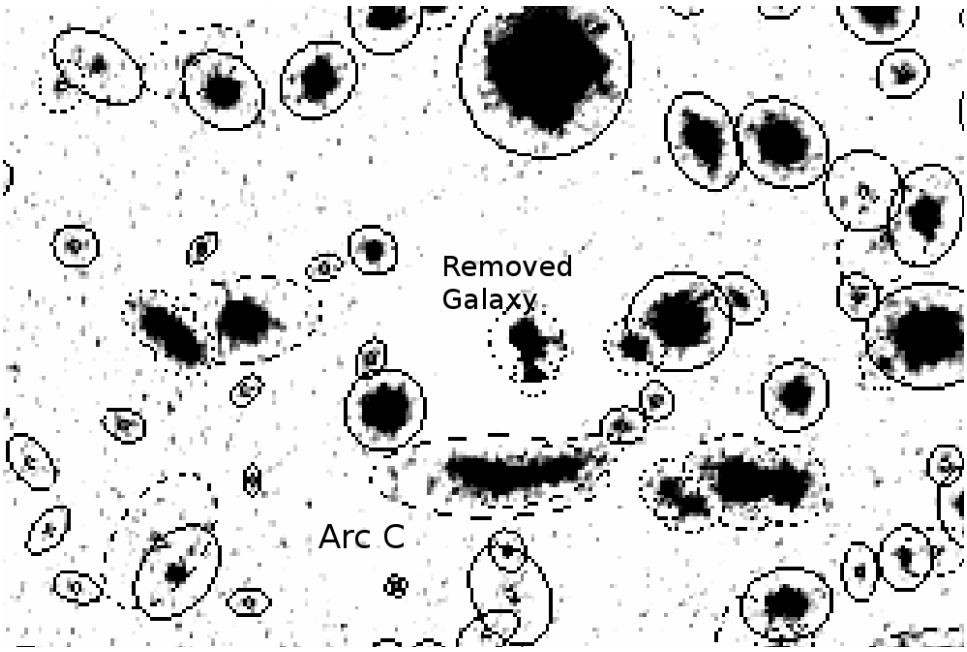


FIGURE 3.3: The aperture check image for MOSCA 685 g band. The Kron ellipse for Arc C no longer overlaps with the now missing bright cluster galaxy. The $MAG_{AUTO}$ from SExtractor for this image is 18.72.

The Kron ellipse for Arc C is now much better deblended from its line of sight neighbors and a more accurate absolute magnitude is calculated. The magnitude has dropped by .04 as a result of the galaxy removal.

GALFIT has proven very useful in extracting magnitudes for radial arcs and some tangential arcs that lie very close to their lensing centers.

### Other Photometry Parameters for SExtractor

There are a few other photometric variables that warrant mentioning in the image analysis process: pixel size as angular distance, the image seeing, and the convolution filter.

The amount of sky represented in each image pixel is informed by the FITS header. The information is needed for each SExtractor text input file for the image under study. Specific values for the telescopes and instruments utilized are presented in Chapter 4.

The seeing is defined as the combined atmospheric blurring, lens aberrations, and beam width of the CCD instruments that combine to spread the detection of a point source. The seeing is determined during observational runs by studying the instrumental detection of a well known star. The measured spread of the point source is determined by the full width half max (FWHM) in angular units of arcseconds on the sky. The FWHM is the distance from the central brightest point of the source detection to the radial point in which the brightest signal is exactly half. The image seeing

is much more important for images taken from ground based telescopes as the HST images have very similar low seeing values. The qualities of earth's atmosphere provide a large variance in the seeing for the small sky regions involved in extragalactic observations.

SExtractor uses an filter image of the Gaussian convolution of the point spread function to mask help mask background noise, pixel read errors, and gamma rays randomly hitting the detector. The filter images used are square Gaussian filters whose pixel size corresponds to the size of the seeing FWHM of the image. A set of image files ranging from 2x2 pixels up to 7x7 were employed in the SExtractor anaysis based on the seeing value of the image. Where the image seeing was not available at the time of analysis, SExtractor determines a seeing FWHM of the image that can be used to re-run the photometric analysis with greater accuracy.

**Calculation of Arc Magnitude**

With the SExtractor inputs tailored for each image, the program analyzes the image and outputs a catalogue of detected sources with calculations including the image x,y position, RA, DEC, angular position, elliptical parameters a and b, and the four calculated magnitudes .

Extended arcs, especially giant arcs, were often deblended into multiple catalogue entries-sometimes up to 40 different entries. The task was then to determine which catalogue entries corresponded to the arc, which were attributable to other nearby objects, and which were the result of combining sources. In terms of the latter, SExtractor sometimes had to be re-run with more sensitive deblending parameters or GALFIT had to be utilized to subtract bright galaxies or false detections too near the arc for accurate magnitude calculation.

Once the SExtractor catalogue sufficiently isolated the arc under photometric analysis, and Imcat tool, plotcat, was used to display a Matlab normalized sub image of the arc region in order to clearly see the arc and its boundaries, then to overplot the catalogue entries. Plotcat was a useful tool for compiling the subset of SExtractor catalogue entries pertaining to the arc itself. Another Imcat tool,*catstats*, was utilized to measure the variance of the image background in order to produce a more distinctive logarithmic image that highlighted foreground objects and reduced noise and oversaturation of bright cluster galaxies and foreground stars. Another useful feature of plotcat was the ability to overplot the SExtractor catalogue as a function of one or more of the catalogue parameters. For this study, the SExtractor entries were plotted as bright circles whose radius was a scaled value of the associated object's $MAG_{AUTO}$ calculation. This helps visually determine if a nearby object is too bright and may be saturating the SExtractor calculations of magnitude. When this occurs, it is best to employ the more sophisticated extraction methods of GALFIT for the bright source, and then reproduce the SExtractor catalogue.

Below is a plotcat image showing the formation of the SExtractor subset attributed to a giant arc.

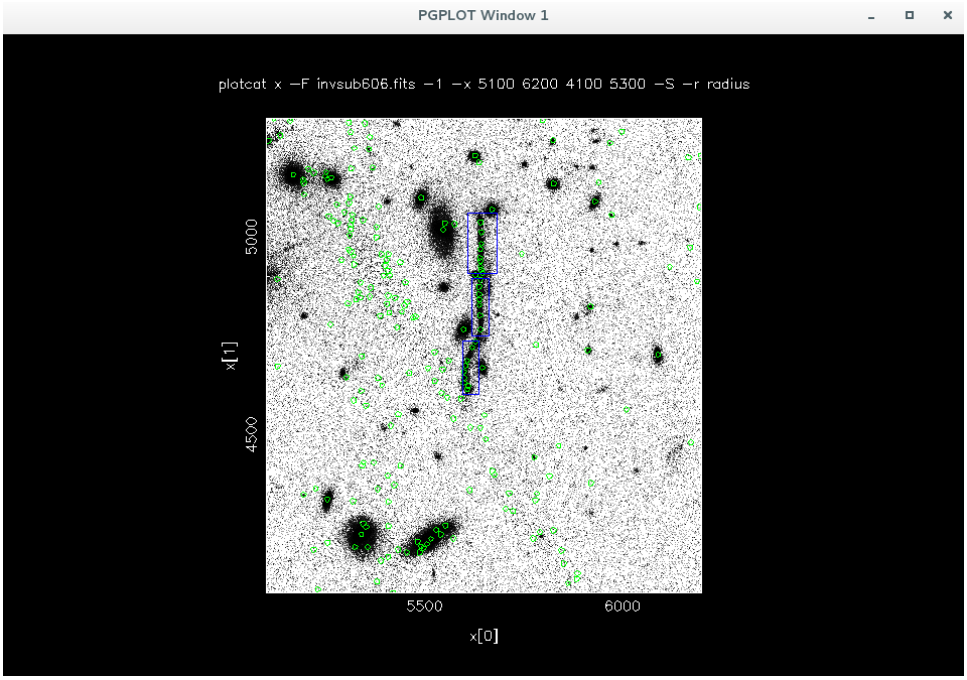


FIGURE 3.4: The arc region for the giant arc found in the cluster MACS 1206. The SExtractor catalogue entries are depicted as green circles.

In plotcat, the selected contents of the blue boxes seen above are then exported to a new catalogue file. A subset catalogue was produced for each strongly lensed image in the cluster survey. Each $MAG_{AUTO}$entry in the subset catalogue file was logarithmically added together to produce the total absolute magnitude for the strongly lensed image:

$$MAG_{total} = -2.5log\left(\sum_i 10^{(-0.4 \cdot MAGAUTO^i)}\right) \tag{3.7}$$

where i represents each entry in the arc subset file of the SExtractor catalogue. The results were compiled for the relevant tables in Appendices A and B.

### Distance to Brightest Cluster Galaxy

The Einstein radius describes the angular distance to the critical curve of the cluster lens. As explained earlier, a source object directly behind a spherical lens along our line of sight will create an Einstein ring with angular radius equal to the Einstein radius. For a spherically symmetrical galaxy cluster, the Einstein radius can be approximated by the distance from the mass center to the tangentially oriented arcs. In practice,

the mass distributions of galaxy clusters are never spherical and arc radii from lensing centers can provide a useful constraint on the cluster's distribution. Elliptical mass distributions will produce arcs at different radii from the cluster center. Also, off center source positions yield different magnification patterns. In order to better understand the mass distribution of the lensing clusters, the distances between the cluster centers and the location of the lensed arcs allows us to reconstruct the Einstein radius through various methods. These include looking separately at radial and tangential arcs in order to reconstruct the caustic and critical curves of the lensing cluster as well as utilizing the median arc distance to the brightest cluster galaxy (hereon BCG) as a statistical determination of cluster masses. More will come in Chapter 5, but here let's focus on how the distances are measured.

As shown in Chapter 1, the Einstein radius depends on the distances from the observer to the lens and from the lens to the source as well. While these are computed elsewhere, an important first measurement in the image analysis is the distance between the lensing center and the identified lensed objects. The brightest cluster galaxy often lies very close to the cluster's actual mass center and is easily identifiable in the image for most massive clusters. In my analysis, the brightest cluster galaxy is identified either using SExtractor catalogues or visually with ds9 to analyze individual galaxy brightness in clusters. Also, several papers that have previously studied some of the lensing clusters included in this survey contain BCG locations or modeled mass centers.

The BCG is the mass center for *cD* clusters, which are the most common configuration of rich clusters, the ones most likely to exhibit strong lensing. For the minority lensing spiral-rich clusters, using the brightest cluster galaxy in a cluster is a simplification of the actual cluster mass center that some researchers estimate through sophisticated cluster modeling. A mass reconstruction involving observed strong and weak lensing, and cluster galaxy relative velocities was not possible within the PSZ1 survey set breadth and project scope. The discrepancy between the locations of BCGs and true cluster mass centers are diminished when analyzing the findings of the entire statistical set. Using ds9, the distance in arcseconds between the center of the arc and the center of the BCG is found as follows:

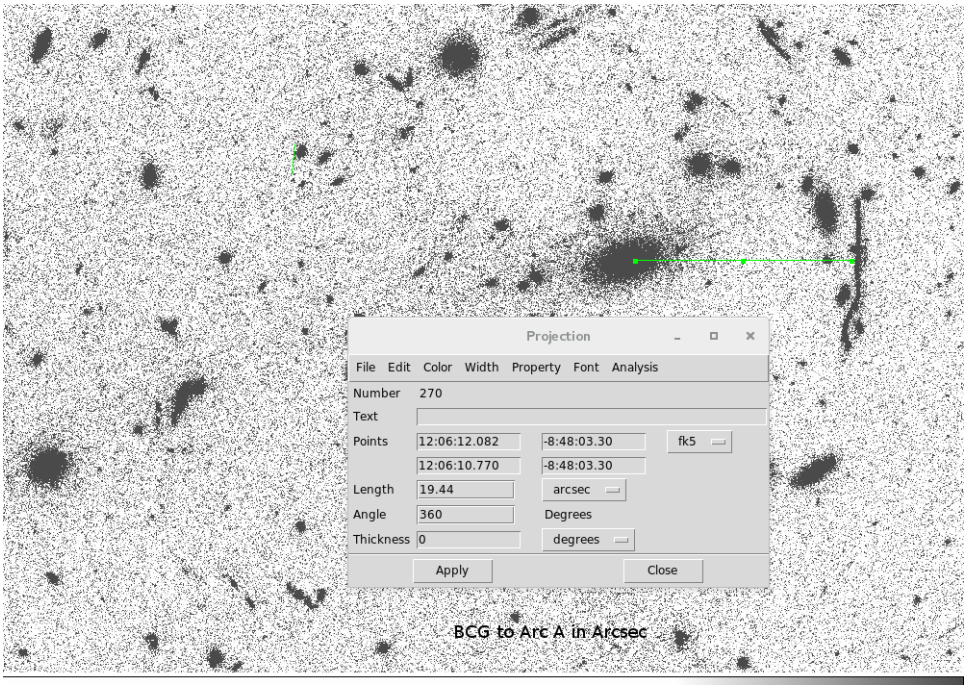


FIGURE 3.5: The center of the brightest cluster galaxy measured to the giant arc of MACS1206 in arc seconds.

ds9 includes a straightforward tool to calculate the distance between the center of the brightest cluster galaxy and the center of the arc segment. By selecting $Region->Shape->Projection$, a line can be drawn with length recorded in arcseconds.

### Length to Width Ratio

The length to width ratio is an often reported arc statistic that helps determine the amount of image distortion of the source. This helps to determine the critical curves and caustic lines of the galaxy cluster and hence the cluster mass distribution. The length to width ratio also informs lensed object detection algorithms. Strong lens detections still depend predominantly on human determination.

We define the length of an arc as the major axis of a lensed object. The length is then determined in ds9 using the length tool $Region->Shape->Projection$ for straight objects. We can use $Region->Shape->Circle$ to measure the length of curved objects. The width is defined as the perpendicular minor axis of the lensed object. For objects with low length to width ratios, the width can be determined similarly to the length. For extended objects with very high length to width ratios, the width may only be a few pixels in the FITS image, and photometry needs to be considered. Using ds9 or the IRAF toolkit, the width for extended objects has been calculated by creating a 1D histogram of pixel values for a cross section of the width. While most of the extended objects are fairly uniform

in width, there has been consistency in the analysis by taking a cross section of the thickest region of the arc in order to have conservative values in terms of length to width.

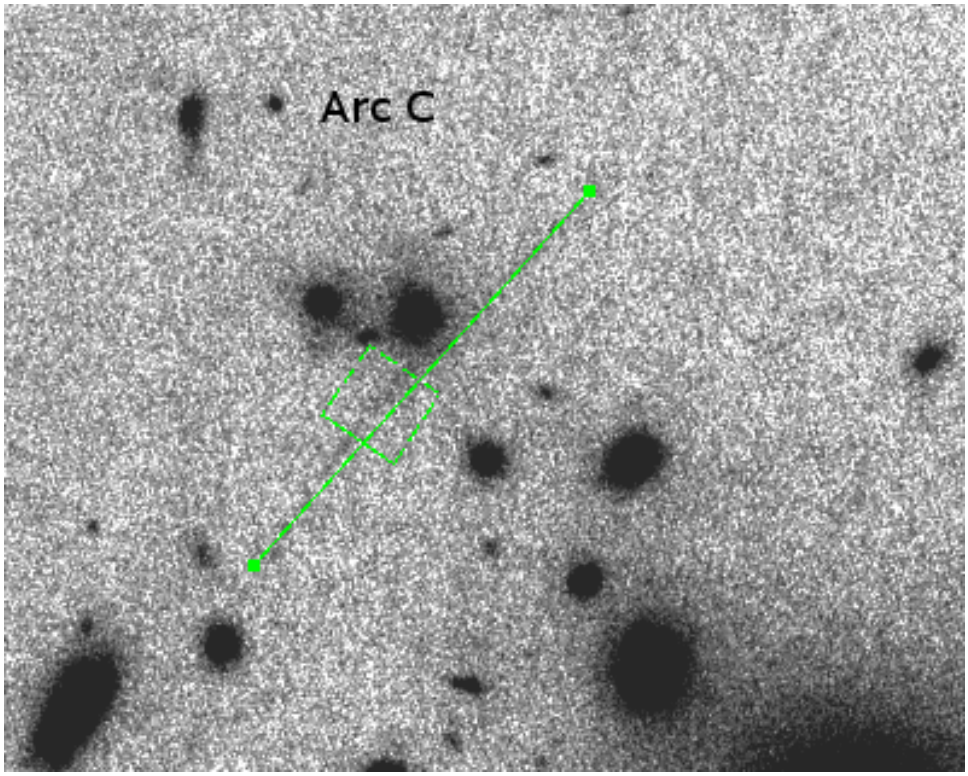


FIGURE 3.6: The length and width are both determined from ds9. The width involves taking the full width half max across a set interval along the arc's thickest section.

The cross section for each width calculation is 2 arcseconds along the length of the arc for consistency. The width is recorded as the distance between the two values full width half max (FWHM) centered around the peak pixel value. This accounts for the variance in exposures across the image set.

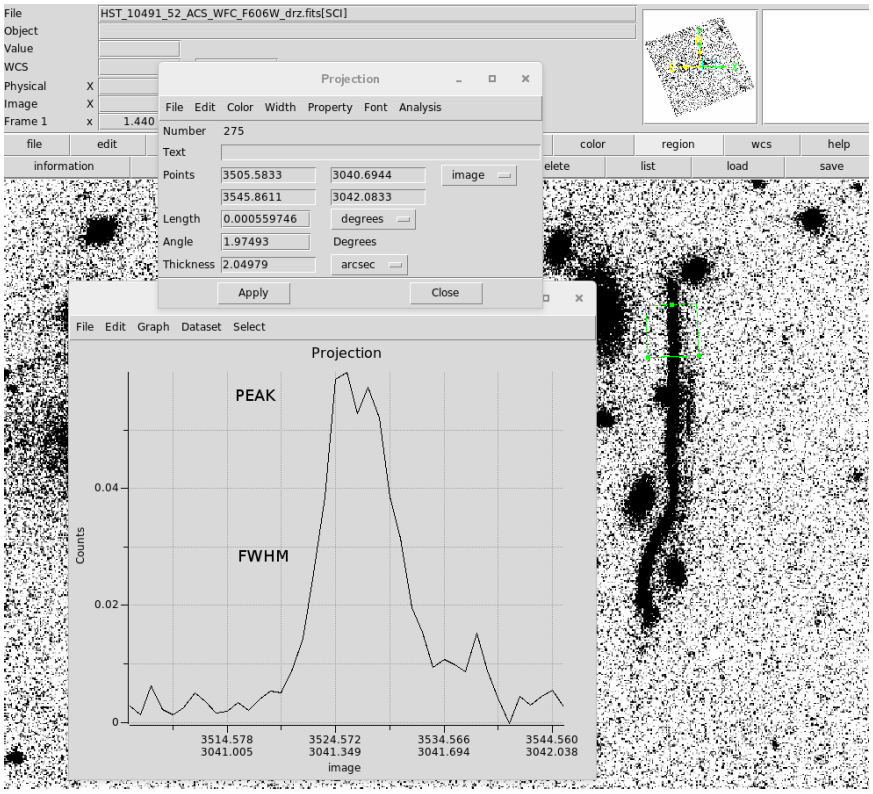


FIGURE 3.7: The 1D histogram is shown. The FWHM is 7.5 pixels in the above image.

### Tangential and Radial Arcs

Strong lensing can massively distort the background sources and the orientation relative to the cluster contains important information about the mass distribution of the lensing cluster. The source object can create both a radially oriented arc close to the cluster's mass center and a tangentially oriented arc beyond the critical curve as shown in Chapter 1. Giant arcs often lie tangentially along the critical curve as the source object in this case is closely aligned with the mass center along our line of sight.

For each analyzed arc candidate, the orientation of the elongation relative to the BCG or otherwise determined lensing center is recorded in the tables in the Appendices.

### Surface Brightness

SExtractor provides the photometric analysis tools for the cluster FITS images as explained above. Using SExtractor's photometric toolkit to get the magnitude of the lens, ds9 is used to calculate the visible surface area of the arc segment using $Region->Shape->Projection$. Using the area of the extended object, we can calculate the surface brightness as

$$S_b = MAG_{AB} + 2.5 * log\left(Area\left[arcsec^2\right]\right) \tag{3.8}$$

as the magnitudes are logarithmic values. Following is an example of the area calculation utilizing an HST FITS file for a giant arc and ds9 to calculate the area.

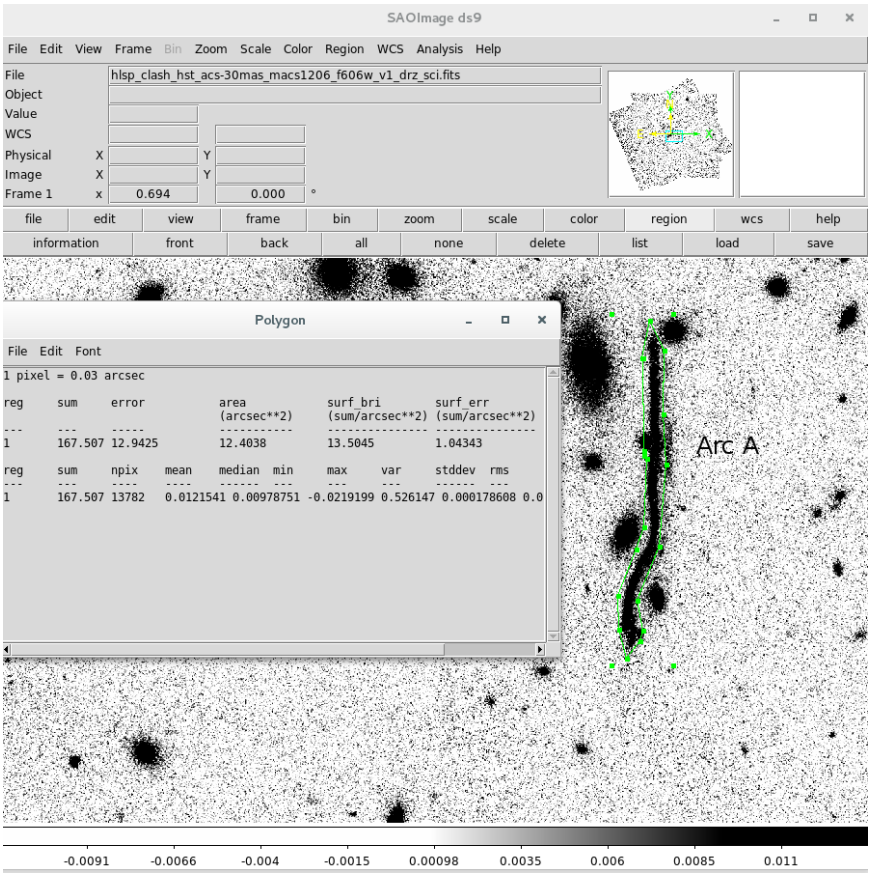


FIGURE 3.8: .

### 3.1.2 Spectroscopic Redshift

Spectroscopic analysis is important to discover and validate likely lensing clusters. In order to compare the lensing strength and masses derived from the arc radii from the cluster lensing center, the distances between the observer, the lens, and the source galaxy need to be known. Spectroscopy of lenses is outside the scope of this project however, so the source redshifts available for the PSZ1 cluster set are taken directly from previously published work or estimated based on cosmological models.

Spectroscopy of lensed objects is needed to determine how strong of a lens a galaxy cluster is. This information is also key in comparing the relative strength of lensing clusters, which allows us to build our 3D map of the visible universe and better constrain cosmological simulations. Bayliss et al 2011 provides a good outline of the spectroscopic analysis of strong lenses. Their work utilizes spectroscopic observations from the Gemini Multi-Object Spectrograph (GMOS) that pre-selected strong lensing clusters from the Sloan Digital Sky Survey (SDSS) that contained giant arcs.

Where source spectroscopy does not exist, it will have to be estimated according to the next section. Many of the arcs are simply too faint for spectroscopic analysis at this time. The statistical catalogue compiled here will become more accurate as more source redshifts become available and further analysis of cluster distances become available.

#### Estimates of Spectroscopy

Other spectroscopy studied sources of arc redshifts for HST data are referenced in the tables in Appendix A. There was no available spectroscopic data for the NOT, Subara, or CFHT images and the source redshifts were derived from cosmological model studies. For these, $z_{source} = 2 \pm 1$ as based on analysis found in the literature (Fedeli et al 2006). They showed that the optical depth $\tau$ peaks with $z_{source} = 2 \pm 1$ for giant arcs with length to width ratios greater than 7.5. Using this value most efficient lensing distance for source distance estimates makes sense for unknown arc spectroscopies where the arc has nevertheless been observed.

### 3.1.3 Photometric Redshift

The use of color images is useful visual tool to distinguish lensed objects from foreground clusters. While Appendices C and D contain mostly single band gray-scale images for clarity, some strong lens detections were aided by visually inspecting color images.

# Chapter 4

# Analysis and Results from Cluster Images

This chapter presents the observational data available in the search for strong lensing in the cluster set.

## 4.1 Hubble Space Telescope Clusters

Space telescopes offer a clear observational advantage over the best ground-based telescopes, so analyzing as many clusters as possible with the Hubble Space Telescope (HST) There are 62 clusters from the original survey with clear images of the cluster centers and with valid filters for lensing analysis found on the Hubble Legacy Archive.

From the Lensing Analysis Set of 147 galaxy clusters, Of the 62 clusters, 57 indicated lensing and 5 were determined to have no clear gravitational lensing whatsoever and were not included the final statistical table located in Appendix A. Images for these clusters were found in several of Hubble's instruments and detectors including the Wide Field Planetary Camera 2 (WFPC2), the Wide Field Camera 3 (WFC3) for IR and UV filters, and the Advanced Camera for Surveys (ACS/WFC). For the HST instruments, there is important information in the FITS image header file that is needed for SExtractor calibration. We must define the zero point magnitude for the date and HST camera associated with the cluster image.

### 4.1.1 Sample set from HST Legacy Archive

As the SZ effect depends on the electron density of the ICM, the cluster positions are more susceptible to position errors. The resolution of the data for an all sky CMB survey, the primary Planck mission, does not need to be collected with very high resolution to reach the mission goals, and this needs to be considered when locating PSZ1 clusters through other observational sources. Planck has shown the position error of its SZ signal versus known cluster centers cross coordinated with other projects.

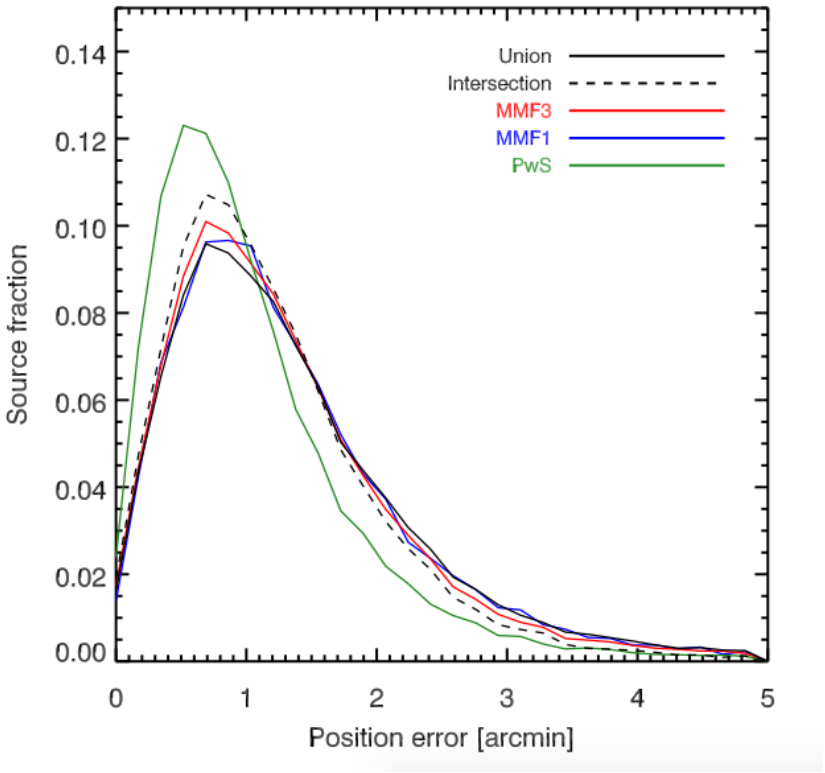


FIGURE 4.1: Most positional error is less than 2 arcminutes from actual location.

In light of this, the HST archive was searched for images that contained Planck cluster RA and DEC to detect actual clusters within 2 arcminutes of PSZ1 reported position to ensure that HST images that contained the surveyed cluster centers were found in cases of high positional error.

### 4.1.2 HST Instruments and Filter Parameters for Analysis

The HST has several different cameras and each has several filters. The HST Legacy Archive is a rich source of archival images and the most studied galaxy clusters have hundreds of images that show the region of interest. Selecting the best images for photometry takes a bit of time and understanding of which filters will best depict the lensing characteristics in this study. Broadband images can often be the best for detection as well as color images, which help determine background lensed sources from more homogeneous foreground cluster galaxies. Arcs are usually more luminous in the blue region of the spectrum than the cluster members, so filters that cover this range are the optimal starting point for visual detections. For the catalog, the filters ranging from F390W to F814W were prioritized. Infrared wavelengths were inspected secondarily when either no primary spectral images were available or when the primary images showed ambiguous arcs or no clear arcs at all.

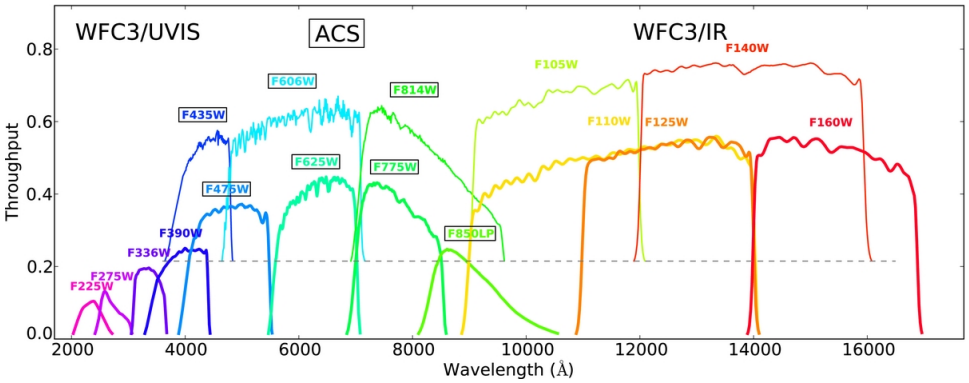


FIGURE 4.2: The HST instruments and available filters. My analysis primarily used the F435, F606W and F814W filters.

Several of the filters are used in this study, but most of the HST images are from the All Camera Survey (ACS ) with the F606W and F814W filters, which lie in the blue and green bands of the spectrum as most arcs emit the strongest magnitudes in blue filters. When using Wide Field Camera 3 (WFC3) images, the F435W filter was prioritized.

In order to calculate the absolute magnitudes of the arcs collected in the study, an objective normalizing zero-point magnitude is needed to be calculated for each image. Here is a brief overview of the calculation done for each HST instrument.

### HST Resolution

An important parameter needed for astrometry is the image pixel size. The Pixel sizes are given in the table below for all relevant cameras/instruments.

TABLE 4.1: HST Pixel Sizes

| Instrument/Detector | Pixel Size in Arcseconds |
|---|---|
| WFPC2/WF | 0.1 |
| WFPC2/PC | 0.05 |
| ACS/WFC | 0.05 |
| ACS/HRC | 0.025 |
| ACS/SBC | 0.025 |
| NICMOS/NIC1 | 0.025 |
| NICMOS/NIC2 | 0.05 |
| NICMOS/NIC3 | 0.1 |
| WFC3/UVIS | 0.04 |
| WFC3/IR | 0.09 |

**All Camera Survey (ACS) and Wide Field Camera 3 (WFC3) Photometry**

The ACS/WFC was used for 35 of the 58 HST images. The WFC3/UVIS instrument was used for 10 of the analyzed cluster images. For both the ACS/WFC and WFC3/UVIS instruments, the header of the FITS files contained the information needed for the calculation. The FITS header contains information to calculate three different absolute flux derived magnitudes:

$$VEGAMAG = -2.5log\left(\frac{F}{F_{vega}}\right) \tag{4.1}$$

$$ABMAG = -2.5log\,(F_{\nu}) - 48.6 \qquad STMAG = -2.5log\,(F_{\lambda}) - 21.1 \tag{4.2}$$

VEGAMAG is the logarithm of the ratio of the object's flux to that of the star Vega, such that VEGAMAG is always zero for Vega. STMAG is the flux density in wavelength units, and the ABMAG is the flux density in frequency units. The ABMAG relates to the SExtractor photometric output, and thus the ABMAG zeropoint had to be calculated for each ACS/WFC image and entered into the SExtractor input file. Two header files are needed for this calculation: PHOTPLAM, which is the pivot wavelength in Angstroms, or effective wavelength of the filter. The other is the inverse sensitivity PHOTFLAM ($ergcm^{-}2sec^{-1}$Å$^{-1}$), which is the constant flux level requeired to produce a 1 electron per second count rate as found in the STsCI ACS data handbook. The zeropoint for each image was calculated as follows:

$$ZEROPT_{ABMAG} = -2.5log(PHOTFLAM) - 5log(PHOTPLAM) - 2.408 \tag{4.3}$$

For the ACS/WFC, the pixel size and the FWHM are the other necessary photometric input parameters. The STScI Instrument science report states that the instrument is stable across most bands at 0.10" − 0.12" along the minor axis and 0.11" − 0.14" along the major axis. SExtractor requires a one dimensional FWHM value, and 0.11" was used for all ACS/WFC analysis.

For the WFC3/UVIS image, the average FWHM for the PSF was measured at 2.0 pixels. From the table above, the pixel size is 0.04", which gives a FWHM for the SExtractor text input file of 0.08".

**Wide Field Planetary Camera 2**

The WFPC2/PC and WFPC2/WF were used for 13 of the analyzed HST images. The header files for WFPC2 only contain the information to calculate the STMAG zeropoint which can be derived from the detected counts

parameter, PHOTFLAM (as above), and the PHOTZPT, which is a constant in all images at -21.1. The zero point magnitude can then be found by

$$STMAGZPT = -2.5log(PHOTFLAM) - 21.1 \tag{4.4}$$

In the STScI data handbook for WFPC3, there is a conversion table that we can use to extrapolate the AB magnitude zeropoint needed for SExtractor. The ST mag and AB mag zeropoints are nearly equivalent for the $547\lambda$ band, so analyzing images near this wavelength yield nearly equivalent zeropoint magnitudes in both regimes. The best images for WFPC3 were often the F606W band, which is close to F547W and where the difference in AB and ST zeropoints only differed by 0.57%, which translates to little error in the SExtractor determined AB magnitudes.

The FWHM for WFPC2/PC was found on average to be 4.5 pixels, which at a pixel size of 0.05" yields a FWHM of 0.22", which was used in the SExtractor text input file.

### 4.1.3 Results from Analysis

The tables in Appendix A are divided into two categories: table A.1: 28 HST lensing clusters which were primarily analyzed in this study (note some lensing clusters have been previously published with partial completion for this study) with 105 individual arc images tallied. And table A.2: 29 HST lensing clusters which were primarily analyzed in previously published works but also had HST images that showed the cluster regions of interest for further analysis. Table A.2 contain many more arcs as this list includes well two lensing clusters: Abel 1689, with 140 individual lensed images, and MACS J01717.5+3745, which has 85 individual lensed objects. Both clusters have been well studied elsewhere and the large number of entries is not included in Table A.2 but basic cluster information is provided, and the compiled catalogues are referenced. The redshifts included in A.1 come from published works as listed and other annotations denote information sourced elsewhere. Similarly some of the astrometric calculations in table A.2 were conducted in this research in order to include previously incomplete or not found data in the cluster statistics. Images of the whole HST image and the selected cluster regions with arc labels are included in Appendix C for all clusters in table A.1.

Looking at all HST clusters, 57 of the 62 HST analyzed images contain at least one strong gravitational lensing candidate. This yields a high lensing cluster percentage of 92%. However, there are methodological reasons for this. Since space based data is at higher resolution and is subject to much better observation conditions than ground based telescopes, the entire Lensing Analysis Set was searched for in the HST Legacy Archive. Many of the clusters discovered by the Planck SZ detections have been the subject of previous optical, X-ray selected cluster studies and also cluster lensing

studies, both strong and weak. Most of the strongest lensing candidate clusters were found in this archive so it isn't surprising that such a high percentage exhibited lensing. Thus, if we examine just at the HST cluster set in terms deriving arc statistics and looking at the cluster lensing ratio as a test of cosmological structure parameters, the results will be biased. The lensing statistics from a large SZ detected cluster set should address some of the concerns regarding the arc statistics observational overabundance as detailed in Meneghetti et al 2010 and elsewhere. Chapter 5 will synthesize the data for cross comparison statistics and address other issues that arise from comparison of different instruments.

For table A.1 several quantities were determined for the clusters and strongly lensed images through methods explained in Chapter 3.

#### Arc Nomenclature and Locations in Image

The arcs themselves are named alphabetically, beginning with A, and continuing until the lens candidate list is complete for each cluster. When two lensed images are determined to be multiple images of the same source, they are named alphanumerically, i.e. A1, A2, A3 etc. No greater multiplicity than 3 separate images of the same source were found in table A.1.

In all instances, the $(x, y)$ image arc coordinates were recorded in the table for ease of reference to HST Archive images or the labeled images presented in Appendix C.

#### Arc Lensing Center Coordinates and Distances to the Lensing Center

The cluster BCG was recorded for all images both in terms of the $(x, y)$ coordinates of the image as well as the RA and DEC values on the sky. In most cases for these massive clusters, the BCG is located at the mass and lensing center. There are some instances of merging clusters or other complicated cluster morphology that were evidenced by the strong arcs. Some clusters contain multiple lensing centers or individual cluster members are most directly responsible for the lensed image. Also, the Einstein rings found are singularly lensed. In these instances, the RA and DEC for the center of the main lensing source is also recorded on the line for the lensed arc. The radial distance between the arc and the lensing center is then calculated using these coordinates for cluster lensing strength estimates and comparisons seen in Chapter 5.

For example, with PSZ1G002.80+39.24, arc B is seen to have a peculiar arc indicating that two foreground galaxies are lensing the background source. The lensing center in this case is determined to be the less luminous galaxy on the right, due to the lens' proximity.

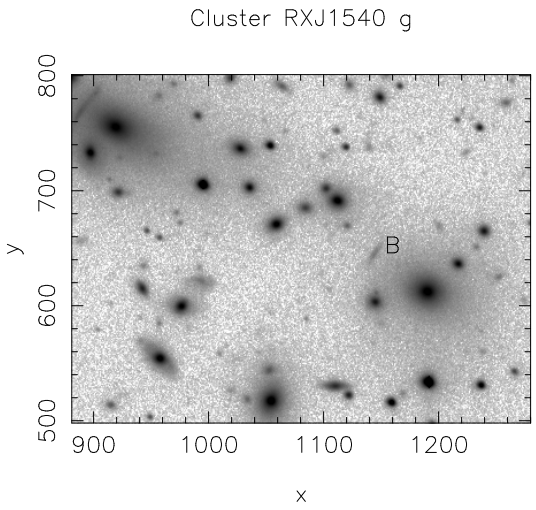


FIGURE 4.3: The galaxy on the right is the primary gravitational lens and the radius for Arc B is calculated accordingly.

### Length to Width Ratio

The arc length to width ratios presented are calculated according to Chapter 3. The values are only recorded to the nearest tenth in order to account for calculation errors. All arc length to width ratios were able to be determined for table A.1. The length to width ratios are incomplete in table A.2 where they are not available in the literature for the clusters with the highest occurrence of lenses. Where the lensed image locations were determined in this study, length to width ratios were calculated.

### Arc Area

Arc areas were also calculated geometrically according to Chapter 3. All arc areas were able to be determined.

### Absolute Magnitudes

As described in Chapter 3, The absolute magnitudes were computed using GALFIT, SExtractor, and plotcat. There were two multiply lensed images, A2 and A3, in cluster PSZ1 G068.32+81.81 that were too faint to register in SExtractor with the most sensitive input parameters.

**Arc Orientations Found in HST Set**

A cluster with tangential and radial arcs can give great insight into the cluster mass distribution. A great example involves the cluster MACS 2137, where observations of only the positions of a radial and tangential arc from separate sources are used to estimate the cluster radial density profile and hence constrain the cluster mass (Lachieze-Rey page 218-221). The lensing mass estimate is independently derived from the X-ray mass and the SZ $M_{500}$ masses, so comparing the estimate differences helps to determine cluster structure.

Also, the overall ratio of radial to tangential arcs in the statistical set has been shown to be insightful for constraining cosmological parameters (Oguri et al 2002). **more here**

The full image set is in Appendix **??** for table A1. To illustrate the detected radial and tangential, here are two nice examples from the set:

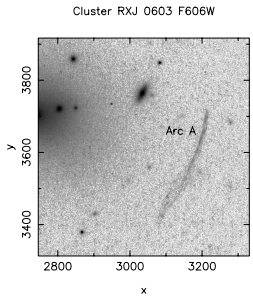


FIGURE 4.4: Example of detected Giant Tangential Arc in PSZ1 G170.22+09.74.

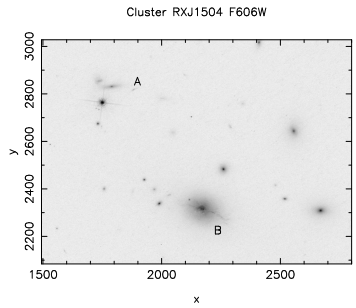


FIGURE 4.5: Example of detected radial arc. B in PSZ1 G355.07+46.20.

Einstein rings can Three partial or nearly complete Einstein rings were also found in the A.1 set, and here are the two clearest images:

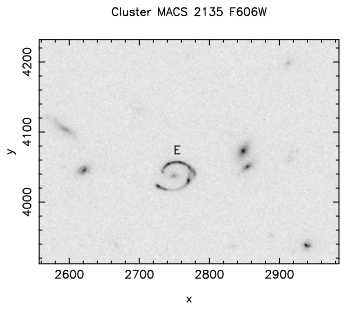


FIGURE 4.6: Einstein Ring in PSZ1 G053.42-36.25.

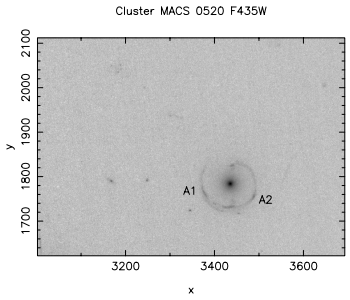


FIGURE 4.7: Example of ring with two separate photometric analyses. A1, A2 in PSZ1 G195.78-24.29.

Chapters 5 and 6 will explore the statistics of the arc orientations across the whole LAS.

## 4.2 Ground Based Telescope Clusters

The higher resolution of the HST makes it the primary target for evaluating the LAS. With 42% of the set analyzed with HST, there are plenty of clusters left to analyze.

### 4.2.1 NOT Instrument and Filter Parameters for Analysis

The NOT is a 2.5m located in the Canary Islands. The two instruments utilized in this study are the Andalucia Faint Object Spectrograph and Camera (ALFOSC) and Mosaic Camera (MOSCA). In 2014, a MOSCA observation run was conducted to cross validate some of the clusters of the PSZ1 catalogue. After this run and combined with previous NOT cluster detections, 44 MOSCA observed clusters and 4 ALFOSC observed clusters (selected only when there was not existing MOSCA image data) were analyzed for evidence of strong lensing.

#### NOT Resolution

The MOSCA instrument has a pixel size of 0.217” per pixel for all images, and, equivalently, the ALFOSC instrument has a pixel size of 0.21” per pixel. Subject to atmospheric variations as well as intrinsic FWHM beam

width of the instruments, the seeing FWHM values are taken from analysis done during the nights of observation at the telescope. The seeing values range from [0.50", 1.45"], with a median value of 1.00".

#### Magnitude Calculation

Where available magnitudes were calculated using SExtractor for 3 bands, *gri*. The band which showed the clearest and brightest arc was used as an astrometric reference image, with SExtractor then running the photometry on the secondary band image to calculate the absolute magnitudes for all 3 filters.

The magnitude zero points needed for the most accurate calculations were not available at the time of analysis. Instead a zero point magnitude of 30.0 was used for all NOT images, so the catalog will need to be recalibrated when actual image zero points are determined.

### 4.2.2 Subaru Telescope and Parameters for Analysis

After the NOT analysis, the still missing cluster images from the LAS was screened for existing Subaru data. There were 13 clusters found in the Subaru archives not found in the HST Legacy Archive, or part of the NOT observations.

#### Subaru Prime Focus Camera (Suprime-cam) and Resolution

The images were made using the 8.2 m University of Hawaii telescope and the optical Suprime-cam instrument which creates a mosaic image from 10 individual 2048 x 4096 CCD exposures examined here in the g', B, and V band filters. The images' resolution was 0.2", and the image's seeing values range from [0.68", 0.72"]. Magnitude zero points were not available at the time of analysis, so as with the NOT images, a placeholder value of 30.0 was used for photometry.

### 4.2.3 Canada-France-Hawaii Telescope

The final archival data set checked for clusters was the Canadian Megapipe Archive, which contained observational data from the MegaPrime/MegaCam instrument of the 3.6 m optical/infrared Canada-France-Hawaii Telescope. The remaining clusters of LAS yet to analyzed were searched for in the archival data (Canadian Megapipe) and 2 clusters were found, with neither showing any strong lens candidates.

#### CFHT MegaPrime Resolution

The resolution per pixel is 0.187” and the seeing for the two examined clusters had a FWHM of 0.7”.

### 4.2.4 Clusters Analyzed with Ground Based Images

Of the 47 clusters detected (43 with MOSCA, 4 with ALFOSC) at NOT, 16 were found to have at least one strong lensing candidate, with 40 separately lensed images in total. 39 were tangentially oriented arcs, and 1 radial arc was found. For the Subaru Telescope, 3 of the 13 showed a strong lensing candidate with 7 tangential arcs in total. The results for all ground based cluster images are located in Appendix B.

#### Photometric Redshift Arc Detections

The use of color images to distinguish between cluster member galaxies and magnified images of distant galaxies is important for visual detection of strong lens candidates. This method is of course useful for HST images as well, however the lower angular resolution and higher seeing values of the ground based telescopes made the use of visually different redshifts more important in selecting lens candidates.

Once such example is for PSZ G132.49-17.29, a MOSCA cluster. There are 7 blue arcs apparent in the cluster that are much more difficult to distinguish in the single band photo on the right

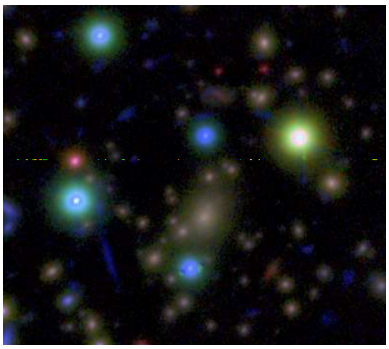

FIGURE 4.8: MOSCA 475 gri color image showing cluster center.

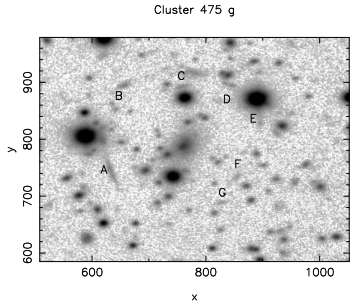


FIGURE 4.9: g-band image identifying the arc candidates.

This cluster has the largest number of separate arcs among the ground based cluster set and illustrates the importance of multiband photometric analysis to identify arcs.

### Length to Width Ratio and Arc Areas

For all arcs found in ground based images, the length and width were calculated, and their ratios recorded in table B.1. The areas of each arc candidate are also calculated so surface brightness of the objects can be determined.

### Arc Orientations

Only 1 radial arc of the 40 total arc candidates was detected in the ground based data. There were 3 giant arcs with $L/W > 7.5$ and $MAG < 24.0$ in the set. Following are two nice examples from the ground based set, one of the giant arcs and the sole radial arc.

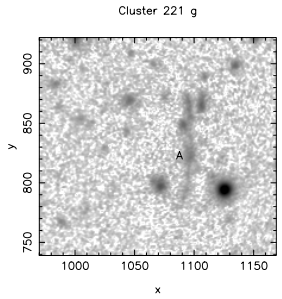


FIGURE 4.10: Giant arc in PSZ1 G066.41+27.03.

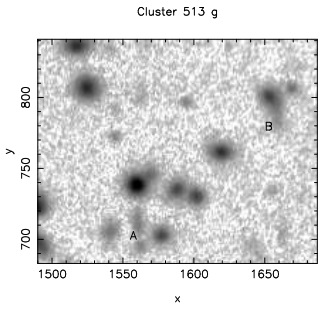


FIGURE 4.11: Radial arc in PSZ1 G143.28+65.22.

With the cluster set analyzed and the statistics compiled, we can look at some interesting results.

# Chapter 5

# Arc Statistics of the Lensing Analysis Set

## 5.1 Analysis of the LAS

There are 22 clusters that did not have sufficient data from any of the observational sources. So the original 147 clusters will drop to 125 for the statistical analysis. 72 lensing clusters in total for a cluster lensing percentage of 57.6% for the entire Lensing Analysis Set.

## 5.2 Statistical Outcomes of Analysis

### 5.2.1 Comparing HST to Ground Based Cluster Images

As described in Chapter 4 among the entire LAS, there are instrumental differences between telescopes and an HST selection preference that should be addressed. In order to minimize variables for presenting the statistical analysis, the ground based and HST data will need to be distinguishable in the results.

#### Ground Based Seeing and Resolution Constraints

The ground based images are susceptible to atmospheric variations, and this variability needs to be accounted for in order to compare space based and ground based data. These ground based issues can have a great affect on the arc catalogue because arcs are often very thin. An arc in an HST image may have a high length to width ratio with obvious lensed characteristics, whereas the FWHM seeing value of a ground based image may obscure the extended arc and reduce the observed length to width ratio to a point in which it is very difficult to differentiate between lensed objects and cluster member galaxies.

Looking at the lensing data from NOT, Subaru, and CFHT images, generally, as the seeing is worse the fraction of clusters with observed lenses

relative to the whole cluster set decreases. Therefore we can apply a correction factor to the lensing fraction of the ground based data for images with poor seeing values. This raises the lensing fraction of ground based clusters but there are still other reasons why the Hubble data has a higher ratio including the prevalence of X-ray selected clusters in the HST archive.

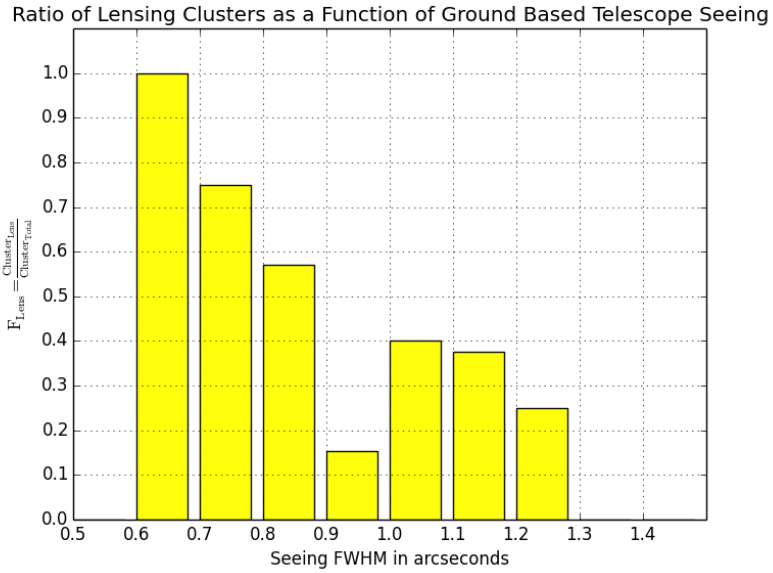


FIGURE 5.1: There are 60 PSZ1 clusters with ground based observational data analyzed in this project. The above histogram shows the cluster lensing fraction in 0.1" bins.

There is a reduction in the lensing clusters as the seeing FWHM increases, and a linear relation is a reasonable fit to the data. 0.5" to 0.6" FWHM seeing values are needed in order to pick up at last one arc per cluster. In order to combine the HST images with the ground based data for an estimated total lensing count and frequency ratio, we could utilize the following regression to predict the number of lensing clusters missed due to poor seeing conditions.

$$F_{Lens} = -0.61 \pm 0.28 \cdot FWHM + 0.92 \pm 0.29 \tag{5.1}$$

Resolution is 2-4 times better for HST images than NOT, Subaru, and CFHT which further complicates the direct comparison between the two telescope classes. For many statistical conclusions presented here, it makes sense to consider the two classes separately. The image quality suggests that the frequency of lensing detections will be lower for ground based data. However, as mentioned in Chapter 4, the HST archive can be biased towards X-ray selected cluster surveys which have tended to show an overabundance of lenses. These considerations should be kept in mind when analyzing total set statistics but the large survey size helps to balance out these effects, and through looking at the set as whole, we can

make significant comparisons between an SZ selected cluster survey to previous X-ray and optically selected surveys.

#### Cluster Masses

The SZ masses from the HST set are on average larger than the ground based masses. This can be attributed somewhat to the selection bias of past HST cluster surveys, some of which are addressed in Chapter 2. There is an overabundance of X-ray selected clusters in the HST archive, and this presents a another challenge to direct comparisons between HST and ground based cluster image observations.

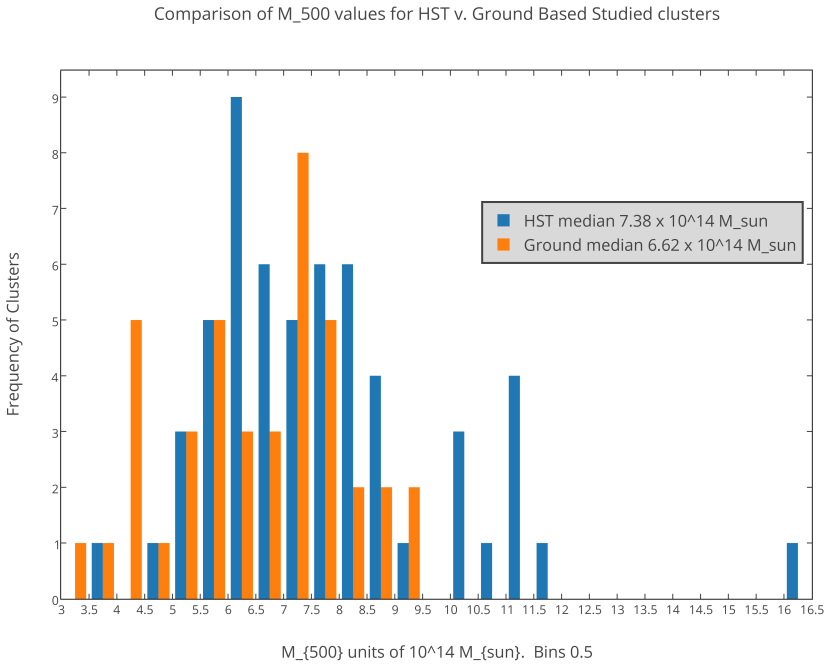


FIGURE 5.2: The HST clusters are on average more massive than the ground based clusters analyzed.

As described in Chapter 4, the most massive clusters tend to have HST data, based on previous cluster sets and HST observation runs, and are thus more likely to be lenses. The HST data is still SZ selected and will be comparable to lensing statistics of X-ray and optical sets more reliably than the ground data. Now let's look at the total LAS set, and the frequency of strong lenses.

### 5.2.2 Lensing Cluster Ratio

For the 124 confirmed and observed clusters, 72 contain at least one strongly lensed candidate. For the 62 HST clusters, 57 are lenses for 91.9% lensing fraction. Of the 63 ground based images analyzed, 19 are lenses for a

lensing fraction of 30.2%. The overall statistics of clusters help to explain some differences between these two sets.

### Cluster Redshift

Looking at the redshift of the total observed clusters compared to those with lens candidates, we see an overall increase in redshift in the lensing clusters.

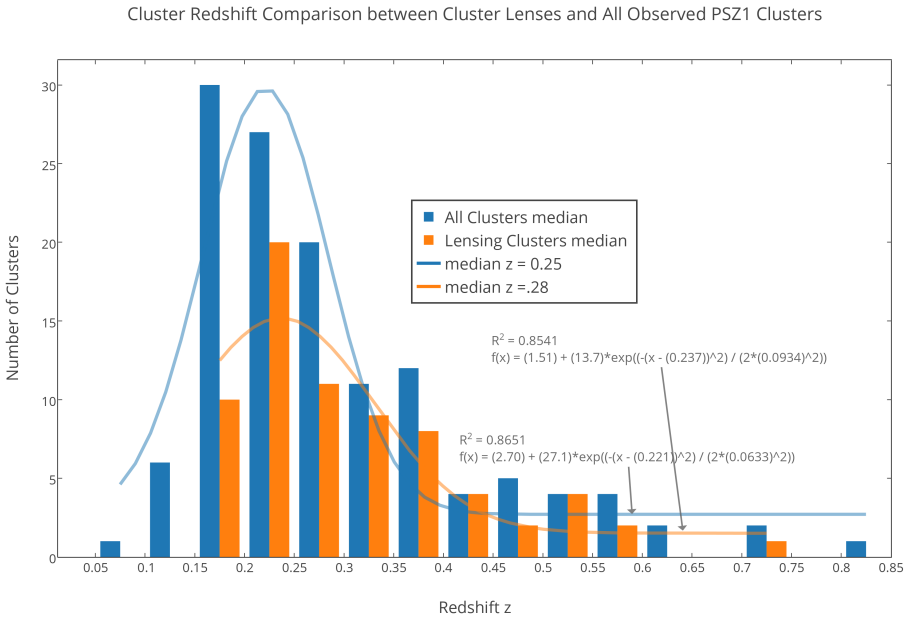


FIGURE 5.3: The redshift of clusters exhibiting strong lenses have on average a higher redshift of 0.03

The lensing cluster fit also exhibits a longer tail than the overall cluster set. A much higher fraction of the high redshift clusters were determined to be lensing clusters than the low redshift end of the spectrum. We see then that higher redshift is correlated with more efficient cluster lensing within the dataset.

### Cluster Signal to Noise

We can look at how the fraction of these clusters with lenses changes as a function of the signal to noise ratio determined by the Planck Sunyaev-Zel'dovich survey. As described in Chapter 2, the original PSZ1 cluster subset includes only clusters with signal to noise ratios greater than or equal to 6.0.

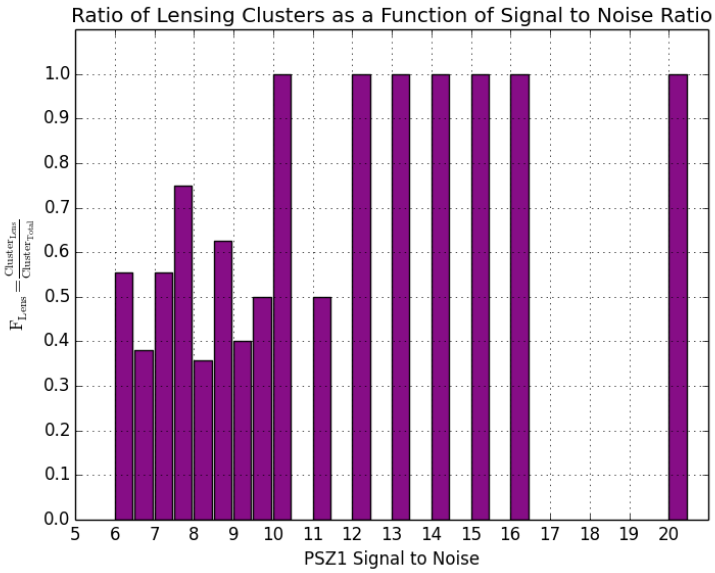


FIGURE 5.4: The entire data set is included in this plot. The above histogram shows the cluster lensing fraction in $\Delta SNR = 0.5$ bins for $SNR < 10.0$.

We see that the strongest SZ signals in the cluster set tend to be lenses. All clusters, except one, with $SNR > 10$ are lenses.

### 5.2.3 Arc Radius to Lensing Center

Now let's look at the distribution of the arc radii to the lens center across the LAS. The Einstein radius can be approximated by the tangential arc angular distances from the cluster center. Following is the cumulative distribution for the un-normalized arc radii to lensing centers in the whole set.

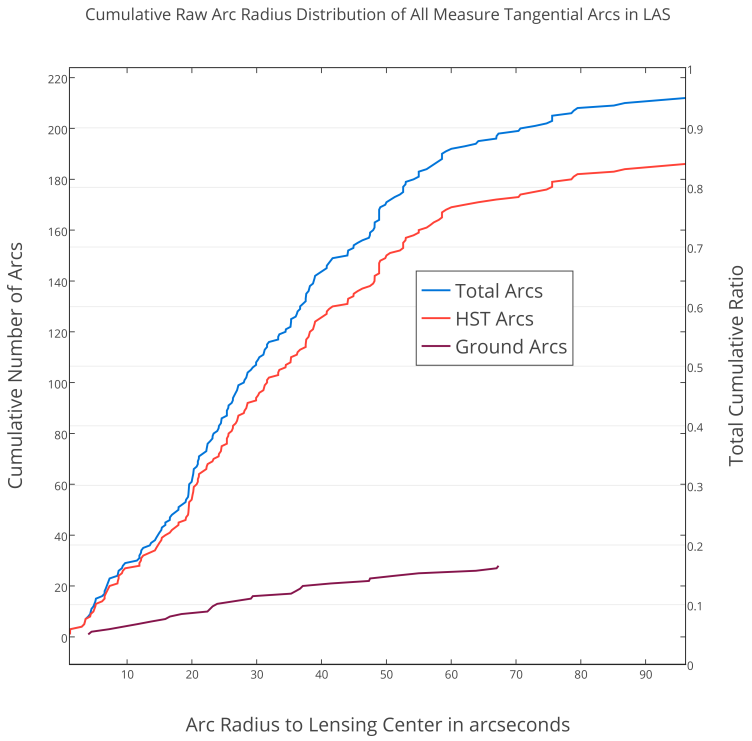


FIGURE 5.5: The completeness of the LAS as a function of the arc radius from its lensing center.

There is a greater distribution of radii in the HST data and a long tail end for completeness as shown in the plot above.

### Radius Normalization

We must normalize for the distances between the three objects creating the lens: the observer, the galaxy cluster, and the background source. This is necessary to compare the radii, and then compare the mass distributions, of the galaxy clusters. In order to normalized and compare across clusters, recall the geometrical calculation of the Einstein radius:

$$R_{arc}^2 = \Theta_E^2 = \frac{4GM}{c^2}\left(\frac{D_{LS}}{D_{OS}D_{OL}}\right) = \frac{4GM}{c^2}D \tag{5.2}$$

, defining D as the distance parameter. Since the 3 distances that D depends on differ from cluster to cluster, the observational arc radii will change accordingly. To normalize, we can calculate $D_{avg}$, or $\overline{D}$, for the all lensing clusters and normalize the arc radii by:

$$\Theta_E^{norm} = \sqrt{\frac{\overline{D}}{D_{LENS}}} \tag{5.3}$$

Note that the constant terms and mass dependencies cancel out. The parameters of $D_{avg}$ are derived from the entire set of HST and ground based clusters with at least one tangential arc that have PSZ redshifts and calculated arc radii. To calculate the angular distances from the PSZ redshifts, I adopt a flat $\Lambda CDM$ cosmology with the pressureless matter content $\Omega_m = 0.3$ and the cosmological constant $\Omega_\Lambda = 0.7$. We then calculate the angular distances in Mpc according to the following equations:

$$D_L = \frac{c}{H_0}(1+z)\left[\eta(1,\Omega_m) - \eta\left(\frac{1}{1+z},\Omega_m\right)\right] \tag{5.4}$$

where $D_L$ is the luminosity distance, $H_0$ is the Hubble constant and $\eta$ is the conformal time,

$$\eta(a,\Omega_m) = 2\sqrt{s^3+1}\left[\frac{1}{a^4} - 0.154\frac{s}{a^3} + 0.434\frac{s^2}{a^2} + 0.19097\frac{s^3}{a} + 0.066941 s^4\right]^{-\frac{1}{s}} \tag{5.5}$$

and

$$s^3 = \frac{1-\Omega_m}{\Omega_m} \tag{5.6}$$

Finally, we can get the angular distance $D$ from $D_L$,

$$D = \frac{D_L}{(1+z)^2} \tag{5.7}$$

$\overline{D}_{OL}$ is derived from median z of the tangential lensing clusters: 0.25. $\overline{D}_S$ is determined to be the median arc redshift of the whole set of tangential arcs. Most arcs do not have redshift values, so we turn to the literature of past surveys to find an average redshift of lensed sources. Xu et al has found a median photometric redshift of 1.9 from their own calculations and the X-ray selected CLASH survey. There is much estimation in this parameter, and they have shown that an accurate median source redshift is more accurately $z_s \approx 2 \pm 1$. This study utilizes this information and sets the angular source distance for all tangential arcs without previously determined source redshifts (Bayliss et al 2011) (Bayliss 2012).

In the absence of more sophisticated mass distribution estimations for the clusters, the statistical set employs the spherical approximation outlined in Chapter 1. For lenses with multiple tangential arcs around the same lensing center, the method I adopt for $\Theta_E$ is the median tangential arc radius. The maximum tangential $L/W$ ratio for each lens is another valid approximation. The median tangential radius for 33 HST tangential lensing median centers are presented as a histogram.

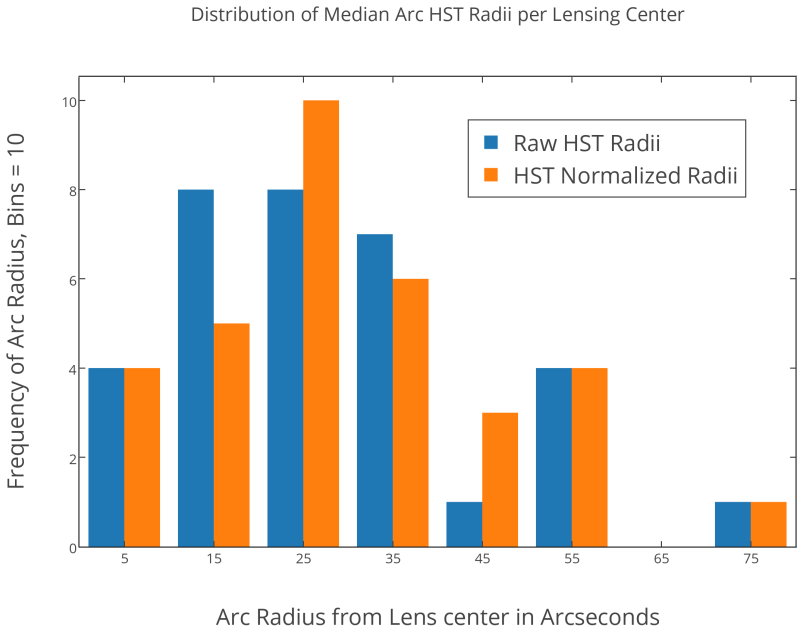


FIGURE 5.6: Comparison of the arc radii between the distanced normalized arc radii and the raw radii measured for each cluster.

Here we see that the normalized radius calculation has a tighter distribution than the raw radii.

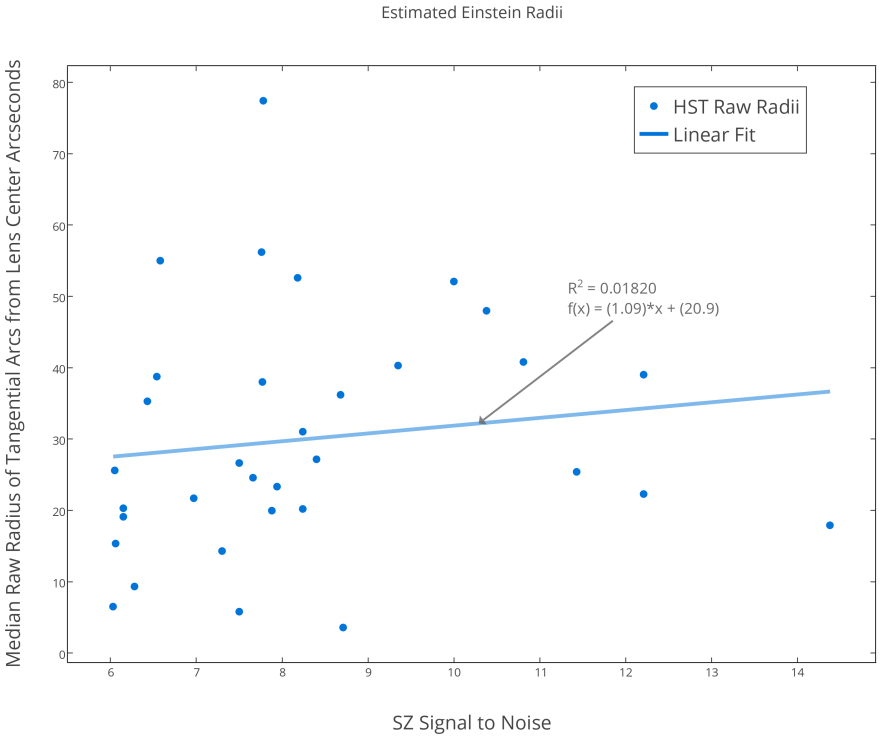


FIGURE 5.7: Un-normalized median arc radii with linear regression.

There is a good deal of variation among the more numerous low signal to noise clusters. The median radius here is 25.6". There is an upward trend of radial distance of the median cluster as the mass of the cluster increases.

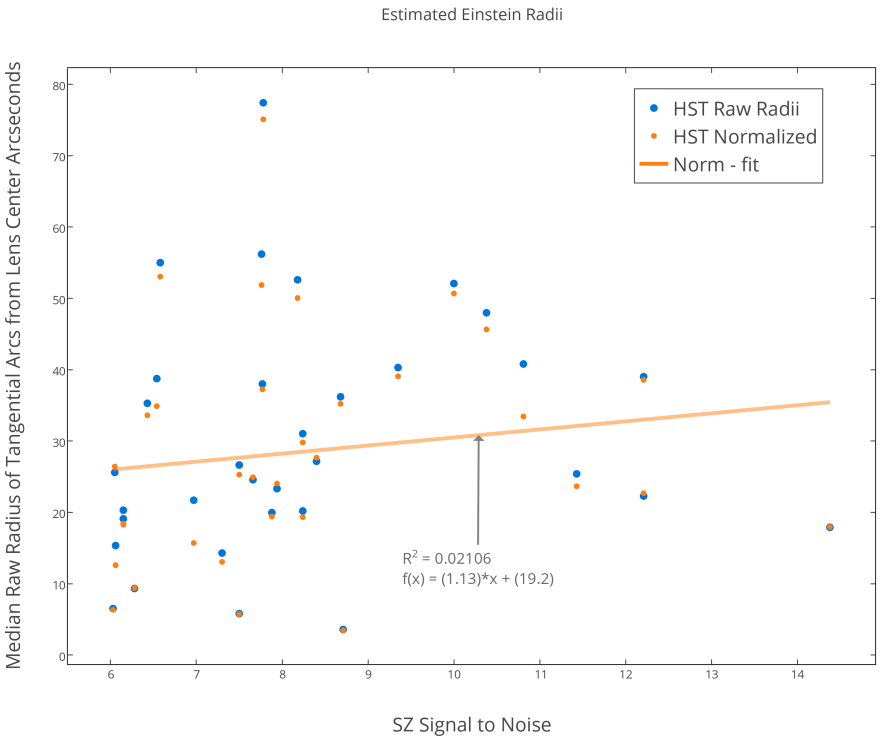


FIGURE 5.8: Normalized mean arc radius for each cluster. Large signal to noise is correlated to more massive clusters.

The normalized radii allows us to compare the strength of the lenses across the different clusters. Notice how the difference between the raw and normalized radii tends to increase but the normalized is almost always a lower value. However, the linear fit shows that there is a slightly stronger correlation between the normalized radii to the signal to noise; the higher the signal, and the higher the mass, the larger the Einstein radius. The raw radius is now presented as a function of redshift instead of signal to noise for all tangential arcs in HST and ground based sets.

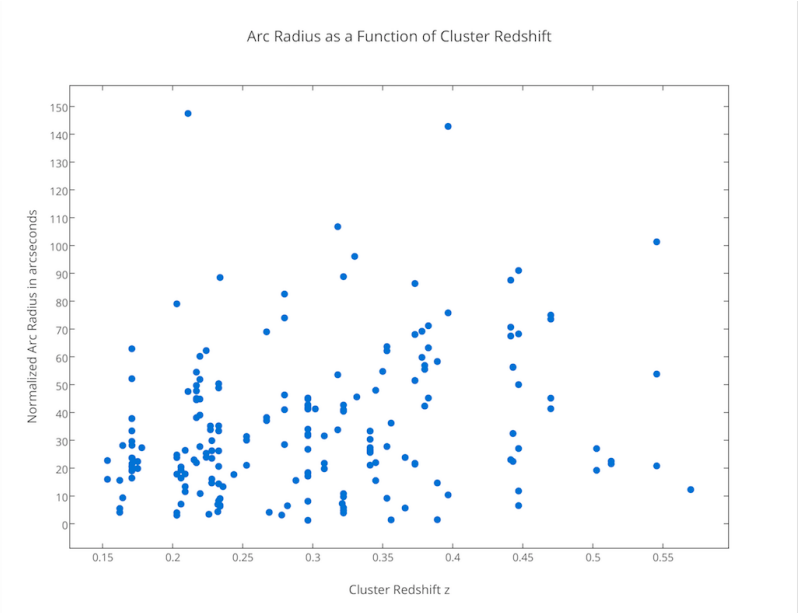


FIGURE 5.9

There is a lot of dispersion with the raw data. Comparing the total lens radius to that of the median radius for each tangential lensing cluster. Below the raw and normalized radii are compared across the statistical set. The median arc for the raw radius is actually larger than the normalized median radius.

TABLE 5.1: Statistics of Arc Radii

| Type | Number of Tangential Arcs | Raw median R | Norm median R |
|---|---|---|---|
| All arcs | 203 | 29.65” | 31.00” |
| Lensing cluster median arc | 64 | 26.36” | 25.96” |

Now let's turn to the number of lensed images seen per cluster.

#### Arc Frequency

To compare the SZ set with other cluster surveys in the literature, we can plot the frequency of arcs occurring in clusters in the whole set.

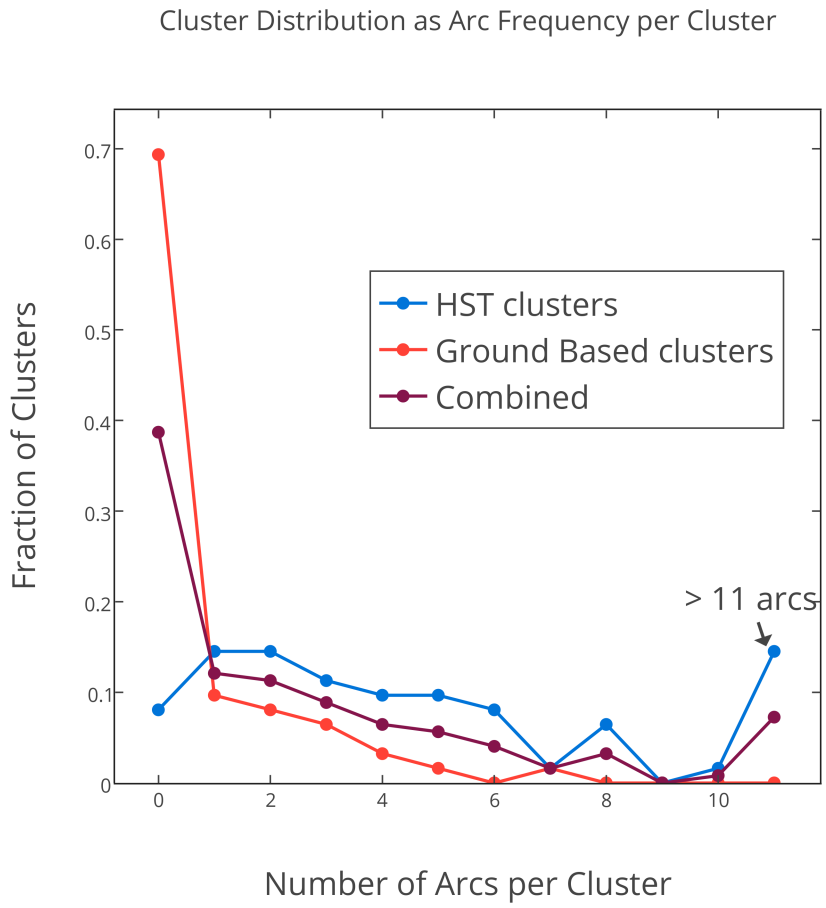


FIGURE 5.10: The number of arcs per cluster for all 124 observed set clusters. Note that 9 HST clusters had more than 10 arcs, ranging from 11 to 140.

We can compare this observed arc distribution to the literature. See Horesh et al for direct comparison.

### 5.2.4 Length to Width Ratio Distributions

All arcs are presented here in two histograms for HST and ground based data.

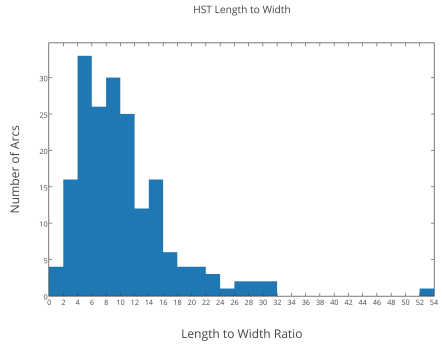


FIGURE 5.11: Distribution of Length to Width Ratios for HST strong arc candidates. Bin size = 2.

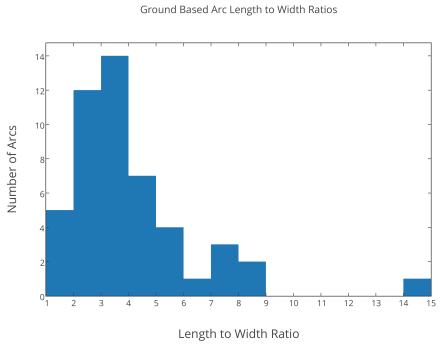


FIGURE 5.12: Distribution of Length to Width Ratios for ground based strong arc candidates. Bin size = 2.

The distribution of $L/W$ ratios for the HST and ground datasets are presented. There is a greater sample set for the HST, but both show similar trends. For the HST data, the prevalence of arcs with $L/W > 14$ is much less than less extended arcs. We can utilize this data to help classify giant extended arcs from other arcs in the strong lensing spectrum.

The ground based data shows the arcs detected here have more equal lengths and widths than the HST data. The seeing is one cause of this, where widths are widened. This also helps to explain why fewer arcs are found in this data as seen in the first section of this chapter. The better conditions for HST images make the left histogram more representative of actual length to width ratios of the arcs across the SZ cluster set.

### 5.2.5 Arc Magnitudes

The distribution of the HST arc magnitudes are presented below. The ground based images are not included because of the 30.0 magnitude zeropoint values used as placeholders for the magnitudes derived there. However all magnitudes are available as preliminary values in Appendix B.

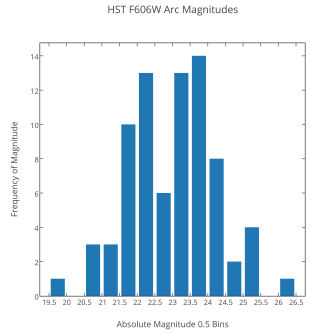


(A) HST 606 band

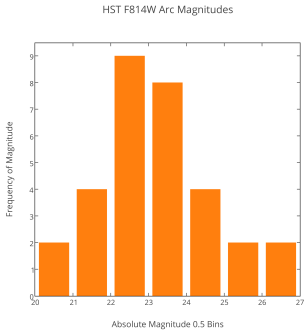


(B) HST 814 band

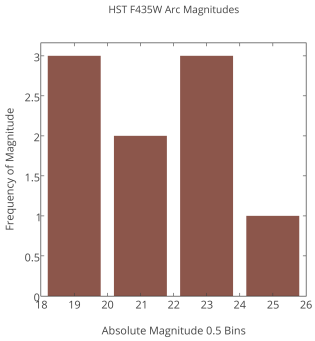


(C) HST 435 band

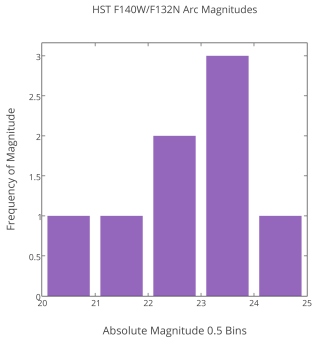


(D) HST 140/132 band

FIGURE 5.13: Illustration HST magnitude by filter

The four main HST image bands analyzed here are shown above for the AB magnitudes of detected arcs, where we can see the completeness of detection frequency relative to the set of actual lenses in the surveyed volume. We can see the completeness limits for the 606 and 814 bands, from which there is enough statistical sampling to show a clear dropoff in arc detection below a threshold magnitude. For the 606 band, the number of arcs found drops off quickly for arcs fainter than 24. A similar threshold of ABMAG < 24 appears for the 814 band as well. This helps us to better analyze the completeness of the sample and predict detection rates for more sensitive instruments moving forward. Constraining the requirements for lens detections within the completeness range of the instrument allows a better correspondence with arc abundance predictions.

### Giant Arcs

Giant arcs have been defined in some previous works as having the parameters $L/W > 10.0$ and $MAG < 21.5$ for arcs studied in the SDSS $r'$ filter (Zaritsky and Gonzales 2003). A more lenient threshold for giant arcs was analyzed (Horesh et al 2010), which utilized a giant arc selection of $L/W > 7.5$ and $MAG < 24.0$ for HST images observed with the F606W and F814W filters. Here we can tally the prevalence of giant arcs in the

HST clusters for both cases, where both parameters exist in the cluster survey, and present for observational comparison to the literature. Since the ground based table B.1 used a placeholder magnitude zeropoint of 30, the data can't be subject to the same analysis and comparison to the previously published giant arc surveys, but the preliminary values are included in the following summaries.

TABLE 5.2: Giant Arcs in LAS with $L/W$>10.0 and $Mag$ < 21.5.

| LAS table | Tan. Lens Clusters | Giant Arc Clusters | $\#ArcsL/W$>10.0 | $\cap Mag$<21.5 |
|---|---|---|---|---|
| HST A.1 | 28 | 2 | 34 | 2 |
| HST A.2 | 29 | 4 | 43 | 4 |
| Ground B.1 | 19 | 1 | 1 | 1 |

The number of giant arcs found in the whole study with the above constraints is 6. When we lower the giant arc constraint, we see 90 total giant arcs in the set.

TABLE 5.3: Giant Arcs in LAS with $L/W$>7.5 and $\cap Mag$<21.5

| LAS table | Tan. Lens Clusters | Giant Arc Clusters | $\#ArcsL/W$>7.5 | $\cap Mag$<24.0 |
|---|---|---|---|---|
| HST A.1 | 28 | 19 | 46 | 37 |
| HST A.2 | 20 | 16 | 60 | 50 |
| Ground B.1 | 19 | 3 | 3 | 3 |
| Total | 72 | | | |

The HST clusters have a tangential lensing frequency of 88.9% (or 48/54 tangential lens clusters with magnitude and orientation reported) among the observed clusters. For the ground based data, the tangential lensing frequency becomes 31.7% ( or 19/60 tangential lens clusters) Now we can compare this findings in this study with the Horesh study. They report a frequency of 1.2 ± 0.2 arcs per X-ray selected cluster and 0.2 ± 0.1 arcs per optically selected cluster. Looking at the total 120 confirmed and evaluated tangential lensing clusters, 76 are lenses. So an all arc conclusive comparison for the SZ selected set is an arc frequency of 1.7 arcs per cluster for the entire set. However, when only the giant arcs, defined by Horesh, are selected as a determinant of a lensing cluster, the ratio drops substantially to a lensing frequency of 90/120, or 0.726 giant arcs/cluster. This breaks down to a frequency of 0.05 giant arcs/cluster for ground based data and 1.208 giant arcs/cluster for HST observed images. This number is essentially the same as found the in giant arc lensing X-ray selected clusters (Horesh et al 2010). The discrepancy here is high due to the method of initial HST search for images before ground based data, so a next step would be to evaluate a larger PSZ defined cluster set with the HST.

## 5.3 Conclusions

The result of 0.726 giant arcs/cluster is roughly right in between the X-ray and optically selected cluster frequencies in the study, and the comparison to just the HST subset is virtually the same as in the literature (Horesh et al 2010). For reasons mentioned in the last two chapters, The HST data set avoids many of the observational restrictions of ground based telescopes. HST projects to observe more of the Planck SZ selected, or other methods of unbiased sampling of Planck SZ clusters, will provide richer statistical analysis of cluster lenses.

# Chapter 6

# Next Steps

After the analysis period, it is clear there is still work to be done for greater accuracy and completeness of the compiled statistics.

## 6.1 REionization LensIng Cluster Survey (RELICS)

A new program under development is the RELICS HST program, which will survey 46 strongly lensed regions from 41 of the most massive Planck SZ clusters to study the lens properties and discover very high-redshift source galaxies (Coe et al 2015). The project seeks to be done by late 2017 and will provide many opportunities for testing many more arc statistics from the PSZ catalogue that have been presented in this thesis.

## 6.2 Arc Detection and Photometric Reconstruction Algorithms

Much of this analysis was performed through visual inspection of images, but a more robust and accurate survey could be realized through an algorithm that automatically detects arc candidates and performs photometric measurements. There are various packages out there referenced in several papers (see Xu et al 2016, Meneghetti et al 2013). The detection performance would likely improve for weak lensing and strong lenses that are not as obviously distended as most arcs in this survey. Also some faint LAS arc magnitudes close to bright foreground cluster members were not able to be obtained through SExtractor and GALFIT. Developing a flux calculation algorithm from the skeleton of the arc and reconstructing its brightness through a psf convolution will give estimates for the arc magnitudes and add to the statistical sample set.

The arc magnitudes can be caclulated for some of the missing values in the LAS through an arc-based algorithm that can go beyond the capabilities of SExtractor. In this project, some code was developed to measure the magnitude of the giant arc in MACS 1206 following the analysis presented in Wuyts et al 2012. The algorithm developed here for lens analysis

TABLE 6.1: Einstein Rings Found in LAS

| Cluster | Ring RA | Ring DEC | Radius | MAG |
|---|---|---|---|---|
| PSZ1 G195.78-24.29 | 04:54:13.129 | 02:57:32.77 | 3.58" | 22.46 |
| PSZ1 G107.14+65.29 | 13:32:40.955 | 50:33:45.59 | 4" | 22.10 |
| PSZ1 G053.42-36.24 | 21:35:12.699 | -01:01:43.14 | 0.9" | 20.91 |

is summarized in Appendix F.
Further work needs to be done in terms of automation across the data set.

## 6.3 Einstein Rings as a Tool to Constrain Cosmic Parameters

The Einstein rings found across the study can be helpful for future cosmological constraint anaysis arising from strong lensing. This table shows presents the astrometry and photometry associated with the rings.

Einstein rings within clusters most often necessitates multiple lensing centers within a cluster. The prevalence of Einstein rings then signals greater mass distribution complexity to the cluster. For these clusters, more spectroscopic and photometric redshift analysis may need to be done in order to ensure that the single cluster entries in the catalogue are indeed correlated and not falsely categorized together. This analysis will further refine cluster catalogues and statistical analyses.

## 6.4 Planck Cosmology

There is an unresolved discrepancy between the Planck SZ cluster survey count and the expected count from derived from $\sigma_8$, the normalization of the matter power spectrum. The SZ value for $\sigma_8$, derived at low redshifts, tends to be lower than the value calculated from the CMB analysis. This discrepancy leaves uncertainty as to the most accurate $\sigma_8$ value, which has implications into the fitting of observed data to theoretical lensing plots seen in Chapter 5. (Planck Collaboration 2015.2).

# Appendix A

# Arc Statistics Table of HST Legacy Archive Cluster Lens Database

TABLE A.1: Arc Statistics Table for HST Cluster Images Analyzed in this Thesis. Note: arc redshifts where available sourced from previously published work.

| Cluster Name | Arc Name | RA | DEC | RA BCG | DEC BCG | $S/N$ | M500 | Cluster redshift | Filter | $L/W$ | Orientation | Arcsec to BCG | Arc redshift | Arc Coordinates | AB mag | Area($arcsec^2$) |
|---|---|---|---|---|---|---|---|---|---|---|---|---|---|---|---|---|
| PSZ1 G111.60-45.72[a] | | 00 18 34.6 | 16 25 34 | 00 18 33.633 | 16 26 16.53 | 6.54 | 8.675 | 0.5456 | F606W/WFPC2 | | | | | | | |
| | A | | | | | | | | | 9.6 | Tangential | 38.75 | - | (2774,2176) | 23.074 | 1.225 |
| | B | | | | | | | | | 20.7 | Tangential | 72.95 | - | (3390,1903) | 24.2 | 0.635 |
| | C | | | | | | | | | 52.3 | Tangential | 14.98 | - | (1923,2786) | 25.06 | 2.68 |
| PSZ1 G159.81-73.47 | | 01 31 53.4 | -13 34 27 | 1 31 52.60 | -13 36 39.91 | 12.21 | 8.172 | 0.206 | F606W/ACS | | | | | | | |
| | D1 | | | | | | | | | 8.0 ± .3[b] | Tangential | 22.29 | - | (3327,2977) | 21.60 ± .02[b] | 7.08 |
| PSZ1 G157.32-26.77 | | 03 09 00.0 | 26 45 30 | 3 08 55.986 | 26 45 37.30 | 8.24 | 10.026 | 0.356 | F606W/ACS | | | | | | | |
| | A | | | | | | | | | 9.7 | Tangential | 31.03 | - | (2950,2087) | 21.8 | 4.63 |
| | B | 03 09 01.625 | 26 45 21.81 | | | | | | | 11.3 | Tangential | 1.22 | - | (1605,2394) | 25.09 | 1.165 |
| PSZ1 G205.94-39.46 | | 04 17 36.2 | -11 54 12 | 4 17 34.74 | -11 54 32.92 | 11.43 | 11.7 | 0.443 | F606W/ACS | | | | | | | |
| | A1 | | | | | | | | | 12.5 | Tangential | 25.4 | - | (2528,3231) | 23.89 | 1.6 |
| | A2 | | | | | | | | | 17.25 | Tangential | 25.4 | - | (2408,3052) | 23.53 | 2.1 |
| | A3 | | | | | | | | | 14.25 | Tangential | 25.4 | - | (2953,2931) | 23.47 | 1.4 |
| | B1 | | | | | | | | | 1.4 | Radial | 8.61 | - | (2261,2745) | 20.89 | 11.6 |
| | B2 | | | | | | | | | 1.1 | Radial | 5.96 | - | (2420,2714) | 20.73 | 10.6 |
| | B3 | | | | | | | | | 1 | Radial | 16.66 | - | (2777,2376) | 21.52 | 5.2 |
| | C1 | | | | | | | | | 2 | Tangential | 17.54 | - | (2017,2763) | 23.3 | 2.2 |
| | C2 | | | | | | | | | 8.8 | Radial | 12.08 | - | (2299,2356) | 23.48 | 2.9 |
| | C3 | | | | | | | | | 2.8 | Radial | 19.56 | - | (2696,2251) | 23.66 | 2.7 |
| | D1 | | | | | | | | | 23.4 | Tangential | 44.11 | - | (1794,1647) | 23.98 | 1.6 |
| | D2 | | | | | | | | | 14.9 | Tangential | 44 | - | (1928,1556) | 24.23 | 1.7 |
| PSZ1 G195.78-24.29 | | 04 54 15.9 | 02 57 10 | 4 54 14.045 | 2 57 09.9.0 | 8.4 | 7.059 | 0.203 | F435W/ACS | | | | | | | |
| | A1 | | | | | | | | | 14.8 | Ring | 3.38 | - | (3355,1736) | 22.46 | 18.3 |
| | A2 | | | | | | | | | 15.8 | Ring | 4.38 | - | (3355,1736) | 23.46 | 19.3 |
| | B | | | | | | | | | 2.4 | Tangential | 27.16 | - | (3205,1242) | 19.1 | 0.15 |
| | C | | | | | | | | | 3.4 | Radial | 28.16 | - | (3205,1242) | 20.1 | 1.15 |
| | D | | | | | | | | | 4.4 | Radial | 29.16 | - | (3205,1242) | 21.1 | 2.15 |
| PSZ1 G170.22+09.74 | | 06 03 21.5 | 42 13 56 | 6 03 16.796 | 42 14 42.15 | 14.38 | 11.117 | - | F606W/WFC3 | | | | | | | |
| | A | | | | | | | | | 20.1 | Tangential | 17.91 | - | (3197,3642) | 21.84 | 16.5 |
| PSZ1 G187.53+21.92[f] | | 07 32 15.6 | 31 37 34 | 7 32 20.386 | 31 37 59.25 | 6.05 | 4.867 | 0.171 | F606W/WFPC2 | | | | | | | |
| | A | | | | | | | | | 12.4 | Tangential | 23.16 | - | (904,1208) | 19.64 | 94.7 |
| | B | | | | | | | | | 1.9 | Tangential | 25.6 | - | (840,756) | 21.77 | 21.77 |
| | C | | | | | | | | | 4.5 | Tangential | 33.5 | - | (1065,1180) | 23.83 | 23.83 |
| PSZ1 G184.70+28.92 | | 08 01 01.7 | 36 05 06 | 8 00 56.769 | 36 03 23.03 | 6.06 | 5.851 | 0.288 | F126N/WFC3 | | | | | | | |
| | A[g] | | | | | | | | | 30.6 | Tangential | 15.35 | 1.12 | (2335,2665) | 20.44 | 14.17 |
| PSZ1 G186.37+37.26 | | 08 42 59.6 | 36 21 10 | 08 42 57.572 | 36 21 59.72 | 15.86 | 11.481 | 0.282 | WFPC2/F606W | | | | | | | |
| | A1 | | | | | | | | | 8.3 ± 1.9* | Tangential | 6.14 | - | (1420,1468) | 22.79 ± 0.23 | 6.61 |
| PSZ1 G218.83+35.49 | | 09 09 06.9 | 10 57 45 | 9 09 12.627 | 10 58 28.00 | 7.94 | 5.535 | 0.1751 | F606W/WFPC2 | | | | | | | |
| | A | | | | | | | | | 4.1 | Tangential | 23.33 | - | (920,853) | 23.38 | 8.53 |
| | B | | | | | | | | | 5.4 | Tangential | 26.31 | - | (487,763) | 26.31 | 7.43 |
| PSZ1 G135.03+36.03 | | 09 47 00.2 | 76 23 44 | 9 47 12.645 | 76 23 13.92 | 6.15 | 6.271 | 0.345 | F132N/WFC3 | | | | | | | |
| | A[a] | | | | | | | | | 14.3 | Tangential | 13.5 | - | (838,692) | 22.3 | 12.5 |
| | B[b] | | | | | | | | | 14.7 | Tangential | 41.7 | - | - | 22.6 | - |
| | C[c] | | | | | | | | | 23 | Tangential | 19.1 | | - | 23.4 | - |
| PSZ1 G216.60+47.00 | | 09 49 48.5 | 17 08 19 | 09 49 51.8 | 17 07 10.84 | 8.18 | 8.22 | 0.3826 | F606W/ACS | | | | | | | |

TABLE A.1: Arc Statistics Table for HST Cluster Images Analyzed in this Thesis. Note: arc redshifts where available sourced from previously published work.

| Cluster Name | Arc Name | RA | DEC | RA BCG | DEC BCG | $S/N$ | M500 | Cluster redshift | Filter | $L/W$ | Orientation | Arcsec to BCG | Arc redshift | Arc Coordinates | AB mag | Area($arcsec^2$) |
|---|---|---|---|---|---|---|---|---|---|---|---|---|---|---|---|---|
| | A[a] | | | | | | | | | 8.8 | Tangential | 37.6 | - | (2287,2214) | 22.8 | 5.2 |
| | B1 | | | | | | | | | 10.3 | Tangential | 52.6 | - | (2645,1753) | 25.34 | 0.9 |
| | B2 | | | | | | | | | 7.9 | Tangential | 52.6 | - | (2795,1779) | 24.26 | 1.2 |
| | B3 | | | | | | | | | 6.3 | Tangential | 52.6 | - | (2862,1778) | 24.69 | 0.7 |
| | C | | | | | | | | | 4.8 | Tangential | 59.2 | - | (3218,1770) | 24.3 | 2.9 |
| PSZ1 G150.56+58.32 | | 11 15 10.8 | 53 19 39 | 11 15 14.843 | 53 19 54.40 | 7.76 | 7.962 | 0.47 | F606W/ACS | | | | | | | |
| | A[b] | | | | | | | | | 10.2 | Tangential | 31.6 | - | (2610,3095) | 23.6 | 10.1 |
| | B1[a] | | | | | | | | | 10.3 | Tangential | 56.2 | - | (2699,2180) | 22.9 | 5.1 |
| | B2[a] | | | | | | | | | 8.5 | Tangential | 57.3 | - | (2793,2132) | 23.5 | 7.3 |
| | C | | | | | | | | | 8.5 | Tangential | 34.5 | - | (2962,2549) | 22.3 | 9 |
| PSZ1 G139.17+56.37[c] | | 11 42 24.5 | 58 31 41 | 11 42 24.811 | 58 32 05.34 | 8.68 | 7.142 | 0.322 | F814W | | | | | | | |
| | A1 | | | 11 42 24.811 | 58 32 05.34 | | | | | 6.3 | Tangential | 36.2 | - | (2322,1628) | 23.57 | 1 |
| | A2 | | | 11 42 24.811 | 58 32 05.34 | | | | | 3.9 | Tangential | 36.3 | - | (2397,1655) | 23.33 | 1 |
| | A3 | | | 11 42 24.811 | 58 32 05.34 | | | | | 10.3 | Tangential | 36.7 | - | (2700,1702) | 23.65 | 1 |
| | A4 | | | 11 42 24.811 | 58 32 05.34 | | | | | 11.4 | Tangential | 38.2 | - | (2839,1710) | 22.65 | 1 |
| | B | | | 11 42 24.811 | 58 32 05.34 | | | | | 28.5 | Tangential | 8.7 | - | (2408,2489) | 26.07 | 1.61 |
| | C | | | 11 42 24.811 | 58 32 05.34 | | | | | 8.6 | Tangential | 79.5 | - | (2909,415) | 21.39 | 4.2 |
| | D1 | | | 11 42 26.919 | 58 30 44.66 | | | | | 5 | Tangential | 5.2 | - | (2027,822) | 22.13 | 1 |
| | D2 | | | 11 42 26.919 | 58 30 44.66 | | | | | 5 | Tangential | 3.5 | - | (2157,809) | 21.54 | 1 |
| | D3 | | | 11 42 26.919 | 58 30 44.66 | | | | | 5 | Tangential | 4.3 | - | (2226,710) | 22.58 | 1 |
| | E | | | 11 42 26.26 | 58 32 44.57 | | | | | 21.5 | Tangential | 9.7 | - | (2202,3346) | 22.01 | 8.8 |
| | F | | | 11 42 24.811 | 58 32 05.34 | | | | | 4.4 | Radial | 28.6 | - | (2851,2627) | 21.38 | 3.2 |
| PSZ1 G289.19+72.19 | | 12 36 48.9 | 63 10 40 | 12 36 58.721 | 63 11 13.63 | 7.77 | 5.981 | 0.3019 | F814W/ACS | | | | | | | |
| | A[a] | | | | | | | | | 10.6 | Tangential | 38 | - | (2186,2164) | 23.8 | 1.2 |
| PSZ1 G068.32+81.81[h] | | 13 22 48.0 | 31 39 06 | 13 22 48.77 | 31 39 17.8 | 6.97 | 6.633 | 0.3083 | F606W/WFPC2 | | | | | | | |
| | A1 | | | | | | | | | 8 | Tangential | 19.5 | 0.889[d] | | 21.93 | 7.69 |
| | A2 | | | | | | | | | 8 | Tangential | 19.5 | 0.889[d] | | 21.93 | 2.6 |
| | A3 | | | | | | | | | 8 | Tangential | 19.5 | 0.889[d] | | 21.93 | 2.36 |
| | B | | | | | | | | | 4 | Radial | 31.5 | 0.8473[h] | | 23.27 | 2.4 |
| | C | | | | | | | | | 4 | Tangential | 30.2 | 1.1513[h] | | 24.16 | 3.2 |
| | D | | | | | | | | | 8 | Tangential | 21.7 | 0.8121[h] | | 24.34 | 4.8 |
| PSZ1 G107.14+65.29 | | 13 32 39.5 | 50 32 47 | 13 32 38.4 | 50 33 36.48 | 12.21 | 7.991 | 0.2799 | F606W/ACS | | | | | | | |
| | A | | | 13 32 38.058 | 50 35 19.87 | | | | | 4.8 | Radial | 6.4 | | (3141,5031) | 23.008 | 3.1 |
| | B | | | | | | | | | 2.9 | Tangential | 78.54 | | (2845,4529) | 22.22 | 5 |
| | C | | | 13 32 40.955 | 50 33 45.59 | | | | | 4 | Ring | 4 | | (2685,3200) | 22.1 | 1.6 |
| | D | | | | | | | | | 18.7 | Tangential | 27.09 | | (2855,2654) | 23.54 | 2.8 |
| | E | | | | | | | | | 2.1 | Tangential | 39.02 | | (2705,2434) | 20.65 | 22.8 |
| | F | | | | | | | | | 7.3 | Tangential | 44.05 | | (3611,2242) | 22.79 | 4 |
| | G | | | | | | | | | 5.9 | Tangential | 70.39 | | (3923,1796) | 23.18 | 4.7 |
| PSZ1 G004.13+56.84 | | 14 47 22.4 | 08 28 14 | 14 47 26.061 | 08 28 24.73 | 6.43 | 7.461 | 0.38 | F606W/ACS | | | | | | | |
| | A | | | 14 47 23.639 | 8 29 57.53 | | | | | 6.2 | Radial | 11.92 | - | (3920,4720) | 22.36 | 7.6 |
| | B | | | | | | | | | 7.3 | Tangential | 47.47 | - | (2075,2945) | 22.76 | 2.8 |
| | C1 | | | | | | | | | 11.5 | Tangential | 35.29 | - | (3712,2675) | 23.52 | 1.4 |
| | C2 | | | | | | | | | 11.5 | Tangential | 35.29 | - | (3688,2526) | 23.6 | 1.3 |
| | D | | | | | | | | | 2.8 | Tangential | 46.3 | - | (3866,2423) | 22.13 | 12 |
| PSZ1 G355.07+46.20 | | 15 04 05.4 | -02 47 54 | 15 04 07.472 | -2 48 16.95 | 7.66 | 6.98 | 0.2153 | F689M/WFC3 | | | | | | | |
| | A | | | | | | | | | 2.7 | Tangential | 24.58 | - | (1884,2817) | 23.27 | 0.6 |
| | B | | | | | | | | | 7.8 | Radial | 1.85 | - | (2226,2282) | 23.62 | 0.5 |
| PSZ1 G100.16+41.66 | | 15 56 09.1 | 66 22 36 | 15 56 14.078 | 66 20 53.43 | 6.28 | 3.854 | 0.2339 | F606W/ACS | | | | | | | |
| | A1 | | | 15 56 03.911 | 66 22 14.17 | | | | | 13.6 | Tangential | 6.51 | - | (3733,4288) | 22.49 | 6.8 |
| | A2 | | | 15 56 03.911 | 66 22 14.17 | | | | | 13.6 | Tangential | 6.84 | - | (3733,4288) | 22.49 | 6.8 |
| | B | | | | | | | | | 10.3 | Tangential | 91.17 | - | (3959,3960) | 22.4 | 1.3 |
| | C | | | | | | | | | 2.3 | Tangential | 9.33 | - | (2301,2798) | 22.41 | 19.2 |
| PSZ1 G046.09+27.16 | | 17 31 45.4 | 22 51 49 | 17 31 40.022 | 22 51 59.57 | 7.5 | 7.945 | 0.389 | F140W/WFC3 | | | | | | | |
| | A | | | | | | | | | 3.1 | Tangential | 48.19 | - | (559,1228) | 21.095 | 4.6 |
| | B | | | | | | | | | 4.8 | Radial | 26.64 | - | (793,1040) | 23.49 | 11.4 |
| | C | | | | | | | | | 8 | Tangential | 12.12 | - | (919,1125) | 23.5 | 7 |
| | D | | | 17 31 41.749 | 22 51 51.54 | | | | | 2.4 | Tangential | 1.22 | - | (798,1037) | 20.98 | 1.9 |
| | E | | | | | | | | | 5.2 | Tangential | 48.17 | - | (1470,795) | 24.3 | 5.7 |
| PSZ1 G071.21+28.86 | | 17 52 03.1 | 44 40 10 | 17 51 33.396 | 44 39 13.40 | 8.24 | 6.959 | 0.366 | F606W/ACS | | | | | | | |
| | A | | | | | | | | | 5.3 | Tangential | 20.2 | - | (4298,2103) | 25.17 ± 1.15 | 2.5 |
| | B | | | | | | | | | 4.9 | Tangential | 4.8 | - | (4058,2287) | 22.28 ± 0.11 | 21.2 |
| PSZ1 G094.00+27.41[i] | | 18 22 00.4 | 64 20 34 | 18 21 54.495 | 64 20 09.49 | 9.35 | 6.311 | 0.3315 | F814W/ACS | | | | | | | |
| | A | | | | | | | | | 5.8 | Tangential | 40.3 | - | (2422,1423) | 22.27 | 4.8 |
| PSZ1 G049.83-25.22 | | 20 51 20.3 | 02 16 40 | 20 51 9.572 | 02 16 13.66 | 6.03 | 6.127 | 0.3211 | F606W/ACS | | | | | | | |
| | A | | | | | | | | | 5.6 | Tangential | 6.51 | - | (2342,2564) | 22.3 | 6.5 |
| PSZ1 G053.42-36.25 | | 21 35 10.1 | -01 03 15 | 21 35 12.097 | -01 02 57.44 | 7.78 | 7.5711 | 0.33 | F606W/ACS | | | | | | | |
| | A | | | 21 35 14.385 | -01 01 59.39 | | | | | 5.1 | Radial | 1.3 | - | (2210,3703) | 22.19 | 1.6 |

TABLE A.1: Arc Statistics Table for HST Cluster Images Analyzed in this Thesis. Note: arc redshifts where available sourced from previously published work.

| Cluster Name | Arc Name | RA | DEC | RA BCG | DEC BCG | $S/N$ | M500 | Cluster redshift | Filter | $L/W$ | Orientation | Arcsec to BCG | Arc redshift | Arc Coordinates | AB mag | Area($arcsec^2$) |
|---|---|---|---|---|---|---|---|---|---|---|---|---|---|---|---|---|
| | B | | | 21 35 12.097 | -01 02 57.44 | | | | | 8.2 | Radial | 109.46 | - | (3372,3100) | 22.25 | 3.1 |
| | C | | | 21 35 12.097 | -01 02 57.44 | | | | | 7 | Tangential | 85.11 | - | (3038,2637) | 23.05 | 2.5 |
| | D | | | 21 35 12.097 | -01 02 57.44 | | | | | 5.5 | Radial | 77.42 | - | (3132,1833) | 20.38 | 4.2 |
| | E | | | 21 35 12.699 | -01 01 43.14 | | | | | 14.1 | Ring | 0.95 | - | (2749,4039) | 20.91 | 5.3 |
| PSZ1 G044.77-51.30 | | 22 15 03.7 | -13 59 16 | 22 14 57.324 | -14 00 11.54 | 7.3 | 8.461 | 0.5027 | F814W/ACS | | | | | | | |
| | A[a] | | | | | | | | | 12.4 | Tangential | 14.3 | - | (2595,3166) | 22.17 | 22.8 |
| | B[a] | | | | | | | | | 17.9 | Tangential | 20.1 | - | (2608,2488) | 23.54 | 7.7 |
| | C | | | | | | | | | 6 | Radial | 6.4 | | (2706,2883) | 23.26 | 2.3 |
| PSZ1 G056.94-55.06[d] | | 22 43 17.1 | -09 34 50 | 22 43 20.65 | -9 35 18.20 | 10.81 | 10.074 | 0.447 | F814W/ACS | | | | | | | |
| | A1 | | | 22 43 20.65 | -9 35 18.20 | | | | | 12 | Tangential | 70.7 | 2.091[d] | (480,1397) | 24.17 | 5.7 |
| | A2 | | | 22 43 20.65 | -9 35 18.20 | | | | | 12 | Tangential | 53 | 2.091[d] | (619,1206) | 22.42 | 29.8 |
| | B | | | 22 43 20.65 | -9 35 18.20 | | | | | 4 | Tangential | 40.8 | 1.3202[d] | (764,998) | 24.14 | 4.8 |
| | C | | | 22 43 20.65 | -9 35 18.20 | | | | | 6 | Radial | 61.9 | 0.7403[d] | (594,855) | 24.04 | 7.4 |
| | D | | | 22 43 20.65 | -9 35 18.20 | | | | | 4.3 | Radial | 9.5 | | (1228,1081) | 25.66 | 3.1 |
| | E | | | 22 43 20.65 | -9 35 18.20 | | | | | 9 | Tangential | 5.1 | | (1149,1086) | 23.18 | 2.3 |
| | F | | | 22 43 20.65 | -9 35 18.20 | | | | | 4.5 | Tangential | 21.1 | | (1018,1309) | 26.81 | 2.8 |
| | G | | | 22 43 24.456 | -09 35 36.89 | | | | | 7.1 | Tangential | 9.2 | | (509,998) | 25.96 | 2 |
| PSZ1 G087.03-57.37 | | 23 37 43.7 | 00 16 06 | 23 37 39.8 | 0 16 17.09 | 7.5 | 6.965 | 0.2779 | F606W/WFPC2 | | | | | | | |
| | A | | | 23 37 40.215 | 00 16 40.61 | | | | | 3.5 | Tangential | 3 | - | (548,1491) | 22.164 | 5.2 |
| | B | | | 23 37 39.8 | 0 16 17.09 | | | | | 7.7 | Radial | 5.8 | - | (591,1283) | 23.26 | 6.7 |

[a] Previously reported by Horesh et al 2010
[b] Previously reported by Sand et al 2005
[c] See Dahle et al 2002 for previous cluster analysis
[d] Previously reported by Bayliss et al 2011
[e] Previously reported by Richard et al 2010
[f] Previously reported by Cypriano et al 2005
[g] Reported by Xu et al 2016
[h] Previously reported by Limousin et al 2008
[i] Previously analyzed by Wold et al 2002

TABLE A.2: Arc Statistics Table for HST Cluster Images Previously Analyzed in Other Work. Note, Cluster BCG RA DEC, Area, and some arc radii my analysis.

| Cluster Name | Arc Name | RA | DEC | RA BCG | DEC BCG | $S/N$ | Cluster redshift | Filter | $L/W$ | Orientation | Arcsec to BCG | Arc redshift | Arc Coordinates | AB mag | Area($arcsec^2$) |
|---|---|---|---|---|---|---|---|---|---|---|---|---|---|---|---|
| PSZ1 G172.97-53.54[a] | - | 02 39 52.3 | -01 33 23 | 2 39 52.735 | -1 34 19.33 | 6.15 | 0.373 | | | - | | | | | |
| | 1.1 | 2:39:52 | -01:34:37.28 | | | | | | | Tangential | 20.3 | 0.806 | | | |
| | 1.2 | 2:39:54 | -01:34:34.13 | | | | | | | Tangential | 20.2 | 0.806 | | | |
| | 1.3 | 2:39:52 | -01:34:36.22 | | | | | | | Tangential | 20 | 0.806 | | | |
| | 2.1 | 2:39:54 | -01:35:03.58 | | | | | | | Tangential | 48.9 | 0.725 | | | |
| | 2.2 | 2:39:53 | -01:35:06.68 | | | | | | | Tangential | 48.9 | 0.725 | | | |
| | 2.3 | 2:39:53 | -01:35:04.64 | | | | | | | Tangential | 48.9 | 0.725 | | | |
| | 2.4 | 2:39:53 | -01:35:05.39 | | | | | | | Tangential | 48.9 | 0.725 | | | |
| | 2.5 | 2:39:53 | -01:35:05.81 | | | | | | | Tangential | 48.9 | 0.725 | | | |
| | 3.1 | 2:39:52 | -01:34:01.13 | | | | | | | Tangential | 58.6 | $1.52 \pm 0.06$ | | | |
| | 3.2 | 2:39:52 | -01:33:57.38 | | | | | | | Tangential | 58.6 | $1.52 \pm 0.06$ | | | |
| | 3.3 | 2:39:55 | -01:34:02.28 | | | | | | | Tangential | 58.6 | $1.52 \pm 0.06$ | | | |
| | 4.1 | 2:39:55 | -01:34:35.41 | | | | | | | Radial | 43.8 | $1.34 \pm 0.03$ | | | |
| | 4.2 | 2:39:53 | -01:34:35.09 | | | | | | | Radial | 22.2 | $1.34 \pm 0.03$ | | | |
| | 4.3 | 2:39:51 | -01:34:40.97 | | | | | | | Radial | 48.9 | $1.34 \pm 0.03$ | | | |
| | 5.1 | 2:39:54 | -01:35:21.07 | | | | | | | Tangential | 75.6 | $1.30 \pm 0.05$ | | | |
| | 5.2 | 2:39:53 | -01:35:21.67 | | | | | | | Tangential | 75.6 | $1.30 \pm 0.05$ | | | |
| | 5.3 | 2:39:53 | -01:35:20.92 | | | | | | | Tangential | 75.6 | $1.30 \pm 0.05$ | | | |
| | 6.1 | 2:39:53 | -01:34:38.32 | | | | | | | Radial | 20 | $1.30 \pm 0.05$ | | | |
| | 6.2 | 2:39:51 | -01:34:41.52 | | | | | | | Radial | 25.4 | $1.30 \pm 0.05$ | | | |
| | 6.3 | 2:39:55 | -01:34:38.12 | | | | | | | Radial | 43.8 | $1.30 \pm 0.05$ | | | |
| | 7.1 | 2:39:53 | -01:34:49.90 | | | | | | | Radial | 34 | $4.94 \pm 1.17$ | | | |
| | 7.2 | 2:39:53 | -01:34:51.09 | | | | | | | Radial | 34 | $4.94 \pm 1.17$ | | | |
| | 8.1 | 2:39:51 | -01:34:11.67 | | | | | | | - | 35.1 | $3.78 \pm 0.66$ | | | |
| | 8.2 | 2:39:51 | -01:34:25.67 | | | | | | | - | 38 | $3.78 \pm 0.66$ | | | |
| | 9.1 | 2:39:51 | -01:34:40.85 | | | | | | | - | 20 | $1.64 \pm 0.04$ | | | |
| | 9.2 | 2:39:53 | -01:34:34.94 | | | | | | | - | 25 | $1.64 \pm 0.04$ | | | |
| | 9.3 | 2:39:56 | -01:34:36.01 | | | | | | | - | 22 | $1.64 \pm 0.04$ | | | |
| | 11.1 | 2:39:51 | -01:34:10.12 | | | | | | | Radial | 35.3 | $5.93 \pm 0.15$ | | | |
| | 11.2 | 2:39:51 | -01:34:27.36 | | | | | | | Radial | 38.4 | $5.93 \pm 0.15$ | | | |
| | 12.1 | 2:39:53 | -01:34:00.43 | | | | | | | Radial | 35 | $4.59 \pm 0.44$ | | | |
| | 12.2 | 2:39:50 | -01:34:31.50 | | | | | | | Radial | 50 | $4.59 \pm 0.44$ | | | |
| | 12.3 | 2:39:56 | -01:34:15.70 | | | | | | | Radial | - | $4.59 \pm 0.44$ | | | |
| | 13.1 | 2:39:55 | -01:34:18.81 | | | | | | | - | - | $5.97 \pm 0.33$ | | | |
| | 13.2 | 2:39:54 | -01:34:08.02 | | | | | | | - | - | $5.97 \pm 0.33$ | | | |
| PSZ1 G208.80-30.67[b] | | 04 54 05.0 | -10 13 35 | | | 7.07 | 0.2475 | | | | | | | | |
| | A1 | | | | | | | | | | | $1.043 \pm .01$ | (73.526932,-10.223421) | $21.49 \pm .04$ | |
| | A2 | | | | | | | | | | | $1.043 \pm .01$ | (73.527544,-10.222524) | $21.32 \pm .04$ | |
| | A3 | | | | | | | | | | | $1.043 \pm .01$ | (73.529391,-10.221431) | $21.57 \pm .20$ | |
| PSZ1 G180.25+21.03[c] | 85lensobjects | 07 17 28.1 | 37 44 36 | | | 9.88 | 0.546 | | see Kawamata et al 2011 | | | | | | |
| PSZ1 G186.98+38.66 | | 08 50 10.3 | 36 04 47 | 08 50 07.6 | 36 04 35 | 6.58 | 0.378 | | | | | | | | |
| | A | | | | | | | | >5.0 | Radial | 45-55 | <2.0 | - | - | - |
| | B | | | | | | | | >5.0 | Tangential | 55 | 5.03 | - | 25.6 | - |
| | C | | | | | | | | 3.0 | Tangential | 55 | 5.04 | - | 25.65 | - |
| | D | | | | | | | | >5.0 | Tangential | 45-55 | <2.0 | - | - | - |
| PSZ1 G166.11+43.40[e] | | 09 18 04.5 | 51 42 15 | | | 10.38 | 0.217 | | | | | | | | |
| | F0 | | | | | | | | $15.5 \pm 0.9$ | Tangential | (-19.8,-16.3) | 0.65 | | $22.14 \pm .05$ | |
| | F3 | | | | | | | | $9.0 \pm 0.2$ | Tangential | (-17.7,-44.6) | 0.398 | | $21.21 \pm .02$ | |
| | F4 | | | | | | | | $10.5 \pm 0.8$ | Tangential | (-30.2,-49.6) | - | | $23.82 \pm 0.13$ | |
| | F9 | | | | | | | | $9.8 \pm 0.3$ | Tangential | (-17.7,49.9) | - | | $21.58 \pm .03$ | |
| | F11 | | | | | | | | $9.5 \pm 0.5$ | Tangential | (13.0,48.1) | 1.114 | | $22.86 \pm .06$ | |
| | F13 | | | | | | | | $6.6 \pm 0.4$ | Tangential | (-8.1,59.5) | 0.398 | | $21.52 \pm .03$ | |
| | F16 | | | | | | | | $4.6 \pm 0.3$ | Radial | (-4.6,-8.4) | - | | $23.76 \pm .09$ | |
| | F18 | | | | | | | | $10.0 \pm 0.8$ | Tangential | (-10.4,53.2) | 0.487 | | $23.39 \pm .11$ | |
| PSZ1 G244.67+32.47[e] | | 09 45 21.7 | -08 38 19 | 09 45 26.350 | -08 39 05.97 | 7.88 | 0.1535 | | | | | | | | |
| | A1 | | | | | | | | $16.8 \pm 2.1$ | Tangential | (10.3,17.1) | - | (1260,1112) | $22.28 \pm 0.05$ | 1.05 |
| | A2 | | | | | | | | $8.5 \pm 0.8$ | Tangential | (9.9,26.6) | - | (1159,1101) | $24.58 \pm 0.23$ | 0.22 |
| PSZ1 G182.55+55.83[e] | | 10 17 03.0 | 39 02 58 | 10 17 03.656 | 39 02 49.37 | 7.96 | 0.206 | | | | | | | | |
| | H0 | | | | | | | | $15.3 \pm 1.7$ | Tangential | (12.2,-0.3) | 0.117 | | $22.25 \pm 0.06$ | |
| | H1/H2/H3 | | | | | | | | $30.2 \pm 4.0$ | Tangential | (-17.9,-1.5) | 1.958 | | $21.73 \pm 0.06$ | |
| | H5 | | | | | | | | $11.1 \pm 1.1$ | Tangential | (21.7,-4.8) | - | | $23.26 \pm 0.09$ | |
| | A1 | | | | | | | | $8.0 \pm 1.1$ | Tangential | (15.1,14.7) | - | | $25.03 \pm 0.30$ | |
| PSZ1 G228.21+75.20[c] | | 11 49 37.4 | 22 23 35 | | | 6.68 | 0.545 | | | | | - | | | |
| | 1.1 | 11:49:35 | 22:23:46 | | | | | | | | | 1.48 | | | |
| | 1.2 | 11:49:36 | 22:23:51 | | | | | | | | | 1.48 | | | |
| | 1.3 | 11:49:37 | 22:24:09 | | | | | | | | | 1.48 | | | |
| | 2.1 | 11:49:37 | 22:23:23 | | | | | | | | | 1.894 | | | |
| | 2.2 | 11:49:37 | 22:23:33 | | | | | | | | | 1.894 | | | |
| | 2.3 | 11:49:38 | 22:23:34 | | | | | | | | | 1.894 | | | |
| | 3.1 | 11:49:34 | 22:24:00 | | | | | | | | | 2.497 | | | |

TABLE A.2: Arc Statistics Table for HST Cluster Images Previously Analyzed in Other Work. Note, Cluster BCG RA DEC, Area, and some arc radii my analysis.

| Cluster Name | Arc Name | RA | DEC | RA BCG | DEC BCG | $S/N$ | Cluster redshift | Filter | $L/W$ | Orientation | Arcsec to BCG | Arc redshift | Arc Coordinates | AB mag | Area($arcsec^2$) |
|---|---|---|---|---|---|---|---|---|---|---|---|---|---|---|---|
| | 3.2 | 11:49:34 | 22:24:11 | | | | | | | | | 2.497 | | | |
| | 3.3 | 11:49:36 | 22:24:26 | | | | | | | | | 2.497 | | | |
| | 4.1 | 11:49:34 | 22:23:49 | | | | | | | | | 2.57 ± 0.15 | | | |
| | 4.2 | 11:49:35 | 22:24:03 | | | | | | | | | 2.57 ± 0.15 | | | |
| | 4.3 | 11:49:37 | 22:24:22 | | | | | | | | | 2.57 ± 0.15 | | | |
| | 5.1 | 11:49:36 | 22:23:35 | | | | | | | | | 2.61 ± 0.29 | | | |
| | 5.2 | 11:49:36 | 22:23:38 | | | | | | | | | 2.61 ± 0.29 | | | |
| | 5.3 | 11:49:38 | 22:24:13 | | | | | | | | | 2.61 ± 0.29 | | | |
| | 6.1 | 11:49:36 | 22:23:33 | | | | | | | | | 2.59 ± 0.27 | | | |
| | 6.2 | 11:49:36 | 22:23:38 | | | | | | | | | 2.59 ± 0.27 | | | |
| | 6.3 | 11:49:38 | 22:24:09 | | | | | | | | | 2.59 ± 0.27 | | | |
| | 7.1 | 11:49:36 | 22:23:29 | | | | | | | | | 2.54 ± 0.25 | | | |
| | 7.2 | 11:49:37 | 22:23:39 | | | | | | | | | 2.54 ± 0.25 | | | |
| | 7.3 | 11:49:38 | 22:24:04 | | | | | | | | | 2.54 ± 0.25 | | | |
| | 8.1 | 11:49:36 | 22:23:40 | | | | | | | | | 3.10 ± 0.41 | | | |
| | 8.2 | 11:49:36 | 22:23:42 | | | | | | | | | 3.10 ± 0.41 | | | |
| | 8.3 | 11:49:38 | 22:24:20 | | | | | | | | | 3.10 ± 0.41 | | | |
| | 9.1 | 11:49:37 | 22:25:34 | | | | | | | | | 4.03 ± 0.82 | | | |
| | 9.2 | 11:49:37 | 22:25:38 | | | | | | | | | 4.03 ± 0.82 | | | |
| | 9.3 | 11:49:37 | 22:25:38 | | | | | | | | | 4.03 ± 0.82 | | | |
| | 10.1 | 11:49:37 | 22:25:32 | | | | | | | | | 4.13 ± 0.66 | | | |
| | 10.2 | 11:49:37 | 22:25:32 | | | | | | | | | 4.13 ± 0.66 | | | |
| | 10.3 | 11:49:37 | 22:25:36 | | | | | | | | | 4.13 ± 0.66 | | | |
| | 13.1 | 11:49:37 | 22:23:52 | | | | | | | | | 1.31 ± 0.04 | | | |
| | 13.2 | 11:49:37 | 22:23:48 | | | | | | | | | 1.31 ± 0.04 | | | |
| | 13.3 | 11:49:36 | 22:23:38 | | | | | | | | | 1.31 ± 0.04 | | | |
| | 14.1 | 11:49:34 | 22:24:13 | | | | | | | | | 2.85 ± 0.58 | | | |
| | 14.2 | 11:49:34 | 22:24:09 | | | | | | | | | 2.85 ± 0.58 | | | |
| PSZ1 G180.56+76.66[f] | abell1423 | 11 57 19.9 | 33 36 39 | 11 57 17.463 | 33 36 39.43 | 7.87 | 0.2138 | | | | | | | | |
| | C1.1 | 179.31756 | 33.606503 | | | | | | | | | 3.52 | | | |
| | C1.2 | 179.31925 | 33.616867 | | | | | | | | | 3.48 | | | |
| | C2.1 | 179.31899 | 33.611675 | | | | | | | | | - | | | |
| | C2.2 | 179.31908 | 33.610921 | | | | | | | | | - | | | |
| | C2.3 | 179.32264 | 33.606795 | | | | | | | | | - | | | |
| | C3.1 | 179.32009 | 33.612385 | | | | | | | | | - | | | |
| | C3.2 | 179.3202 | 33.610804 | | | | | | | | | - | | | |
| | C3.3 | 179.32298 | 33.608767 | | | | | | | | | - | | | |
| PSZ1 G284.43+52.44[g] | | 12 06 18.9 | -08 47 50 | 12 06 12.154 | -8 48 03.46 | 10 | 0.4414 | F435W | | | | | | | |
| | A | | | | | | | | 15.73 | Tangential | 19.47 | 1.05 | (2790,2454) | 19.76 | 12.3 |
| | B | | | | | | | | 7.51 | Tangential | 52.08 | 2.41 | (3292,2420) | 24.64 | 3.2 |
| | C | | | | | | | | 12.32 | Tangential | 56.79 | 1.56 | (1618,2471) | 23.19 | |
| | D | | | | | | | | 8.57 | Tangential | 78.9 | 0.72 | (3484,3134) | 19.3 | |
| PSZ1 G114.99+70.36[e] | | 13 06 54.9 | 46 31 33 | 13 06 49.993 | 46 33 33.06 | 8.71 | 0.2259 | | | | | | | | |
| | A | | | | | | | | 8.3 ± 3.5 | Tangential | (3.3,-1.4) | - | (2181,2660) | 25.17 ± 1.15 | 2 |
| | B | | | | | | | | 25.3 ± 5.7 | Radial | (3.8,-47.9) | - | (1445,1431) | 22.28 ± 0.11 | 1.2 |
| PSZ1 G313.33+61.13[h] | 140objects | 13 11 26.5 | -01 20 11 | | | 13.06 | 0.1832 | | | | | | | | |
| PSZ1 G114.29+64.91[i] | | 13 15 04.6 | 51 48 48 | 13 15 05.28 | 51 49 02.9 | 7.37 | 0.2836 | | | | | | | | |
| | 1.1 | 198.77725 | 51.81934 | | | | | | | Radial | | 0.8889 ± 0.0003 | | | |
| | 3.1 | 198.76696 | 51.83205 | | | | | | | Tangential | | 3.277 ± 0.002 | | 22.69 ± 0.02 | |
| | 3.3 | 198.75824 | 51.82982 | | | | | | | Tangential | | 3.277 ± 0.002 | | | |
| | 4.2/5.2 | 198.76075 | 51.82487 | | | | | | | Radial | | 1.9082 ± 0.004 | | | |
| | 6.1 | 198.77984 | 51.8264 | | | | | | | Radial | | 2.36 ± 0.002 | | | |
| | 7.3 | 198.75869 | 51.82814 | | | | | | | Radial | | 2.983 ± 0.002 | | | |
| | 10.1 | 198.78708 | 51.81424 | | | | | | | Tangential | | 2.627 ± 0.004 | | | |
| | 11.3 | 198.76242 | 51.80954 | | | | | | | Tangential | | 2.627 ± 0.004 | | | |
| | 15.1 | 198.76284 | 51.81246 | | | | | | | Radial | | 2.355 ± 0.002 | | | |
| | 15.3 | 198.78825 | 51.82173 | | | | | | | Tangential | | 2.355 ± 0.002 | | | |
| | 16.1/16.3 | 198.78851 | 51.82096 | | | | | | | Radial | | 2.81 ± 0.004 | | | |
| | 20 | 198.76659 | 51.83626 | | | | | | | - | | 1.279 ± 0.0005 | | | |
| | 21 | 198.76 | 51.83451 | | | | | | | - | | 1.279 ± 0.0005 | | | |
| | 23 | 198.75612 | 51.80736 | | | | | | | Tangential | | 5.827 ± 0.0015 | | | |
| | 10.4 | 198.77173 | 51.81906 | | | | | | | Radial | | 2.627 | | 24.77 ± .08 | |
| | 12.1 | 198.77456 | 51.829946 | | | | | | | Tangential | | 3.31 ± .16 | | 26.68 ± .1 | |
| | 12.2 | 198.76568 | 51.828658 | | | | | | | Tangential | | 3.35 ± .22 | | 24.47 ± .04 | |
| | 12.3 | 198.75867 | 51.826482 | | | | | | | Tangential | | 3.16 ± .24 | | 26.33 ± .08 | |
| | 13.1 | 198.78238 | 51.821204 | | | | | | | Radial | | 1.15 ± .13 | | 26.93 ± .11 | |
| | 13.2 | 198.76796 | 51.818374 | | | | | | | Tangential | | 0.68 ± .46 | | 24.18 ± .04 | |
| | 13.3 | 198.77204 | 51.814973 | | | | | | | Tangential | | 1.13 ± .08 | | 26.29 ± .08 | |
| | 13.4 | 198.76692 | 51.81513 | | | | | | | Tangential | | 1.07 ± .19 | | 25.12 ± .11 | |

TABLE A.2: Arc Statistics Table for HST Cluster Images Previously Analyzed in Other Work. Note, Cluster BCG RA DEC, Area, and some arc radii my analysis.

| Cluster Name | Arc Name | RA | DEC | RA BCG | DEC BCG | $S/N$ | Cluster redshift | Filter | $L/W$ | Orientation | Arcsec to BCG | Arc redshift | Arc Coordinates | AB mag | Area($arcsec^2$) |
|---|---|---|---|---|---|---|---|---|---|---|---|---|---|---|---|
| | 14.1 | 198.78662 | 51.820542 | | | | | | | - | | 1.58 ± .02 | | 25.4 ± .17 | |
| | 14.2 | 198.76868 | 51.820191 | | | | | | | Tangential | | 1.58 ± .02 | | 26.33 ± .16 | |
| | 14.3 | 198.76447 | 51.812192 | | | | | | | Tangential | | 1.58 ± .02 | | 26.3 ± .15 | |
| | 14.4 | 198.7754 | 51.811945 | | | | | | | - | | 1.58 ± .02 | | 25.29 ± .08 | |
| | 2.2 | 198.77156 | 51.81174 | | | | | | | Tangential | | 2.16 ± .15 | | 26.15 ± .1 | |
| | 2.3 | 198.7697 | 51.81186 | | | | | | | Tangential | | 2.23 ± .19 | | 24.95 ± .06 | |
| | 8.1 | 198.7725 | 51.83045 | | | | | | | Tangential | | 2.80 ± .17 | | 23.06 ± .02 | |
| | 8.2 | 198.76608 | 51.82949 | | | | | | | Tangential | | 2.77 ± .21 | | 25.07 ± .06 | |
| | 8.3 | 198.75863 | 51.8274 | | | | | | | Tangential | | 2.72 ± .20 | | 26.68 ± .15 | |
| | 9.1 | 198.77176 | 51.8303 | | | | | | | Tangential | | 3.271 ± .12 | | 25.32 ± .08 | |
| | 9.2 | 198.7669 | 51.82957 | | | | | | | Tangential | | 2.995 ± .2 | | 25.32 ± .08 | |
| | 9.3 | 198.75813 | 51.82708 | | | | | | | Tangential | | 3.00 ± .37 | | 26.92 ± .12 | |
| PSZ1 G092.67+73.44[e] | | 13 35 18.1 | 41 00 10 | 13 35 20.094 | 41 00 3.94 | 13.52 | 0.2279 | | | | | | | | - |
| | J1 | | | | | | | | 8.7 ± 1.5 | Tangential | (-5.9,14.1) | - | | 24.87 ± 0.28 | |
| PSZ1 G324.05+48.79[g] | | 13 47 33.5 | -11 45 42 | | | 8.86 | 0.4516 | F606W | | - | | | | | |
| | 1 | | | | | | | | 21.51 | - | 55.55 | 1.64 | (3032,1776) | 23.58 | - |
| | 2 | | | | | | | | 11.79 | - | 46.58 | 2.43 | (3141,2064) | 21.57 | - |
| | 3 | | | | | | | | 10.12 | - | 43.42 | 4.28 | (3117,2872) | 24.63 | - |
| | 4 | | | | | | | | 7.51 | - | 29.92 | 0.78 | (2521,2951) | 21.46 | - |
| | 5 | | | | | | | | 13.5 | - | 43.5 | 3.78 | (2549,3162) | 24.22 | - |
| | 6 | 206.87914 | -11.749135 | | | | | | - | - | - | 4.6 | - | - | - |
| PSZ1 G118.46+39.31[j] | | 13 54 48.7 | 77 15 15 | 13 54 42.968 | 77 15 16.81 | 6.47 | 0.3967 | F606W | | - | | | | | |
| | A | | | | | | | | 12.9 | Tangential | 8.5[k] | - | (1417,2505) | 21.7 | 9.5 |
| | B | | | | | | | | 8.8 | Radial | 22.3[k] | - | (952,2152) | 21.1 | 11.4 |
| | C | | | | | | | | 14.6 | Tangential | 2.44[k] | - | (3536,3145) | 23.8 | 2.2 |
| | D | | | | | | | | 17.6 | Tangential | 62.1[k] | - | (2572,2614) | 23.4 | 6 |
| | E[k] | | | | | | | | 6 | Tangential | 1.69[k] | - | (3593,3012) | 21.43[k] | 5.1 |
| | F[k] | | | | | | | | 9.5 | Radial | 45.6[k] | | (2153,2763) | 24.09[k] | 2.2 |
| PSZ1 G340.37+60.57[e] | | 14 01 02.7 | 02 51 56 | 14 01 2.017 | 02 52 41.55 | 9.73 | 0.2528 | | | | | | | | |
| | K0 | | | | | | | | 6.1 ± 0.3 | Radial | (7.2,-1.1) | - | (2853,3935) | 24.10 ± 0.13 | 0.8 |
| | K2 | | | | | | | | 7.7 ± 0.7 | Tangential | (-0.8,20.9) | - | (2421,3756) | 23.45 ± 0.11 | 1.2 |
| | K3 | | | | | | | | 12.0 ± 1.2 | Tangential | (-20.8,23.3) | - | (2435,3394) | 21.71 ± 0.07 | 2 |
| | A1A2A3 | | | | | | | | 15 | Tangential | 29.9(NW) | - | (2509,4262) | 23.08 | 3.3 |
| PSZ1 G067.19+67.44[e] | | 14 26 03.9 | 37 49 35 | 14 25 56.662 | 37 48 59.38 | 12.77 | 0.1712 | | | | | | | | |
| | A1 | | | | | | | | >14.3 | Tangential | (-25.4,-11.8) | - | | 23.35 ± 0.20 | |
| PSZ1 G096.87+52.48[l] | | 14 52 56.4 | 58 03 35 | 14 52 57.363 | 58 02 55.03 | 6.45 | 0.3179 | F814W | | | | | | | |
| | A | | | | | | | | 2.4 | Radial | 16.9 | - | (2666,3021) | 20.584 | 6.7 |
| | B | | | | | | | | 14.6 | Tangential | 30.4 | - | (2010,2981) | 22.986 | 4.9 |
| | C | | | | | | | | 27.4 | Tangential | 48.2 | - | (1723,3310) | 24.535 | 2.2 |
| | D | | | | | | | | 10 | Tangential | 96.1 | - | (3509,1024) | 22.491 | 5.4 |
| PSZ1 G006.76+30.45[j] | | 16 15 49.2 | -06 09 09 | | | 27.2 | 0.203 | F814W | | | | | | | |
| | A | | | | | | | | 8.7 | Tangential | 19.59 | - | (3440,1560) | 20.67 | 5.9 |
| | B | | | | | | | | 19.8 | Tangential | 26.13 | - | (3581,1660) | 21.98 | 3.32 |
| | C | | | | | | | | 7.2 ± 0.9 | Tangential | 86.8 | | (4757,2036) | 23.482 | 1.6 |
| PSZ1 G021.10+33.24[e] | | 16 32 47.8 | 05 35 32 | 16 32 46.927 | 05 34 32.76 | 14.17 | 0.1514 | F606W | | | | | | | |
| | A1 | | | | | | | | 5.9 ± 0.4 | Radial | (7.9,2.7) | - | (1198,1413) | 22.36 ± 0.10 | 2.7 |
| | A2 | | | | | | | | 6.0 ± 0.4 | Radial | (3.4,-0.3) | - | (1167,1463) | 22.56 ± 0.09 | 2.5 |
| PSZ1 G097.72+38.13[e] | | 16 35 52.0 | 66 11 44 | | | 16.6 | 0.1709 | | | | | | | | |
| | M0bcd | | | | | | | | 11.0 ± 0.7 | Tangential | (-16.6,12.7) | 0.702 | | 21.01 ± .01 | |
| | M4 | | | | | | | | 15.3 ± 1.0 | Tangential | (-53.2,35.9) | 1.034 | | 20.25 ± 0.02 | |
| | M1ab | | | | | | | | 6.5 ± 0.7 | Tangential | (22.4,0.9) | 2.515 | | 21.33 ± .02 | |
| | M3ab | | | | | | | | 18.3 ± 0.3 | Tangential | (17.0,-17.6) | - | | 23.03 ± 0.08 | |
| | 730 | | | | | | | | 17.2 ± 0.2 | Tangential | (-59.2,45.6) | - | | 22.02 ± .05 | |
| | 323 | | | | | | | | 7.7 ± 1.6 | Tangential | (-14.3,24.2) | - | | 21.38 ± .02 | |
| | 381 | | | | | | | | 16.2 ± 2.0 | Tangential | (35.1,2.7) | - | | 23.75 ± .16 | |
| | A1 | | | | | | | | 7.2 ± 0.9 | Tangential | (-38.6,9.1) | - | | 23.43 ± .07 | |
| | H2/H3 | | | | | | | | 22.9 ± 3.0 | Tangential | (-32.3,31.3) | - | | 23.19 ± .12 | |
| | H1/273 | | | | | | | | 8.9 ± 1.5 | Tangential | (-20.0,40.2) | - | | 21.73 ± .01 | |
| PSZ1 G072.61+41.47[e] | | 16 40 18.6 | 46 41 55 | | | 20.04 | 0.228 | | | | | | | | |
| | P0 | | | | | | | | 10.0 ± 0.6 | Tangential | (-13.9,10.6) | 1.07 | | 21.58 ± 0.02 | |
| | P2ab | | | | | | | | 26.9 ± 3.0 | Tangential | (17.3,-16.9) | 2.73 | | 22.38 ± 0.05 | |
| | P2c | | | | | | | | 6.0 ± 0.2 | Tangential | (-3.8,-26.7) | 2.73 | | 22.60 ± 0.03 | |
| | P13 | | | | | | | | 9.0 ± 0.7 | Tangential | (4.6,-30.8) | - | | 23.94 ± 0.11 | |
| | A1 | | | | | | | | 5.3 ± 0.5 | Radial | (-19.2, 31.1) | - | | 23.89 ± 0.08 | |
| PSZ1 G049.22+30.84[b] | | 17 20 12.6 | 26 37 23 | 17 20 10.024 | 26 37 32.26 | 10.76 | 0.1644 | | | | | | | | |
| | A1 | | | | | | | | 11.23 | Tangential | 11.9 | 0.82 | (260.04314,26.624351) | 22.74 ± .05 | |

TABLE A.2: Arc Statistics Table for HST Cluster Images Previously Analyzed in Other Work. Note, Cluster BCG RA DEC, Area, and some arc radii my analysis.

| **Cluster Name** | **Arc Name** | **RA** | **DEC** | **RA BCG** | **DEC BCG** | $S/N$ | **Cluster redshift** | **Filter** | $L/W$ | **Orientation** | **Arcsec to BCG** | **Arc redshift** | **Arc Coordinates** | **AB mag** | **Area**$(arcsec^2)$ |
|---|---|---|---|---|---|---|---|---|---|---|---|---|---|---|---|
| | A2 | | | | | | | | 11.23 | Tangential | 11.9 | 0.82 | (260.04247,26.624155) | 22.74 ± .05 | |
| | B1 | | | | | | | | 10.8 | Tangential | 33.32 | 4.38 | (260.03779,26.626930) | 24.85 ± .08 | |
| | B2 | | | | | | | | 10.8 | Tangential | 33.32 | 4.38 | (260.04285,26.626111) | 24.41 ± .07 | |
| PSZ1 G055.58+31.87[g] | | 17 22 21.9 | 32 07 58 | 17 22 27.186 | 32 07 56.87 | 10.61 | 0.224 | F606W | | | | | | | |
| | 3 | | | | | | | | 7.92 | Tangential | 24.54 | 3.54 | (2165,2317) | 23.75 | |
| | 4 | | | | | | | | 14.29 | Tangential | 26.77 | 1.8 | (2902,2395) | 22.07 | |
| | 6 | | | | | | | | 10.2 | Tangential | 66.94 | 1.35 | (2577,3516) | 23.22 | |
| PSZ1 G118.58+28.57[e] | | 17 25 00.4 | 85 53 41 | 17 24 12.14 | 85 53 11.88 | 8.06 | 0.178 | | | | | | | | |
| | A1 | | | | | | | | >13.1 | Radial | (2.3,6.7) | - | - | 24.69 ± 0.81 | |
| | A2 | | | | | | | | >29.0 | Tangential | (-19.9,-24.9) | - | - | 24.09 ± 0.70 | |
| PSZ1 G073.98-27.83[e] | | 21 53 44.0 | 17 41 35 | 21 53 36.825 | 17 41 43.51 | 15.21 | 0.2329 | | | | | | | | |
| | $A/C$ | | | | | | | | 10.7 ± 0.5 | Tangential | (17.7,-33.7) | 1.033 | | 19.9 ± 0.02 | |
| | H3a | | | | | | | | 7.9 ± 0.4 | Tangential | (19.3,-45.1) | 4.04 | | 22.44 ± 0.06 | |
| | H3b | | | | | | | | 4.1 ± 0.1 | Tangential | (9.4,-49.7) | 4.04 | | 22.88 ± 0.06 | |
| | H5a | | | | | | | | 5.0 ± 0.7 | Tangential | (3.6,-20.4) | 4.05 | | 23.53 ± 0.11 | |
| | H5b | | | | | | | | 5.9 ± 0.9 | Tangential | (-9.4,-24.6) | 4.05 | | 22.82 ± 0.06 | |
| | A1 | | | | | | | | 10.4 ± 0.9 | Tangential | (-6.3,5.8) | - | | 23.27 ± 0.11 | |
| | A2 | | | | | | | | 19.1 ± 2.1 | Tangential | (-13.5,6.1) | - | | 20.76 ± 0.04 | |
| | A3 | | | | | | | | 8.1 ± 0.5 | Tangential | (-33.2,9.2) | - | | 22.99 ± 0.11 | |
| PSZ1 G073.85-54.94[n] | | 23 08 28.1 | -02 12 00 | 23 08 22.311 | -2 11 33.4 | 6.21 | 0.2966 | | | | | | | see Newman et al 2013 | |
| | 1.1 | | | | | | | | | | (35.6,11.9) | 2.786 | | | |
| | 1.2 | | | | | | | | | | (38.0,7.2) | 2.786 | | | |
| | 1.3 | | | | | | | | | | (14.3,38.6) | 2.786 | | | |
| | 2.1 | | | | | | | | | | (35.4,12.8) | 2.786 | | | |
| | 2.2 | | | | | | | | | | (38.4,6.4) | 2.786 | | | |
| | 2.3 | | | | | | | | | | (16.6,37.3) | 2.786 | | | |
| | 3.1 | | | | | | | | | | (-15.4,-3.9) | 1.97 | | | |
| | 3.2 | | | | | | | | | | (11.3,12.6) | 1.97 | | | |
| | 3.3 | | | | | | | | | | (-13.6,28.5) | 1.97 | | | |
| | 3.4 | | | | | | | | | | (16.7,-24.8) | 1.97 | | | |
| | 3.5 | | | | | | | | | | (-0.6,1.0) | 1.97 | | | |
| | 4.1 | | | | | | | | | | (-22.6,8.4) | 3.607 | | | |
| | 4.2 | | | | | | | | | | (-19.0,21.3) | 3.607 | | | |
| | 4.3 | | | | | | | | | | (0.0,7.3) | 3.607 | | | |
| | 4.4 | | | | | | | | | | (6.4,15.3) | 3.607 | | | |
| | 4.5 | | | | | | | | | | (17.7,-33.1) | 3.607 | | | |
| PSZ1 G080.66-57.87[o] | | 23 27 33.7 | -02 03 42 | 23 27 30.323 | -2 04 04.83 | 6.37 | 0.705 | | | | | | | | |
| | A.1 | 351.87405 | -2.0643629 | | | | | | | | | 2.98 | | 22.85 | |
| | A.2 | 351.87116 | -2.0624877 | | | | | | | | | 2.98 | | 23.51 | |
| | A.3 | 351.85518 | -2.0652714 | | | | | | | | | 3.00 ± .18 | | 24.65 | |
| | A.4c | 351.86797 | -2.0731903 | | | | | | | | | 3.00 ± .18 | | 22.89 | |
| | A.5c | 351.86785 | -2.0735543 | | | | | | | | | 3.00 ± .18 | | 24.21 | |
| | B.1 | 351.8742 | -2.0723517 | | | | | | | | | 1.42 | | 20.81 | |
| | B.2 | 351.86529 | -2.0669059 | | | | | | | | | 1.42a | | 20.61 | |
| | B.3 | 351.86065 | -2.0682697 | | | | | | | | | 1.42a | | - | |
| | C.1 | 351.86283 | -2.0645228 | | | | | | | | | 2.083b | | 23.06 | |
| | C.2 | 351.86062 | -2.0656345 | | | | | | | | | - | | 23.16 | |
| | C.3c | 351.8795 | -2.0755689 | | | | | | | | | 2.09 | | 24.05 | |
| | D.1 | 351.86267 | -2.064537 | | | | | | | | | - | | 25.1 | |
| | D.2c | 351.86099 | -2.0653389 | | | | | | | | | - | | 23.72 | |
| | D.3c | 351.8795 | -2.0754385 | | | | | | | | | 2.53 | | 25.66 | |
| | E.1 | 351.87138 | -2.0838888 | | | | | | | | | 1.7 | | 22.29 | |
| | E.2 | 351.86734 | -2.0852578 | | | | | | | | | 1.7 | | 22.48 | |
| | E.3 | 351.85361 | -2.0772366 | | | | | | | | | 1.6 | | 23.57 | |
| | F.1cc | 351.86261 | -2.07756 | | | | | | | | | - | | 24.87 | |
| | F.2cc | 351.86165 | -2.07842 | | | | | | | | | - | | 24.46 | |
| | G.1 | 351.86199 | -2.0654498 | | | | | | | | | 2.38 | | 25.53 | |
| | G.2 | 351.86025 | -2.0665151 | | | | | | | | | 2.11 | | 25.63 | |

TABLE A.2: Arc Statistics Table for HST Cluster Images Previously Analyzed in Other Work. Note, Cluster BCG RA DEC, Area, and some arc radii my analysis.

| Cluster Name | Arc Name | RA | DEC | RA BCG | DEC BCG | $S/N$ | Cluster redshift | Filter | $L/W$ | Orientation | Arcsec to BCG | Arc redshift | Arc Coordinates | AB mag | Area($arcsec^2$) |
|---|---|---|---|---|---|---|---|---|---|---|---|---|---|---|---|

[a] Previously reported by Richard et al 2014
[b] Previously reported by Richard et al 2010
[c] See Kawamata et al 2016 for complete analysis of large set
[d] Previously reported by Ammons et al 2014
[e] Previously reported by Sand et al 2005
[f] Previously reported by Zitrin et al 2015
[g] Reported by Xu et al 2016
[h] Full Abell 1689 analysis set by Coe et al 2010
[i] Previously analyzed Richard et al 2009
[j] Previously reported by Sand et al 2005
[k] Calculated in this analysis
[l] Holhjem et al 2009
[m] Soucail 1992
[n] Newman et al 2013
[o] Hoag et al 2015

# Appendix B

# Arc Statistics Table of Ground Based Image Data

TABLE B.1: NOT images from the MOSCA and ALFOSC instruments. Arc to BCG is in arcseconds and area are in square arseconds. Absolute magnitudes are included for all filters with usable photometric data.

| Source ID | Cluster Name | Arc | RA | DEC | BCG X | BCG Y | $S/N$ | M500 | Cluster redshift | Detector | Exposure ($s$) | Filter | Seeing | $L/W$ | Arc Orientation | Arcsec to BCG | Area | g | r | i |
|---|---|---|---|---|---|---|---|---|---|---|---|---|---|---|---|---|---|---|---|---|
| 391 | PSZ1 G107.66-58.31 | | 00 19 35.0 | 03 36 37 | 906 | 956 | 6.49 | 6.354 | 0.35 | MOSCA | 1800 | g-band | 1.07 | | | | | | | |
| | | A | 00 19 39.934 | 03 35 11.32 | | | | | | | | | | 2.7 | Tangential | 47.3 | 20.86 | 19.96 | 21.21 | 19.8 |
| 463 | PSZ1 G155.25-68.42 | none | 01 37 18.7 | -08 28 42 | | | 6.43 | 9.05 | 0.5748 | ALFOSC | 600 | g-band | 1.19 | | | | | | | |
| 475 | PSZ1 G132.49-17.29 | | 01 42 55.5 | 44 37 25 | 793 | 1239 | 8.33 | 8.259 | 0.341 | MOSCA | 1800 | g-band | 1.06 | | | | | | | |
| | | A | 01 42 57.278 | 44 37 55.8 | | | | | | | | | | 7.7 | Tangential | 22.8 | 13.5 | 19.35 | 20.96 | 22.83 |
| | | B | 01 42 56.824 | 44 38 27.83 | | | | | | | | g-band | | 3 | Tangential | 29.1 | 10.6 | 19.99 | 21.18 | 21.34 |
| | | C | 01 42 55.311 | 44 38 26.79 | | | | | | | | g-band | | 1.3 | Tangential | 22.4 | 11.2 | 20.08 | 20.07 | 19.72 |
| | | D | 01 42 53.993 | 44 38 27.58 | | | | | | | | g-band | | 1.7 | Tangential | 26.5 | 11.8 | 20.38 | 20.39 | 20.38 |
| | | E | 01 42 53.164 | 44 38 13.78 | | | | | | | | g-band | | 2.7 | Tangential | 23.9 | 9.6 | NA | NA | NA |
| | | F | 01 42 53.773 | 44 37 53.47 | | | | | | | | g-band | | 2 | Tangential | 18.4 | 7.2 | 21.05 | 20.66 | 19.9 |
| | | G | 01 42 54.163 | 44 37 43.83 | | | | | | | | g-band | | 2 | Tangential | 23.2 | 8.3 | 21.15 | 22.33 | 22.26 |
| 522 | PSZ1 G146.00-49.42 | none | 01 51 34.5 | 10 44 03 | | | 6.62 | 4.04 | | MOSCA | 600 | i-band | 1.13 | | | | | | | |
| 602 | PSZ1 G176.25-52.57 | | 02 48 13.1 | -02 14 21 | 1538 | 582 | 6.93 | 6.375 | 0.236 | MOSCA | 1800 | g-band | 1.12 | | | | | | | |
| | | A | 02 48 09.151 | -02 16 36.85 | | | | | | | | g-band | | 8.7 | Tangential | 13.7 | 47 | 20.77 | NA | 20.83 |
| 686 | PSZ1 G208.59-26.00 | | 05 10 44.3 | -08 01 12 | 963 | 1057 | 7.9 | 7.363 | 0.2195 | MOSCA | 1800 | g-band | 0.94 | | | | | | | |
| | | A | 05 10 50.647 | -08 02 21.90 | | | | | | | | g-band | | 3.4 | Tangential | 55 | 13.8 | 20.26 | 21.29 | 21.91 |
| | | B | 05 10 50.824 | -08 02 03.53 | | | | | | | | g-band | | 7 | Tangential | 47.5 | 17 | 20.41 | 20.51 | 19.92 |
| | | C | 05 10 46.785 | -08 01 21.91 | | | | | | | | g-band | | 6.7 | Tangential | 29.4 | 49.2 | 19.16 | 20.32 | 20.11 |
| | | D | 05 10 46.482 | -08 01 10.28 | | | | | | | | g-band | | 4.5 | Tangential | 41.4 | 16.7 | 20.56 | 21.69 | 21.6 |
| | | E | 05 10 45.472 | -08 00 53.03 | | | | | | | | g-band | | 2.2 | Tangential | 63.8 | 18.4 | 19.6 | 20.09 | 19.84 |
| 548 | PSZ1 G156.88+13.48 | | 05 45 41.3 | 55 30 40 | 1211 | 792 | 6.19 | | 0.227 | MOSCA | 600 | r-band | 1.01 | | | | | | | |
| | | A | 05 45 37.474 | 55 30 18.96 | | | | | | | | r-band | | 3.2 | Tangential | 35.3 | 3 | NA | NA | NA |
| | | B | 05 45 36.493 | 55 30 17.65 | | | | | | | | g-band | 1.50 | 3.9 | Tangential | 36.7 | 9 | 20 | NA | NA |
| 29 | PSZ1 G170.22+09.74 | | 06 03 21.5 | 42 13 56 | 1352 | 1168 | 14.38 | | 0.228 | ALFOSC-HST | 300 | i-band | | | | | | | | |
| | | A | 06 03 17.864 | 42 14 53.19 | | | | | | | | i-band | 0.95 | 8.5 | Tangential | 17.3 | 21 | NA | NA | 20.36 |
| | | B | 06 03 16.693 | 42 14 13.45 | | | | | | | | i-band | | 2.7 | Radial | 29.4 | 5.7 | 20.43 | NA | 19.07 |
| 503 | PSZ1 G139.61+24.20 | | 06 22 13.9 | 74 41 39 | 1669 | 1340 | 7.94 | 7.094 | 0.2671 | MOSCA | 1800 | g-band | 0.90 | | | | | | | |
| | | A | 06 21 41.867 | 74 42 28.12 | | | | | | | | g-band | | 3 | Tangential | 36 | 7.3 | NA | NA | NA |
| | | B | 06 21 40.718 | 74 42 23.11 | | | | | | | | g-band | | 3.4 | Tangential | 37.1 | 23.8 | 21.31 | 22.39 | 21.81 |
| | | C | 06 21 32.494 | 47 42 18.91 | | | | | | | | g-band | | 1.9 | Tangential | 67 | 21 | 21.76 | 22.14 | 21.1 |
| 505 | PSZ1 G224.01-11.14 | none | 06 31 00.7 | -14 50 06 | | | 6.13 | 9.085 | | ALFOSC | 300 | g-band | 1.13 | | | | | | | |
| 529 | PSZ1 G148.20+23.49 | none | 06 37 45.6 | 66 54 24 | | | 8.4 | 4.393 | | MOSCA | 1800 | g-band | 0.87 | | | | | | | |
| 582 | PSZ1 G167.64+17.63 | none | 06 38 02.7 | 47 48 33 | | | 9.71 | 6.518 | 0.174 | MOSCA | 1800 | g-band | 1.01 | | | | | | | |
| 710 | PSZ1 G215.51+06.58 | | 07 19 34.4 | 00 42 58 | 958 | 953 | 8.03 | 7.309 | 0.2197 | MOSCA | 1800 | g-band | 1.17 | | | | | | | |
| | | A | 07 19 37.337 | 00 42 06.79 | | | | | | | | g-band | | 5.4 | Tangential | 11.51 | 17.9 | 19.33 | 18.49 | 18.66 |
| 720 | PSZ1 G217.40+10.88 | none | 07 38 17.7 | 01 01 37.00 | | | 6.26 | 5.355 | 0.189 | MOSCA | 1800 | g-band | 0.89 | | | | | | | |
| 551 | PSZ1 G157.44+30.34 | none | 07 49 00.1 | 59 40 50 | | | 7.54 | 8.621 | | MOSCA | 1800 | g-band | 1.24 | | | | | | | |
| 589 | PSZ1 G171.01+39.44 | | 08 50 59.6 | 48 29 29 | 1527 | 813 | 6.68 | 8.6 | 0.5131 | MOSCA | 600 | i-band | 0.81 | | | | | | | |
| | | A1 | 08 50 59.615 | 48 29 49.42 | | | | | | | | i-band | | 1.7 | Tangential | 15.9 | 3.2 | NA | NA | 21.06 |
| | | A2 | 08 50 59.324 | 48 29 47.73 | | | | | | | | i-band | | 3.8 | Tangential | 16.6 | 3.8 | NA | NA | 21.08 |
| 579 | PSZ1 G166.61+42.12 | | 09 09 34.1 | 51 33 28 | 2071 | 1116 | 6.46 | 5.564 | 0.2323 | MOSCA | 600 | i-band | 0.72 | | | | | | | |
| | | A | 09 09 19.070 | 51 31 24.21 | | | | | | | | i-band | | 2.2 | Tangential | 7.2 | 16.5 | 17.86 | 18.08 | 17.86 |
| | | B | 09 09 17.820 | 51 31 27.43 | | | | | | | | i-band | | 2.6 | Tangential | 4.5 | 9.6 | 17.76 | 17.83 | 17.65 |

TABLE B.1: NOT images from the MOSCA and ALFOSC instruments. Arc to BCG is in arcseconds and area are in square arseconds. Absolute magnitudes are included for all filters with usable photometric data.

| Source ID | Cluster Name | Arc | RA | DEC | BCG X | BCG Y | $S/N$ | M500 | Cluster redshift | Detector | Exposure ($s$) | Filter | Seeing | $L/W$ | Arc Orientation | Arcsec to BCG | Area | g | r | i |
|---|---|---|---|---|---|---|---|---|---|---|---|---|---|---|---|---|---|---|---|---|
| 827 | PSZ1 G244.48+34.06 | none | 09 49 51.8 | -07 29 28 | | | 8.14 | | | MOSCA | 1800 | g-band | 1.14 | | | | | | | |
| 845 | PSZ1 G249.01+73.75 | none | 11 56 46.2 | 16 55 44 | | | 7.14 | | | MOSCA | 1800 | g-band | 1.43 | | | | | | | |
| 513 | PSZ1 G143.28+65.22 | | 11 59 15.8 | 49 47 12 | 1473 | 825 | 8.01 | 7.35 | 0.211 | MOSCA | 1800 | g-band | 1.24 | | | | | | | |
| | | A | 11 59 09.683 | 49 47 56.67 | | | | | | | | g-band | | | Tangential | 51.3 | 10.2 | 20.06 | 21.02 | 21.09 |
| | | B | 11 59 07.486 | 49 48 12.71 | | | | | | | | g-band | | 2.7 | Radial | 76.7 | 6.2 | NA | NA | NA |
| | | C | 11 59 31.283 | 49 47 45.52 | | | | | | | | g-band | | 1.3 | Tangential | 9.14 | 11.2 | 19.87 | 20.64 | 20.45 |
| 773 | PSZ1 G229.70+77.97 | | 12 01 21.1 | 23 06 31 | 1775 | 923 | 8.95 | 7.736 | 0.269 | MOSCA | 1800 | g-band | 1.16 | | | | | | | |
| | | A | 12 01 11.887 | 23 05 59.00 | | | | | | | | g-band | | 3 | Tangential | 4 | 7.9 | 21.03 | 20.39 | 20.71 |
| 685 | PSZ1 G207.87+81.31 | | 12 12 21.3 | 27 33 18 | 1535 | 1364 | 6.81 | 7.128 | 0.353 | MOSCA | 1800 | g-band | 0.86 | | | | | | | |
| | | A | 12 12 17.186 | 27 33 02.65 | | | | | | | | | | 5 | Tangential | 54.8 | 15.5 | 18.36 | 19.68 | 19.88 |
| | | B | 12 12 19.893 | 27 33 28.31 | | | | | | | | g-band | | 4.5 | Tangential | 23.9 | 11.9 | 18.88 | 19.15 | 18.98 |
| | | C | 12 12 19.080 | 27 33 45.85 | | | | | | | | g-band | | 5.4 | Tangential | 7.9 | 16 | 18.72 | 19.27 | 19.02 |
| | | D | 12 12 15.966 | 27 34 27.24 | | | | | | | | g-band | | 7 | Tangential | 53.5 | 6.2 | 20.55 | 22.06 | 22.79 |
| G326+54 | PSZ1 G326.64+54.79 | none | 13 45 20.1 | -05 34 46 | | | 6.61 | | | MOSCA | 1800 | g-band | 1.11 | | | | | | | |
| 415 | PSZ1 G113.84+44.33 | none | 14 14 00.3 | 71 18 23 | | | 8.92 | 5.003 | 0.225 | MOSCA | 1800 | g-band | 1.02 | | | | | | | |
| 4 | PSZ1 G001.00+25.71 | none | 16 18 20.2 | -13 04 12 | | | 6.04 | | | MOSCA | 1800 | g-band | 1.02 | | | | | | | |
| 49 | PSZ1 G019.12+31.23 | none | 16 36 29.4 | 03 08 51.00 | | | 6.95 | 7.084 | 0.28 | MOSCA | 1800 | g-band | 0.91 | | | | | | | |
| 238 | PSZ1 G071.63+29.78 | none | 17 47 18.2 | 45 11 24 | | | 7.7 | 4.393 | 0.1565 | MOSCA | 1800 | g-band | 1.29 | | | | | | | |
| 221 | PSZ1 G066.41+27.03 | | 17 56 48.2 | 40 07 59 | 967 | 1245 | 6.46 | 7.413 | 0.5699 | MOSCA | 1800 | g-band | 0.89 | | | | | | | |
| | | A | 17 56 52.628 | 40 08 07.49 | | | | | | | | g-band | | 14.9 | Tangential | 67.32 | 45.7 | 19.2 | 20.13 | 19.81 |
| 102 | PSZ1 G037.67+15.71 | none | 18 03 14.4 | 11 12 21.00 | | | 6.35 | | | MOSCA | 1800 | g-band | 0.91 | | | | | | | |
| 100 | PSZ1 G036.73+14.93 | none | 18 04 31.1 | 10 03 19.00 | | | 8.6 | 5.538 | 0.1525 | MOSCA | 1800 | g-band | 1.45 | | | | | | | |
| 291 | PSZ1 G085.98+26.69 | none | 18 19 56.7 | 57 10 17 | | | 7.12 | 4.222 | 0.179 | MOSCA | 1800 | g-band | 0.91 | | | | | | | |
| 330 | PSZ1 G094.69+26.34 | | 18 32 33.4 | 64 49 38 | 1116 | 1407 | 7.05 | 3.257 | 0.1623 | MOSCA | 600 | r-band | 1.04 | | | | | | | |
| | | A | 18 32 31.968 | 64 49 40.70 | | | | | | | | r-band | | 3.2 | Tangential | 19 | 11.3 | 17.23 | 17.66 | 17.58 |
| | | B | 18 32 32.212 | 64 49 58.58 | | | | | | | | r-band | | 2.6 | Tangential | 5 | 13.8 | NA | NA | NA |
| | | C | 18 32 33.065 | 64 50 08.69 | | | | | | | | r-band | | 3.5 | Tangential | 6.7 | 19 | NA | NA | NA |
| 225 | PSZ1 G067.36+10.74 | | 19 16 02.3 | 35 24 45 | 1214 | 1811 | 9.09 | 6.269 | 0.209 | MOSCA | 1800 | g-band | 0.89 | | | | | | | |
| | | A | 19 16 02.767 | 35 26 41.25 | 1214 | 1811 | | | | | | g-band | | 5.7 | Tangential | 14.5 | 15.8 | 19.01 | 19.99 | 19.96 |
| | | B | 19 16 01.927 | 35 26 52.05 | 1214 | 1811 | | | | | | g-band | | 4 | Tangential | 28.6 | 7.4 | 19.72 | 20.45 | 20.11 |
| | | C | 19 16 15.387 | 35 24 49.15 | 509 | 1330 | | | | | | g-band | | 2.8 | Tangential | 12.5 | 62.9 | 17.01 | 18.21 | 18.11 |
| | | D | 19 16 07.289 | 35 24 14.68 | 1017 | 1118 | | | | | | g-band | | 3.9 | Tangential | 19.4 | 9.4 | 20.44 | 20.27 | 19.69 |
| 78 | PSZ1 G029.79-17.37 | none | 19 48 26.2 | -10 31 30 | | | 6.59 | 4.996 | | MOSCA | 200 | i-band | 0.92 | | | | | | | |
| 179 | PSZ1 G056.76-11.60 | none | 20 18 54.0 | 15 06 08 | | | 6.56 | 3.965 | | MOSCA | 1800 | g-band | 1.01 | | | | | | | |
| 45 | PSZ1 G072.78-18.70 | none | 21 22 17.3 | 23 12 08 | | | 11.97 | 5.914 | 0.143 | ALFOSC | 300 | i-band | 0.50 | | | | | | | |
| 177 | PSZ1 G055.95-34.87 | none | 21 35 13.6 | 01 25 40.00 | | | 9.09 | 6.924 | 0.231 | MOSCA | 1800 | g-band | 1.02 | | | | | | | |
| 282 | PSZ1 G084.41-12.43 | none | 21 37 51.4 | 35 34 55 | | | 7.06 | 5.8 | | MOSCA | 1800 | g-band | 0.98 | | | | | | | |
| 250 | PSZ1 G074.75-24.59 | none | 21 46 08.9 | 20 28 43 | | | 6.12 | 5.057 | 0.25 | ALFOSC | 1800 | g-band | 0.83 | | | | | | | |
| 284 | PSZ1 G084.62-15.86 | none | 21 49 43.7 | 33 10 24 | | | 6.01 | 6.62 | | MOSCA | 1800 | g-band | 1.00 | | | | | | | |
| 262 | PSZ1 G088.83-12.99 | none | 21 55 55.9 | 37 59 59 | | | 7.72 | 7.353 | 0.292 | ALFOSC | 300 | g-band | 0.58 | | | | | | | |
| 336 | PSZ1 G096.44-10.40 | none | 22 19 35.1 | 44 31 05 | | | 6.55 | | | MOSCA | 1800 | g-band | 0.99 | | | | | | | |
| 239 | PSZ1 G071.64-42.76 | none | 22 30 51.4 | 05 41 07 | | | 8.82 | | | MOSCA | 200 | i-band | 0.99 | | | | | | | |
| 241 | PSZ1 G072.59-43.25 | none | 22 34 15.1 | 05 48 39 | | | 6.08 | 4.401 | 0.159 | MOSCA | 200 | i-band | 0.96 | | | | | | | |
| 360 | PSZ1 G100.18-29.68 | none | 23 20 56.4 | 29 09 44 | | | 6.15 | 7.971 | 0.485 | MOSCA | 1800 | g-band | 0.94 | | | | | | | |
| 394 | PSZ1 G108.18-11.53 | none | 23 22 29.7 | 48 46 30 | | | 6.36 | 7.7 | | MOSCA | 1800 | g-band | 1.25 | | | | | | | |
| 399 | PSZ1 G109.14-28.02 | none | 23 53 08.8 | 33 16 48 | | | 6.51 | 8.094 | 0.4709 | MOSCA | 1800 | g-band | 0.93 | | | | | | | |
| 381 | PSZ1 G105.91-38.39 | none | 23 53 54.1 | 22 34 21 | | | 7.16 | | | MOSCA | 1800 | g-band | 0.91 | | | | | | | |
| 92 | PSZ1 G002.80+39.24 | | 15 40 00.0 | -03 17 34 | 15 40 07.926 | -03 18 15.46 | 7.04 | 5.912 | 0.1533 | SUP | 3600 | G-band | 0.7 | | | | | | | |
| | | A | 15 40 08.324 | -03 18 11.42 | 15 40 07.926 | -03 18 15.46 | | | | | | | | 4.96 | Tangential | 7.22 | 9.4 | 20.7 | | |
| | | B | 15 40 04.596 | -03 18 38.66 | 15 40 03.927 | -03 18 46.39 | | | | | | | | 3.61 | Tangential | 12.81 | 3.9 | 21.3 | | |
| 137 | PSZ1 G083.30-31.01 | | 22 28 29.1 | +20 38 22 | 5871 | 5614 | 6.94 | 7.82 | 0.412 | SUP | 1440 | B-band | 0.72 | | | | | | | |
| | | A | 22 28 26.715 | 50 37 15.80 | | | | | | | | | | 4.99 | Tangential | 97.47 | 10.1 | 21.58 | | |
| | | B | 22 28 28.039 | 20 37 06.11 | | | | | | | | | | 2.75 | Tangential | 79.5 | 2.8 | 23.29 | | |
| | | C | 22 28 32.579 | 20 37 09.73 | | | | | | | | | | 7.2 | Tangential | 16.36 | 9.2 | 21.9 | | |
| 142 | PSZ1 G081.01-50.92 | | 23 11 36.3 | +03 38 38 | | | 8.59 | 7.529 | 0.2998 | SUP | 720 | V-band | 0.68 | | | | | | | |
| | | A | | | | | | | | | | | | 3.04 | Tangential | 81.49 | 4 | 22.56 | | |
| | | B | | | | | | | | | | | | 4.02 | Tangential | 86.82 | 2.7 | 21.81 | | |

# Appendix C

# Images of HST Strong Lenses and Cluster Centers

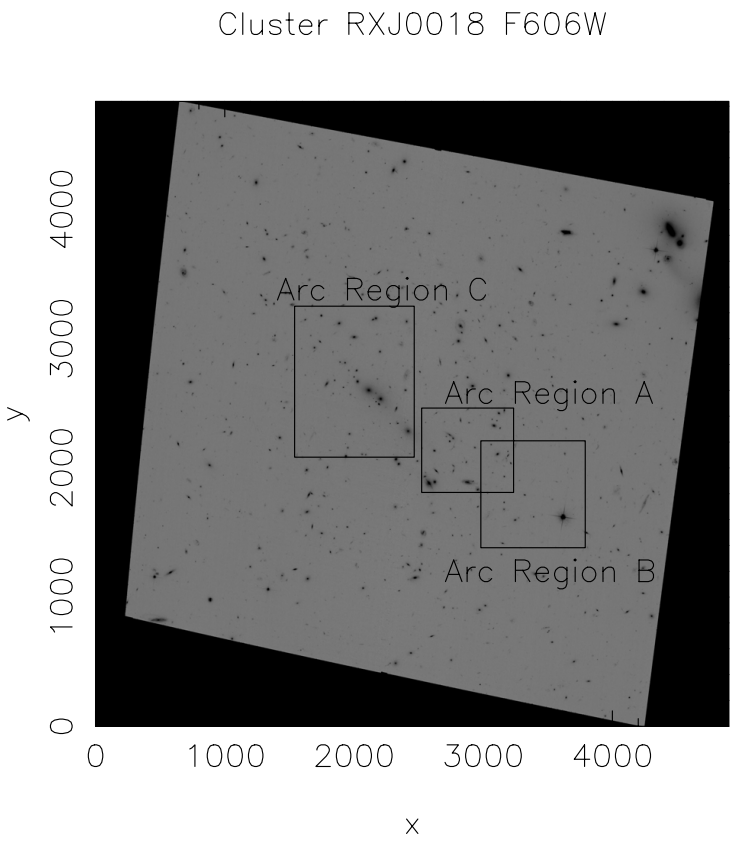


FIGURE C.1: Cluster RXC J0018.5+1626 or PSZ1 G111.60-45.72

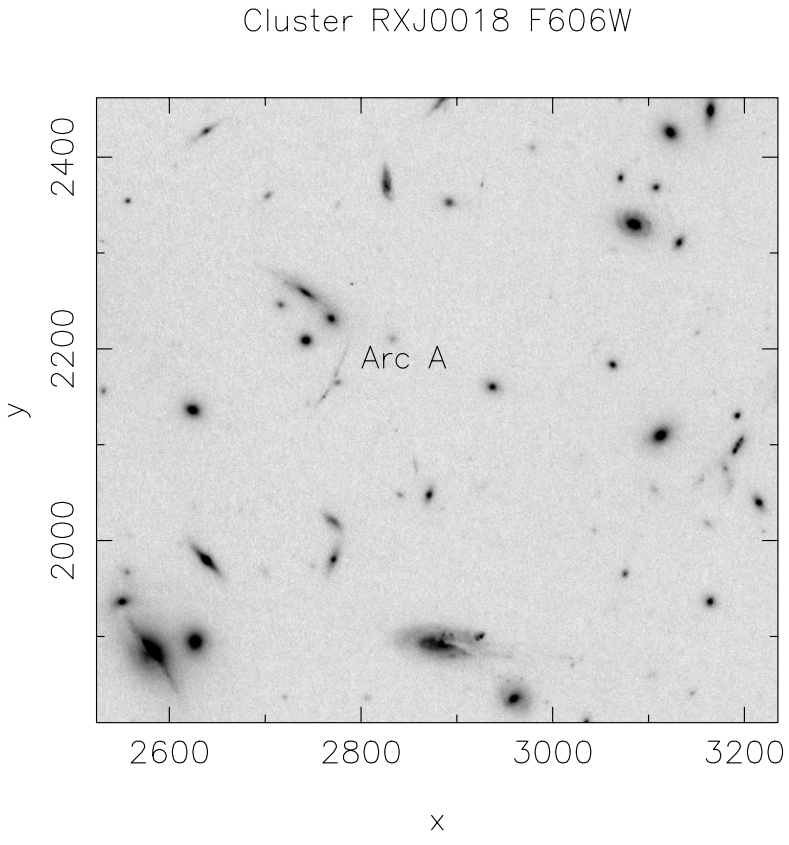


FIGURE C.2: PSZ1 G111.60-45.72 Slim tangential Arc A

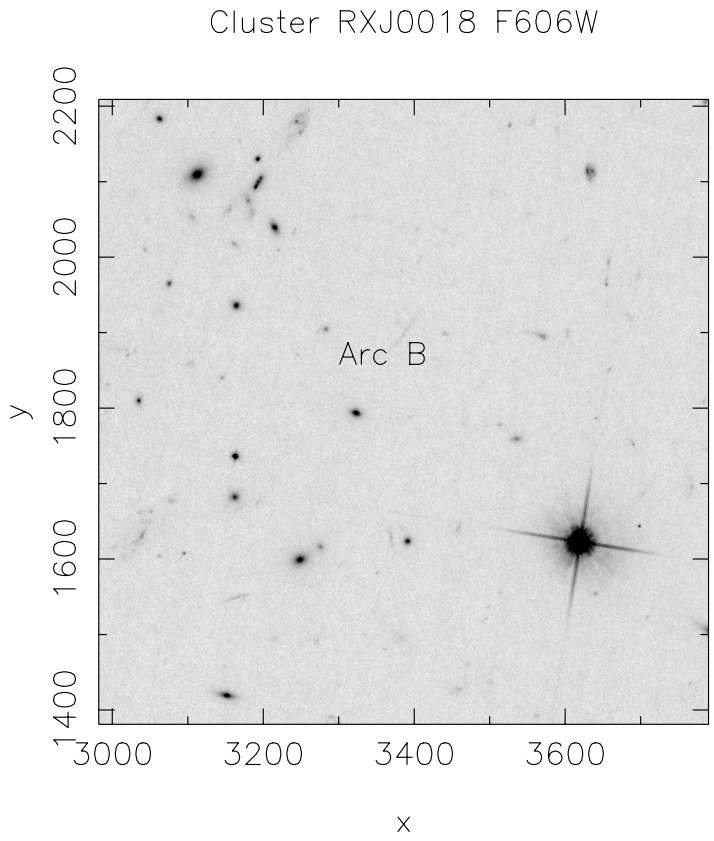


FIGURE C.3: PSZ1 G111.60-45.72 Slim tangential Arc B

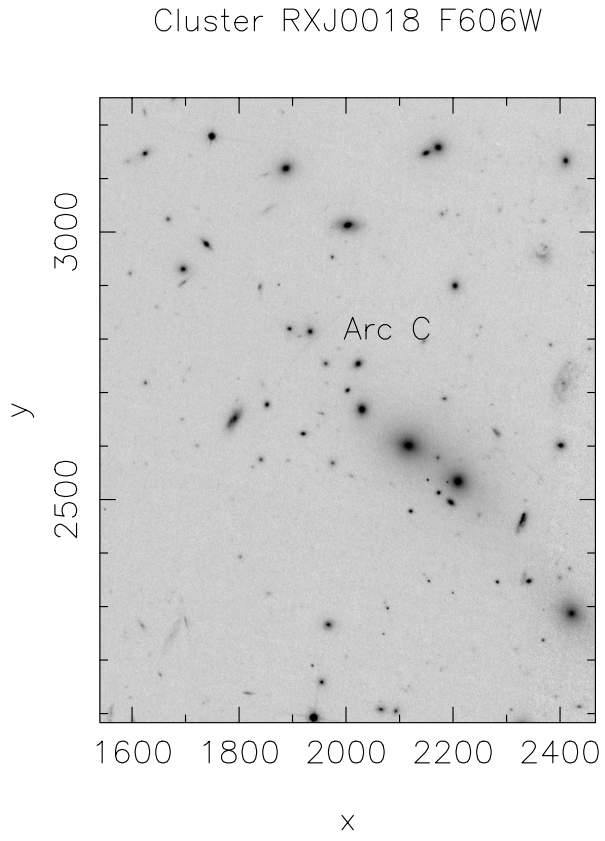


FIGURE C.4: PSZ1 G111.60-45.72 Faint tangential Arc C. $L/W$ of 52

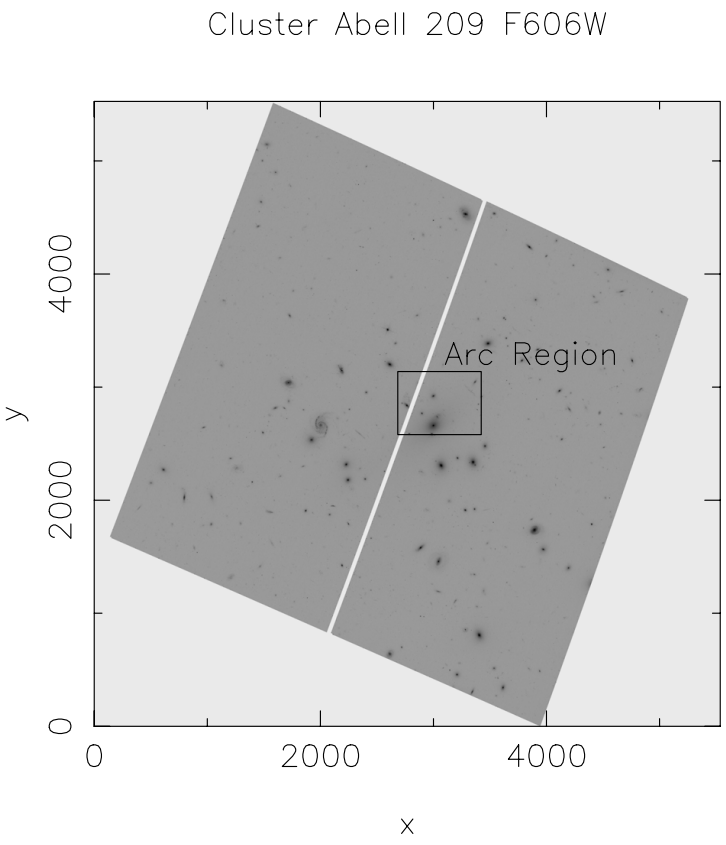


FIGURE C.5: PSZ1 G157.32-26.77 or RXJ0131.8-1336

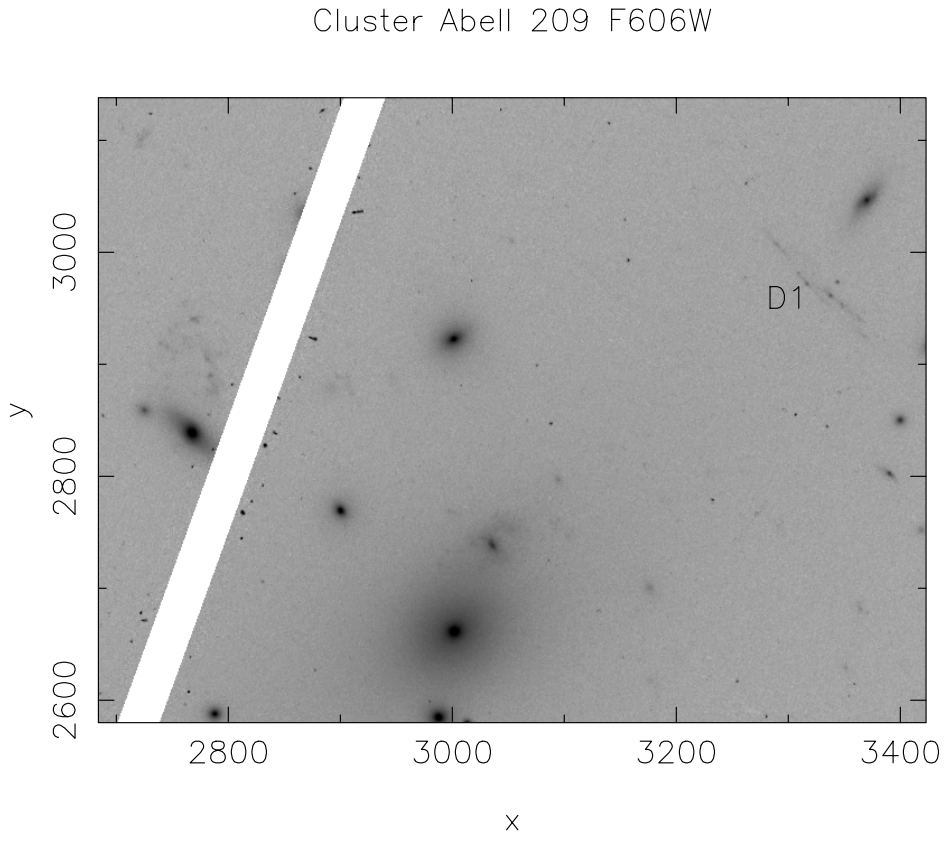


FIGURE C.6: PSZ1 G157.32-26.77 Arc Referred to as D1 by Xu et al 2016

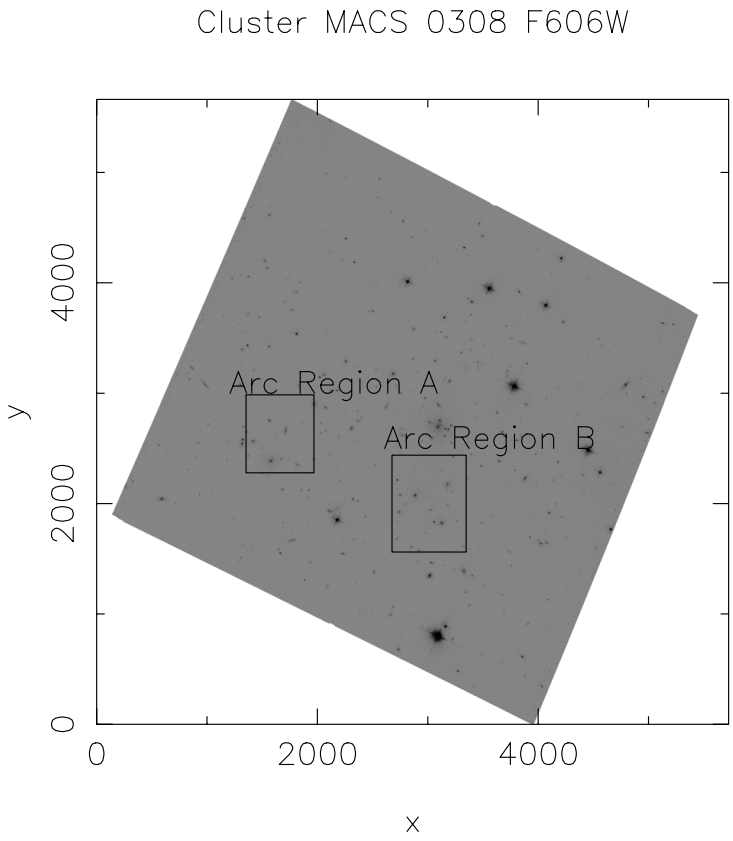


FIGURE C.7: Cluster RXC J0308.9 + 2645 or PSZ1 G157.32-26.77 Arc Coordinates

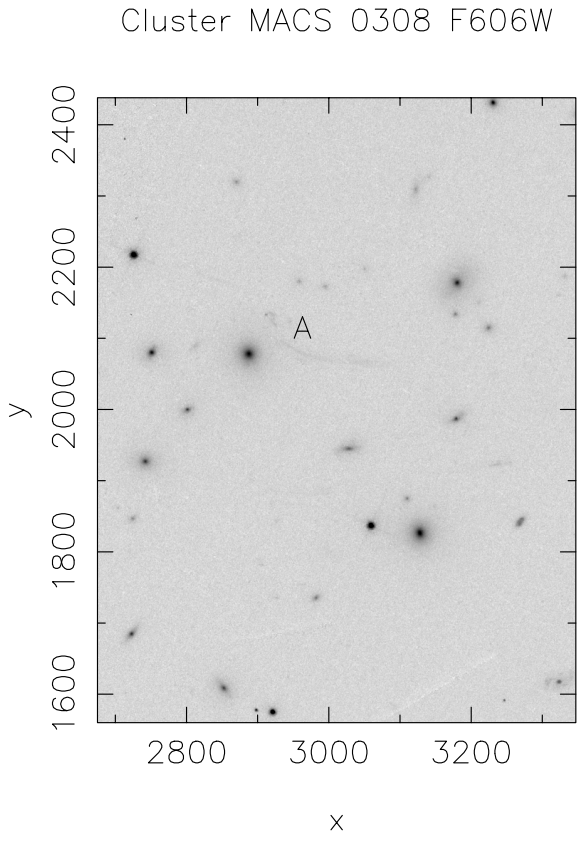


FIGURE C.8: PSZ1 G157.32-26.77 Tangential Arc A

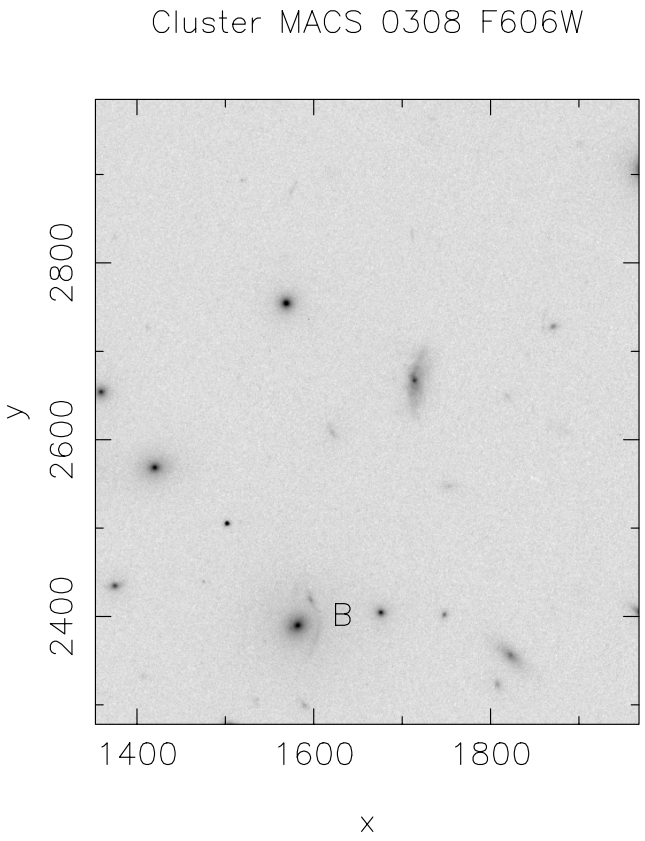


FIGURE C.9: PSZ1 G157.32-26.77 Short radius to different lens center tangential Arc B

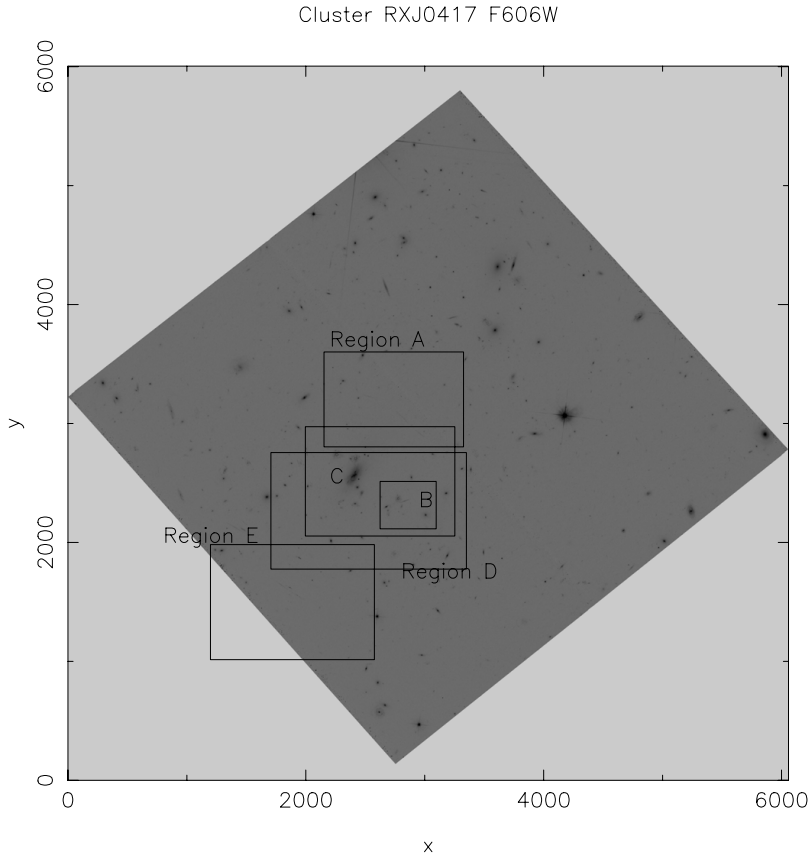


FIGURE C.10: PSZ1 G205.94-39.46 or RXC J 0417.5-1154

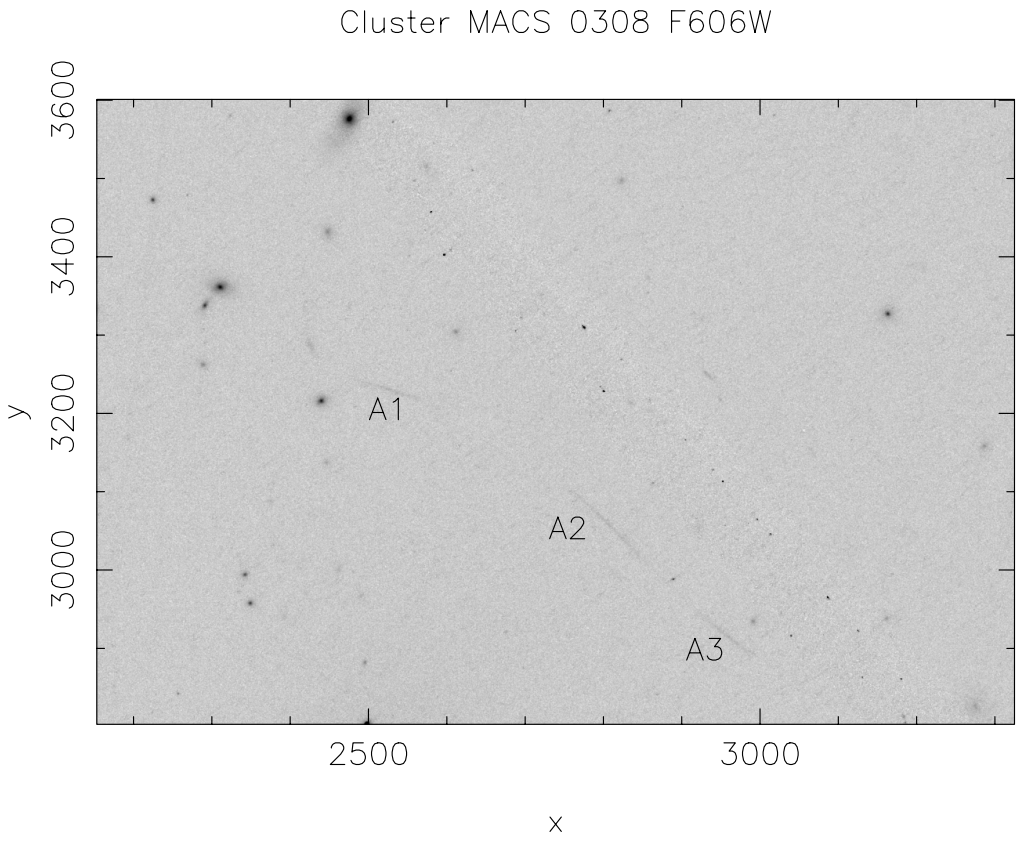


FIGURE C.11: PSZ1 G205.94-39.46 Tangential Arcs A1 A2 A3

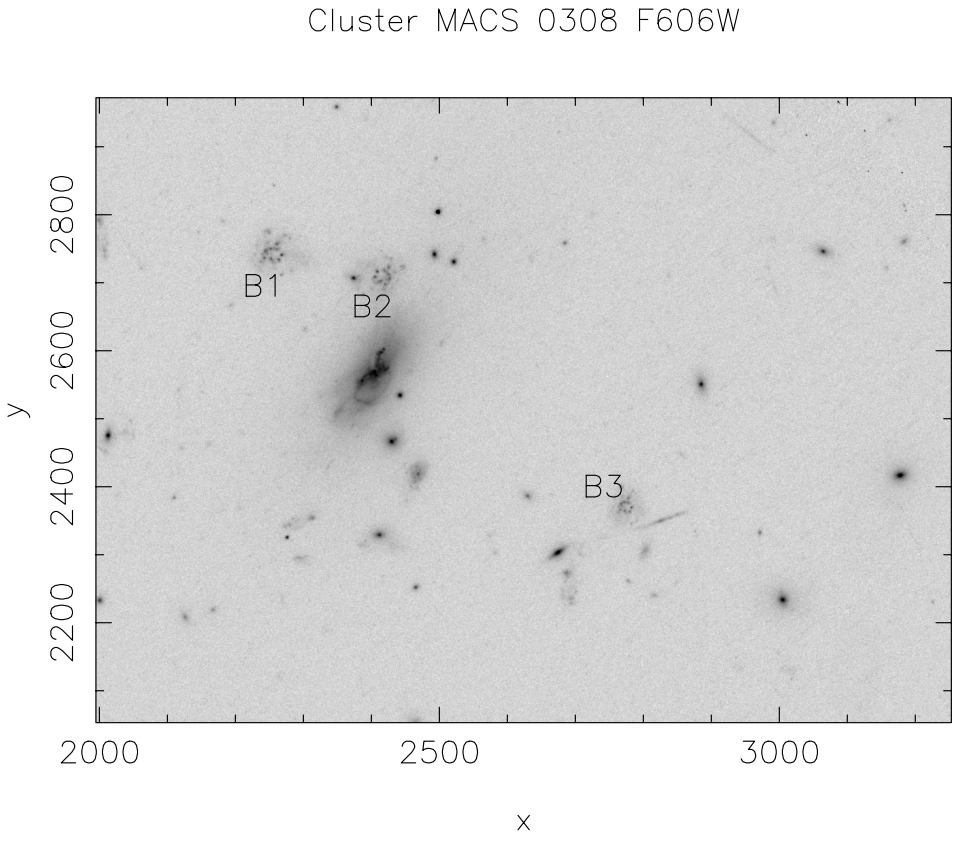


FIGURE C.12: PSZ1 G205.94-39.46 Multiply imaged B1 B2 B3

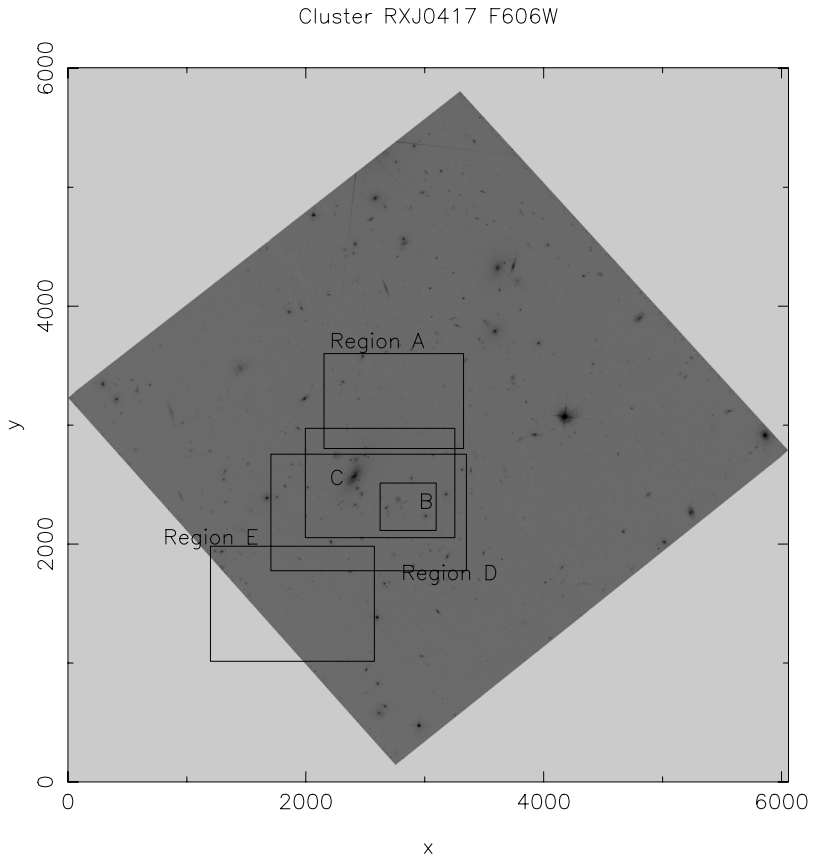


FIGURE C.13: PSZ1 G205.94-39.46 C Removed

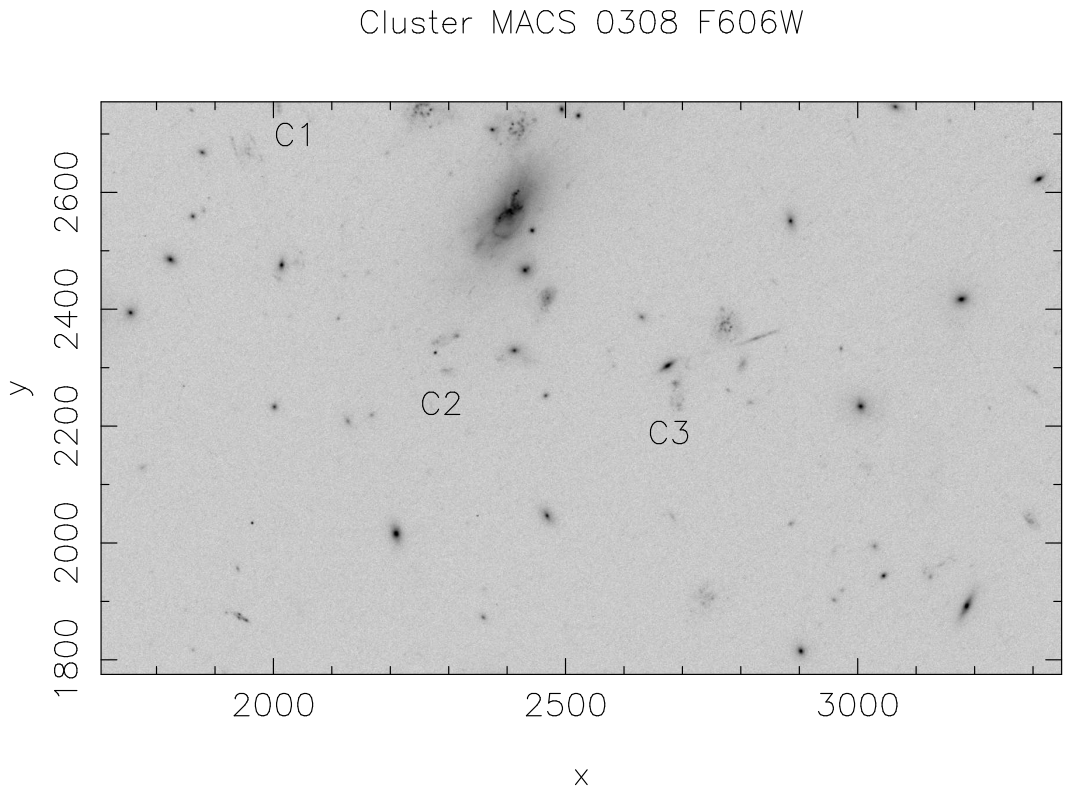


FIGURE C.14: PSZ1 G205.94-39.46 Multiply imaged C1 C2 C3

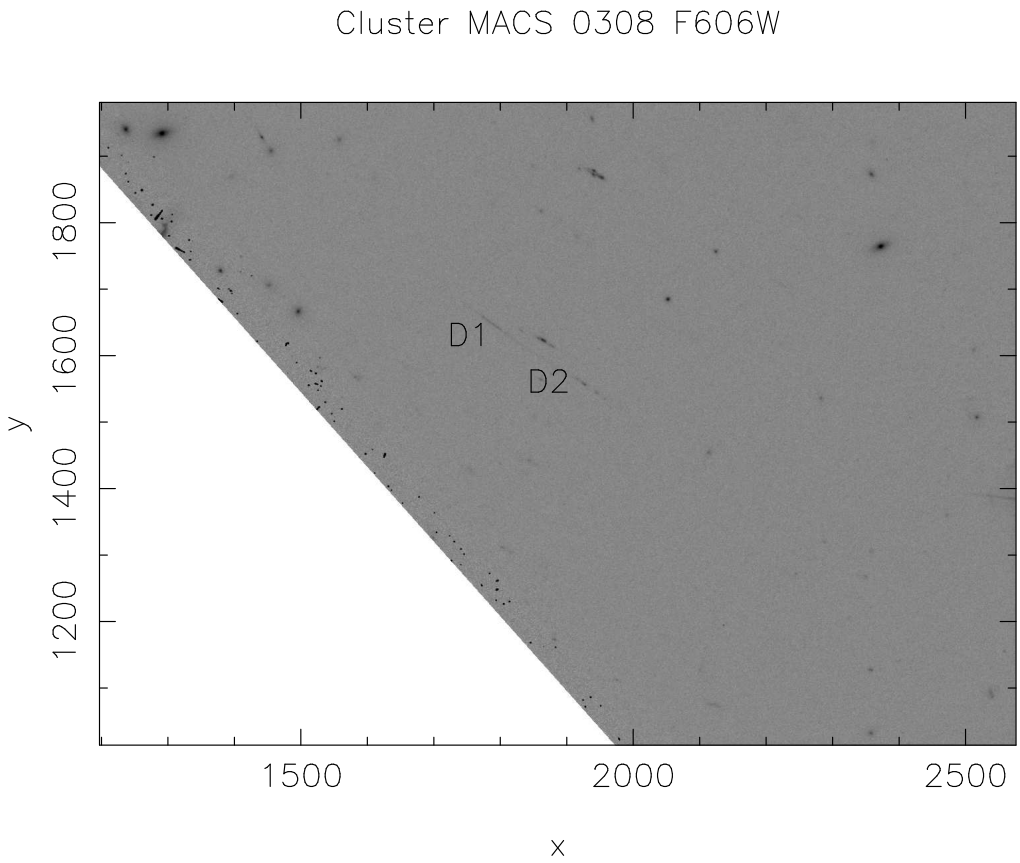


FIGURE C.15: PSZ1 G205.94-39.46 Tangential Arcs D1 and D2.

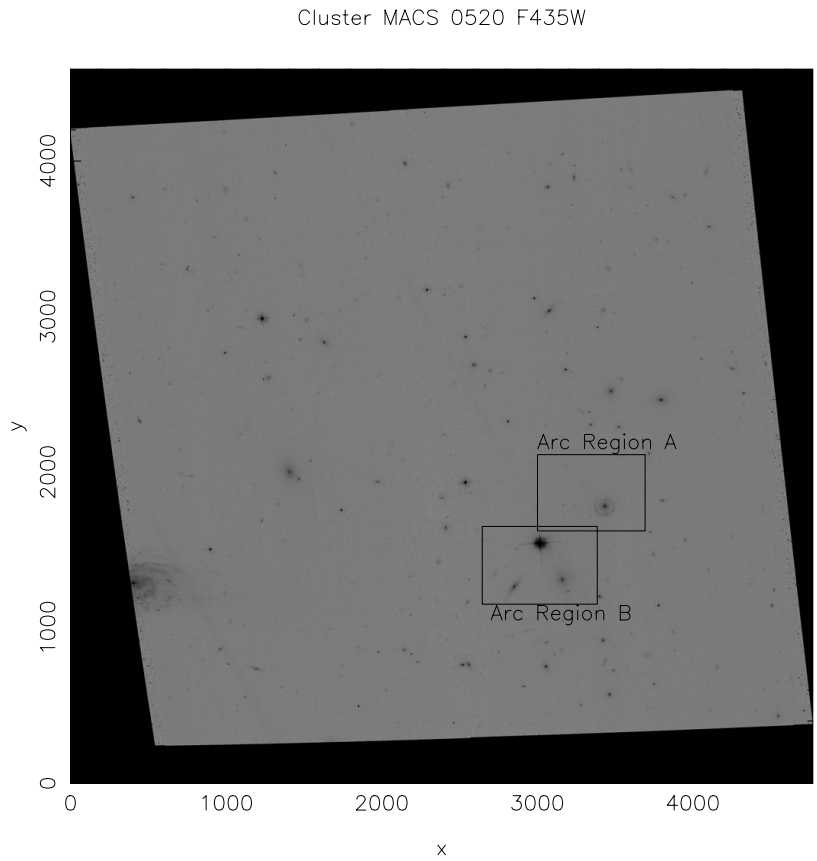


FIGURE C.16: RXJ 0454 or PSZ1 G195.78-24.29 Arc Regions

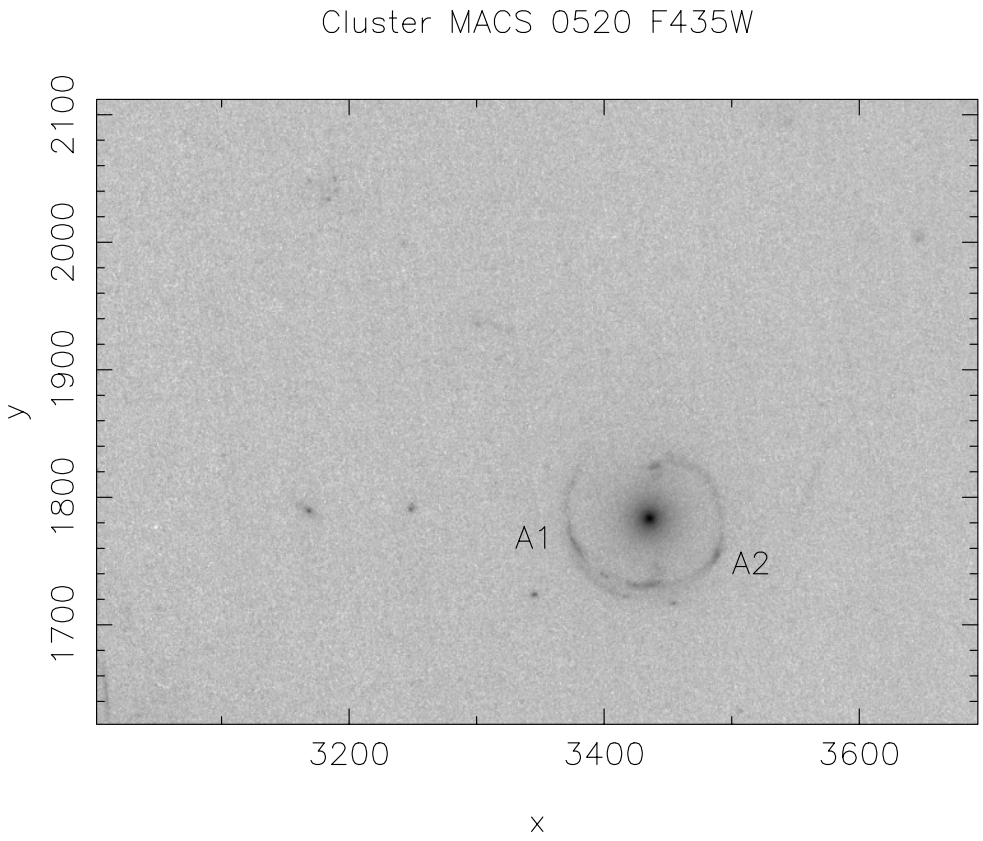


FIGURE C.17: PSZ1 G195.78-24.29 Almost Einstein ring with two photometrically measured segments A1 and A2

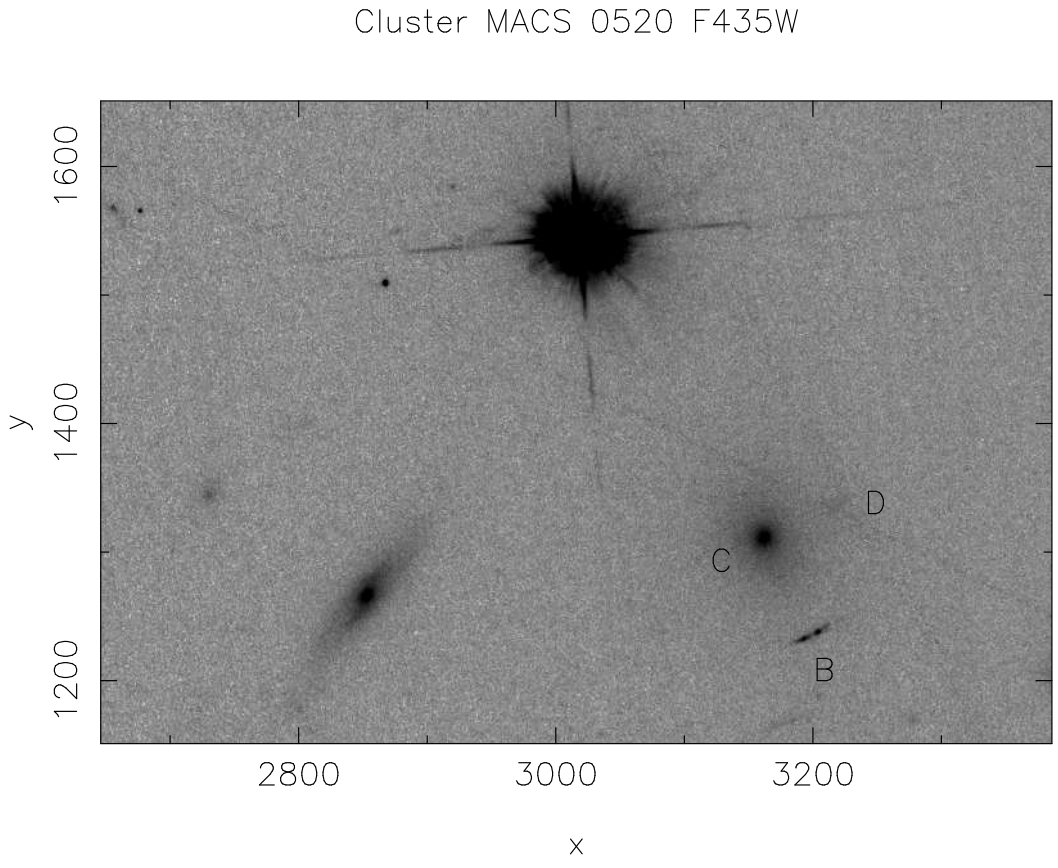


FIGURE C.18: PSZ1 G195.78-24.29 Multiply imaged arcs B1 B2 B3.

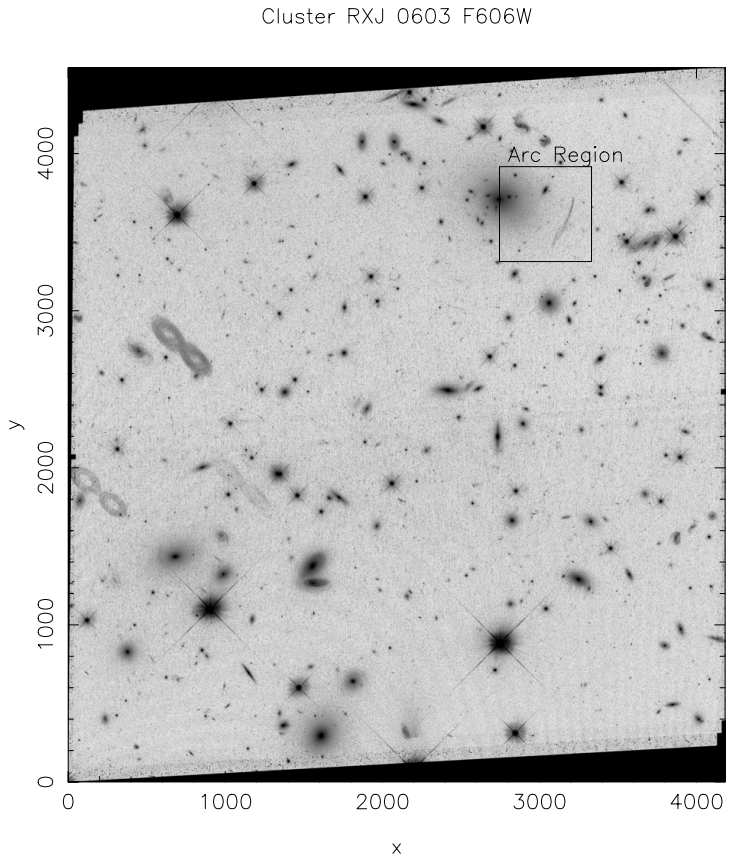


FIGURE C.19: PSZ1 G170.22+09.74 Cluster with one large arc

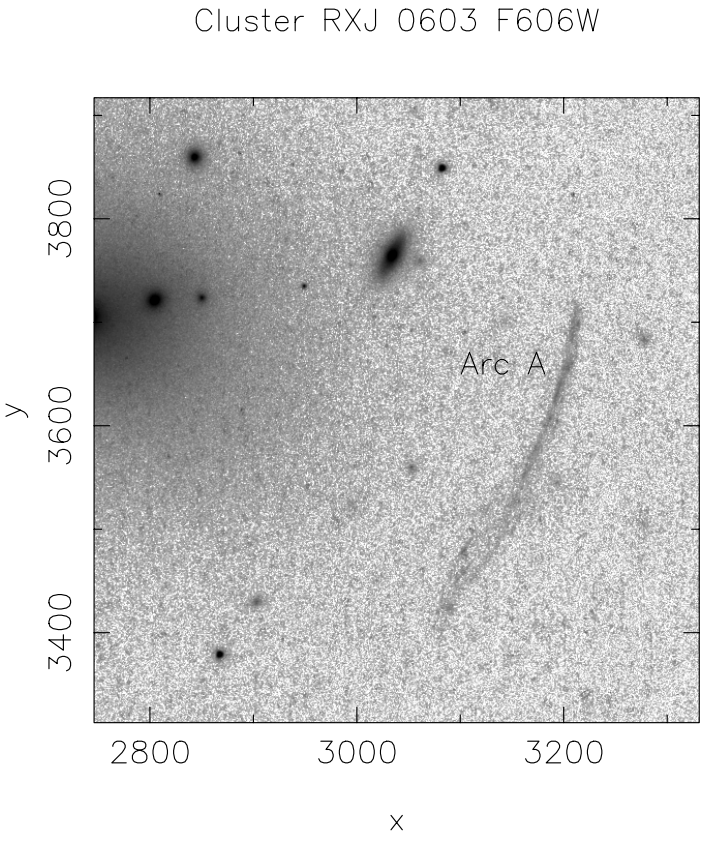


FIGURE C.20: PSZ1 G170.22+09.74 Long tangential Arc with $L/W$ ratio of 21

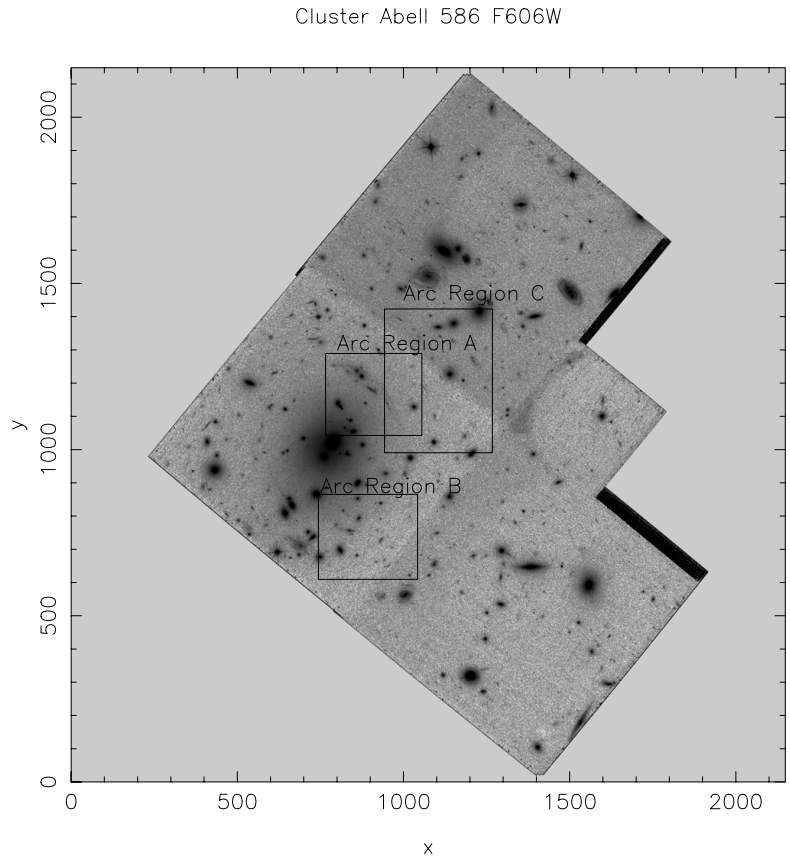


FIGURE C.21: PSZ1 G187.53+21.92 or RXJ0603+3137

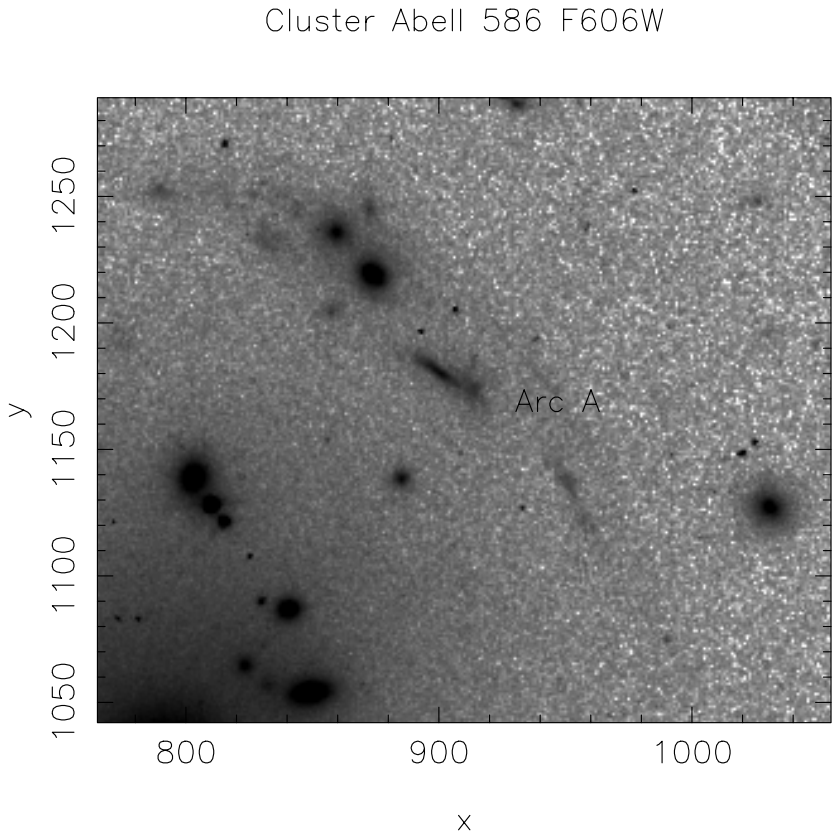


FIGURE C.22: PSZ1 G187.53+21.92 Large tangential arc A

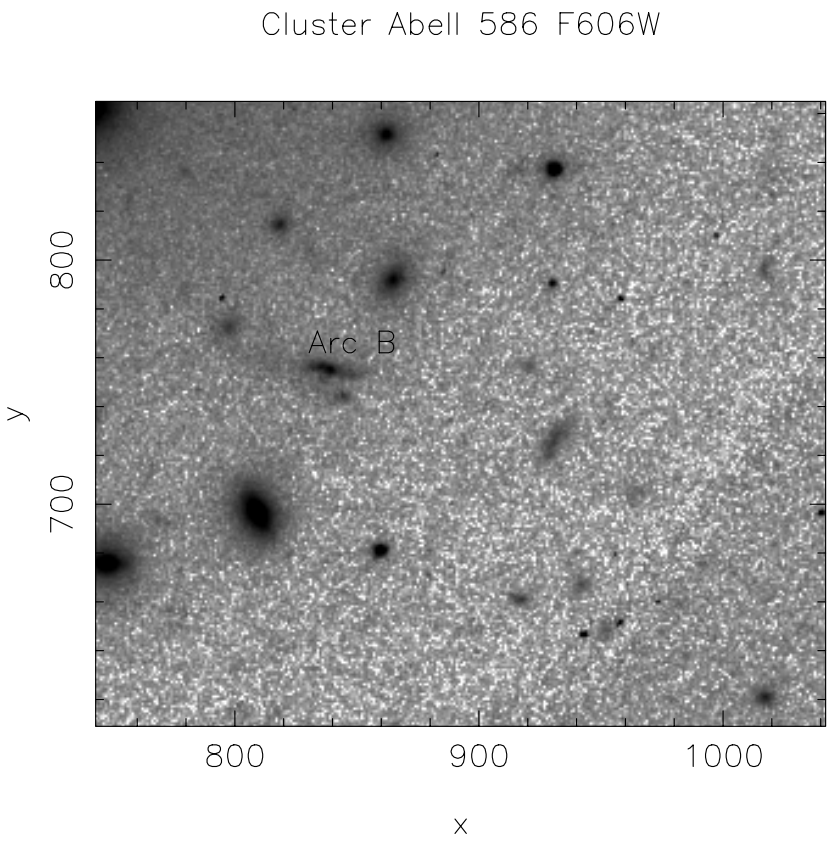


FIGURE C.23: PSZ1 G187.53+21.92 Slightly extended arc B

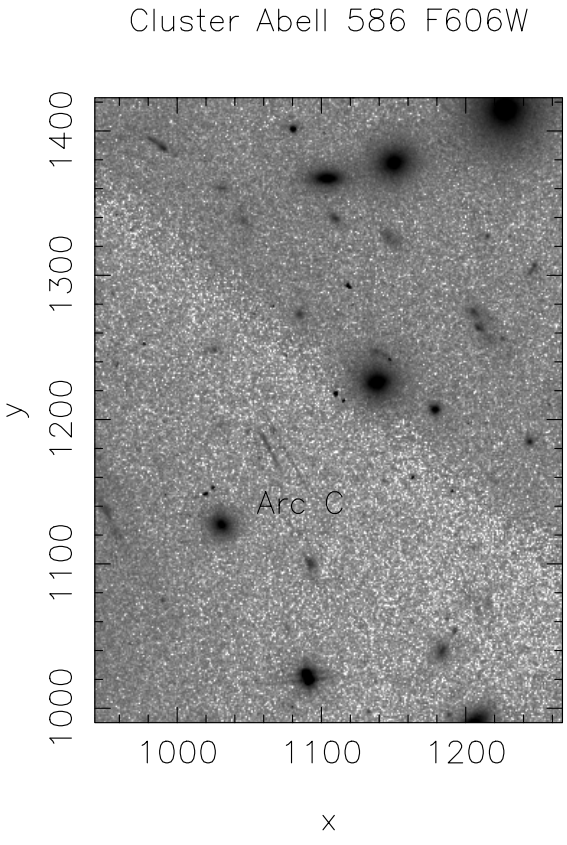


FIGURE C.24: PSZ1 G187.53+21.92 Faint multiple arcs

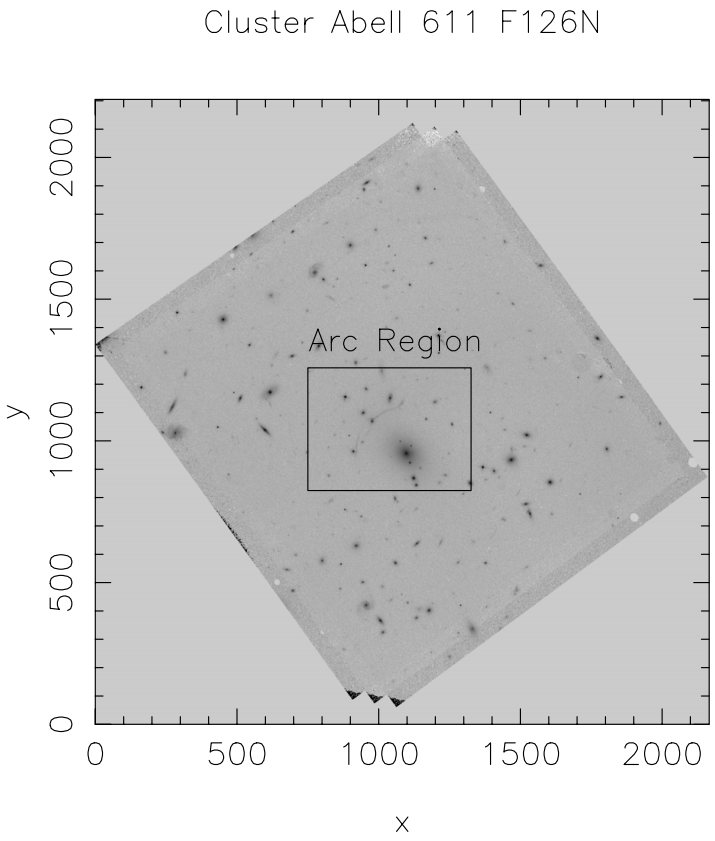


FIGURE C.25: PSZ1 G184.70+28.92 or RXJ0800.9+3602

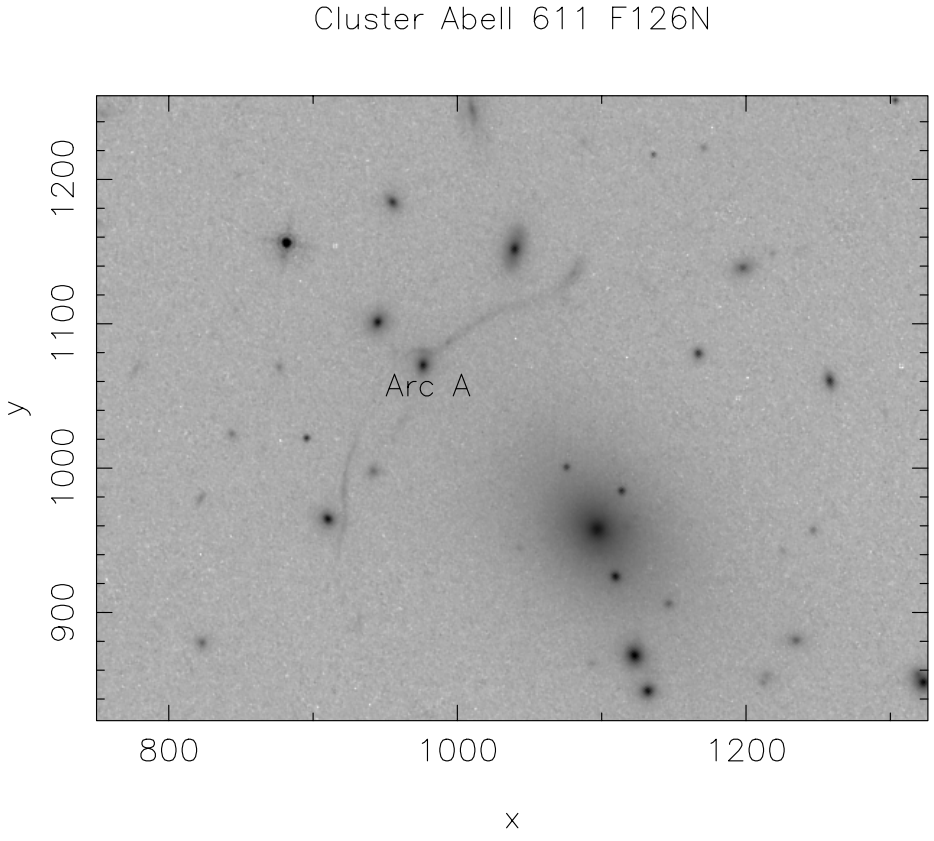


FIGURE C.26: PSZ1 G184.70+28.92 Extended arc segments

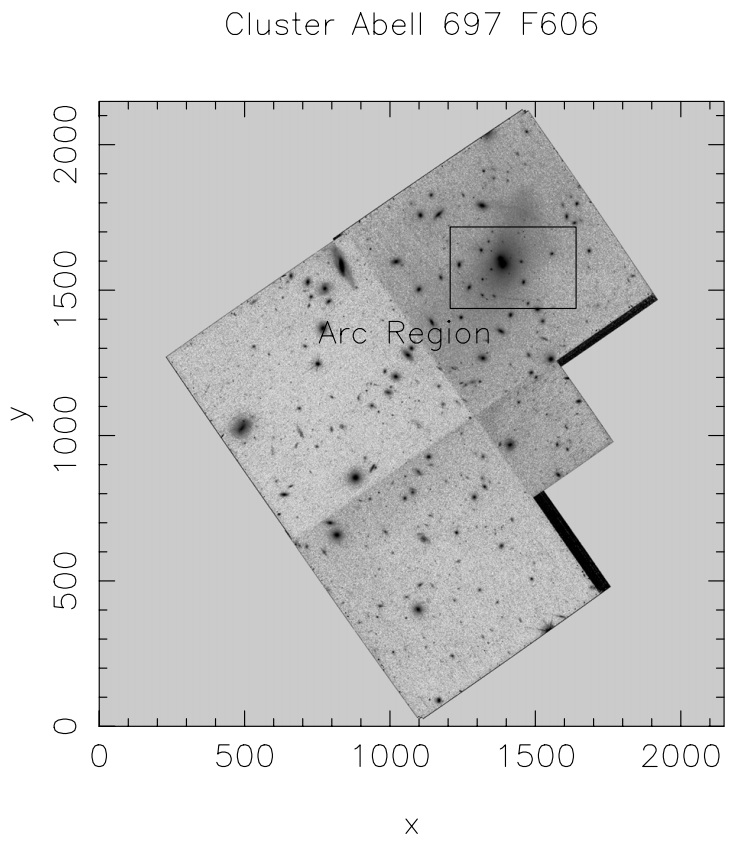


FIGURE C.27: PSZ1 G186.37+37.26 or RXJ0842.9+3621

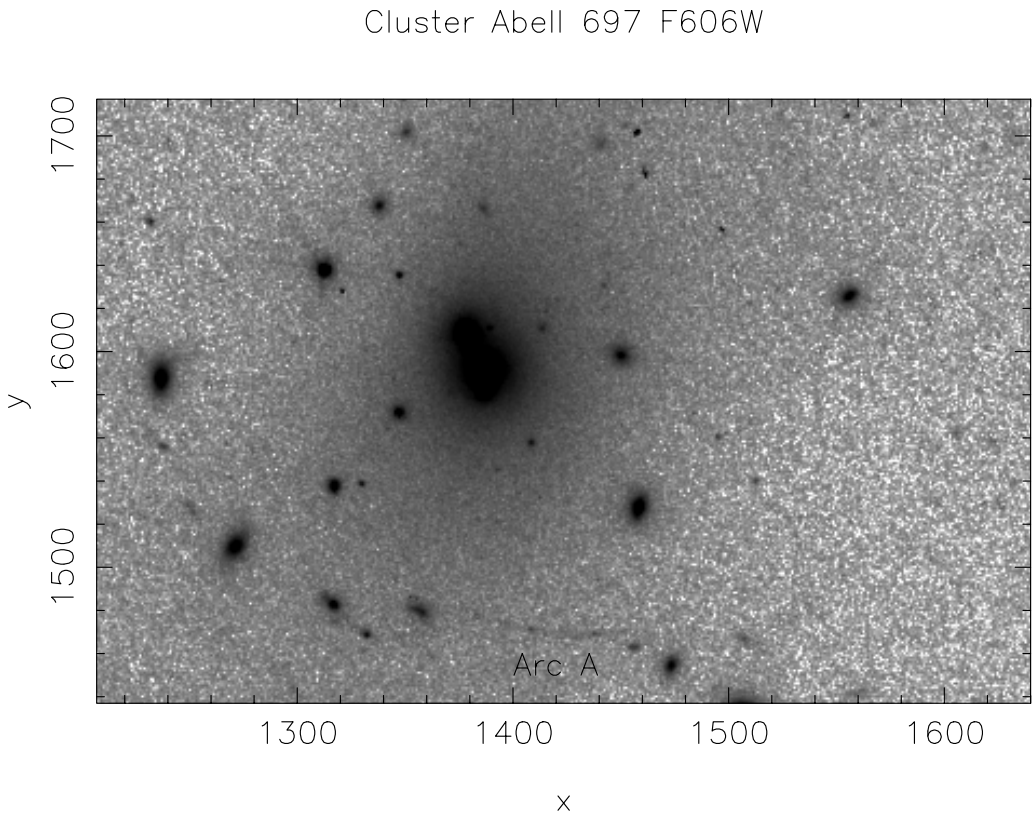


FIGURE C.28: PSZ1 G186.37+37.26 faint long tangential arc

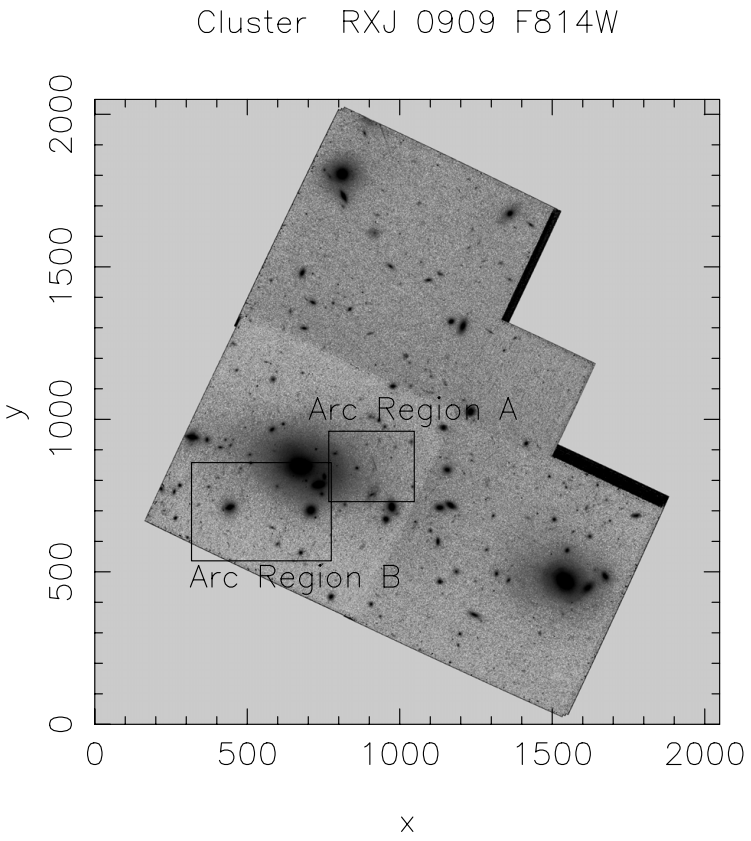


FIGURE C.29: PSZ1 G218.83+35.49

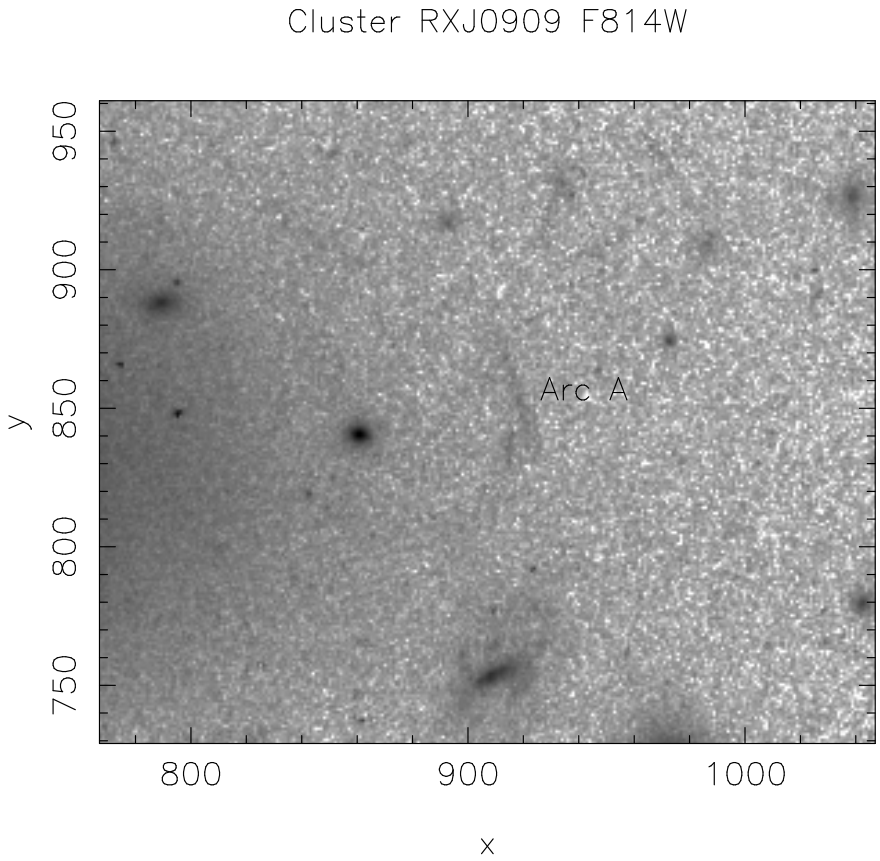


FIGURE C.30: PSZ1 G218.83+35.49 faint tangential arc

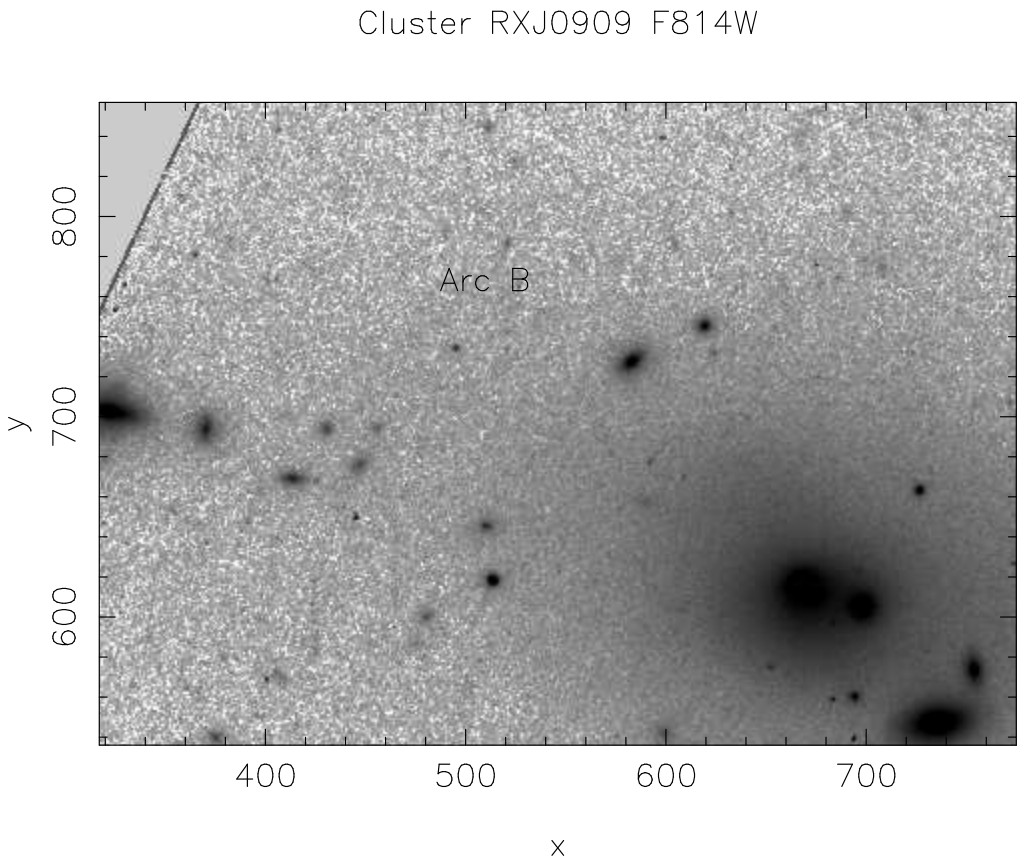


FIGURE C.31: PSZ1 G135.03+36.03 faint extended object B

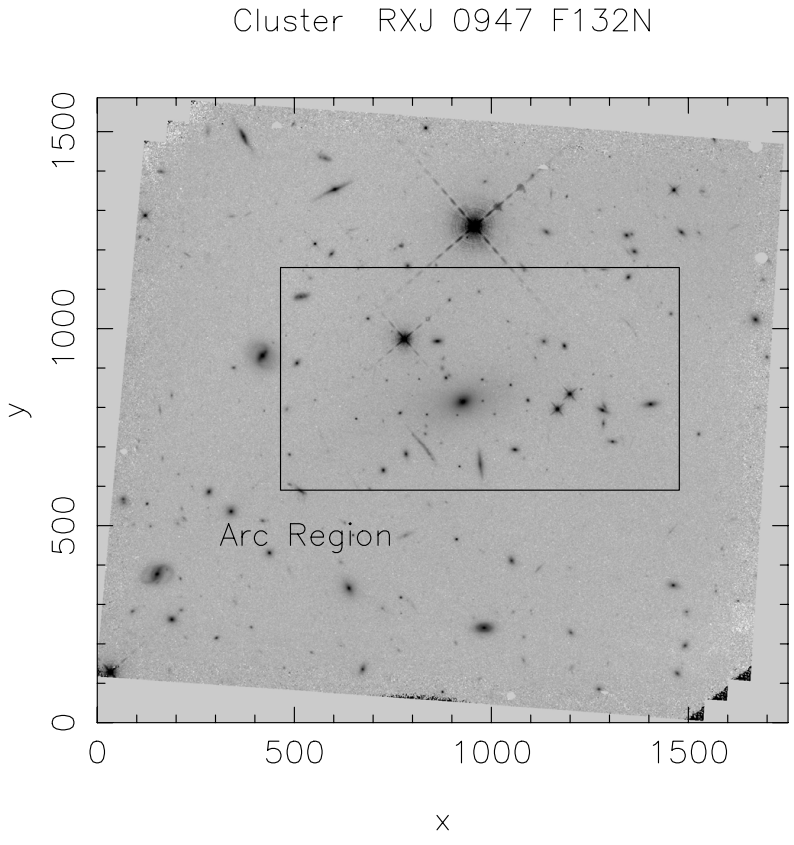


FIGURE C.32: PSZ1 G135.03+36.03 or RXJ0947.2+7623

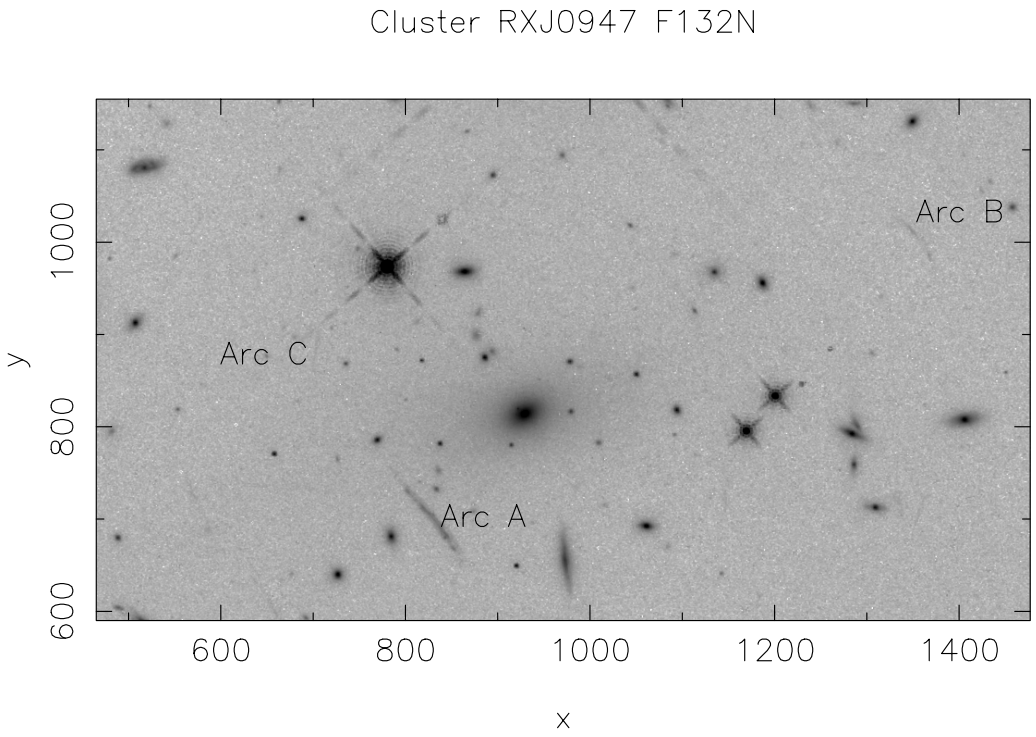


FIGURE C.33: PSZ1 G135.03+36.03 3 tangential arcs seen near BCG

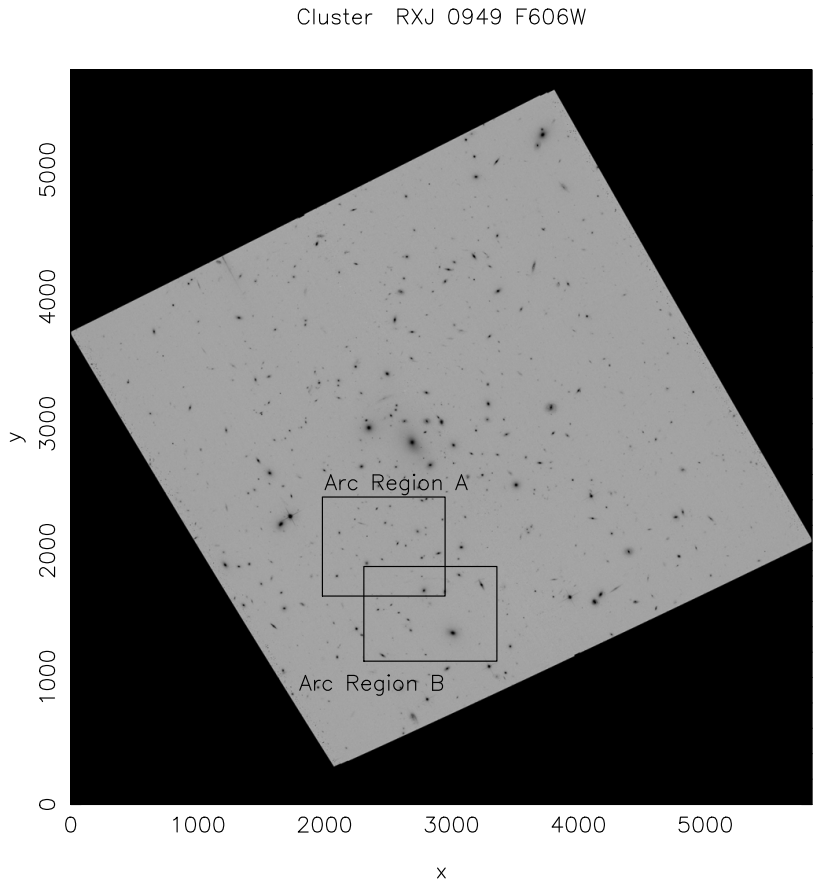


FIGURE C.34: PSZ1 G216.60+47.00 or RXJ0949.8+1707

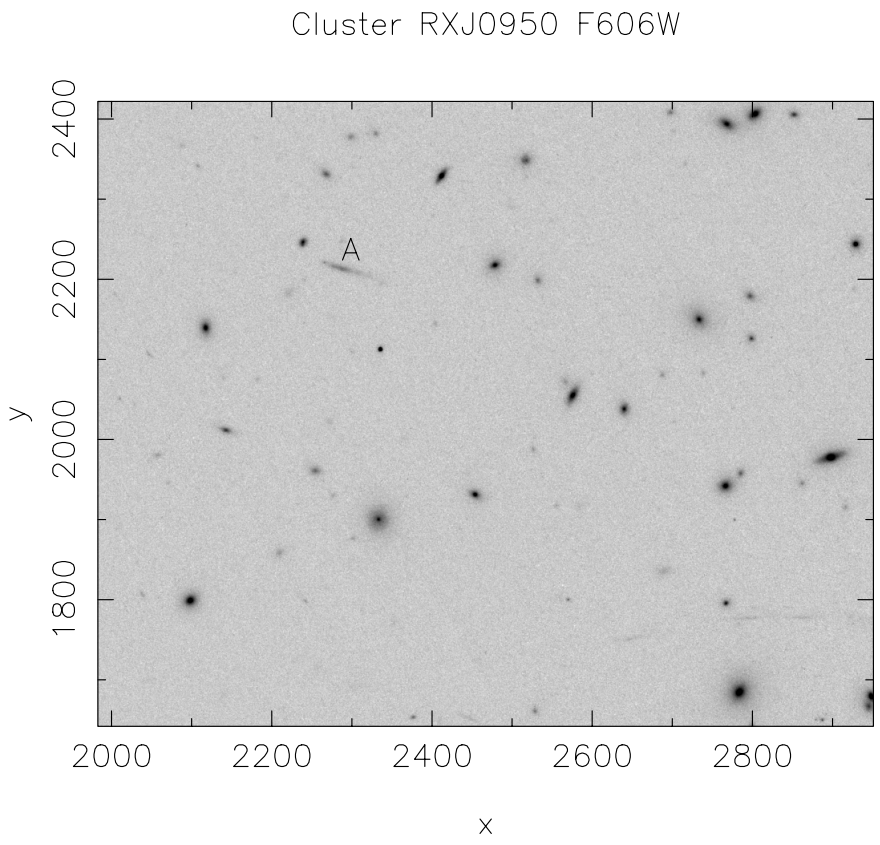


FIGURE C.35: PSZ1 G216.60+47.00 arc A

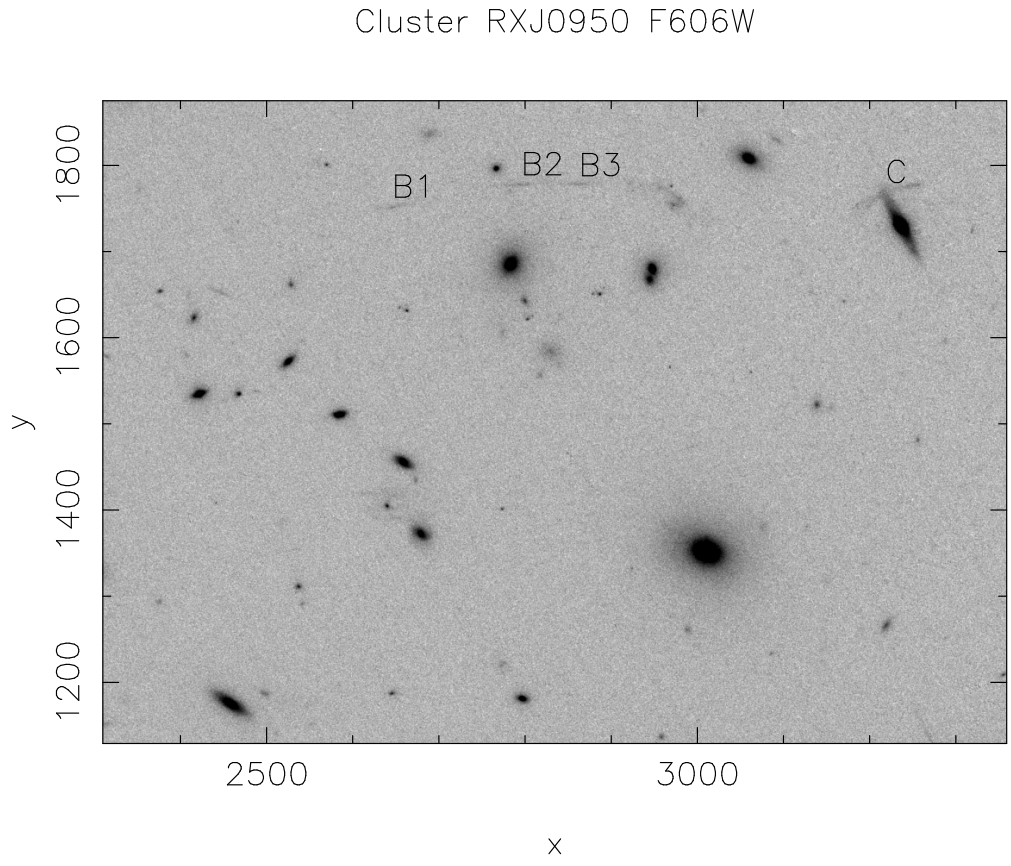


FIGURE C.36: PSZ1 G216.60+47.00 Long arc segments B1 B2 B3 and differently positioned arc C

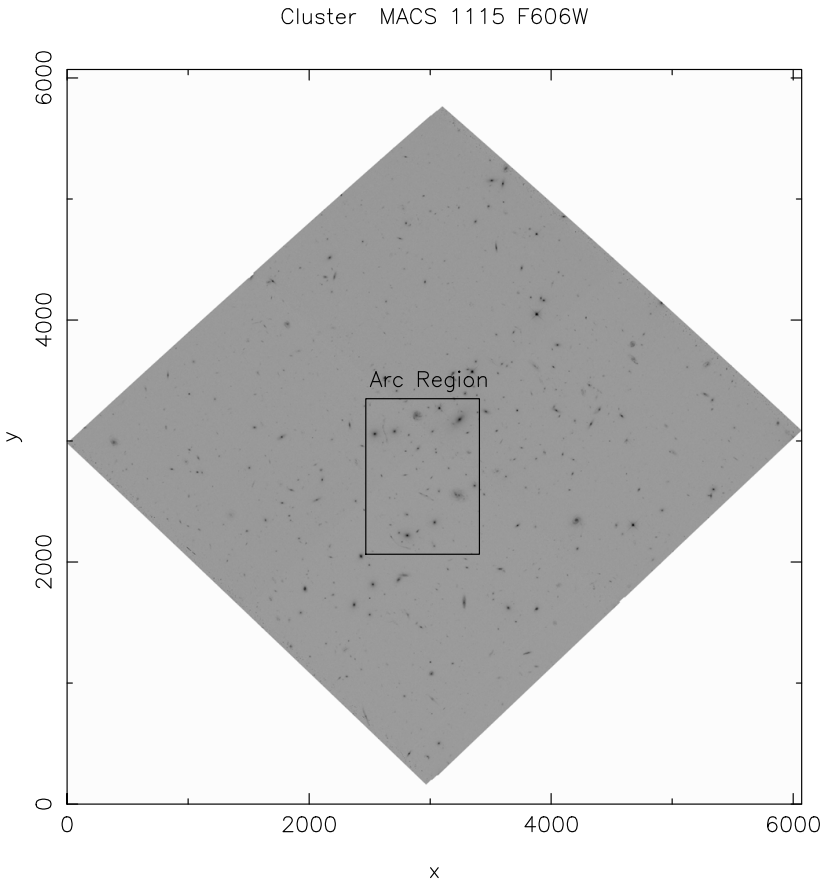


FIGURE C.37: PSZ1 G150.56+58.32 or RXJ1115.2+5320

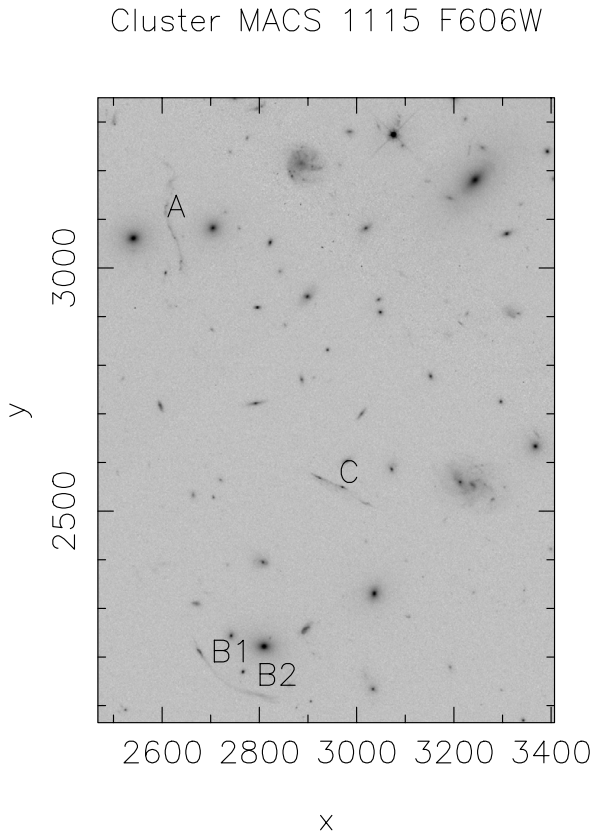


FIGURE C.38: PSZ1 G150.56+58.32 Long curling arc A, extended arc C, and B1 and B2 which are two parts of an arc segment photometrically analyzed separately

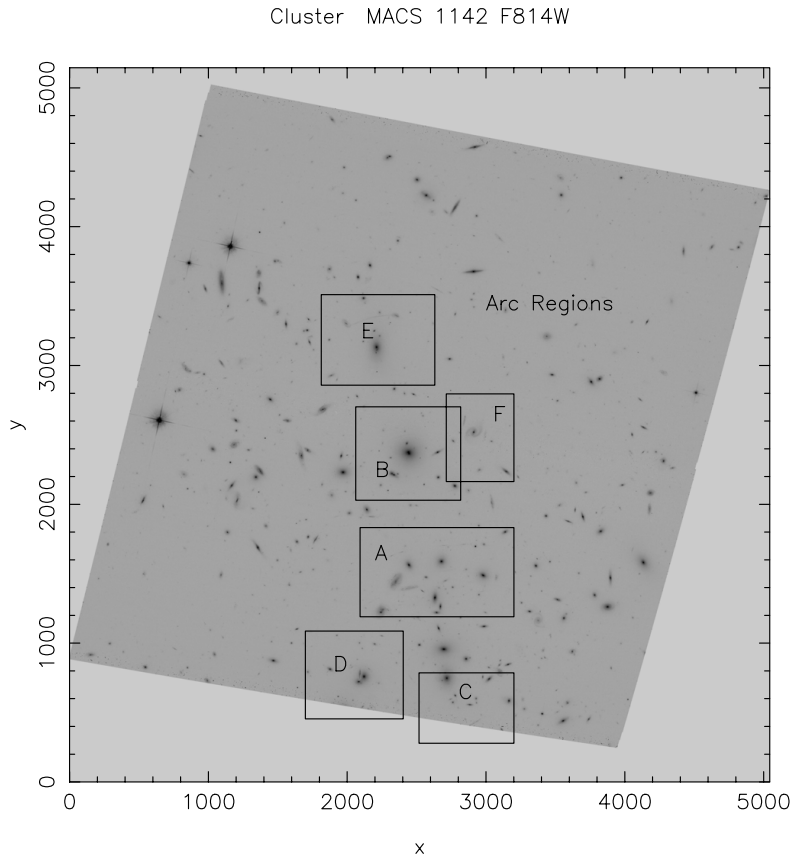


FIGURE C.39: PSZ1 G139.17+56.37 or RXJ1145.5+5832

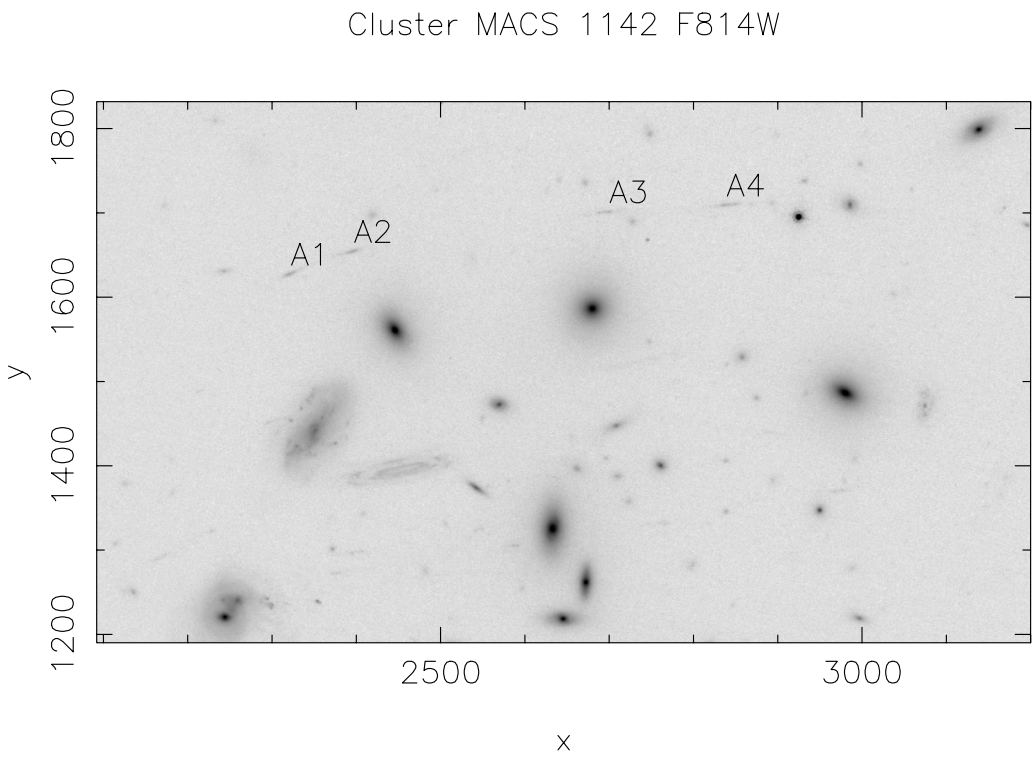


FIGURE C.40: PSZ1 G139.17+56.37 4 long arcs of similar orientation and magnitude

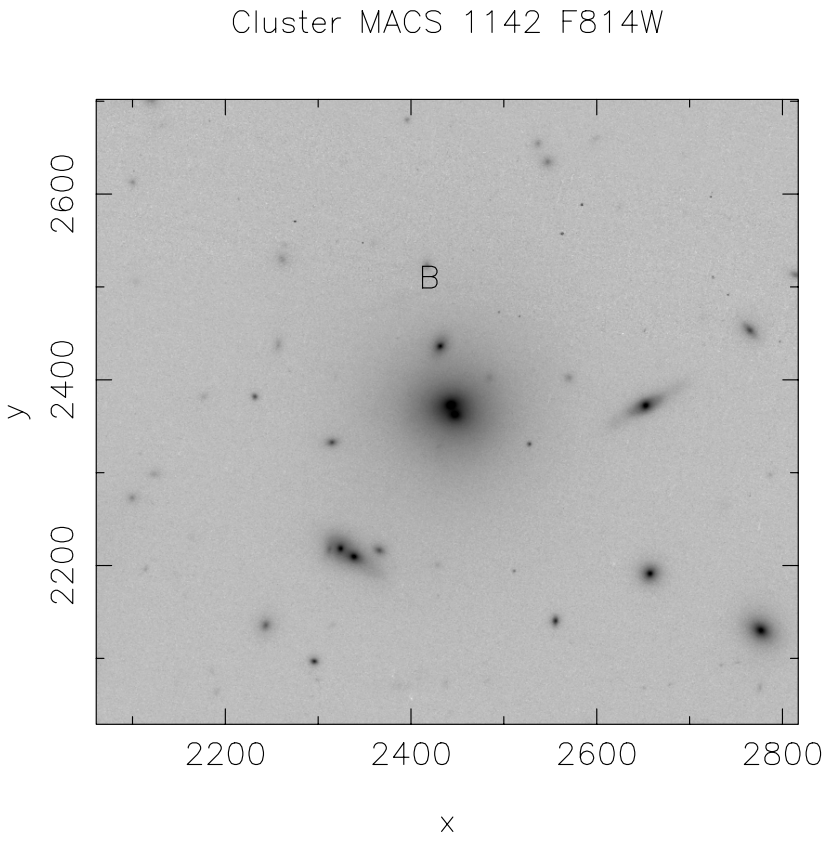


FIGURE C.41: PSZ1 G139.17+56.37 Faint tangential arc near BCG

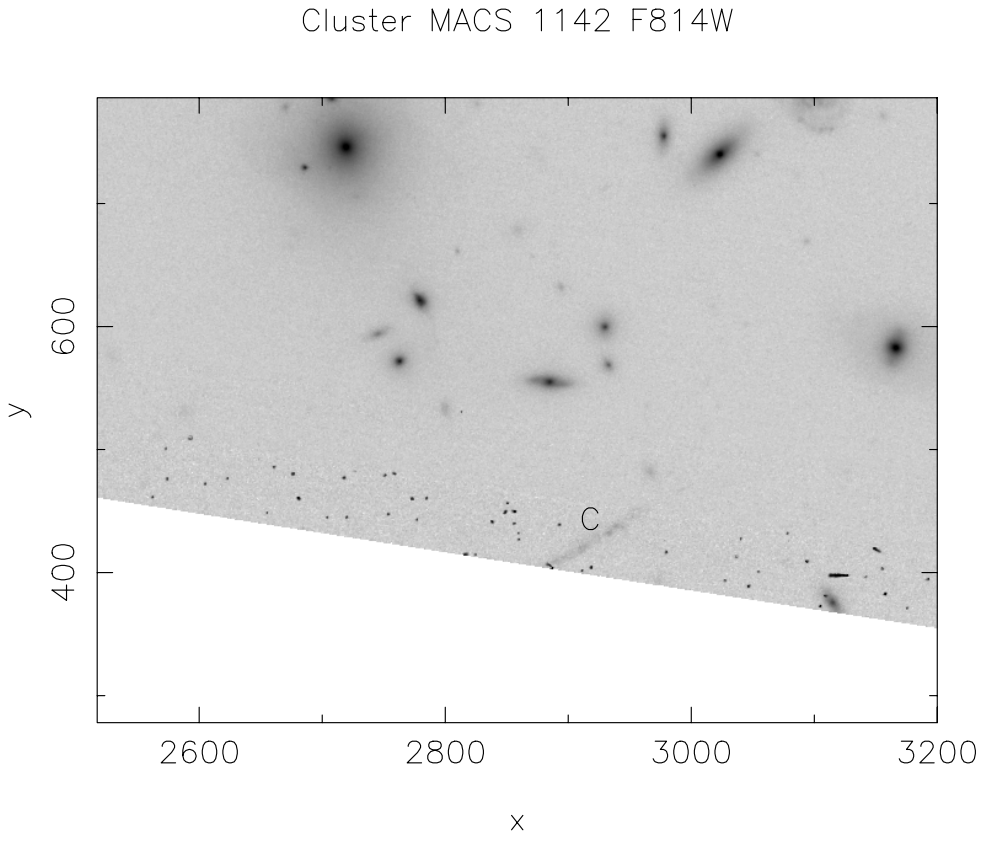


FIGURE C.42: PSZ1 G139.17+56.37 Long arc cut off at edge of frame so length and magnitude are incomplete

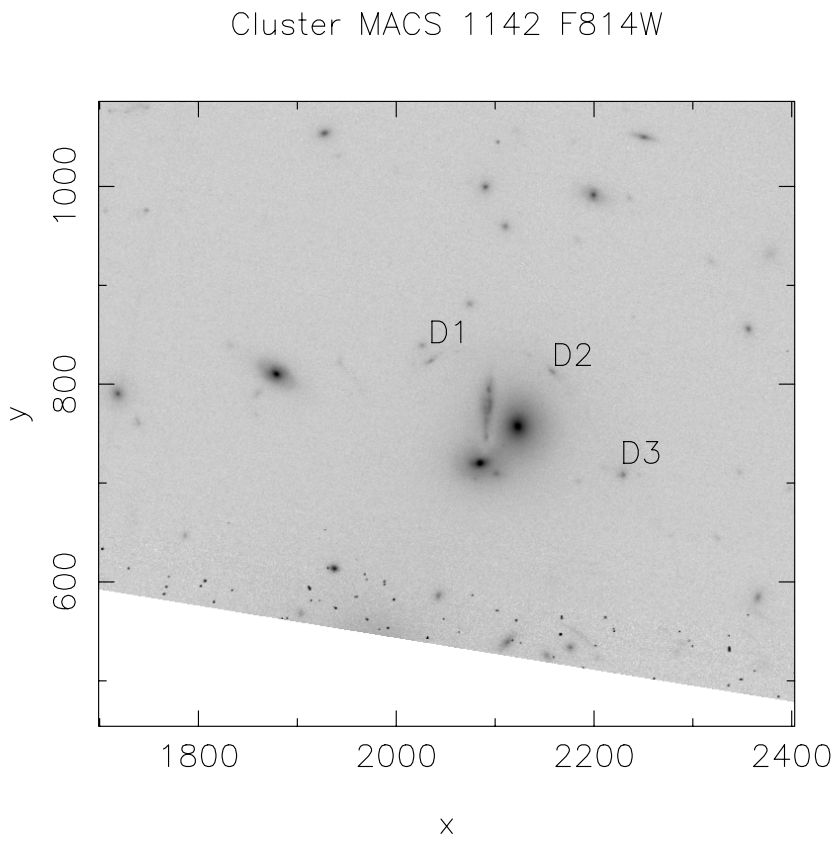


FIGURE C.43: PSZ1 G139.17+56.37 3 tangential arcs lensed by other BCG

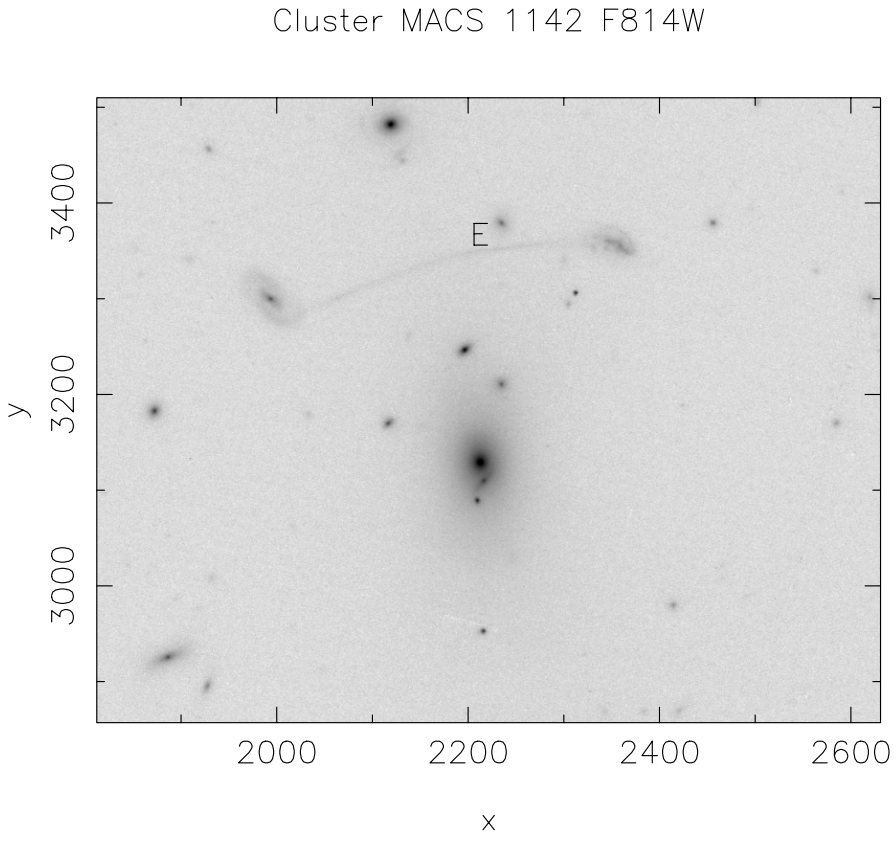


FIGURE C.44: PSZ1 G139.17+56.37 tangential arc near 3rd BCG of cluster

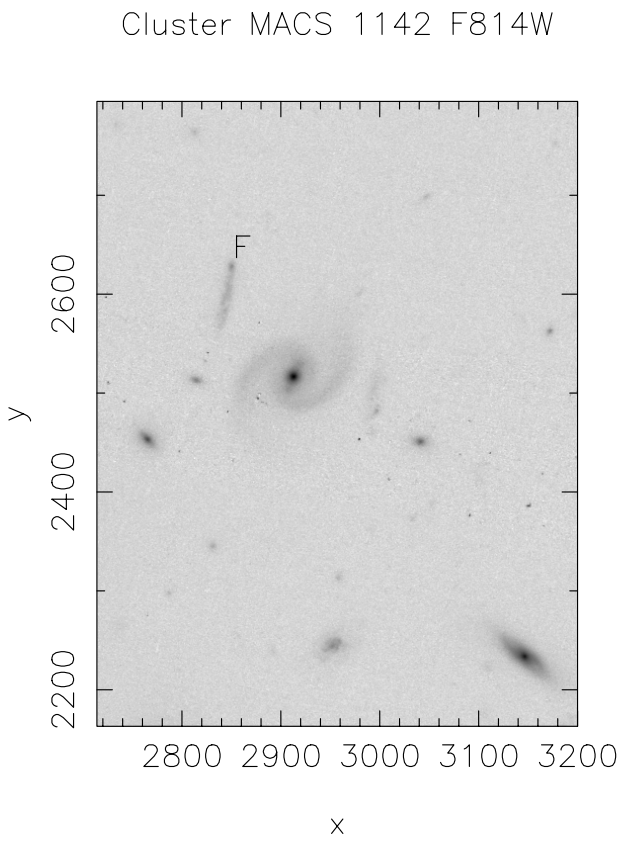


FIGURE C.45: PSZ1 G139.17+56.37 faint tangential arc around main BCG

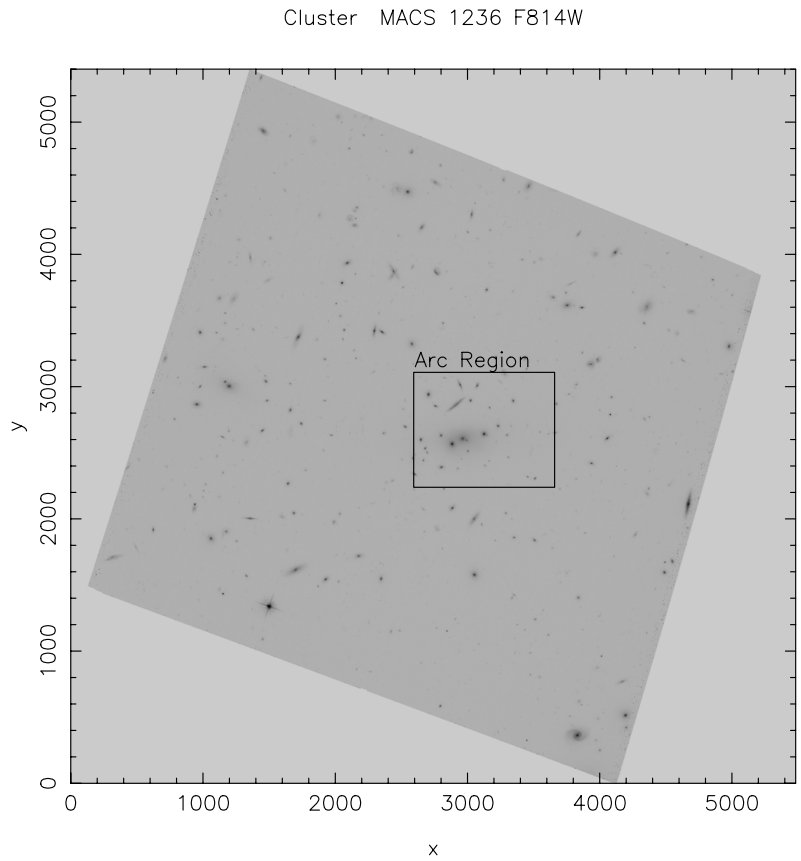


FIGURE C.46: PSZ1 G289.19+72.19 or RXJ1236.9+6311

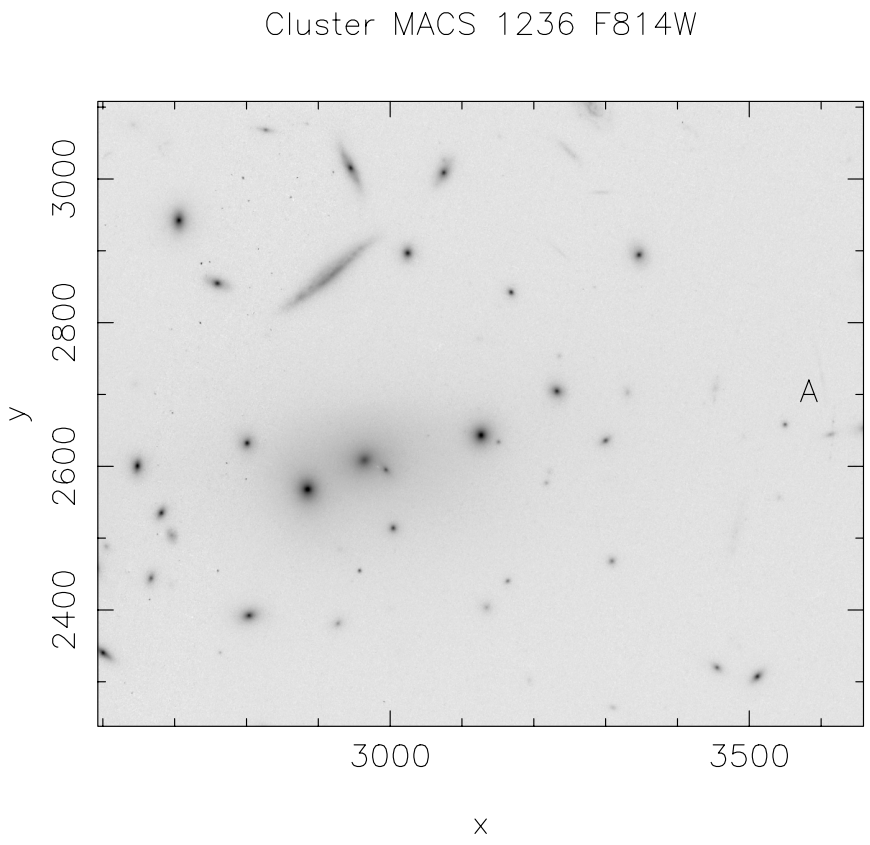


FIGURE C.47: PSZ1 G289.19+72.19 faint arcs along critical curve

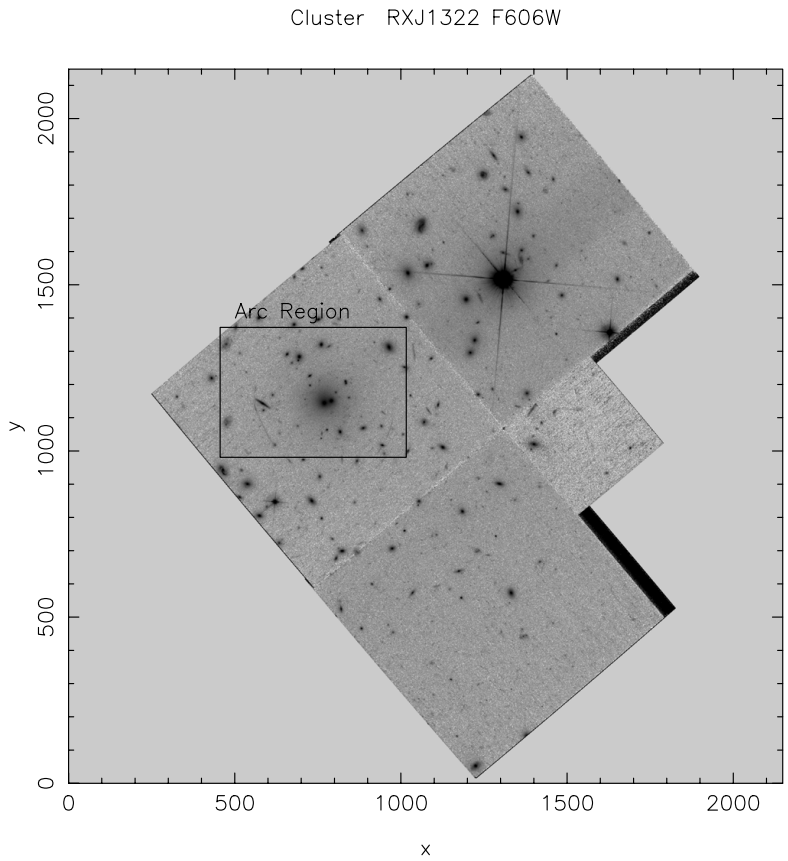


FIGURE C.48: PSZ1 G068.32+81.81 or ZwCl1324.6+0229

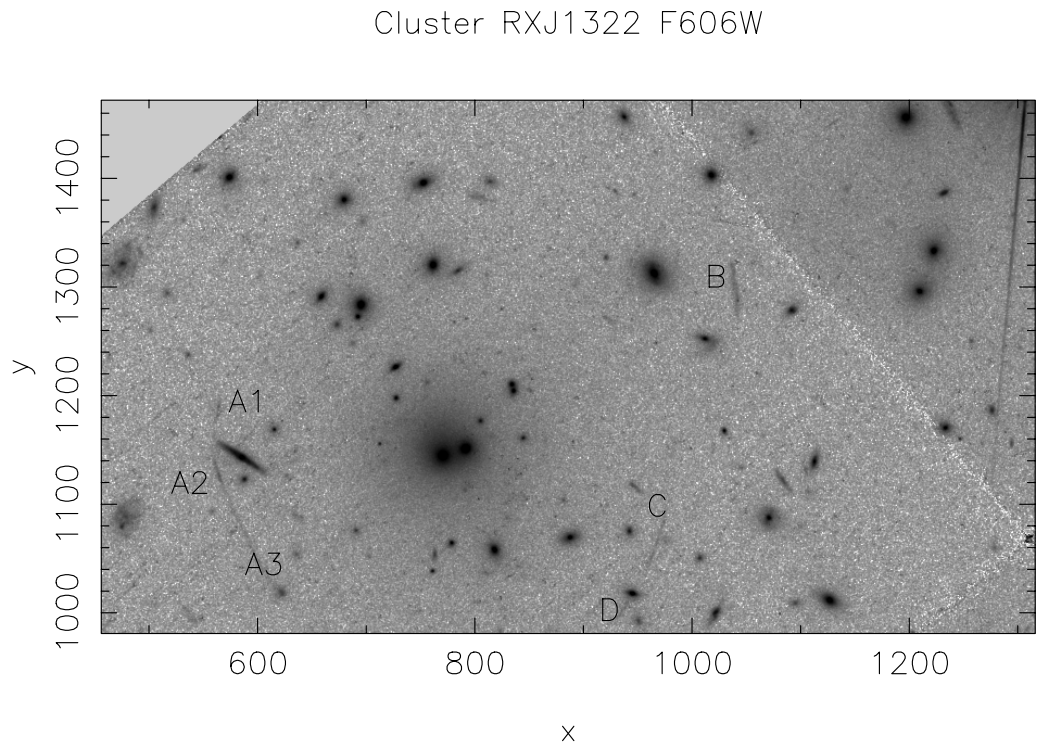


FIGURE C.49: PSZ1 G068.32+81.81 long tangential arc segments A1 A2 A3 and tangential arcs B and C around BCG

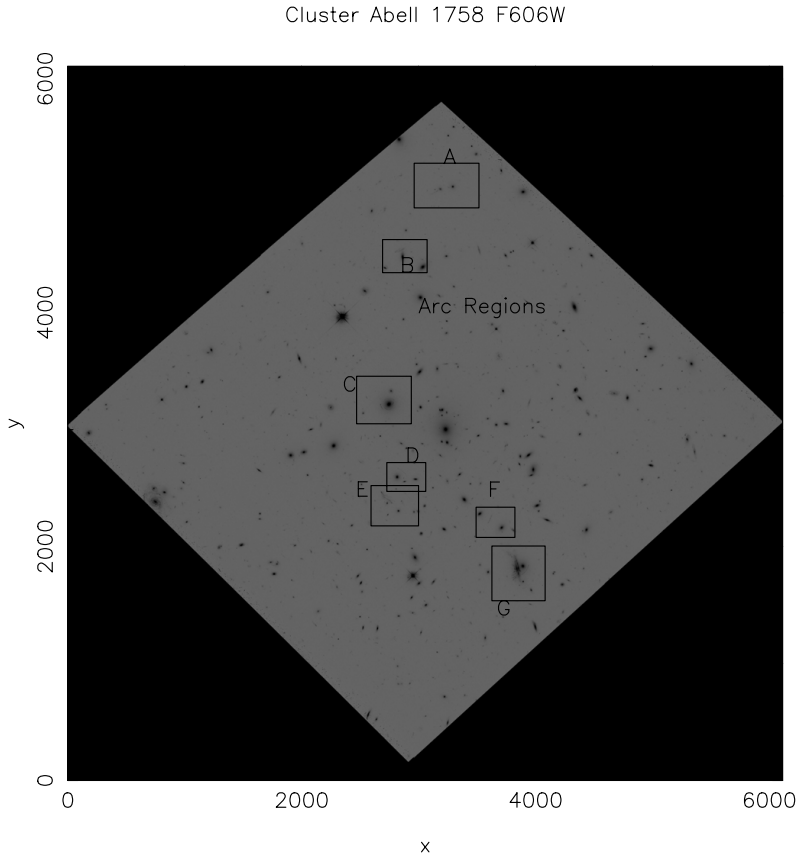


FIGURE C.50: PSZ1 G107.14+14+65.29 or RXJ1332.7+5032

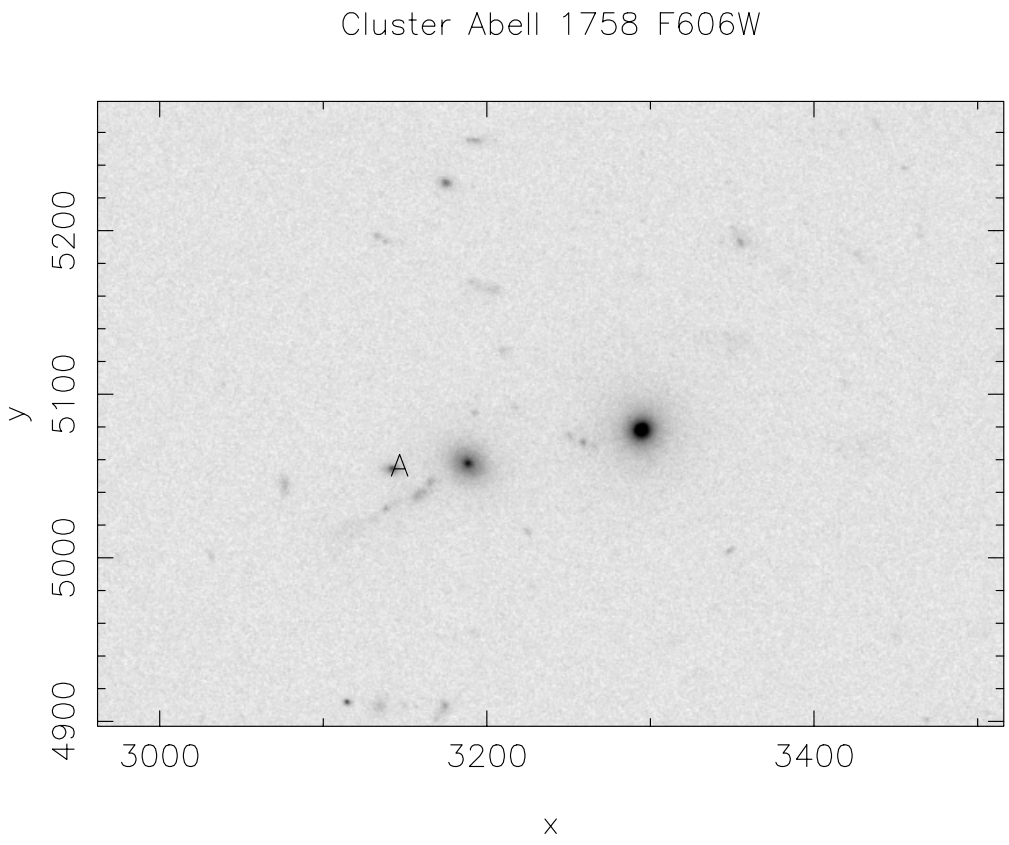


FIGURE C.51: PSZ1 G107.14+14+65.29 Radially oriented arc A

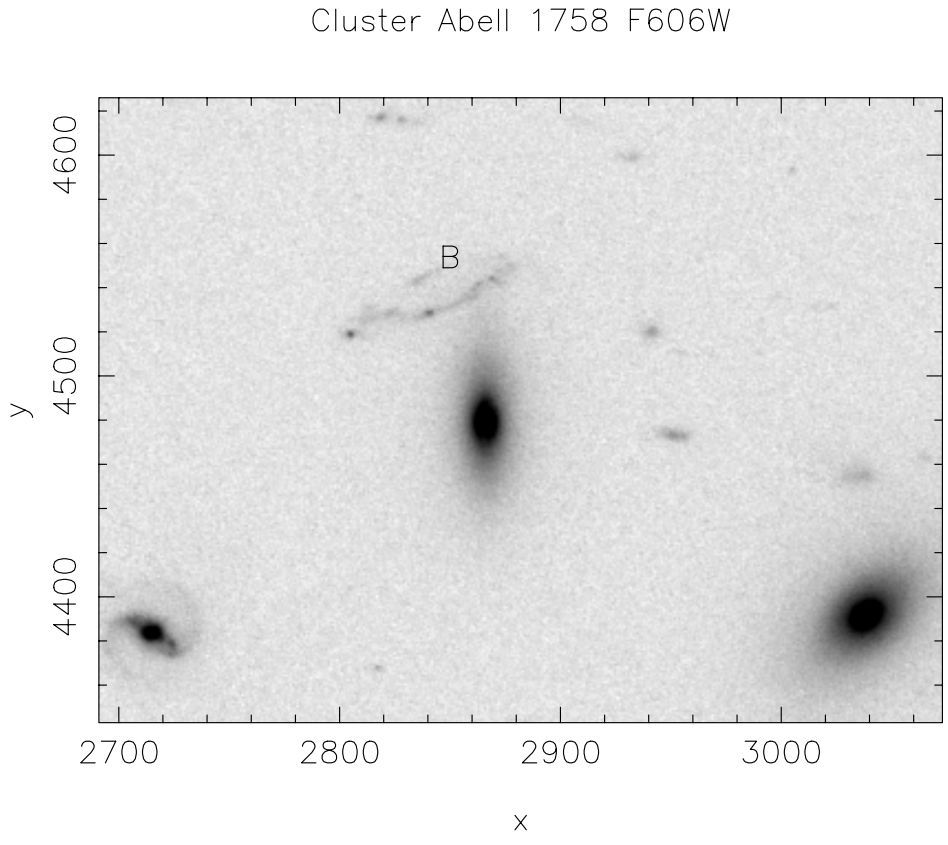


FIGURE C.52: PSZ1 G107.14+14+65.29 Extended tangential arc B

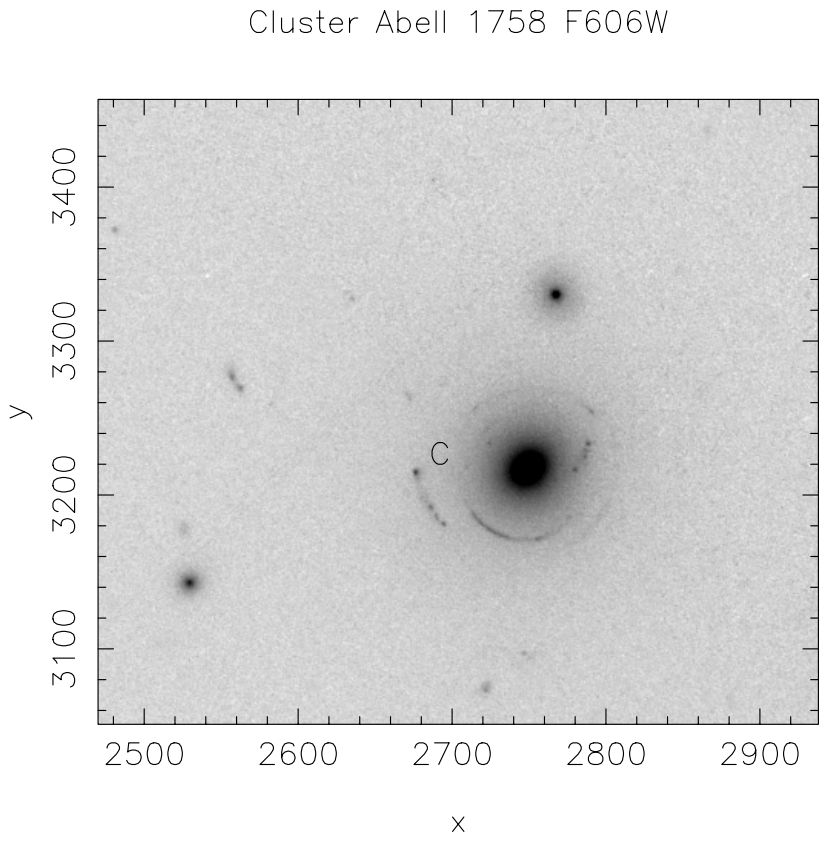


FIGURE C.53: PSZ1 G107.14+14+65.29 Nearly Einstein ring around cluster galaxy

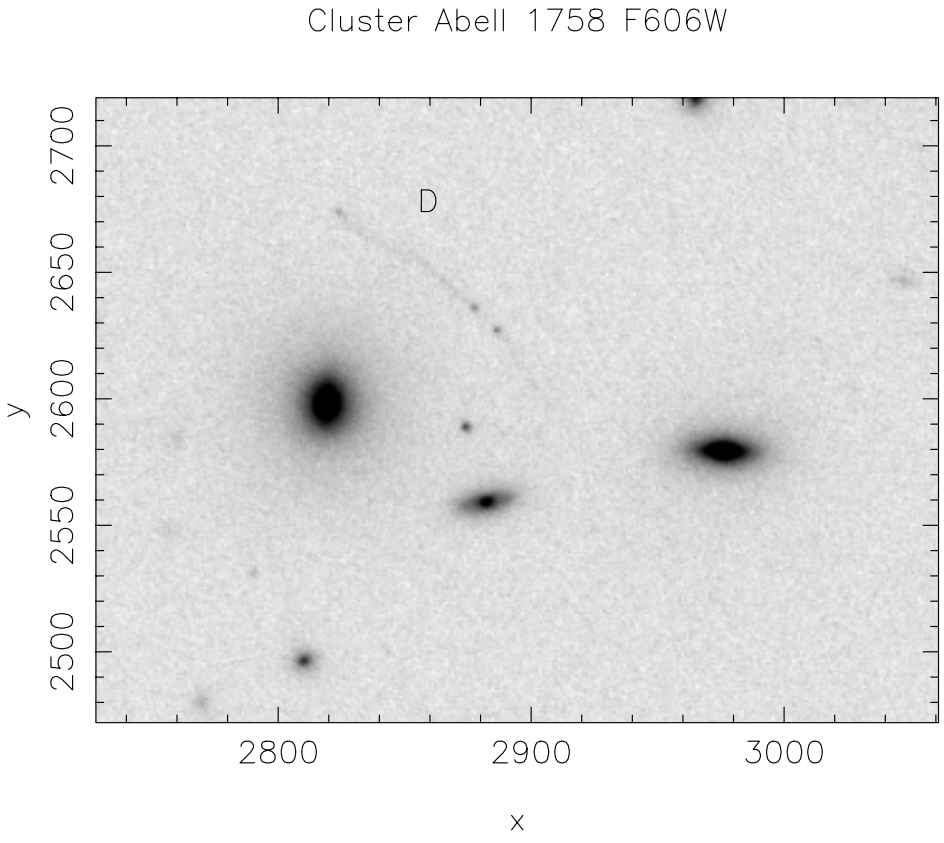


FIGURE C.54: PSZ1 G107.14+14+65.29 Long faint tangential arc

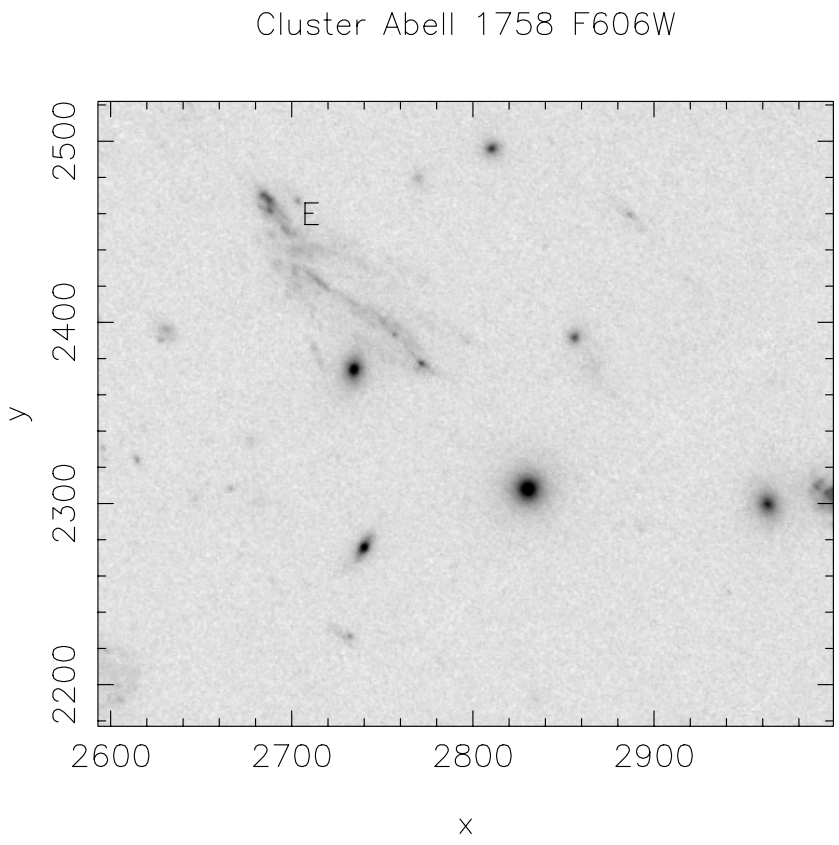


FIGURE C.55: PSZ1 G107.14+14+65.29 Extended object showing complicated mass distribution

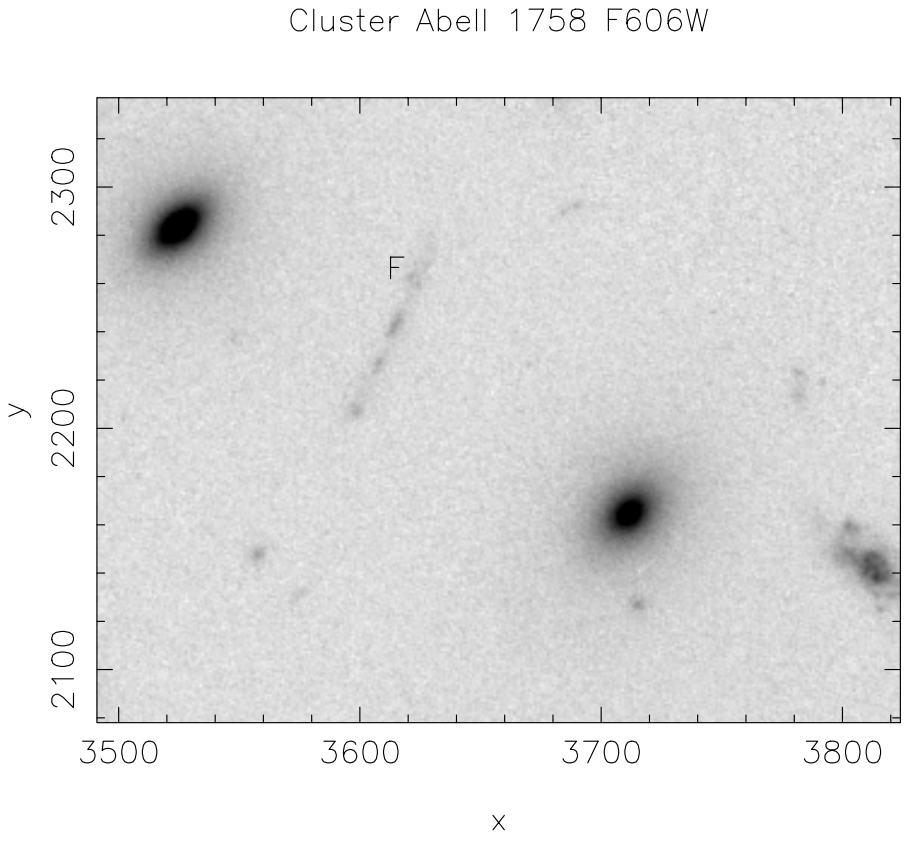


FIGURE C.56: PSZ1 G107.14+14+65.29 Faint tangential arc

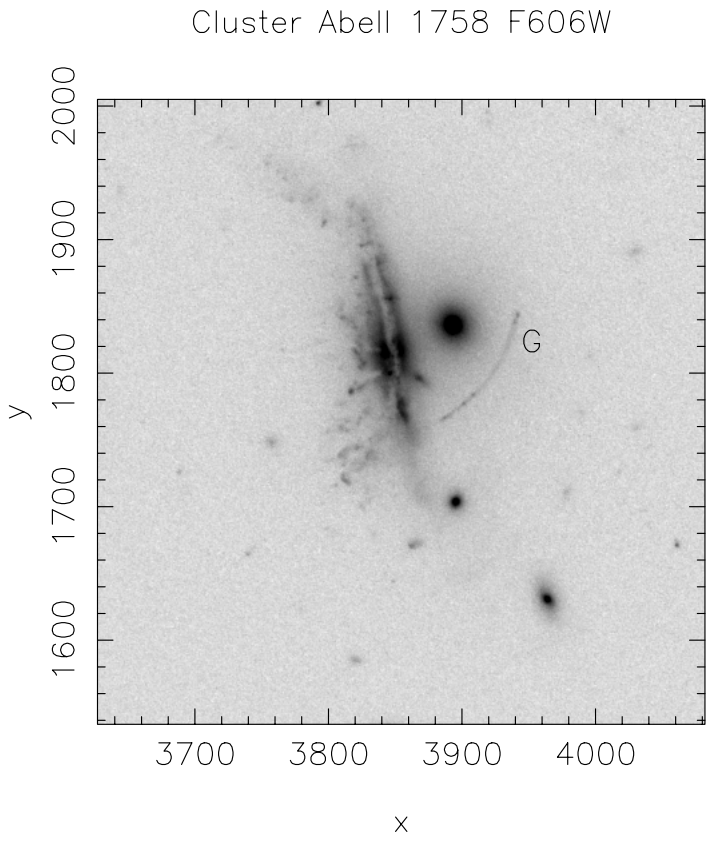


FIGURE C.57: PSZ1 G107.14+14+65.29 Long thin arc near other BCG

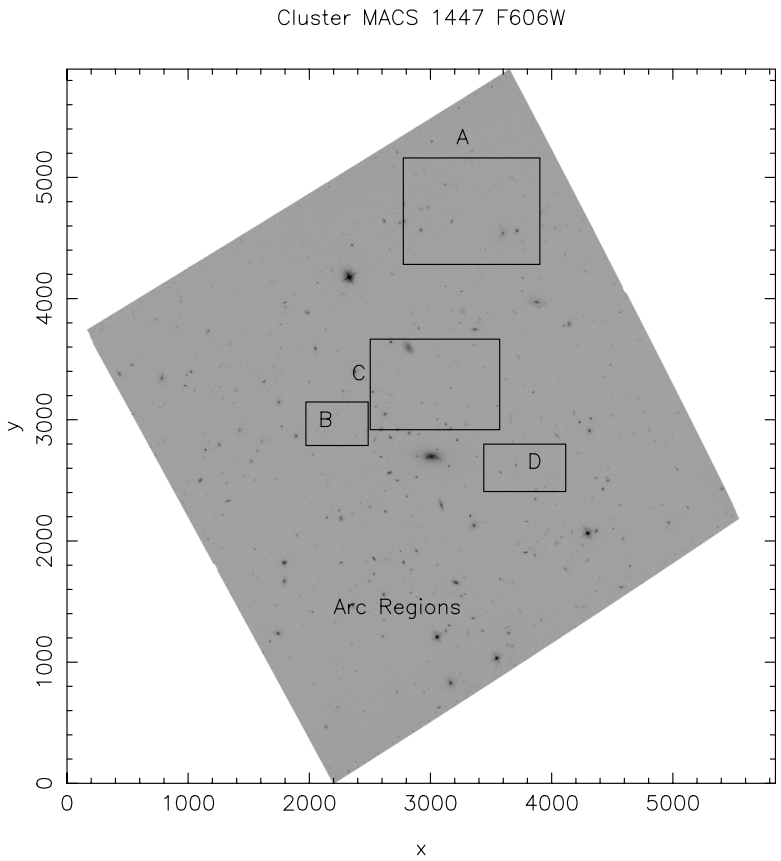


FIGURE C.58: PSZ1 G004.13+56.84 or RXJ1447.4+0827

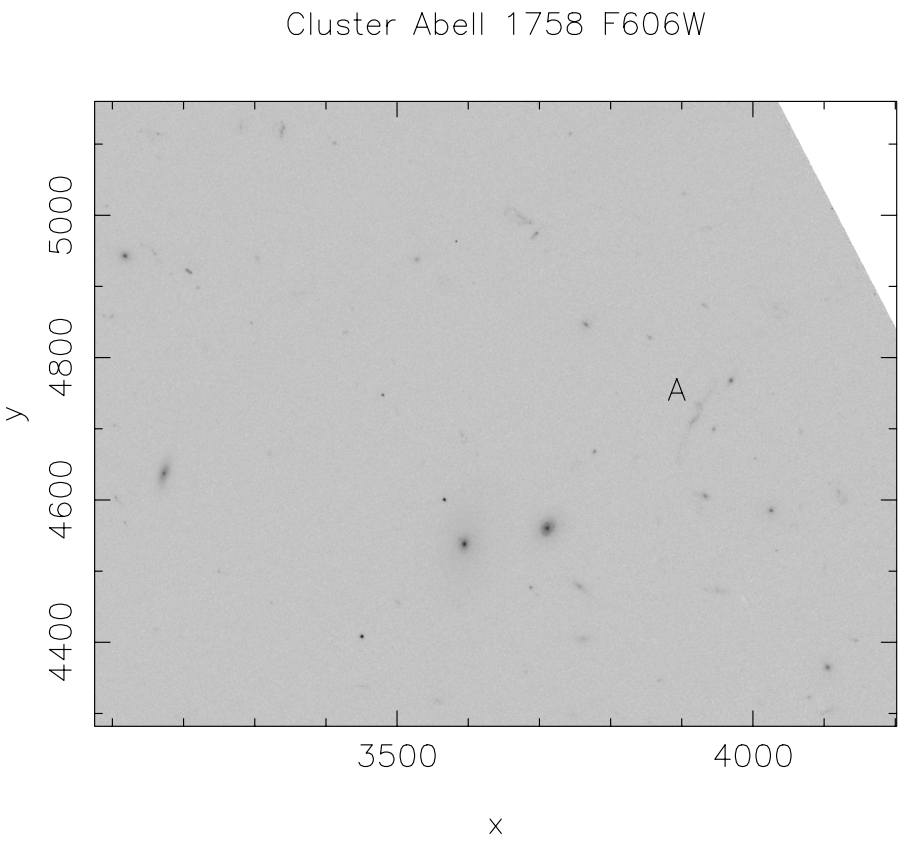


FIGURE C.59: PSZ1 G004.13+56.84 Thin faint radially oriented arc

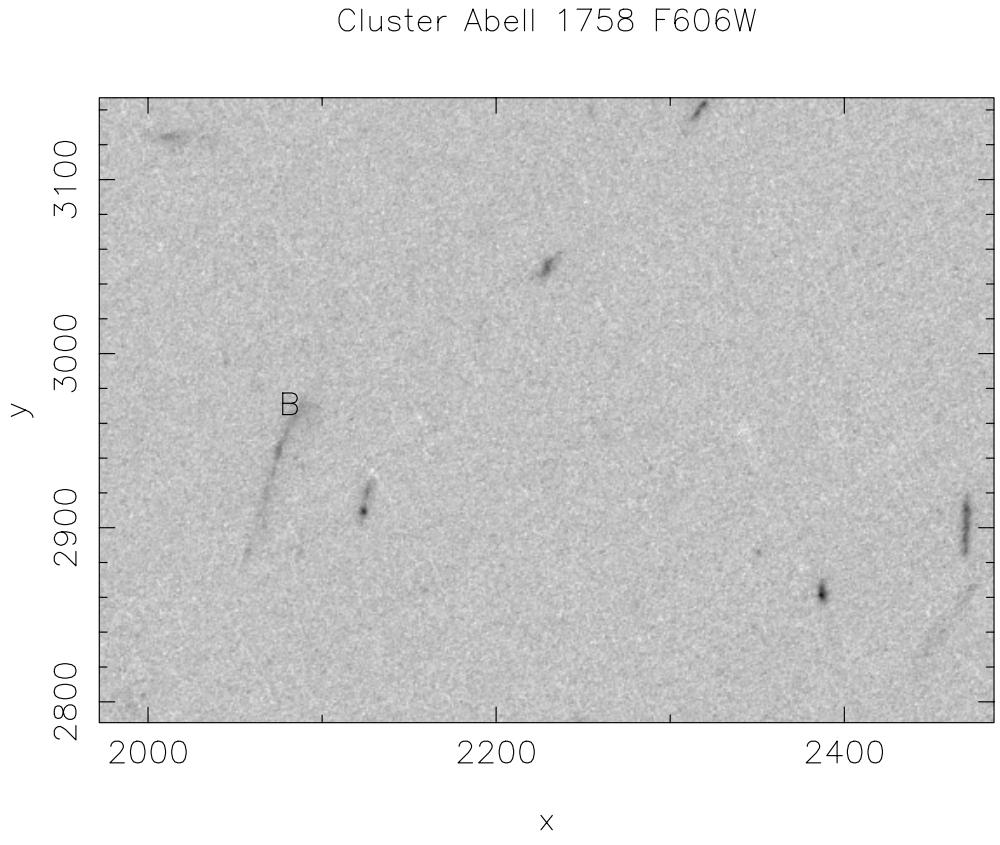


FIGURE C.60: PSZ1 G004.13+56.84 thin faint tangential arc

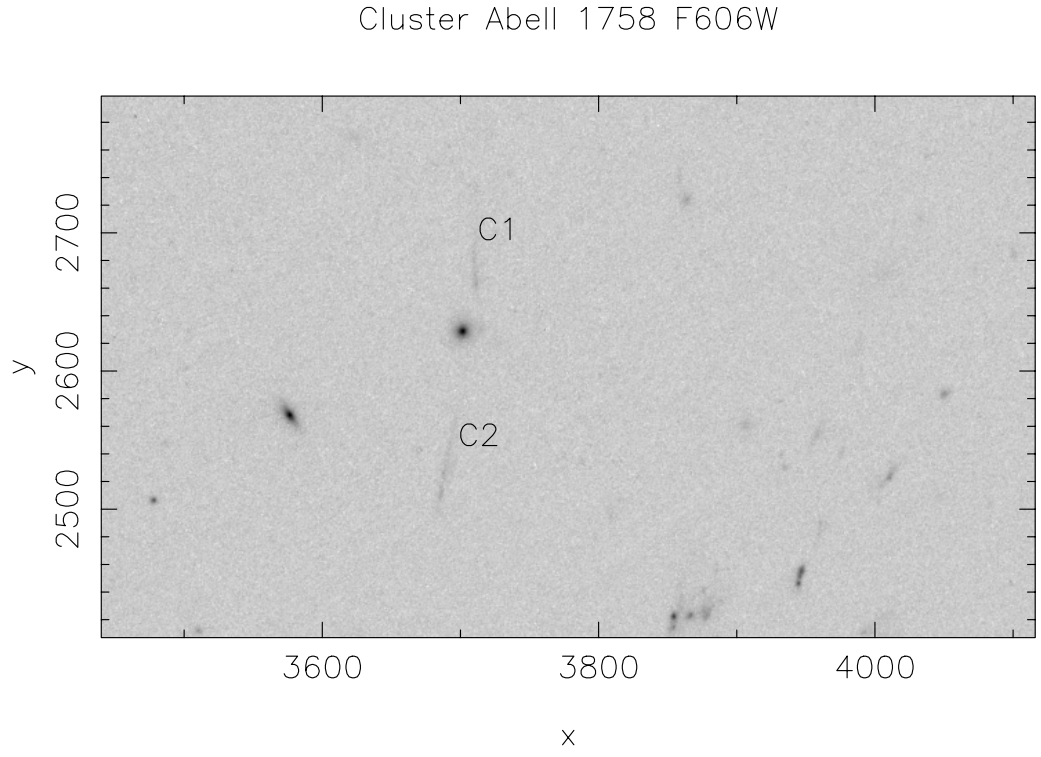


FIGURE C.61: PSZ1 G004.13+56.84 Two thin tangential arc segments C1 C2

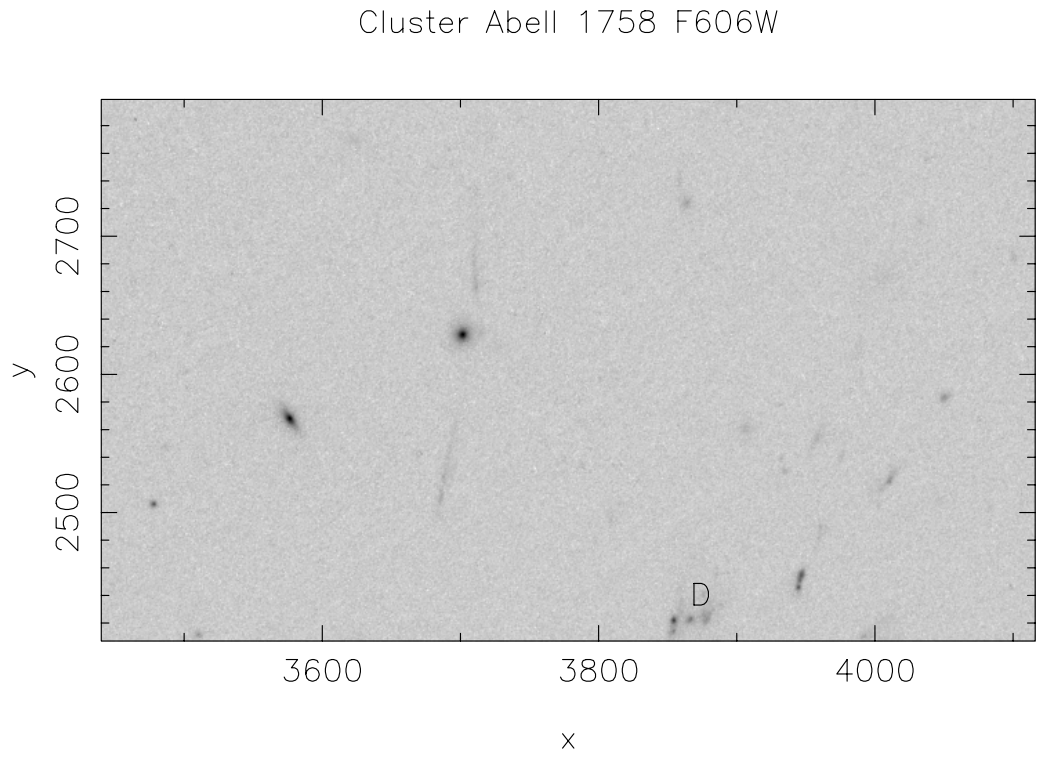


FIGURE C.62: PSZ1 G004.13+56.84 Extended object

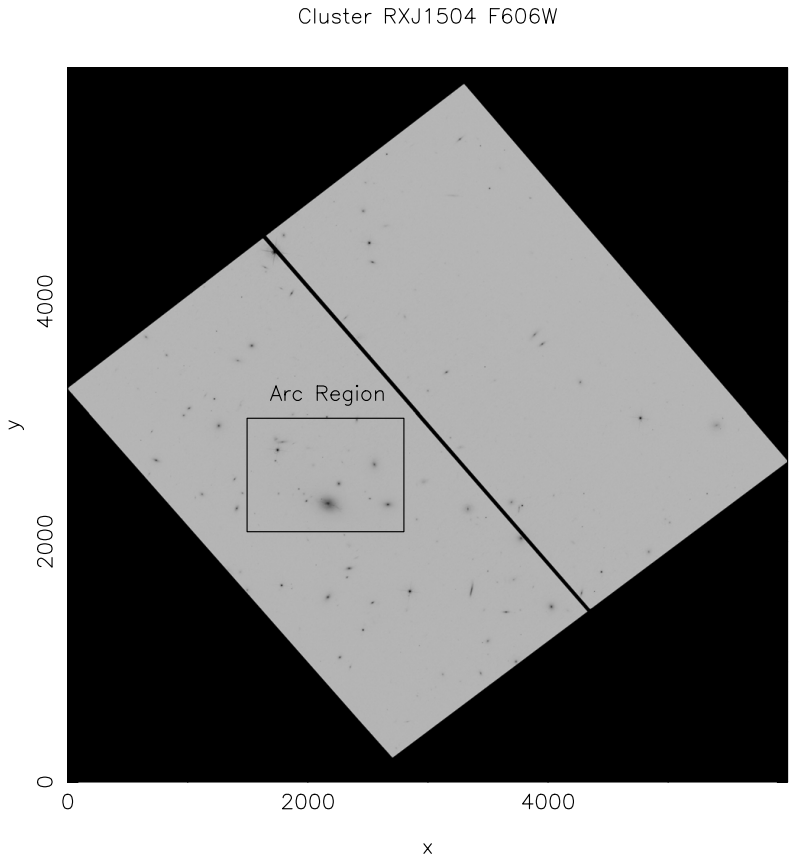


FIGURE C.63: PSZ1 G355.07+46.20 or RXJ1504.1-0248

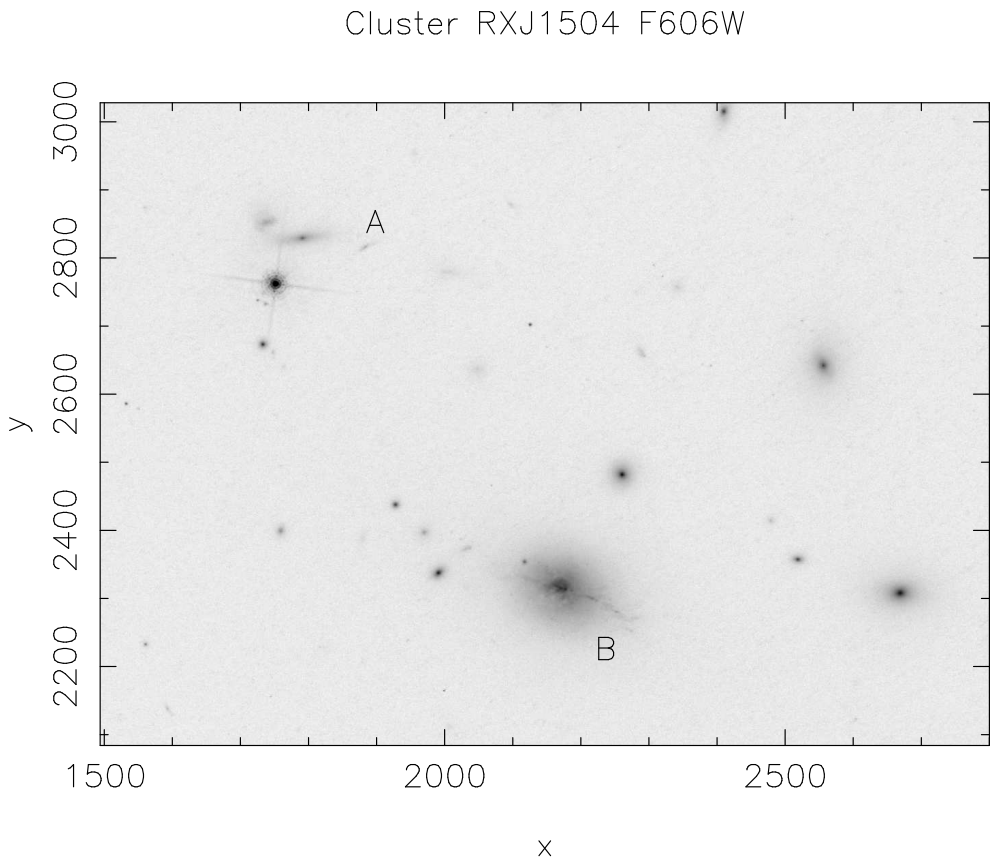


FIGURE C.64: PSZ1 G355.07+46.20 Thin curved extended background object

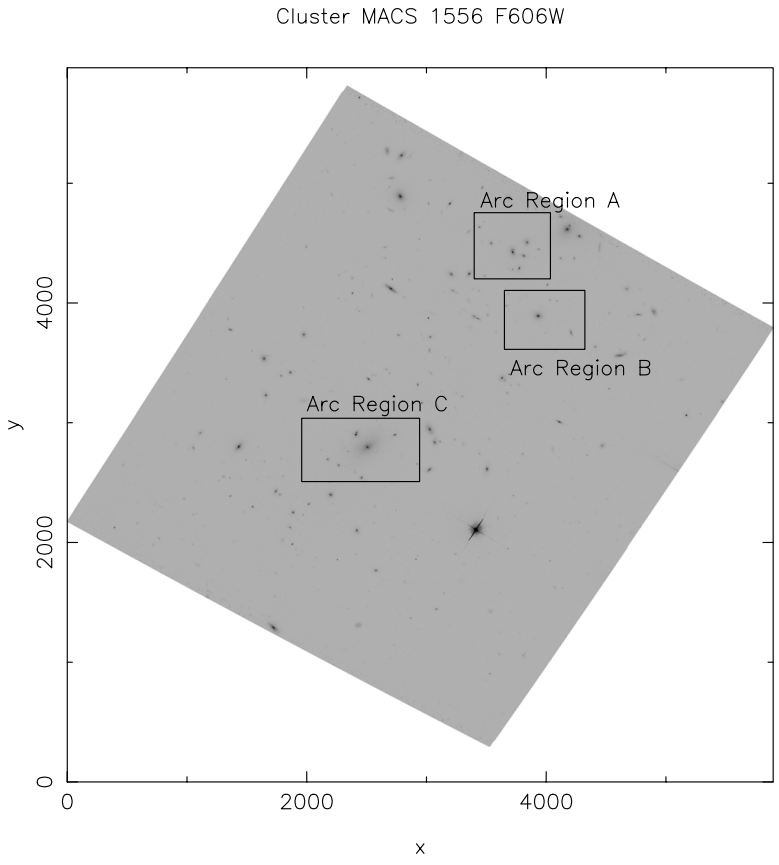


FIGURE C.65: PSZ1 G100.16+41.66 or RXJ1556.1+6621

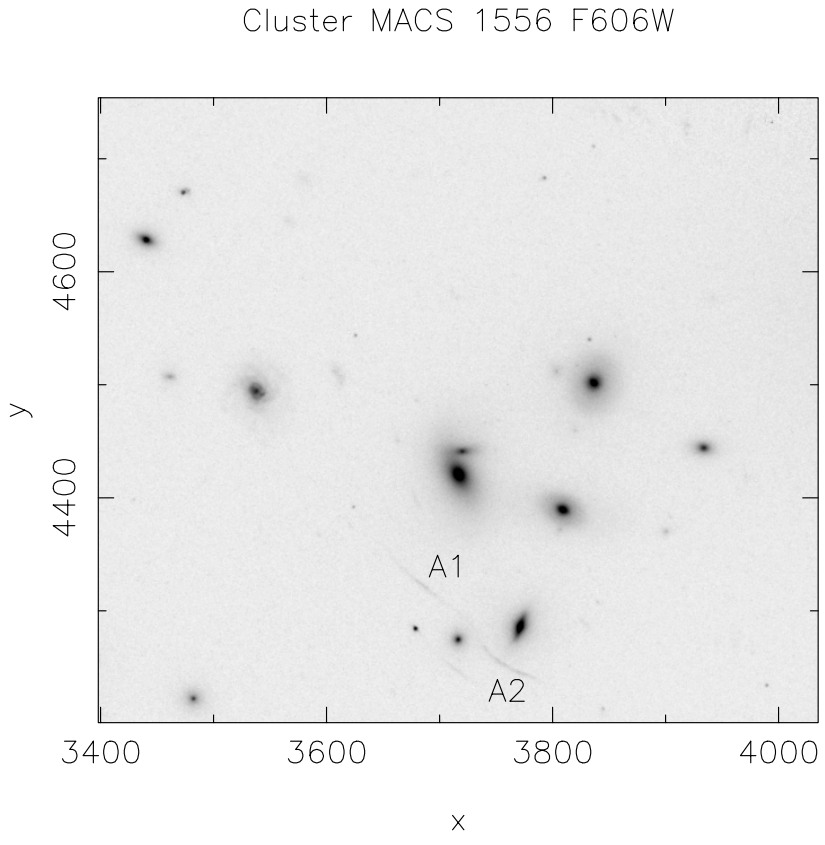


FIGURE C.66: PSZ1 G100.16+41.66 Long thin arc segments A1 A2 around galaxy different from main BCG. A third object was too faint for reliable photometry.

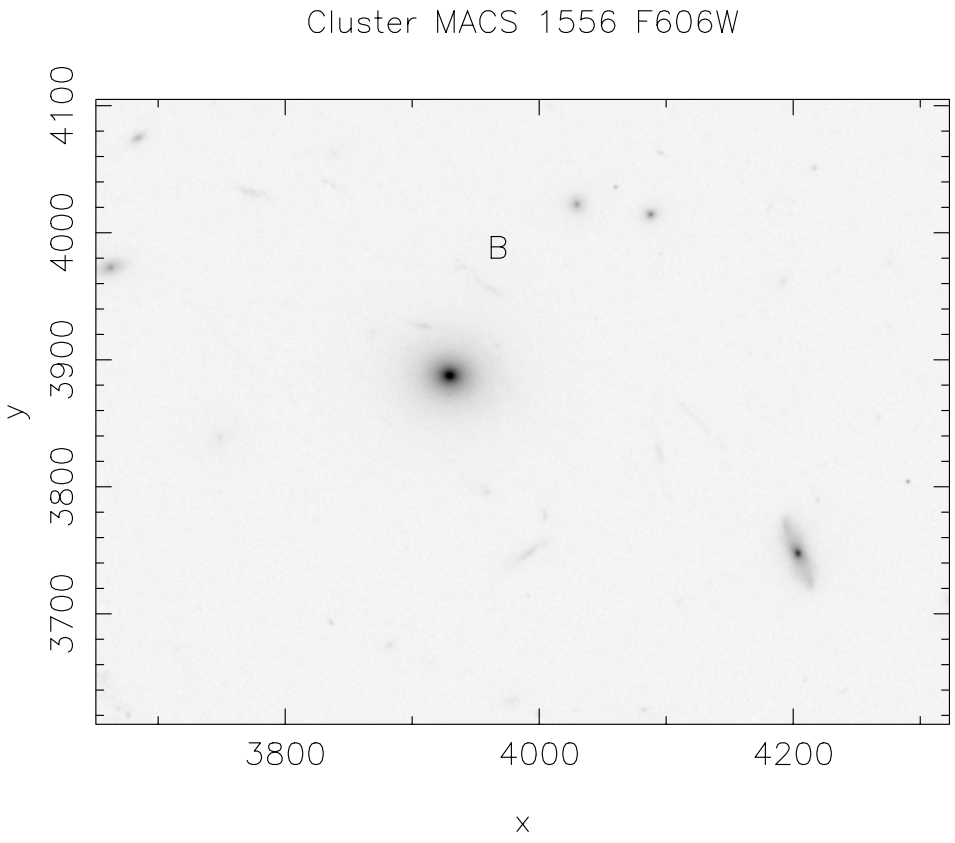


FIGURE C.67: PSZ1 G100.16+41.66 thin tangential 91 arcsec from BCG

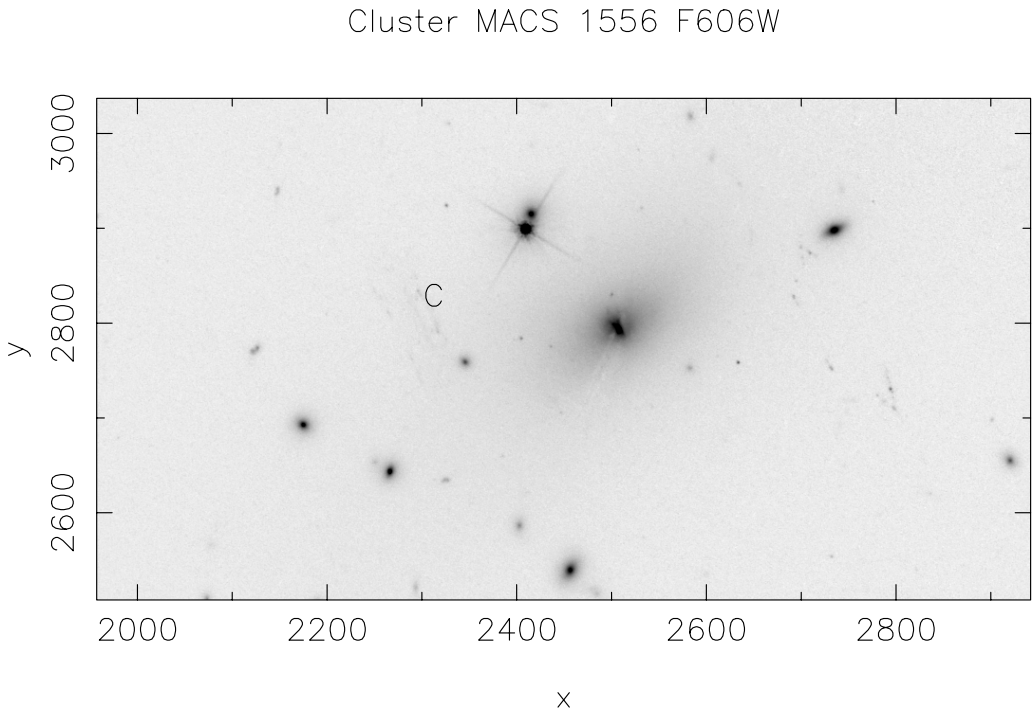


FIGURE C.68: PSZ1 G100.16+41.66 Thin arc segments near BCG

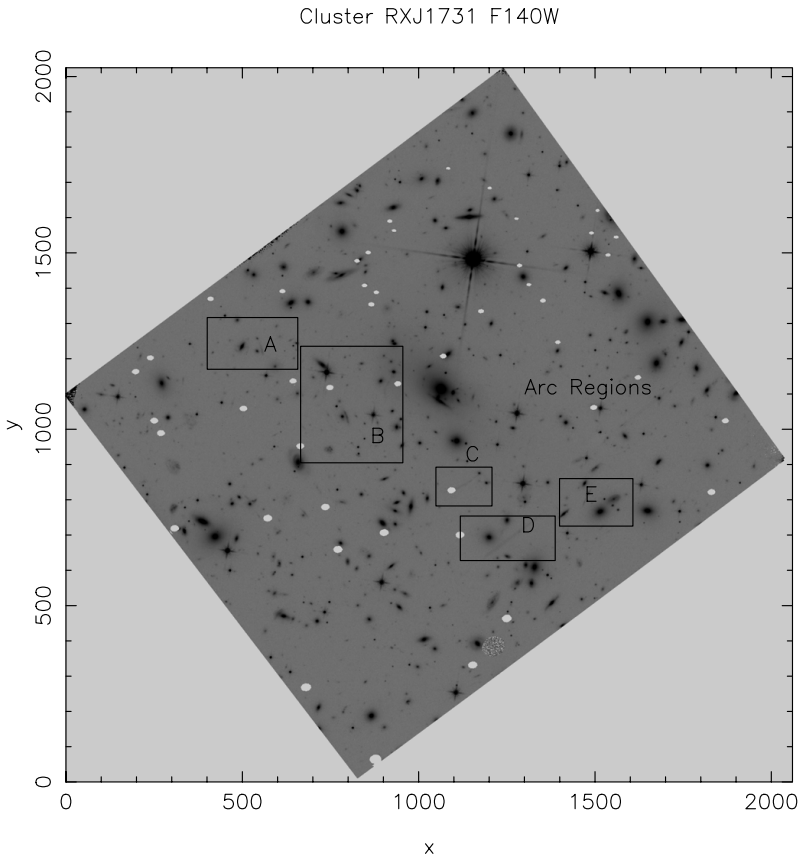


FIGURE C.69: PSZ1 G046.09+27.16 or RXJ1731.6+2251

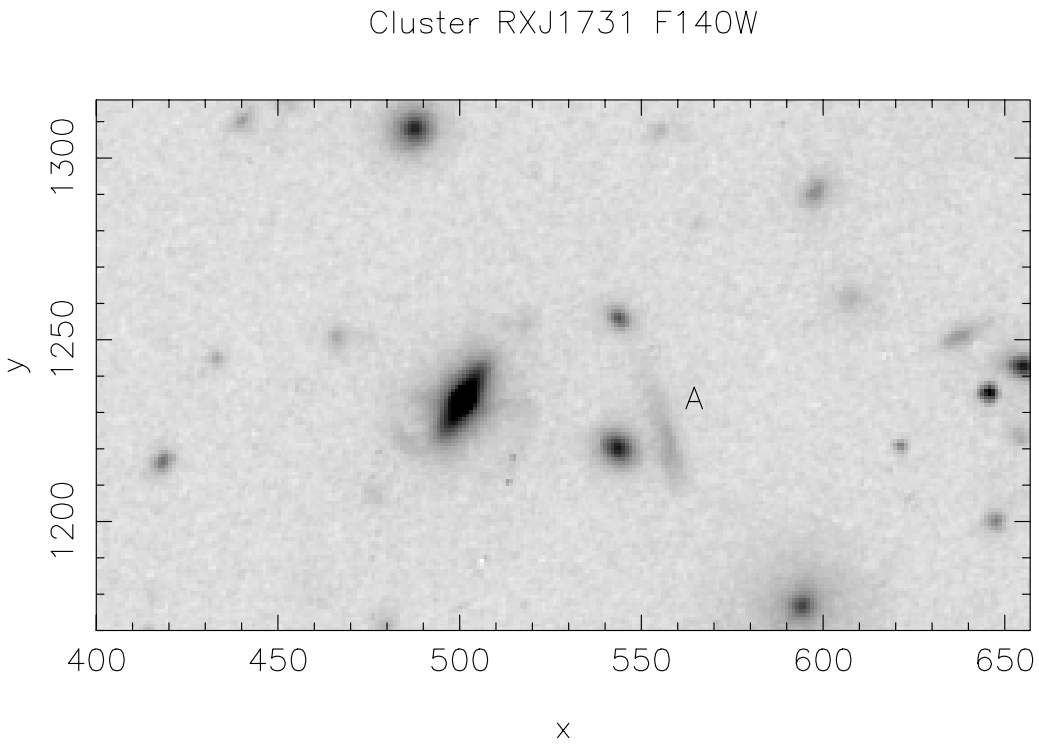


FIGURE C.70: PSZ1 G046.09+27.16 tangential arc A

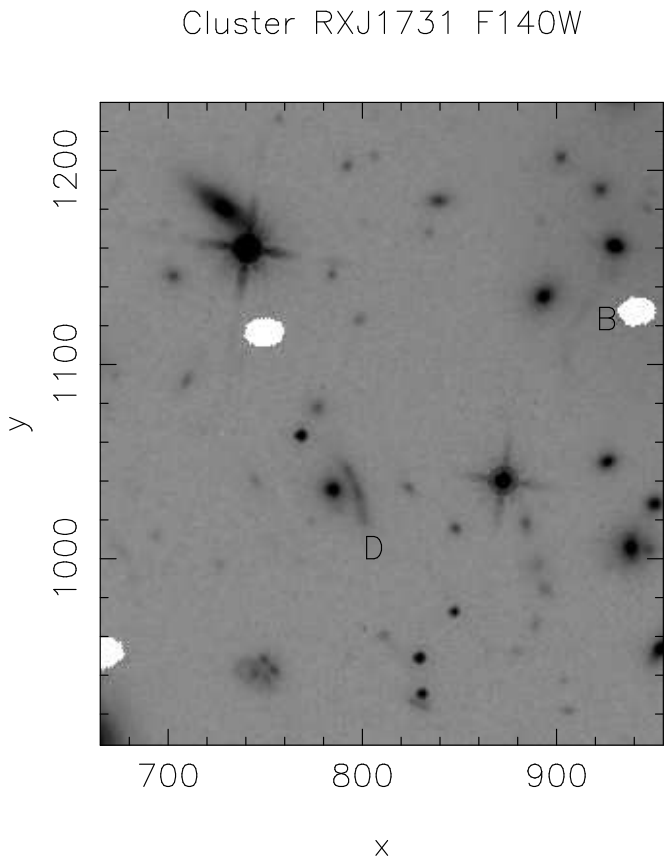


FIGURE C.71: PSZ1 G046.09+27.16 Radial arc B

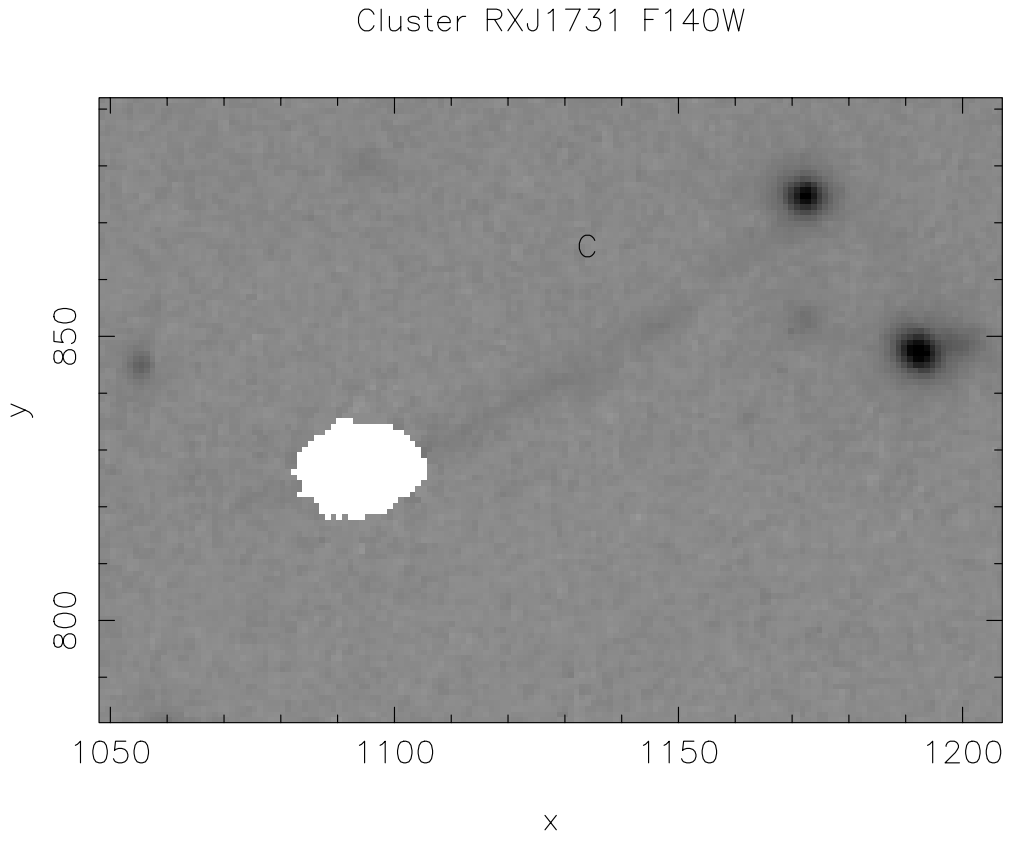


FIGURE C.72: PSZ1 G046.09+27.16 Long thing tangential arc C. Partially obscured by bad pixels

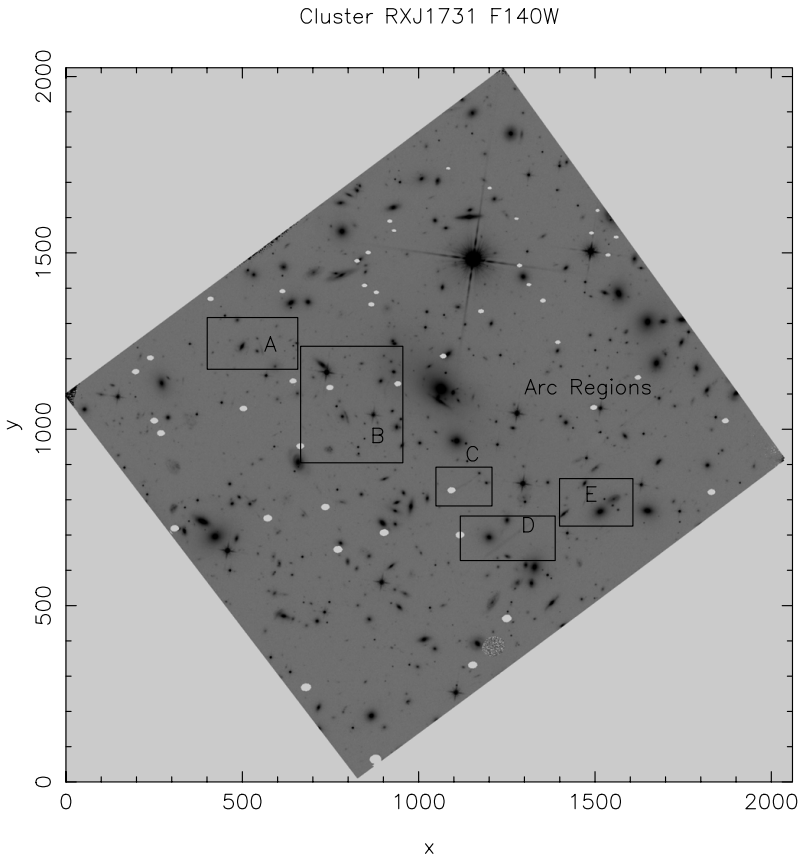


FIGURE C.73: PSZ1 G046.09+27.16 REMOVED ARC D

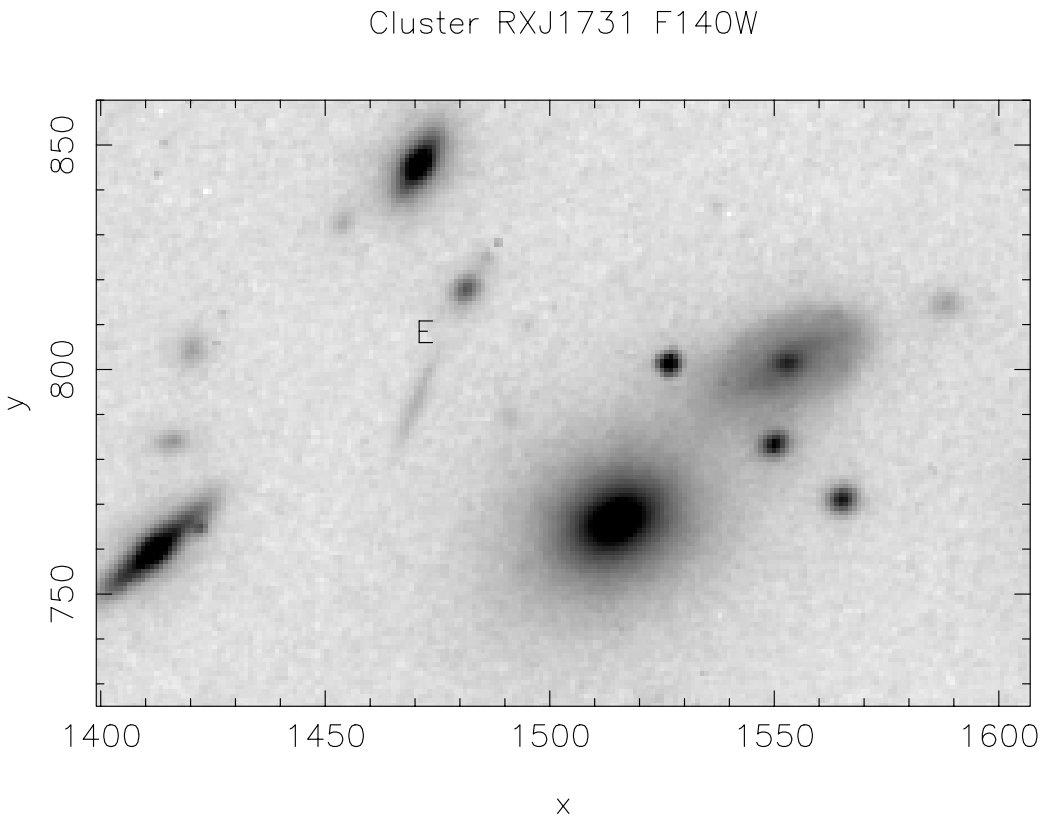


FIGURE C.74: PSZ1 G046.09+27.16 Tangential arc E

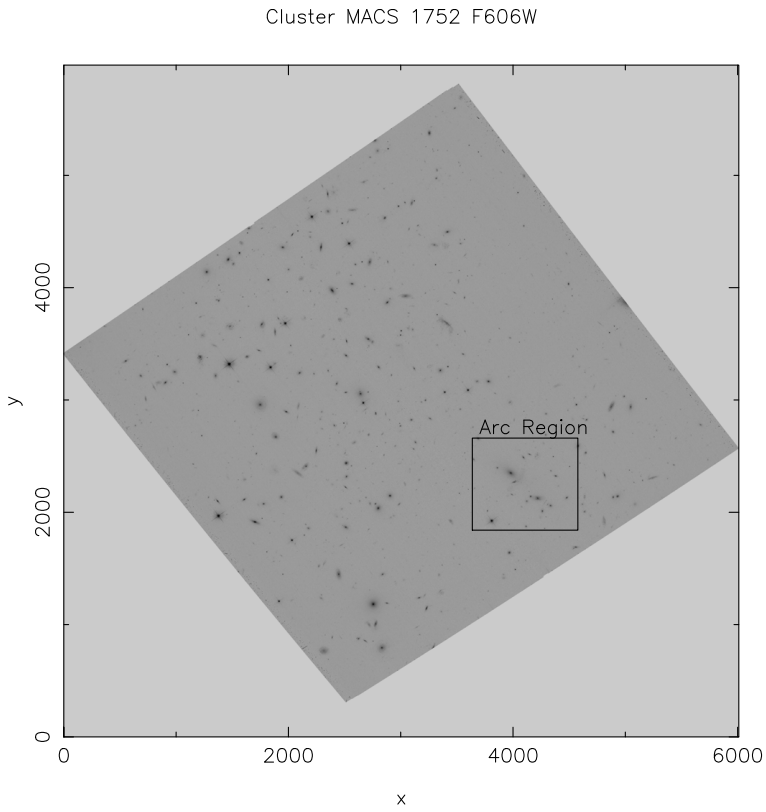


FIGURE C.75: PSZ1 G071.21+28.86 or RXJ1752.0+4440

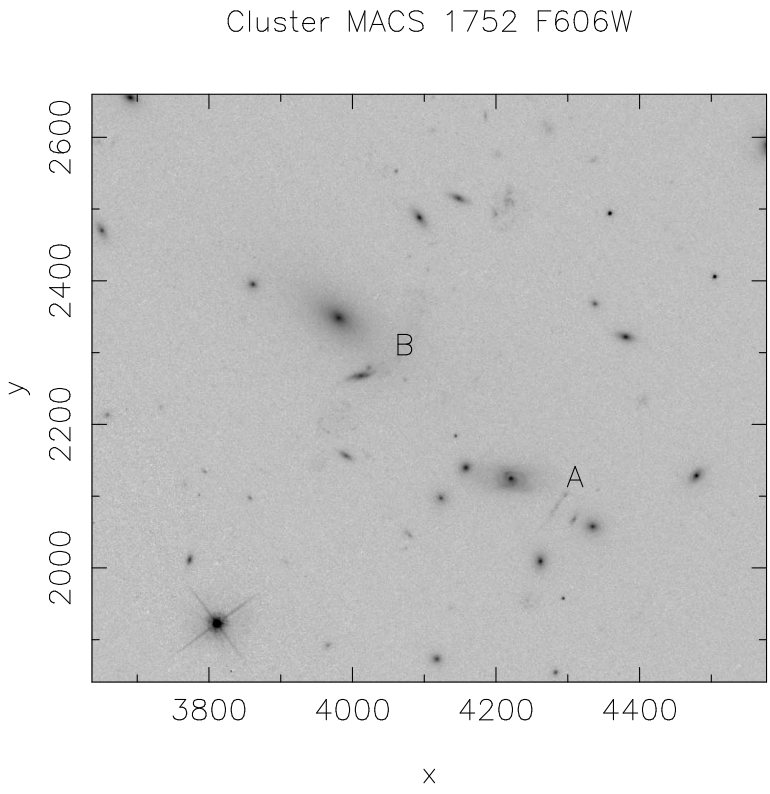


FIGURE C.76: PSZ1 G071.21+28.86 Tangential arcs A and B

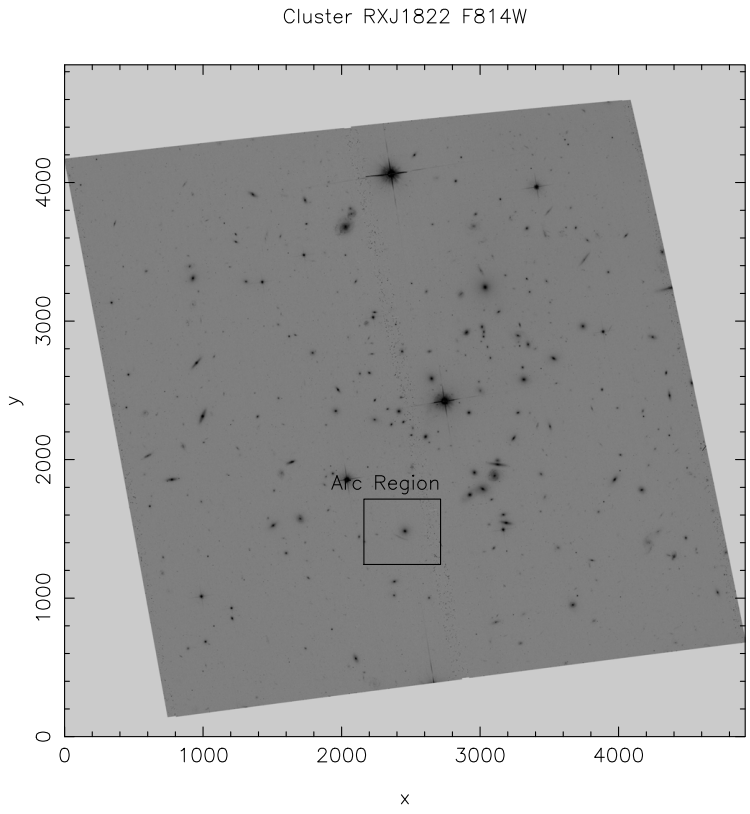


FIGURE C.77: PSZ1 G094.00+27.41 or H1821 +643 Cluster

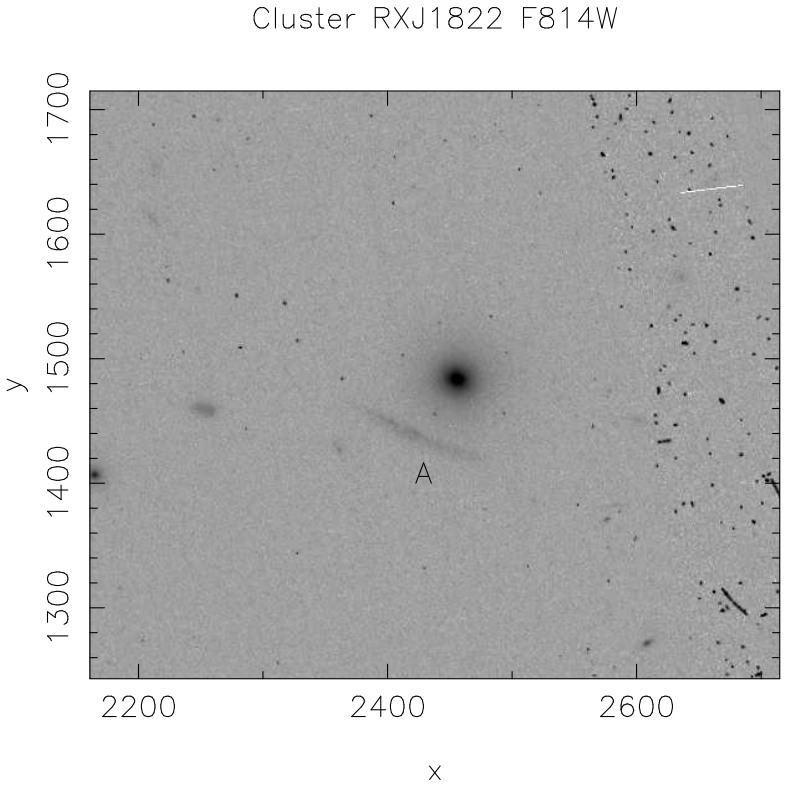


FIGURE C.78: PSZ1 G094.00+27.41 clear tangential arc near BCG

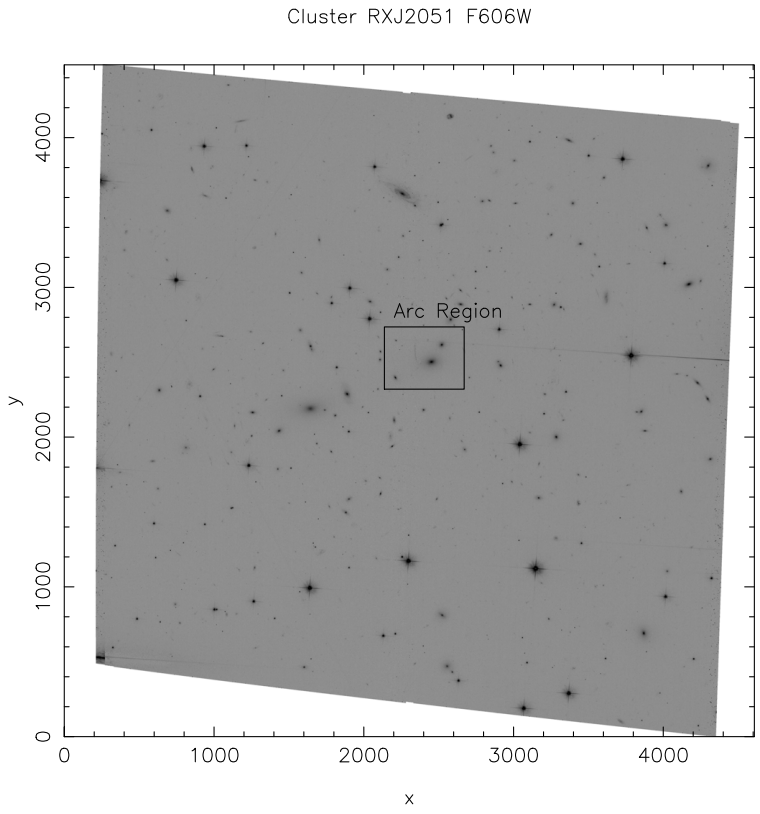


FIGURE C.79: PSZ1 G049.83-25.22 or RXJ2051.1+0216

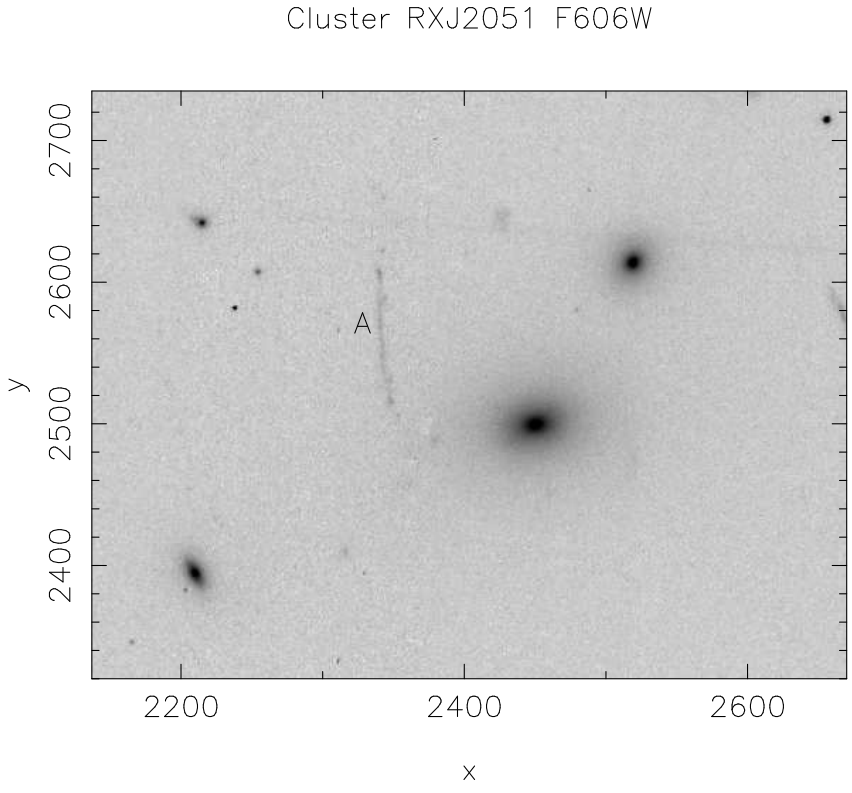


FIGURE C.80: PSZ1 G049.83-25.22 strong arc near BCG

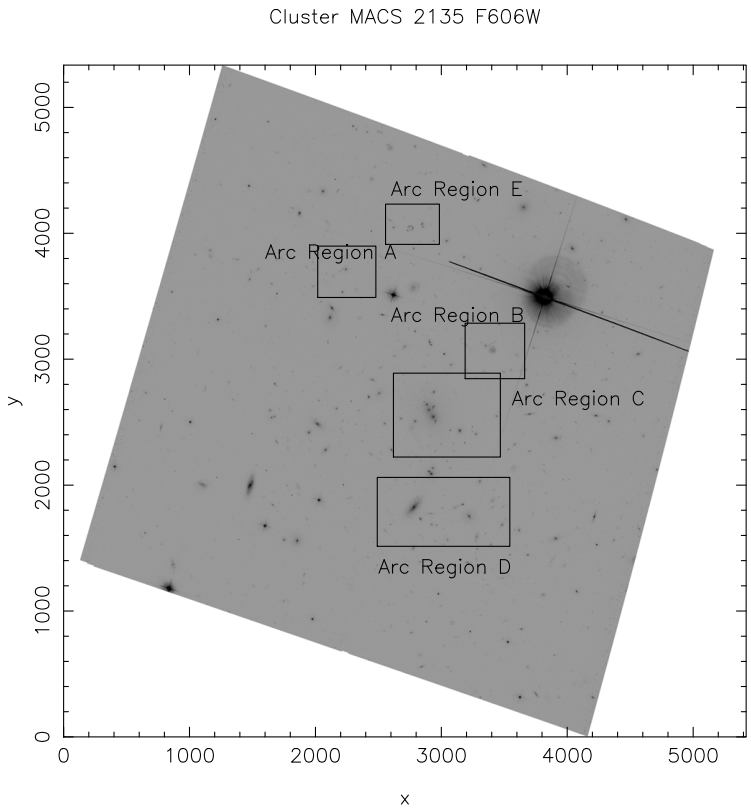


FIGURE C.81: PSZ1 G053.42-36.25 or RXJ2135.2-0102

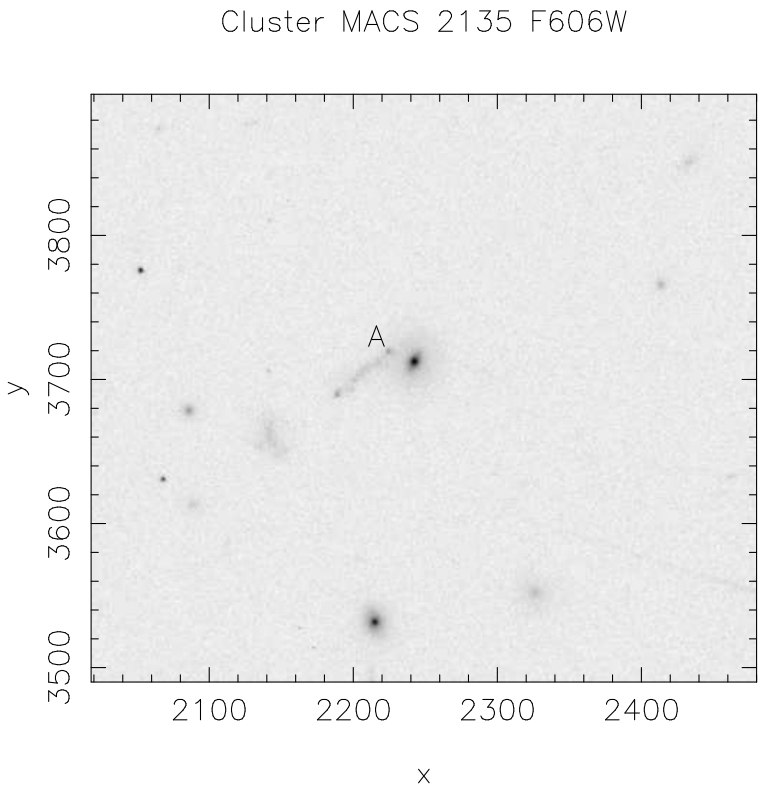


FIGURE C.82: PSZ1 G053.42-36.25 Radial arc near galaxy

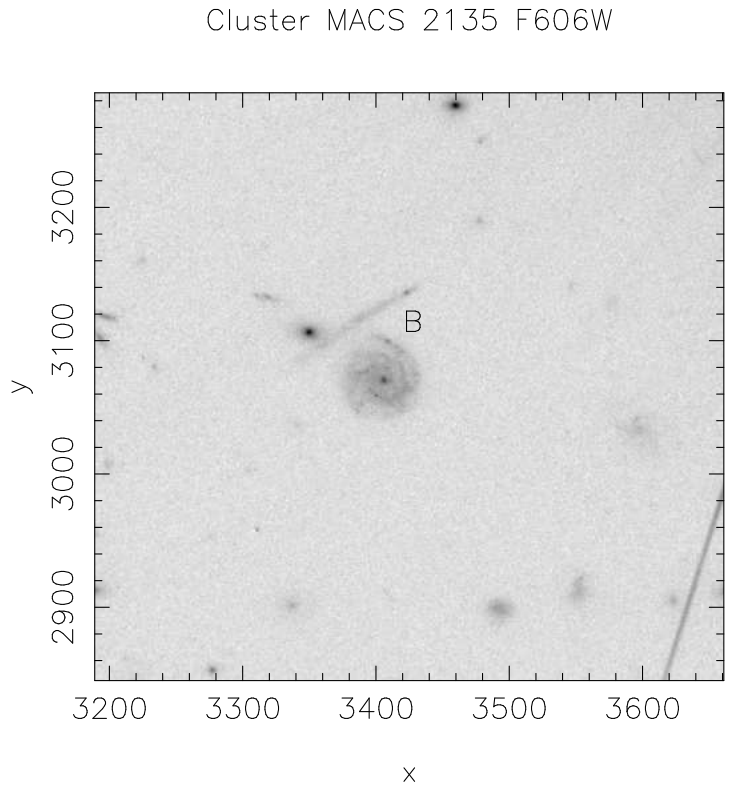


FIGURE C.83: PSZ1 G053.42-36.25 Radially oriented arc B

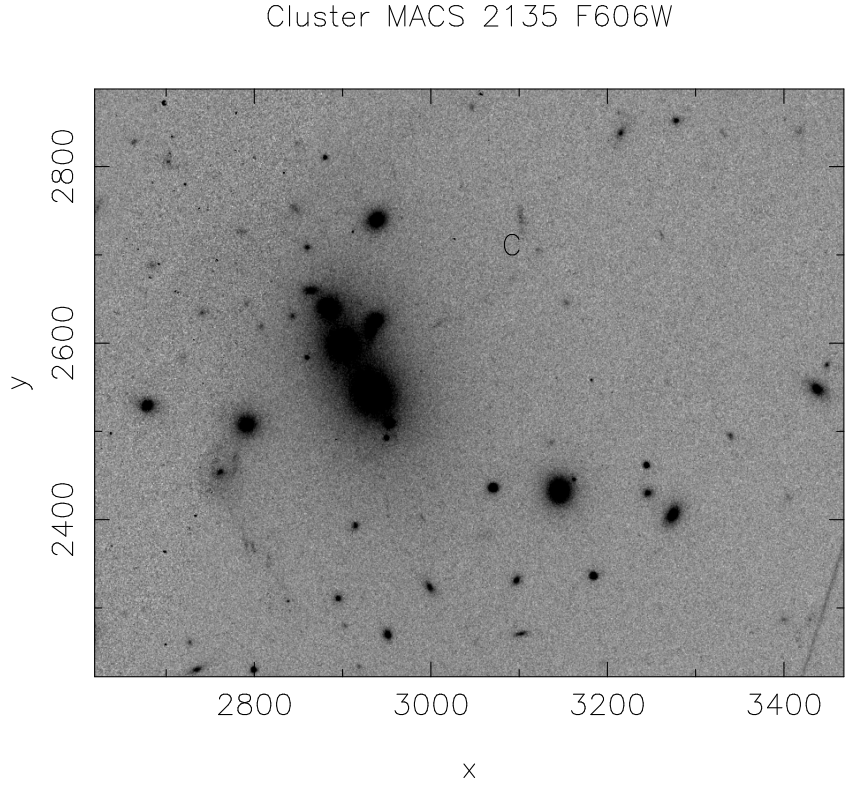


FIGURE C.84: PSZ1 G053.42-36.25 Faint tangential arc C

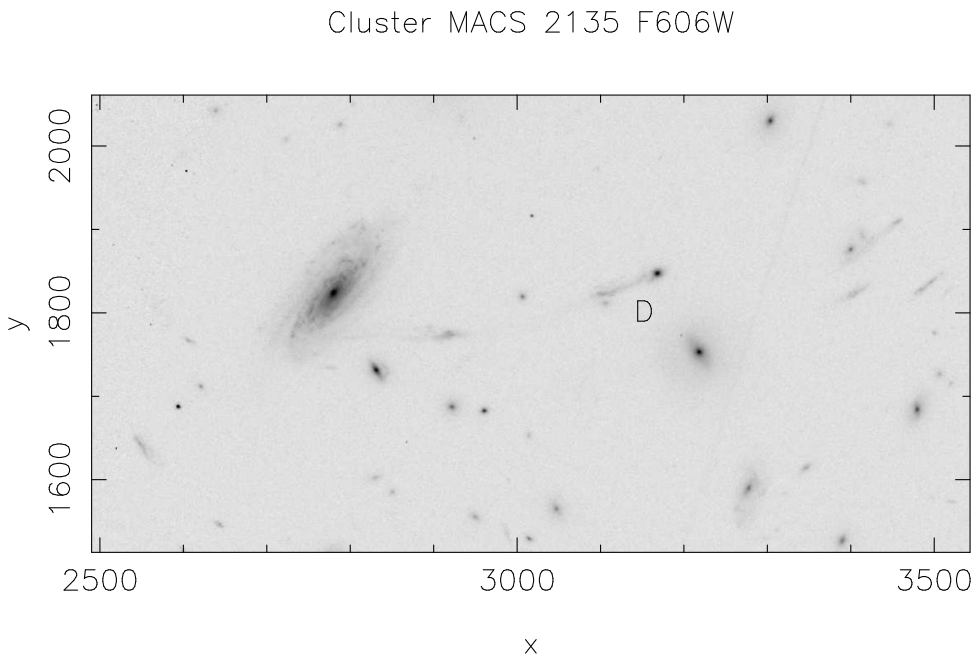


FIGURE C.85: PSZ1 G053.42-36.25 long arc D

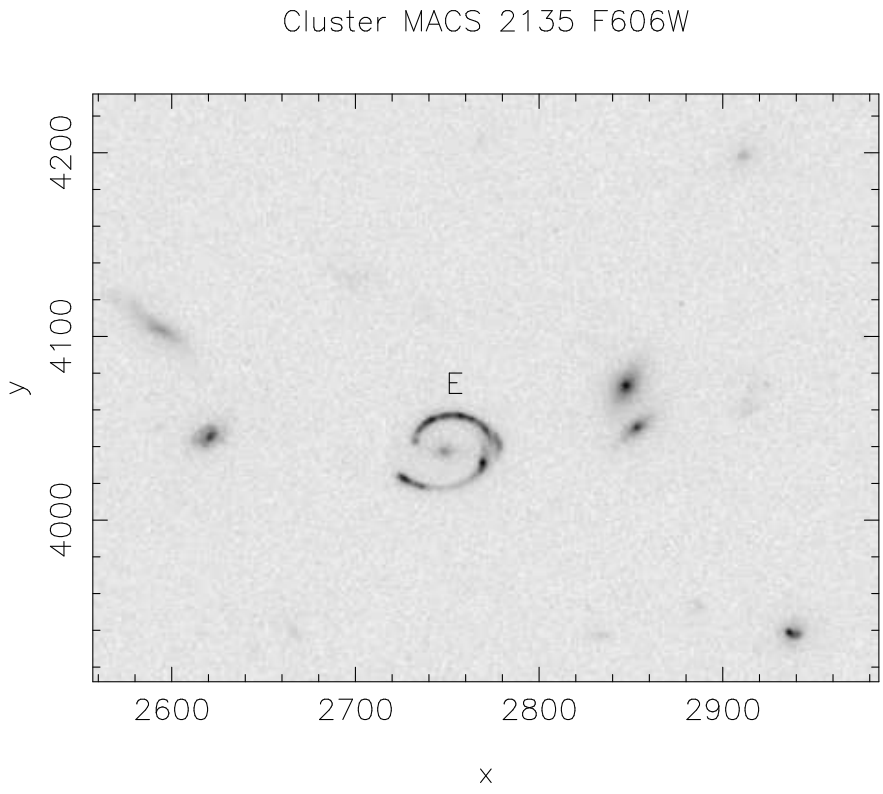


FIGURE C.86: PSZ1 G053.42-36.25 Einstein ring

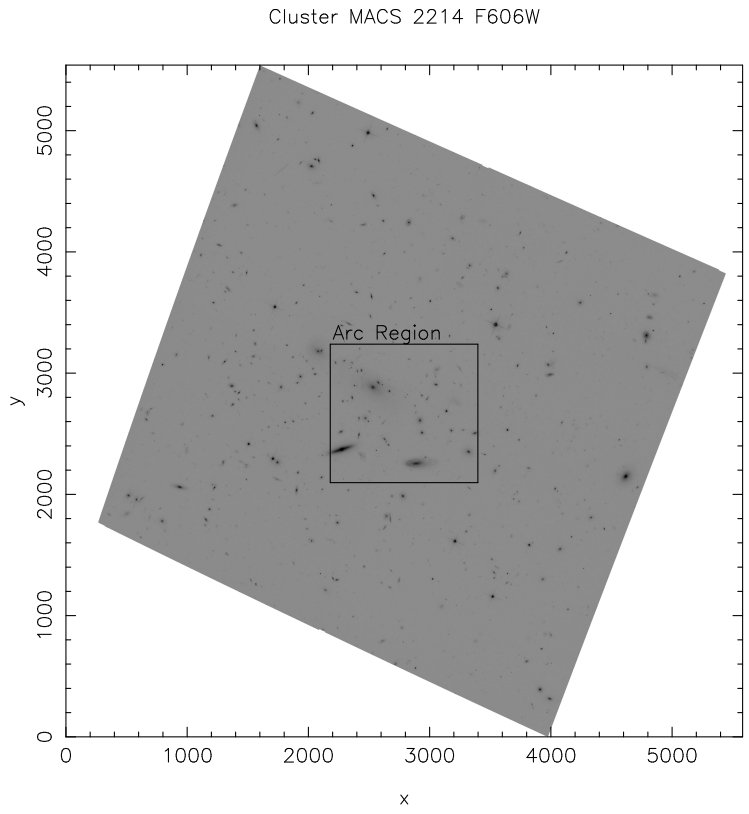


FIGURE C.87: PSZ1 G044.77-51.30 or RXJ2214.9-1400

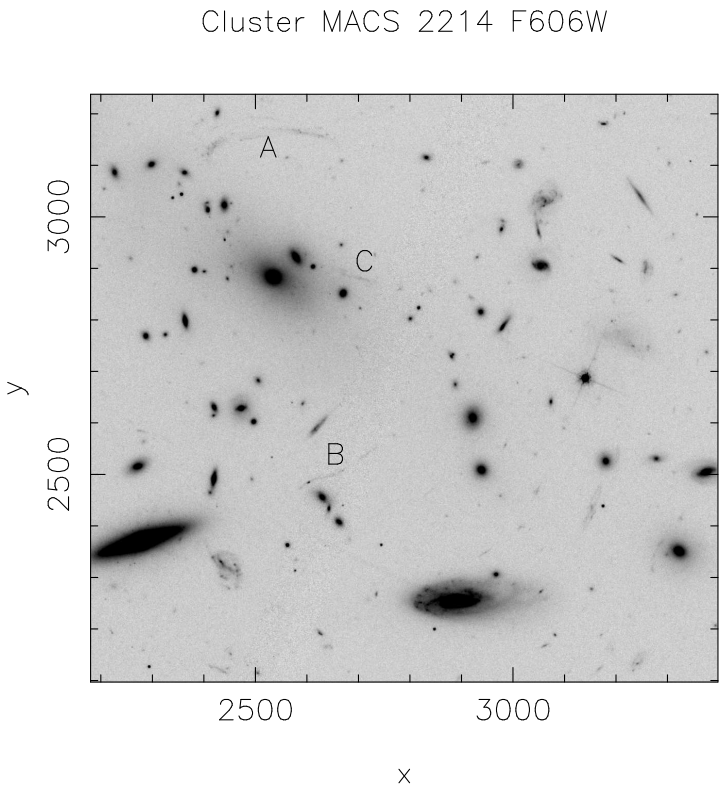


FIGURE C.88: PSZ1 G044.77-51.30 Long tangential arcs A B C

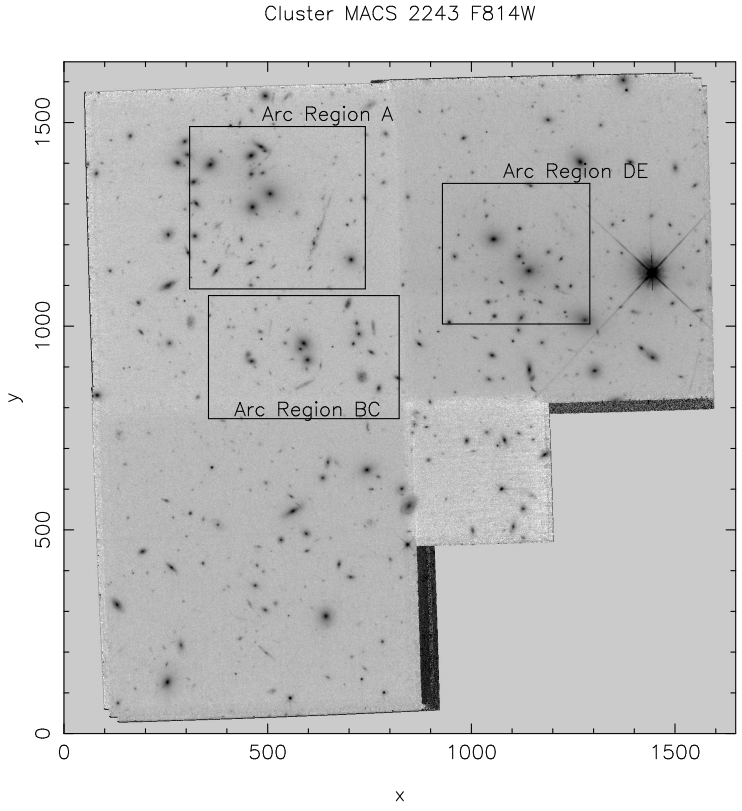


FIGURE C.89: PSZ1 G056.94-55.06 or RXJ2243.3-0935

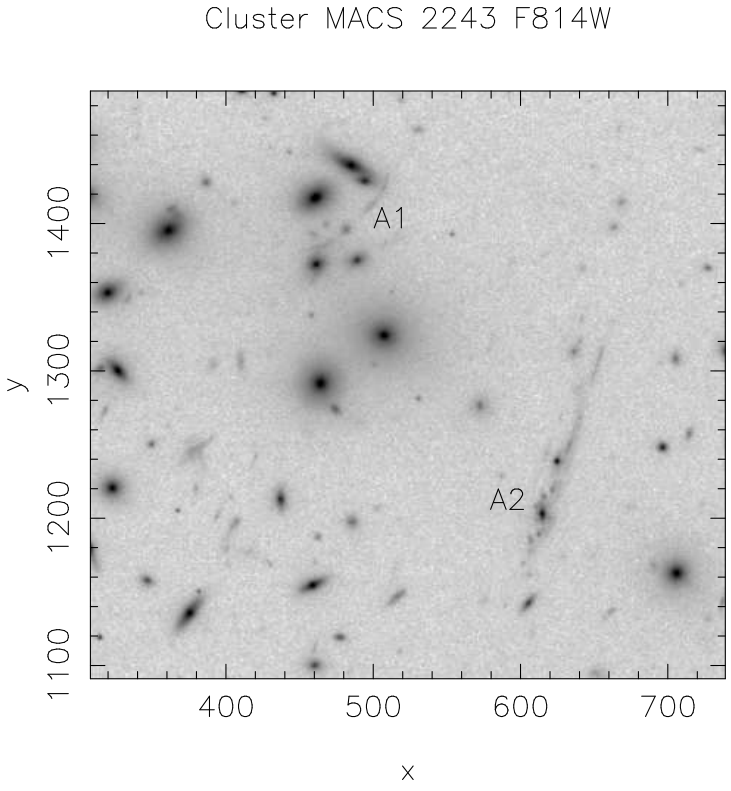


FIGURE C.90: PSZ1 G056.94-55.06 Two extended arcs of the same background galaxy A1 A2

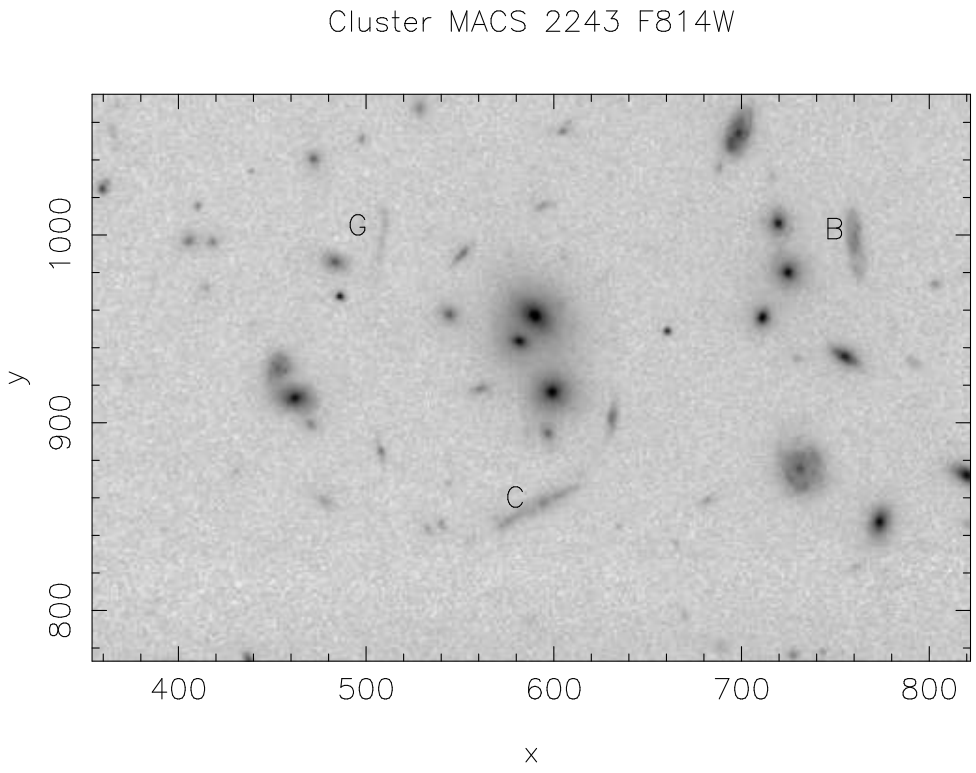


FIGURE C.91: PSZ1 G056.94-55.06

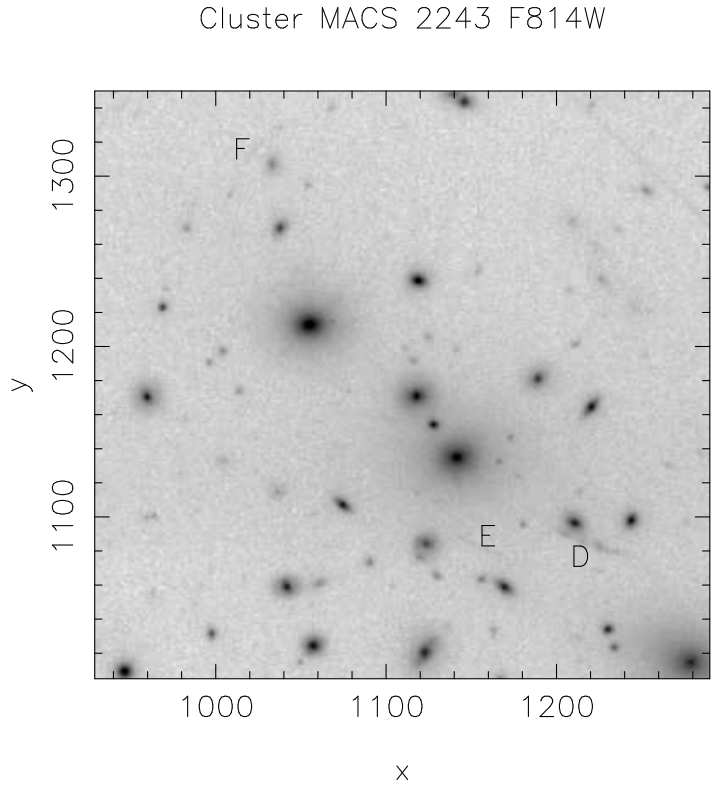


FIGURE C.92: PSZ1 G056.94-55.06 Radial arc D close to BCG and faint tangential arc E

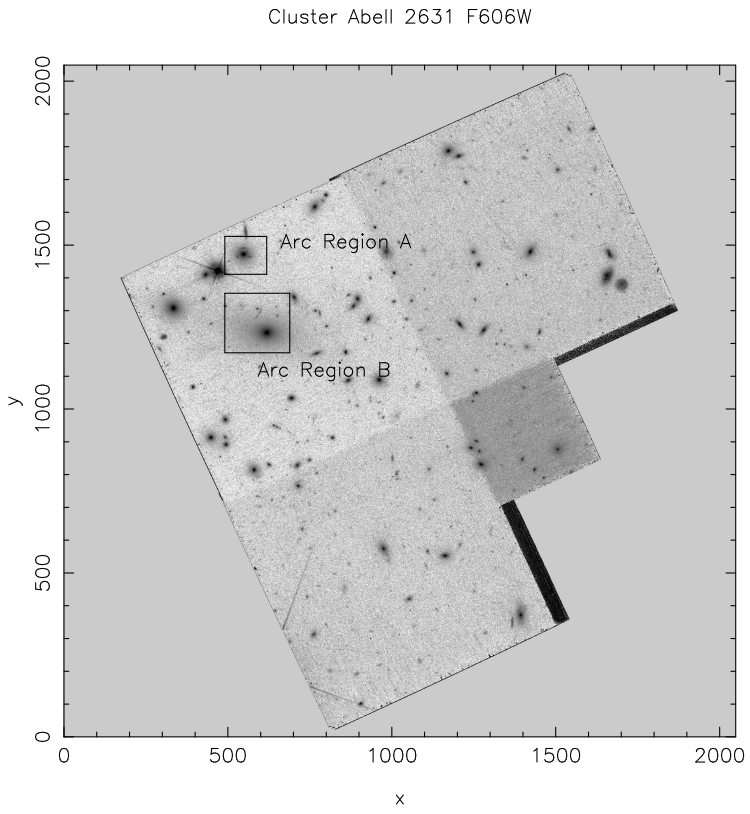


FIGURE C.93: PSZ1 G087.03-57.37 or RXJ2337.6+0016

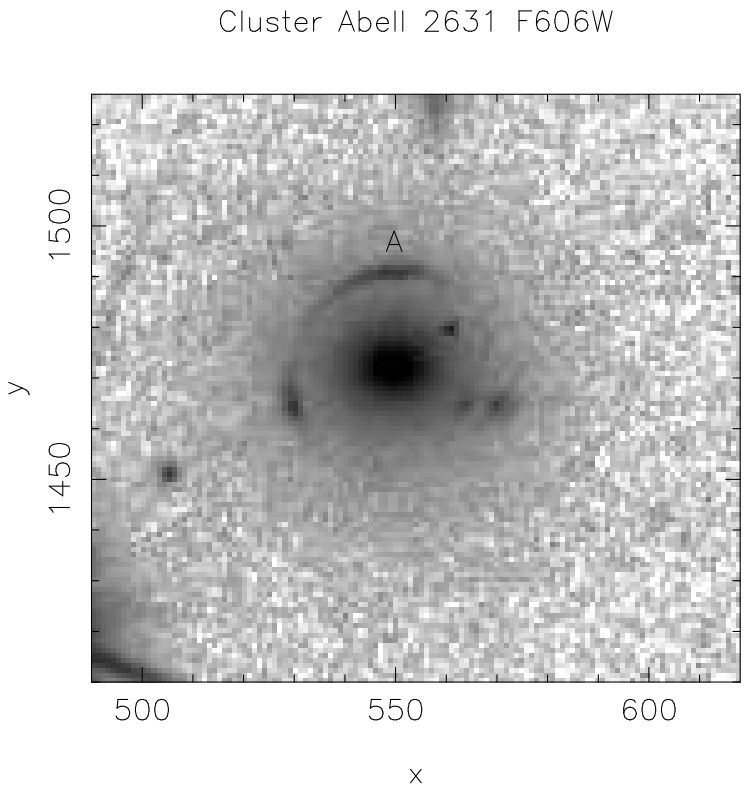


FIGURE C.94: PSZ1 G087.03-57.37 Half ring near cluster galaxy

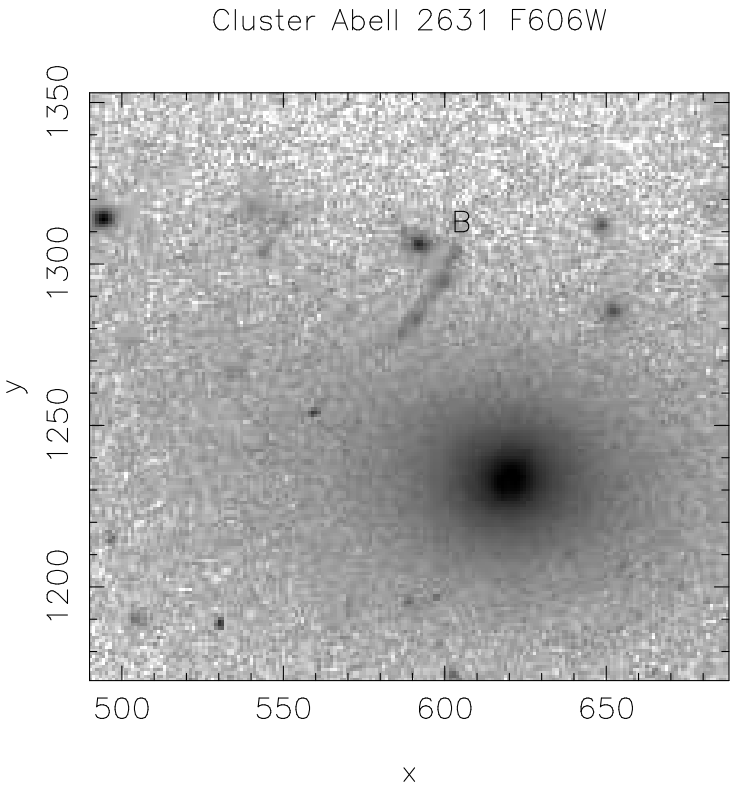


FIGURE C.95: PSZ1 G087.03-57.37 Radial arc near cluster BCG

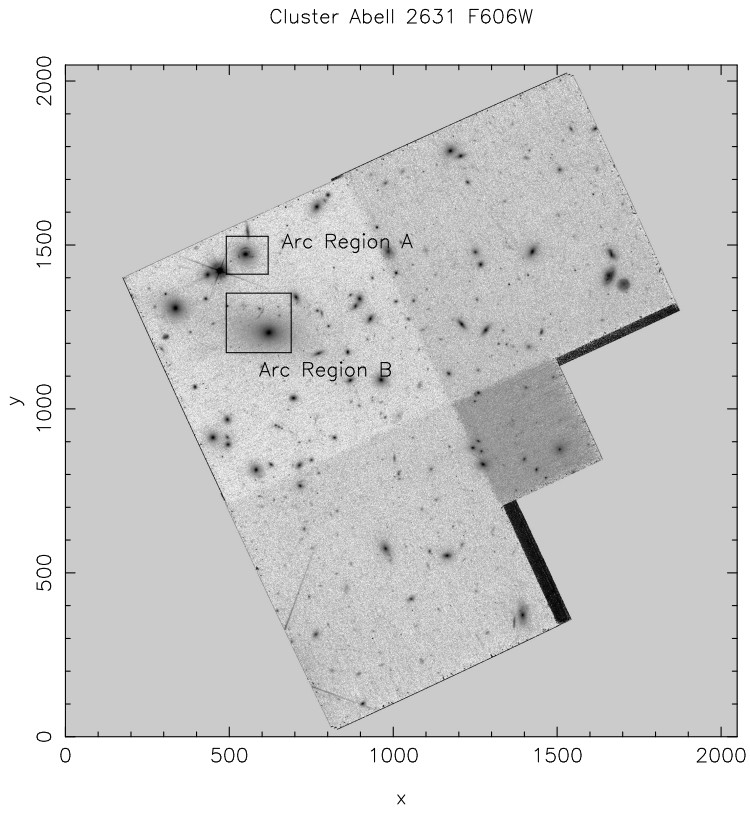


FIGURE C.96: this ends the HST images

# Appendix D

# Images of NOT Strong Lenses and Cluster Centers

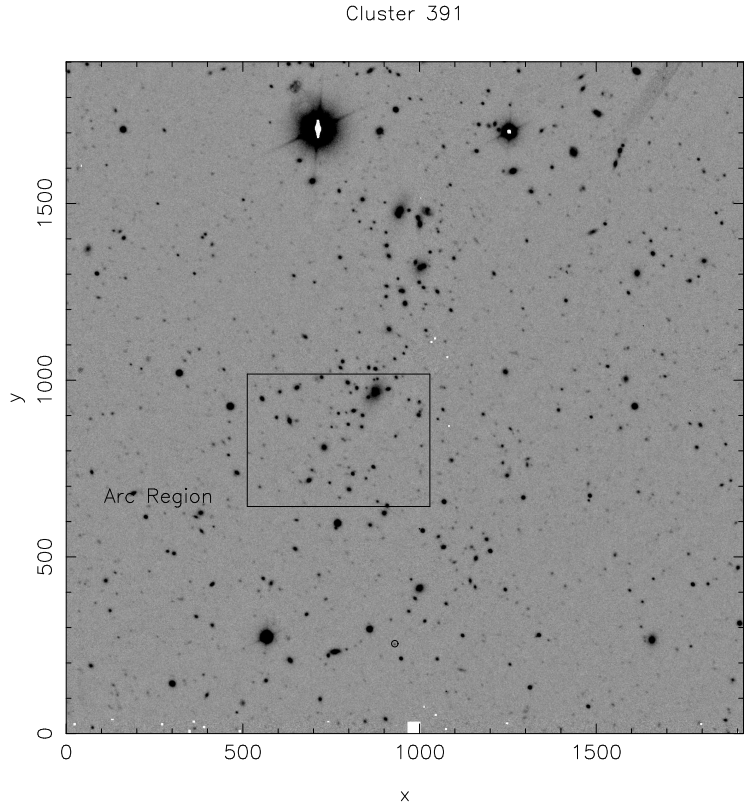


FIGURE D.1: PSZ1 G107.66-58.31 or ZwCl 0017.0+0320

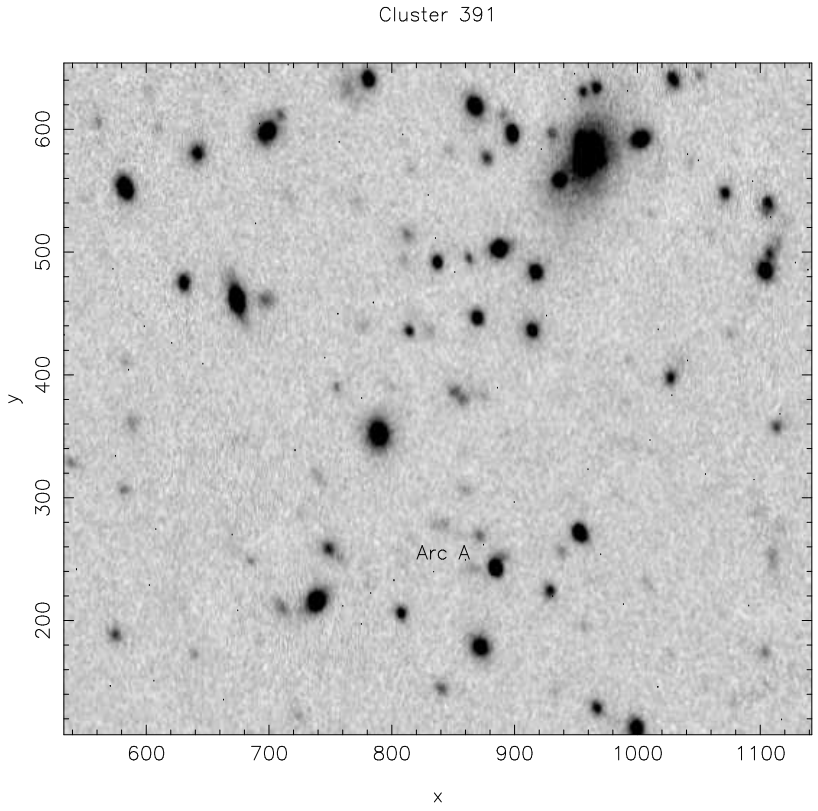


FIGURE D.2: PSZ1 G107.66-58.31 Short tangential arc 47 arcseconds from BCG

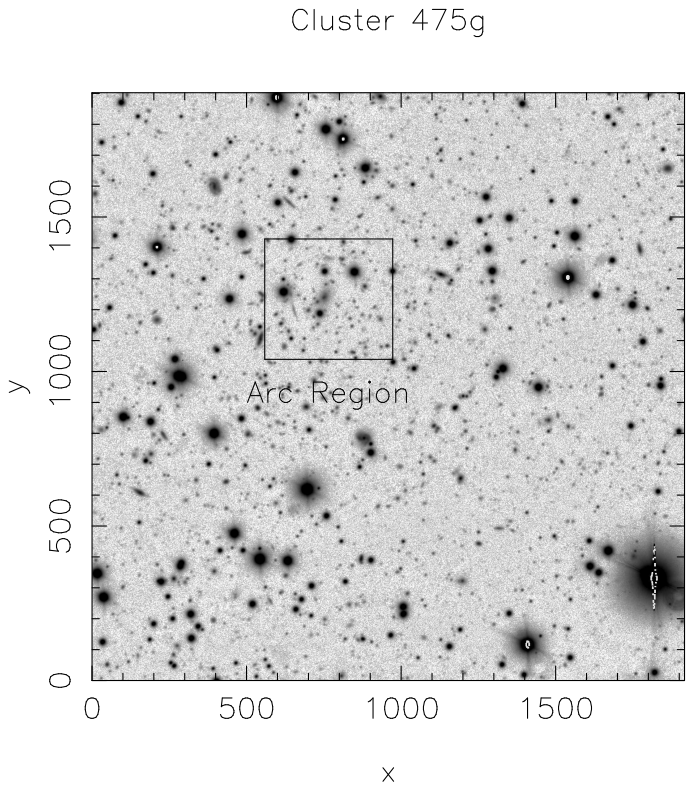


FIGURE D.3: PSZ1 G132.49-17.29 or RXJ0142.9+4438

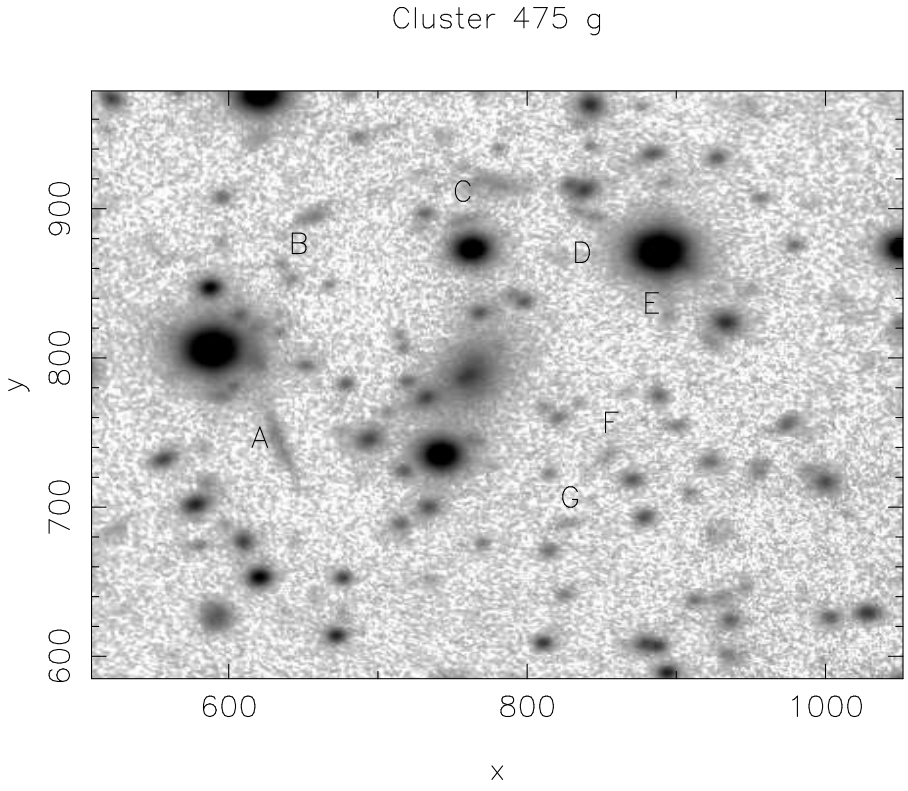


FIGURE D.4: PSZ1 G 132.49-17.29 A grouping of 7 tangential arcs roughly 23 arcseconds from the BCG

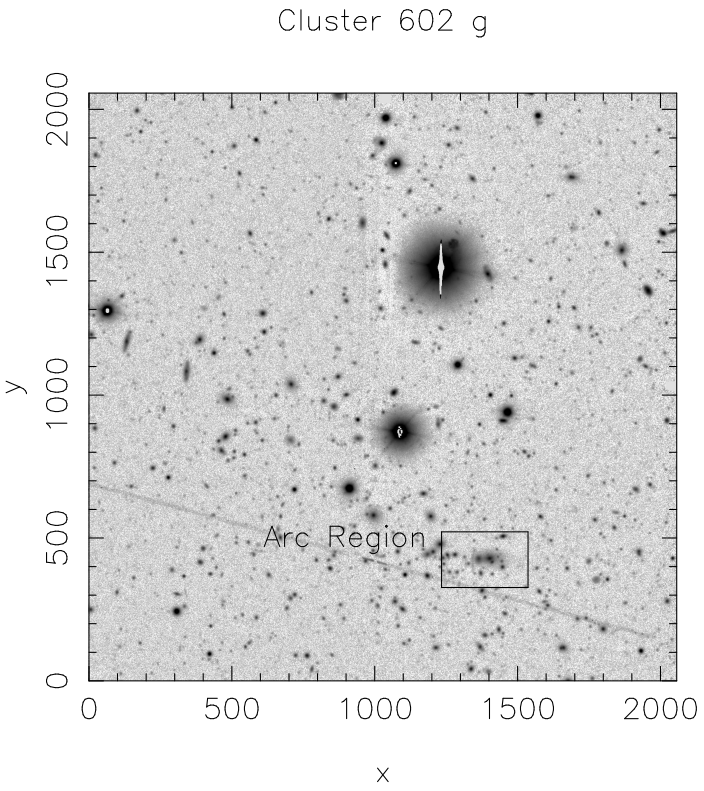


FIGURE D.5: PSZ1 G176.25-52.57 or RXJ0248.2-0216

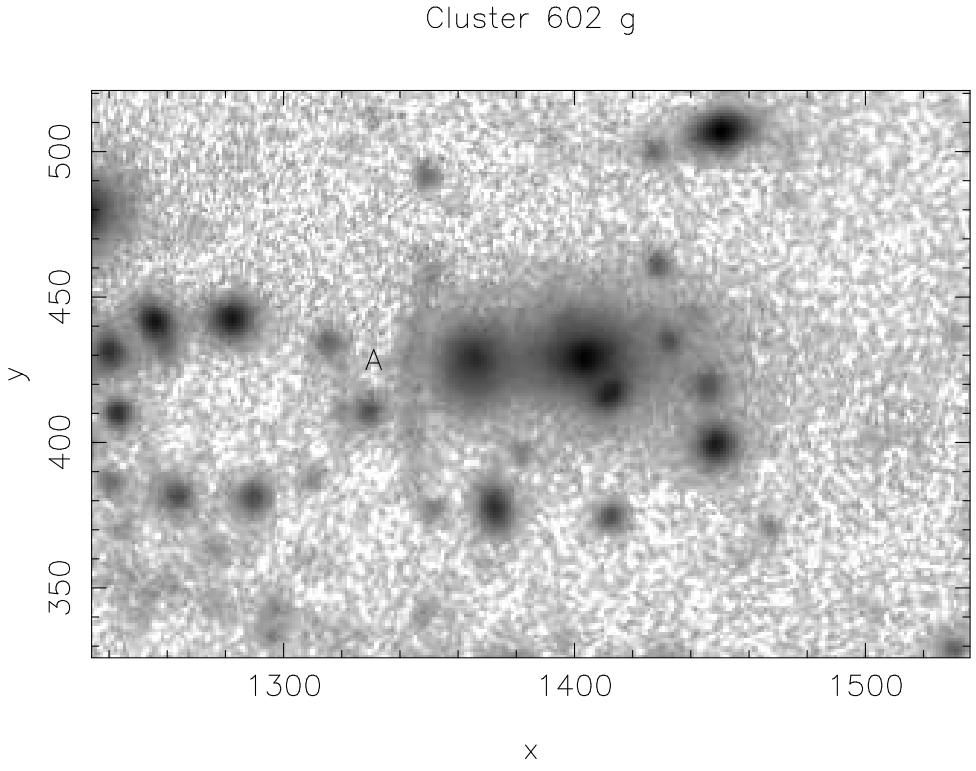


FIGURE D.6: PSZ1 G176.25-52.57 A long tangential arc 14 arcseconds from BCG

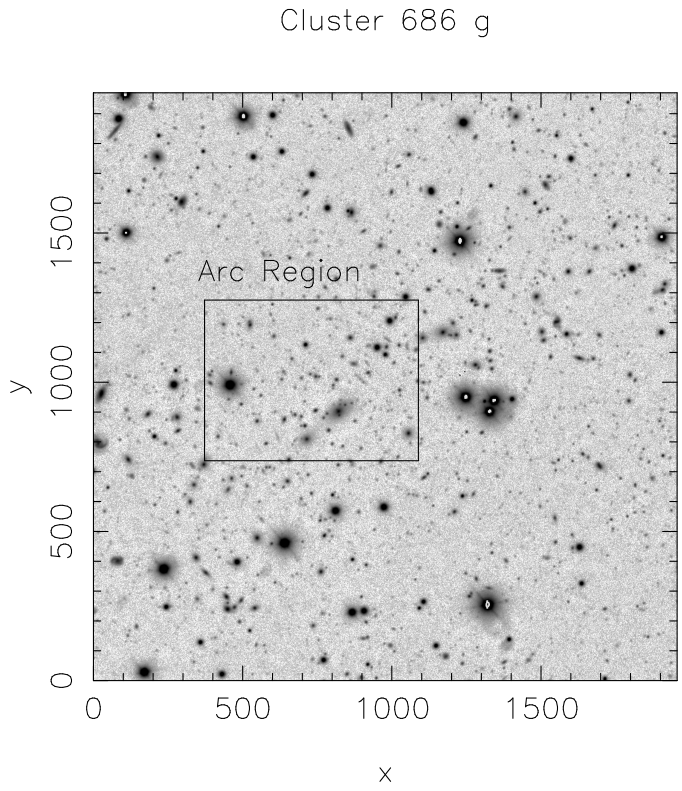


FIGURE D.7: PSZ1 G208.59-26.00 or RXJ0510.7-0801

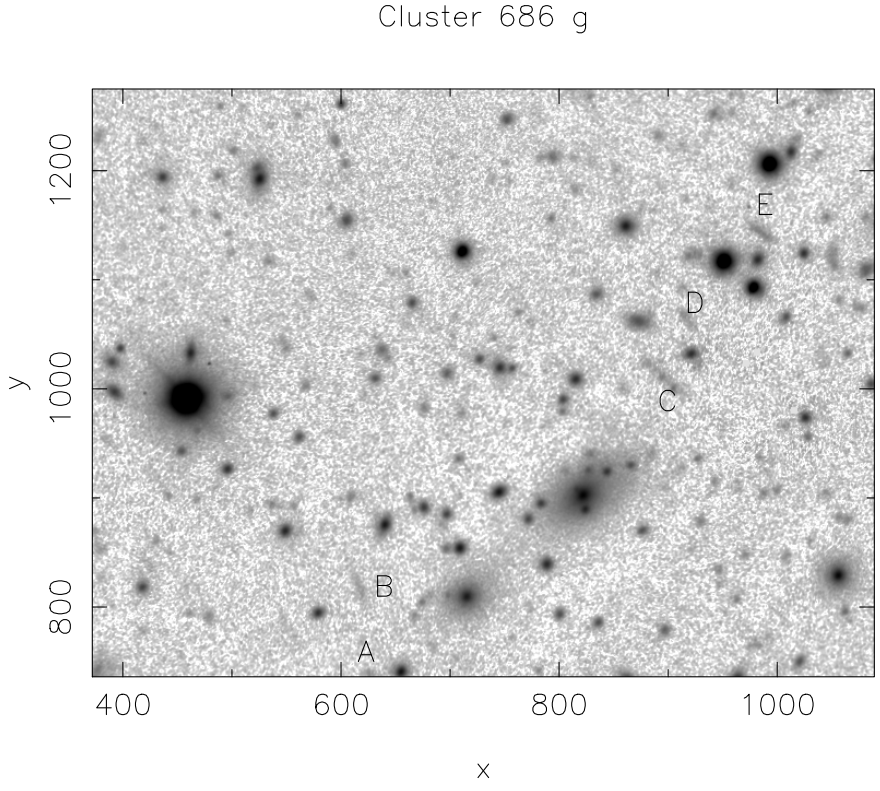


FIGURE D.8: PSZ1 G208.59-26.00 6 short tangential arcs located around the BCG

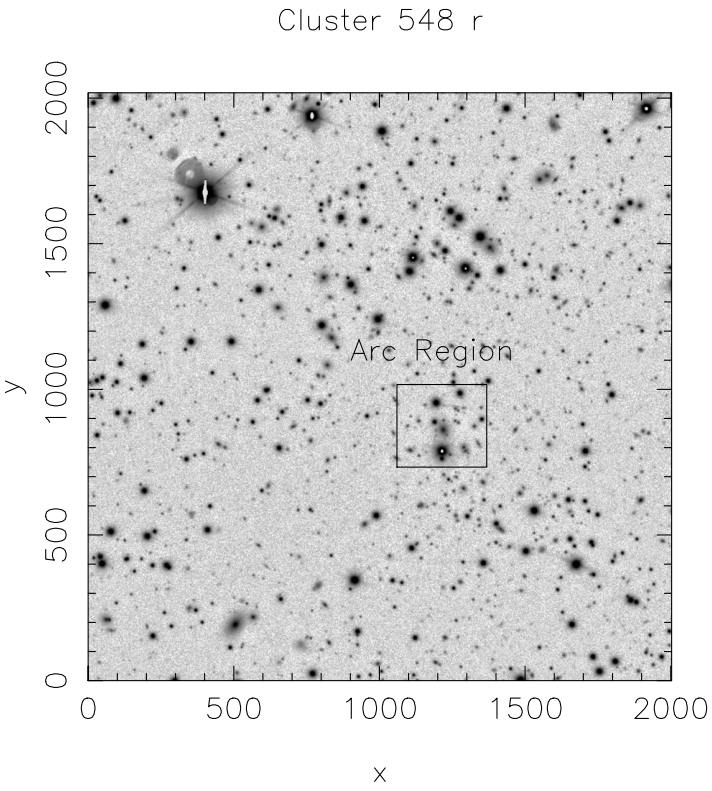


FIGURE D.9: PSZ1 G156.88+13.48

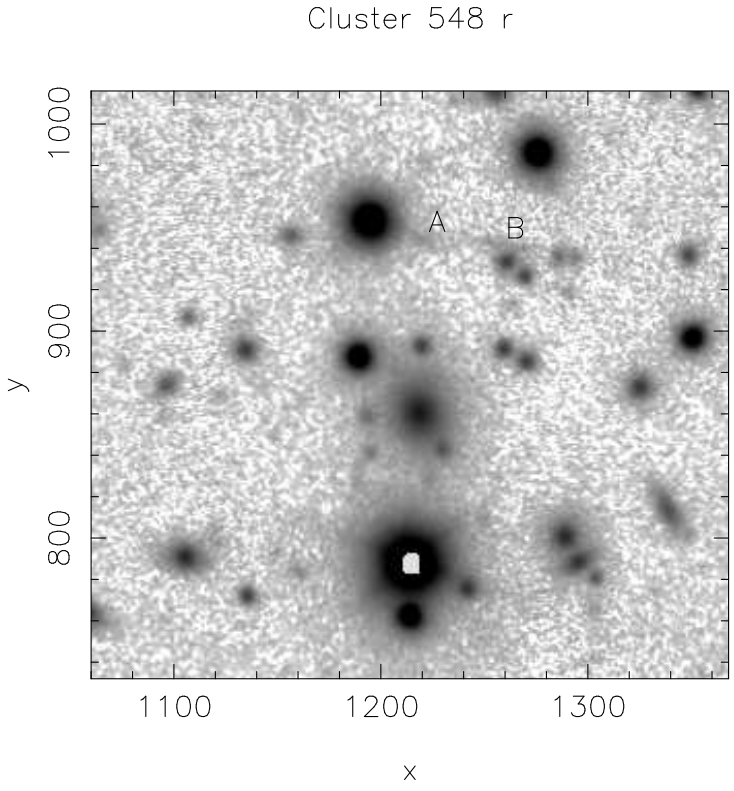


FIGURE D.10: PSZ1 G156.88+13.48 Two tangential arc segments relative to cluster center

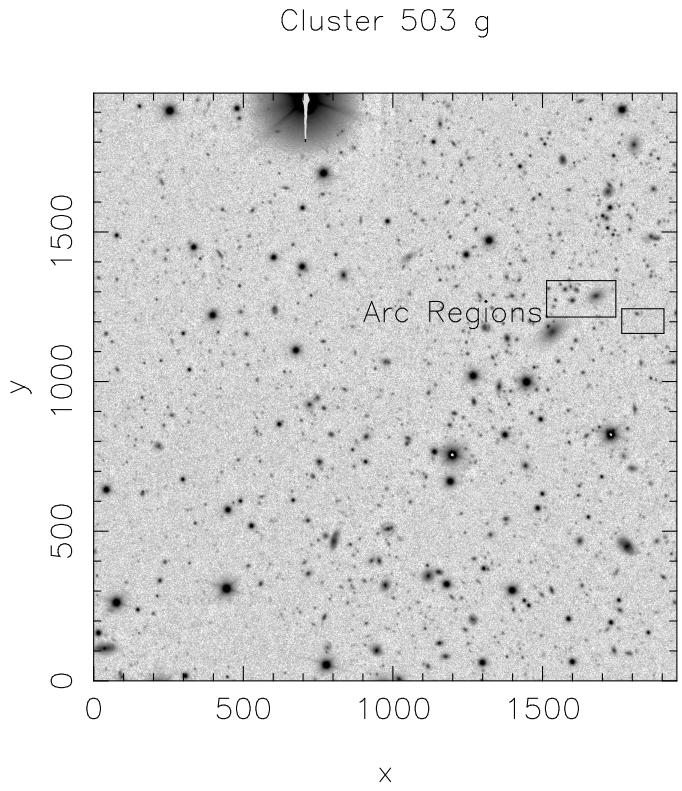


FIGURE D.11: PSZ1 G139.61+24.20

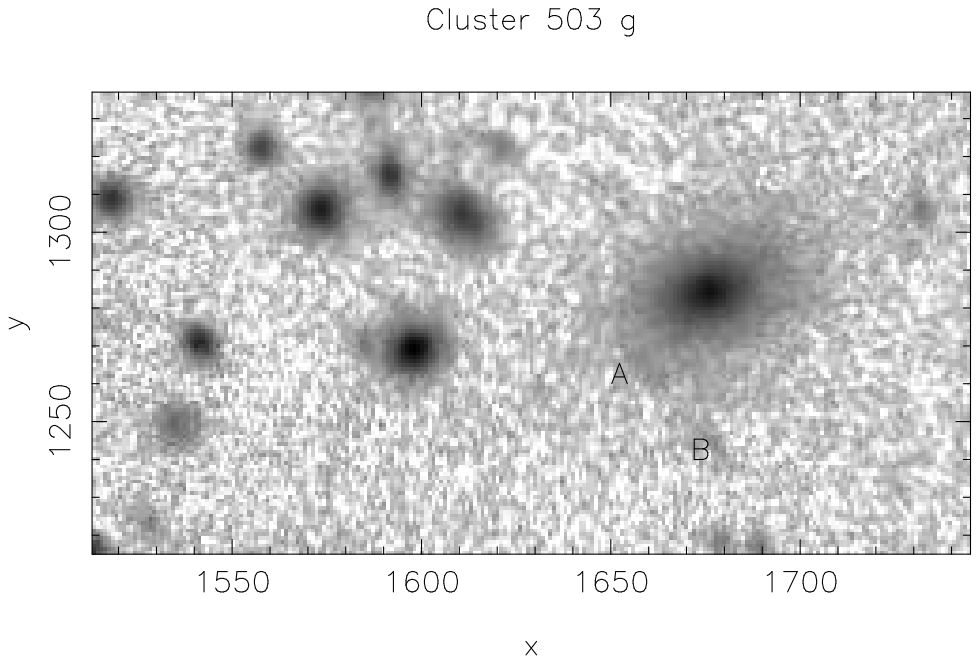


FIGURE D.12: PSZ1 G139.61+24.20 Two tangential arcs

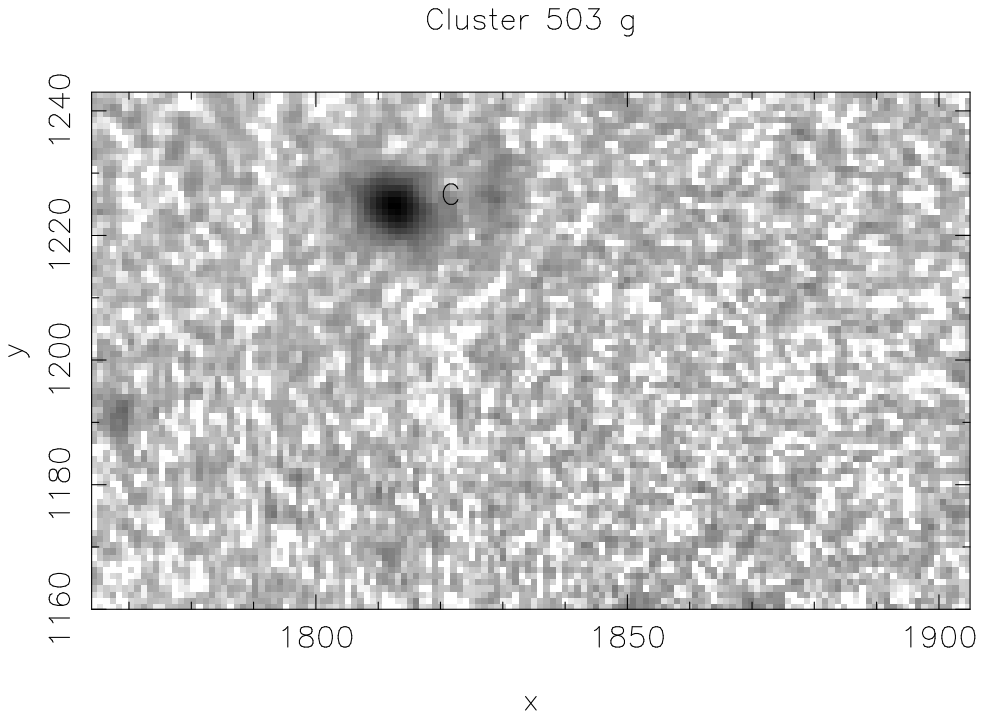


FIGURE D.13: PSZ1 G139.61+24.20 Tangential arc C different lensing center from BCG

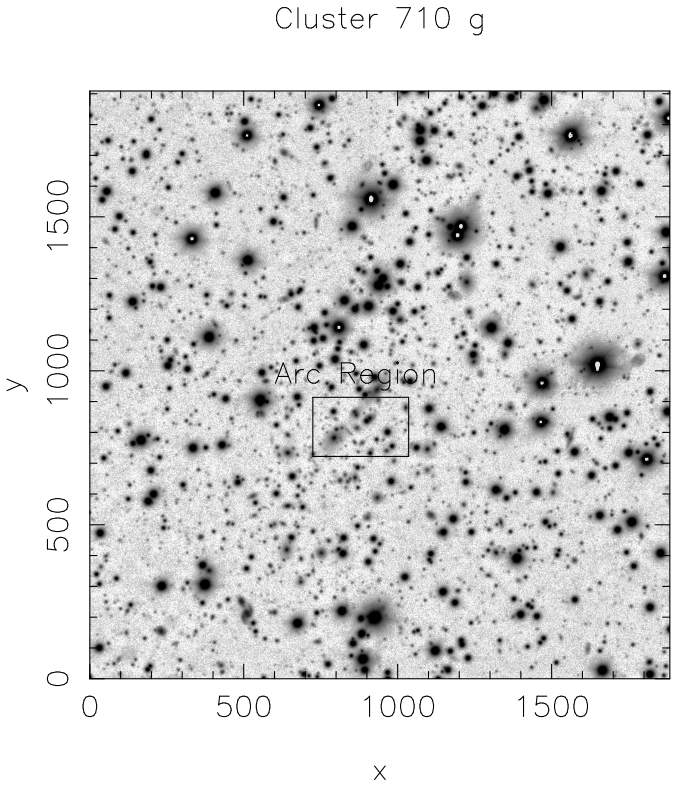


FIGURE D.14: PSZ1 G215.51+06.58 or RXJ0719.5+0043

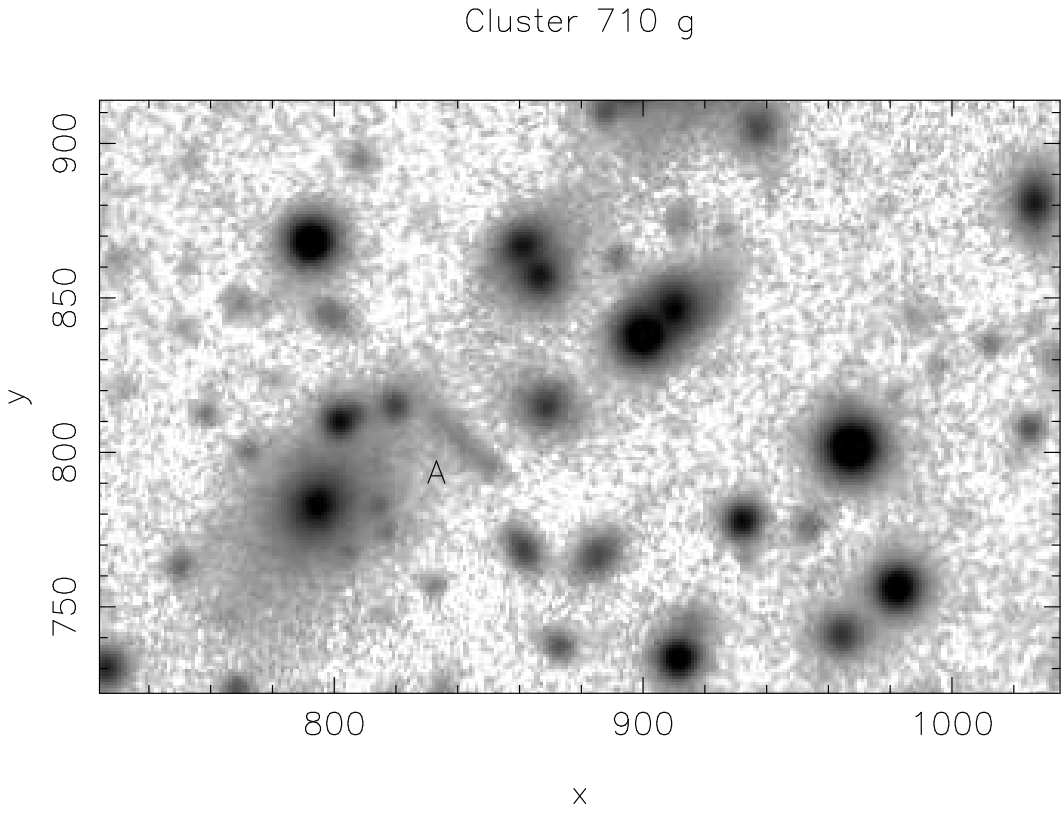


FIGURE D.15: PSZ1 G215.51+06.58 One tangential arc 12 arcseconds from BCG

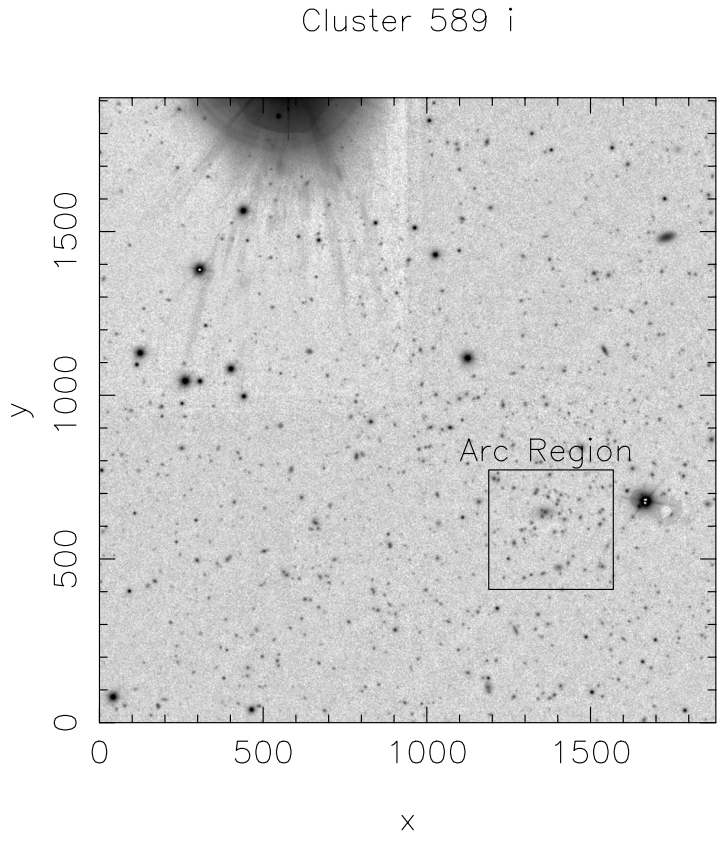


FIGURE D.16: PSZ1 G171.01+39.44

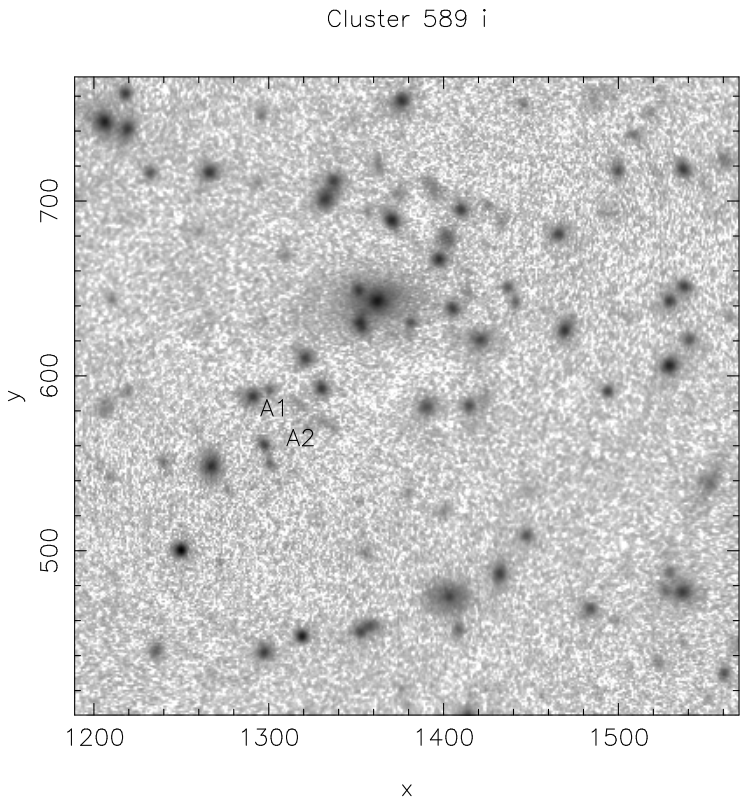


FIGURE D.17: PSZ1 G171.01+39.44 Two tangential arc segments 16 arcseconds from BCG

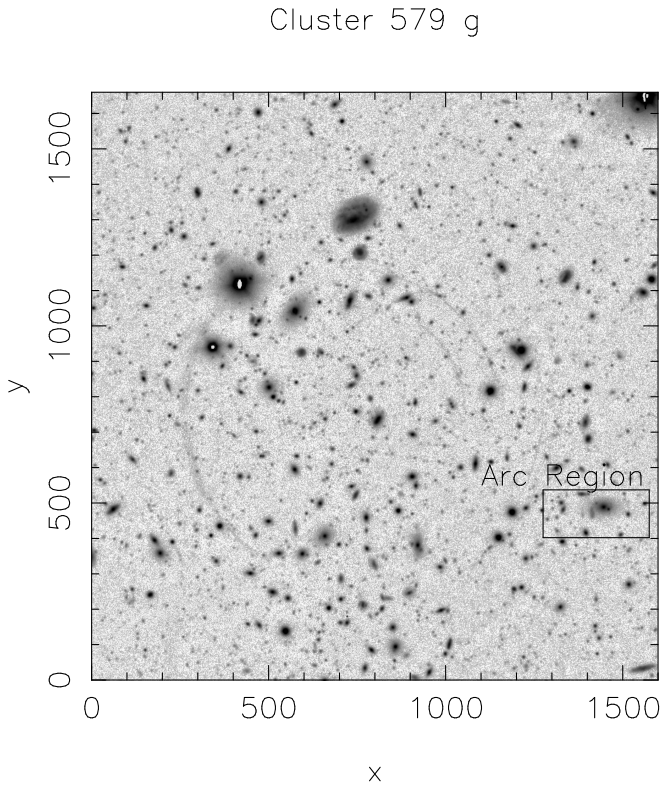


FIGURE D.18: PSZ1 G166.61+42.12 or RXJ0909.3+5133

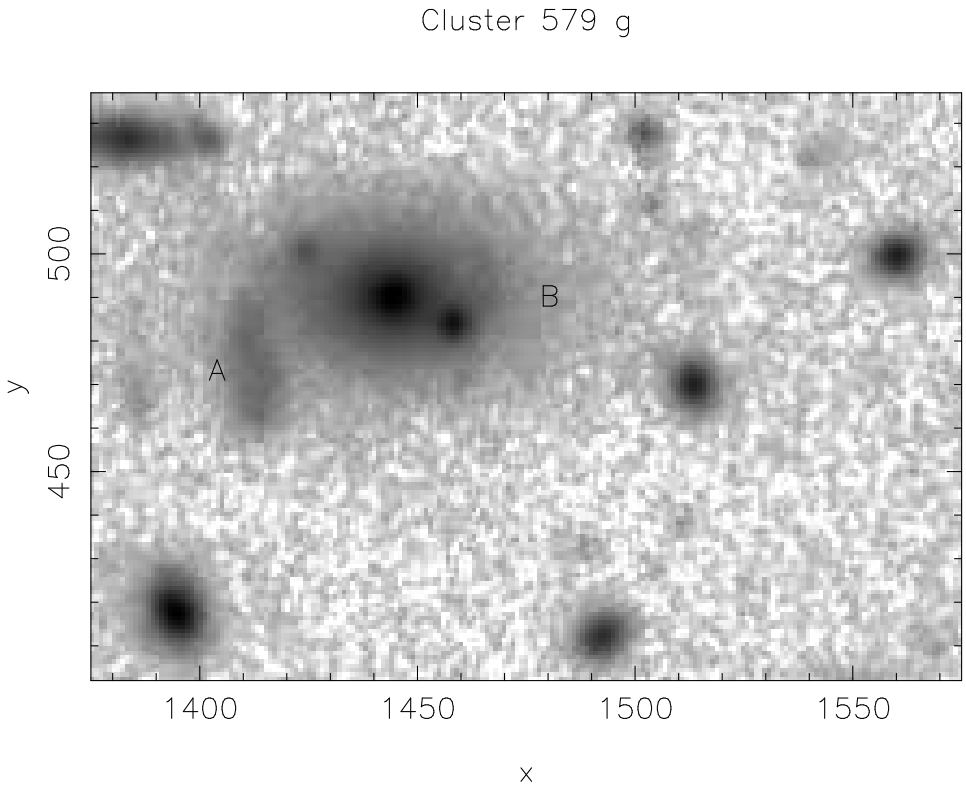


FIGURE D.19: PSZ1 G166.61+41.12 Two tangential arcs located close to BCG

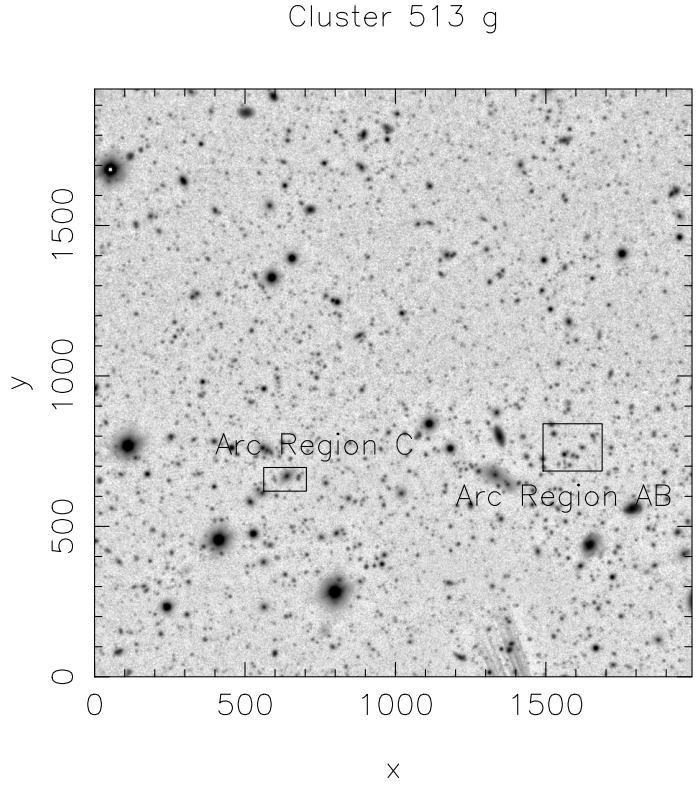


FIGURE D.20: PSZ1 G143.28+65.22 or RXJ1159.2+4947

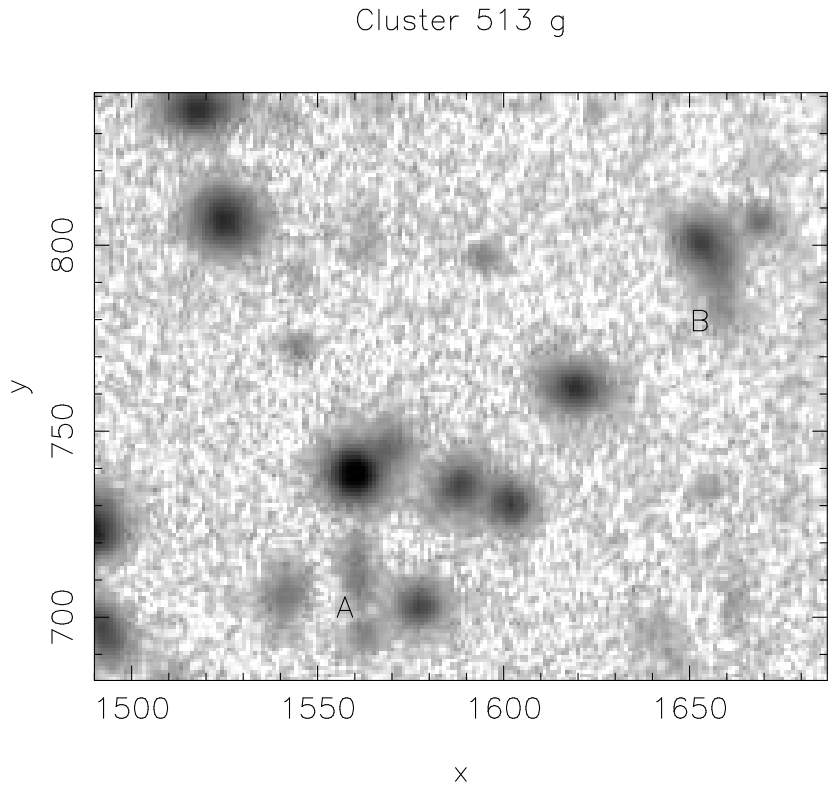


FIGURE D.21: PSZ1 G143.28+65.22 One radial arc from a cluster galaxy and a tangential arc relative to the cluster mass center

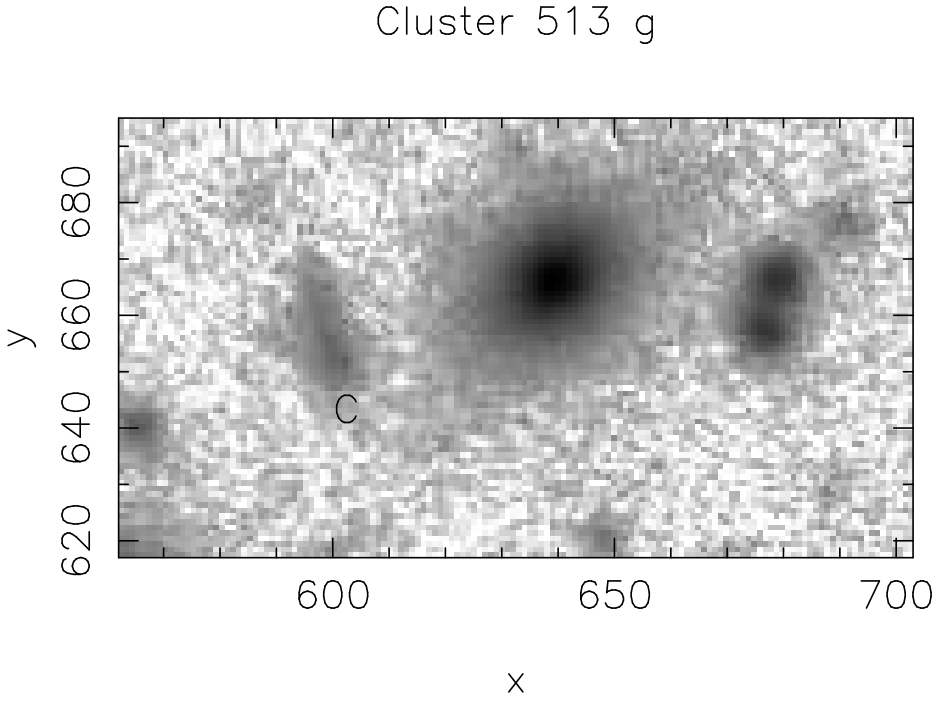


FIGURE D.22: PSZ1 G143.28+65.22 One tangential arc near a different lensing galaxy in the cluster from the BCG

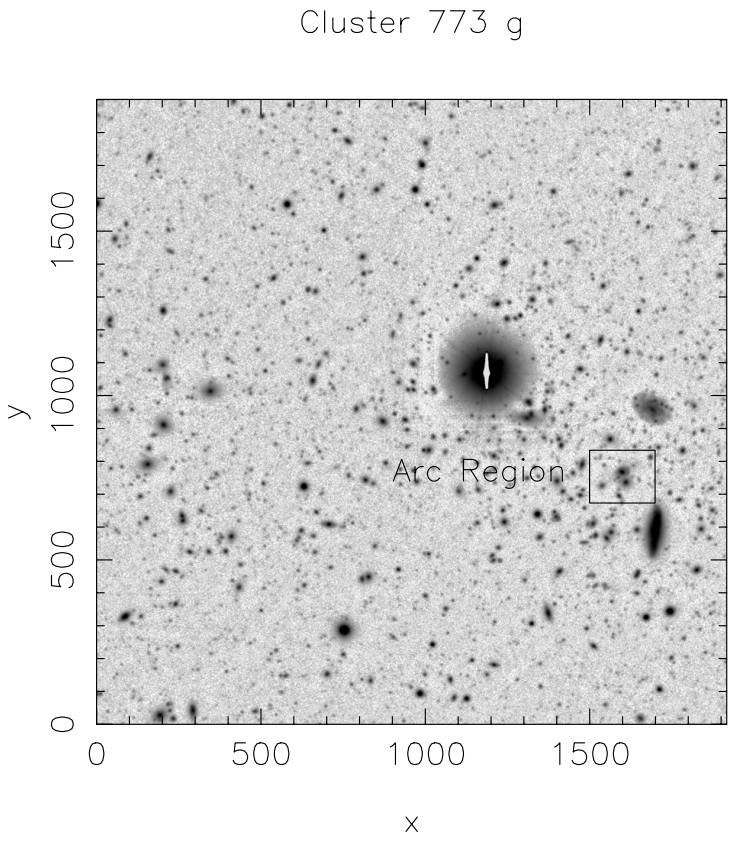


FIGURE D.23: PSZ1 G229.70+7797 or RXJ1201.3+2306

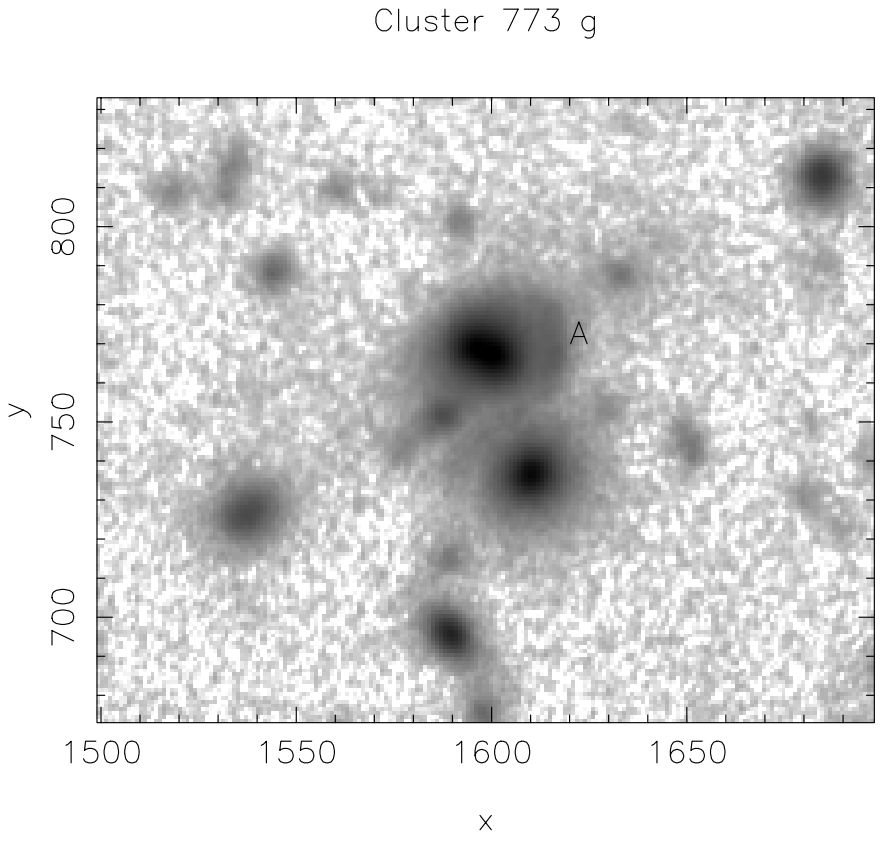


FIGURE D.24: PSZ1 G229.70+7797 One tangential arc located very close to other lens center than BCG

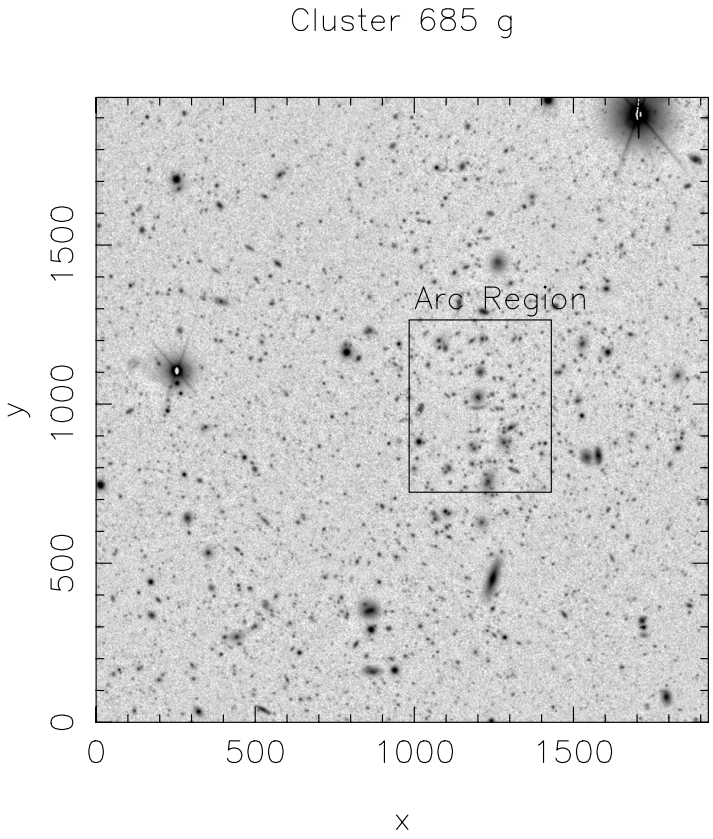


FIGURE D.25: PSZ1 G207.87+81.31 or RXJ1212.3+2733

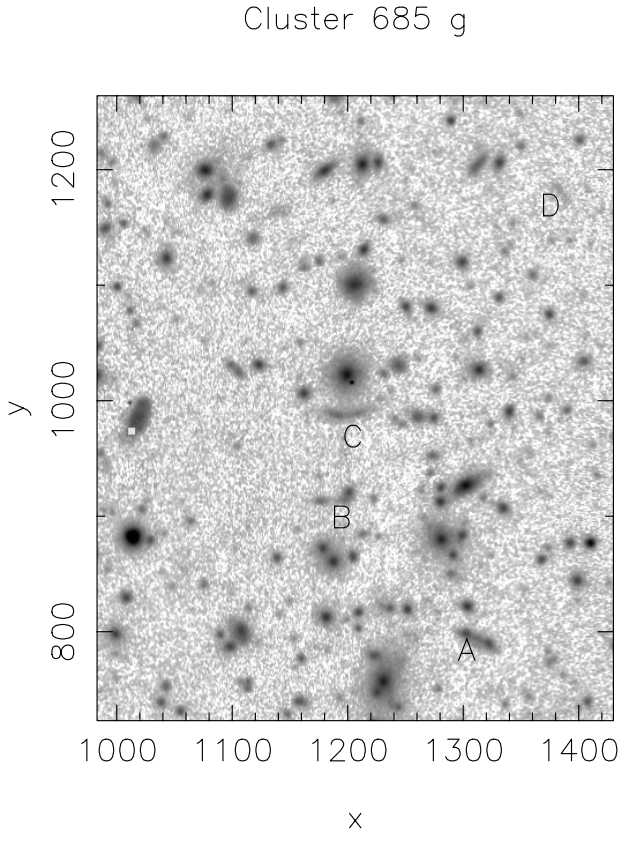


FIGURE D.26: PSZ1 G207.87+81.31 Four tangential arcs around a common center

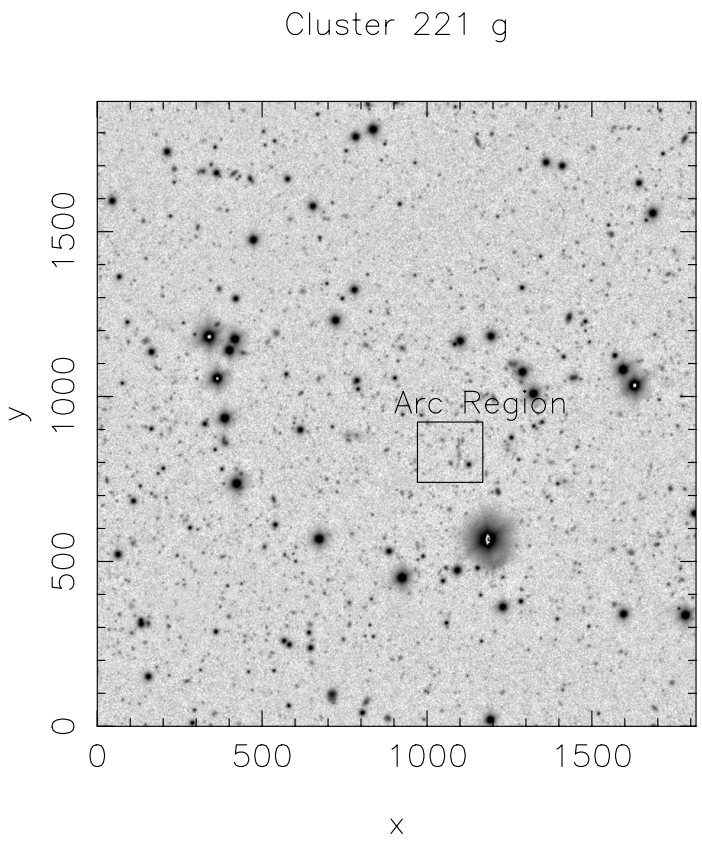


FIGURE D.27: PSZ1 G066.41+27.03 or WHL J269.219+40.1353

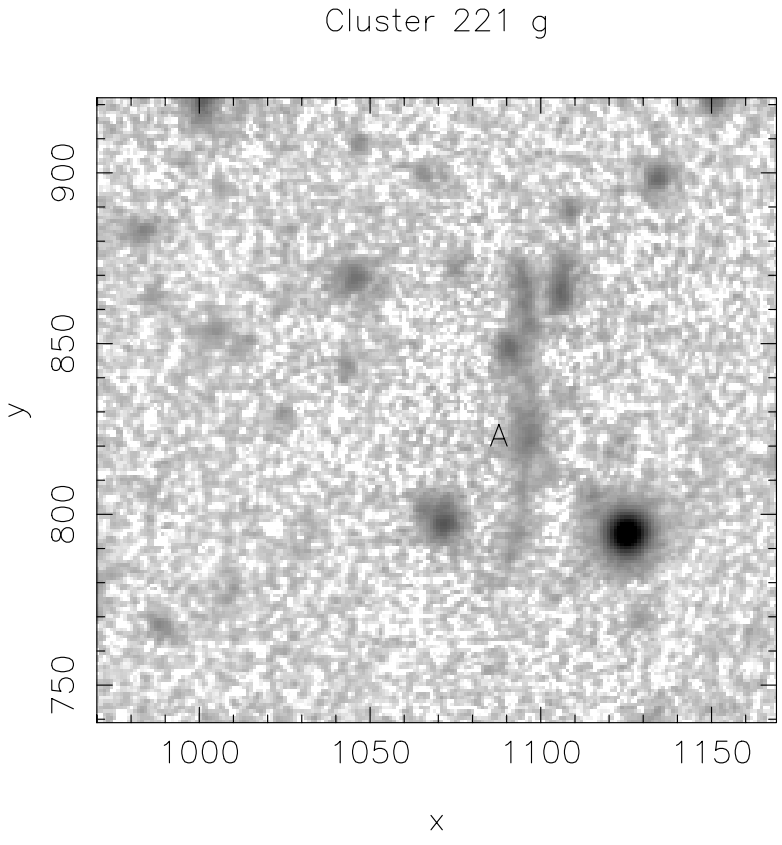


FIGURE D.28: PSZ1 G066.41+27.03 One long tangential arc located 9 arcseconds from the BCG

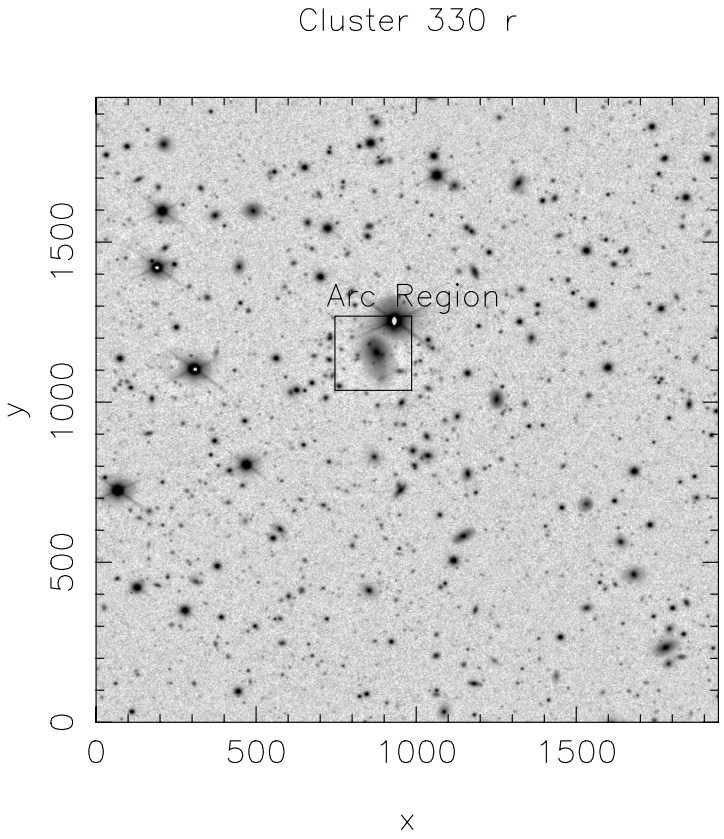


FIGURE D.29: PSZ1 G094.69+26.34 or RXJ1832.5+6449

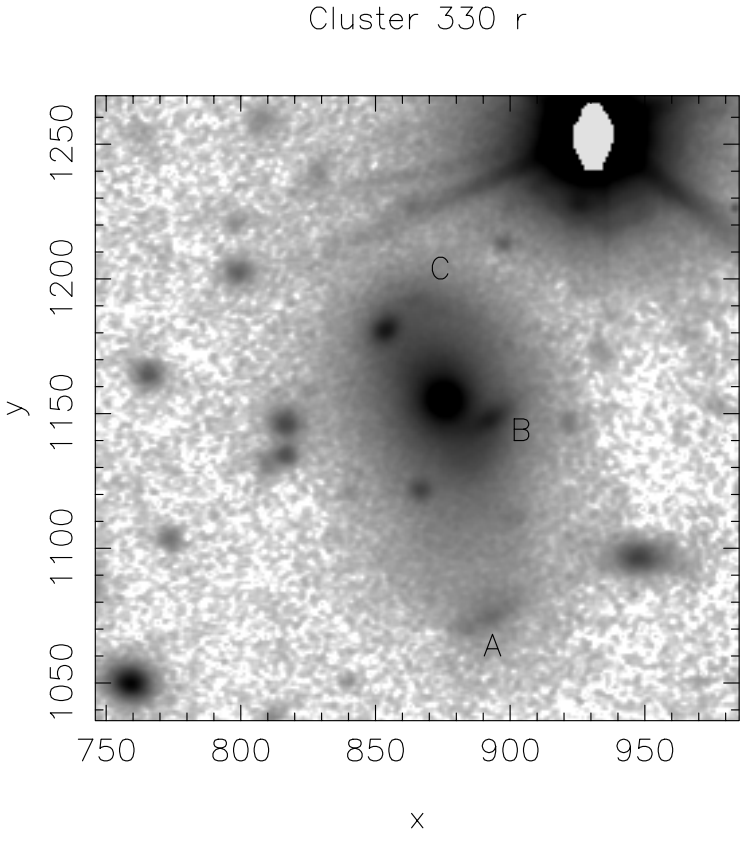


FIGURE D.30: PSZ1 G094.69+26.34 Three tangential arcs located close to the BCG

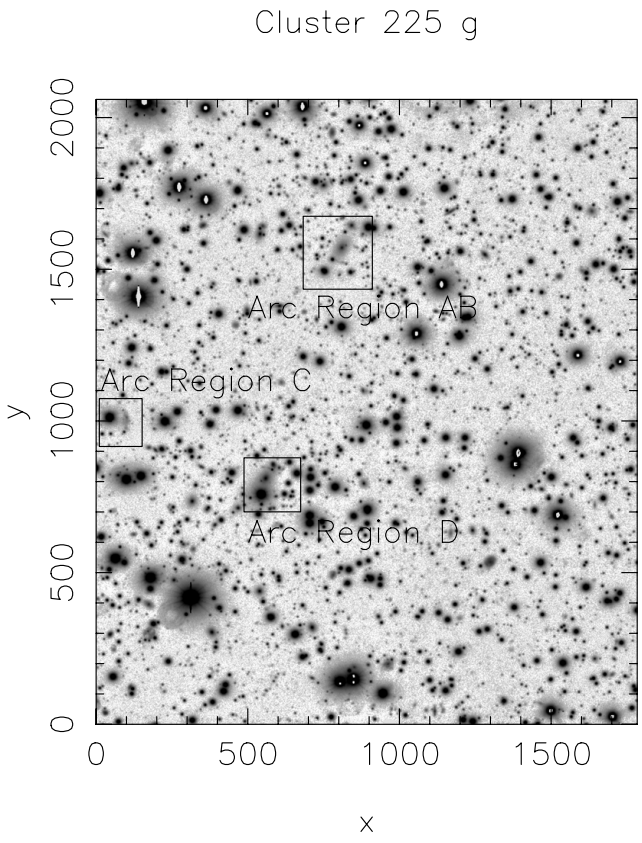


FIGURE D.31: PSZ1 G067.36+10.74 or RXJ1916.1+3525

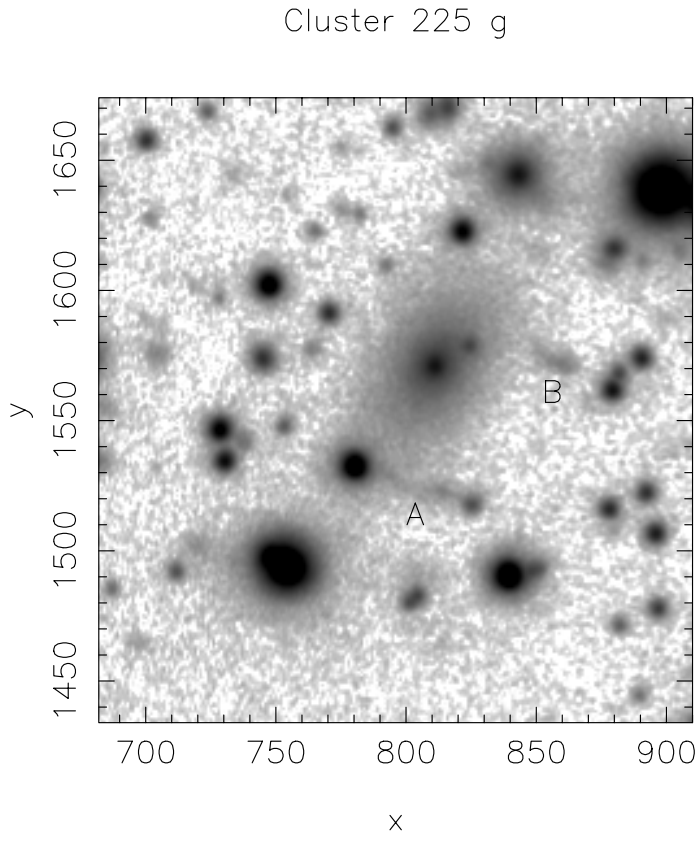


FIGURE D.32: PSZ1 G067.36+10.74 Two tangential arcs oriented similarly to the BCG

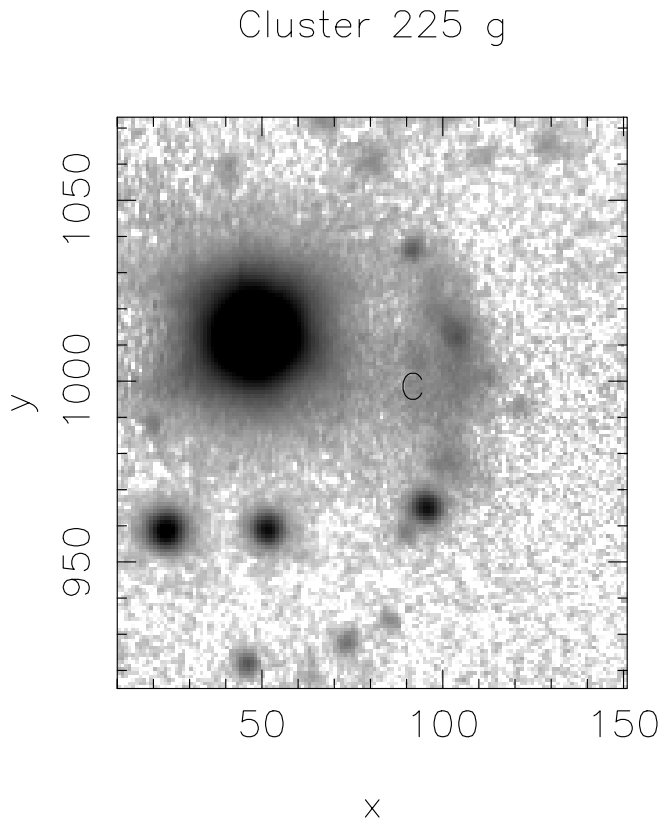


FIGURE D.33: PSZ1 G067.36+10.74 One tangential arc close to another center in the cluster

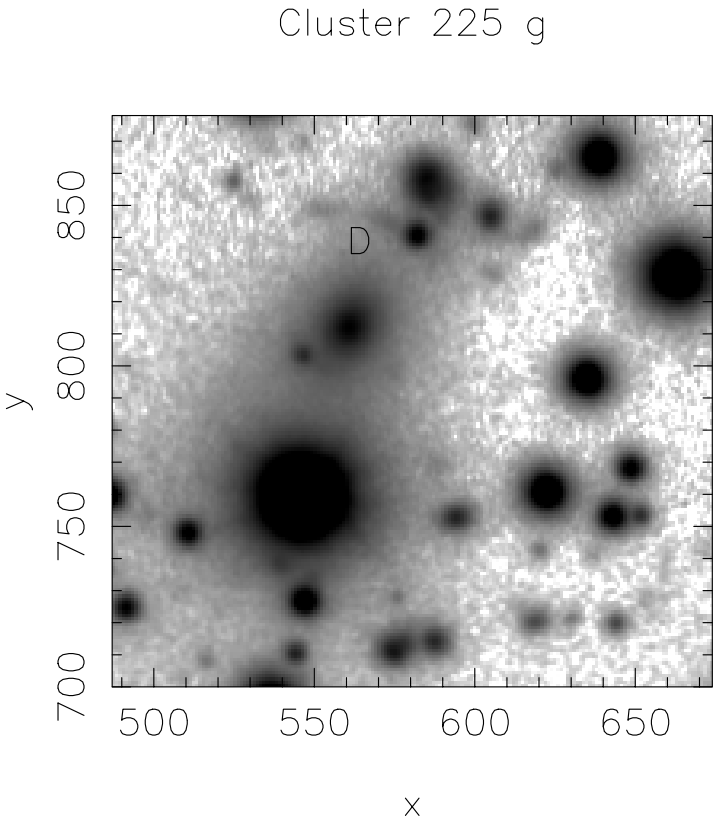


FIGURE D.34: PSZ1 G067.36+10.74 Another tangential arc lensed by the cluster's second center

# Appendix E

# Images of Subaru Strong Lenses and Cluster Centers

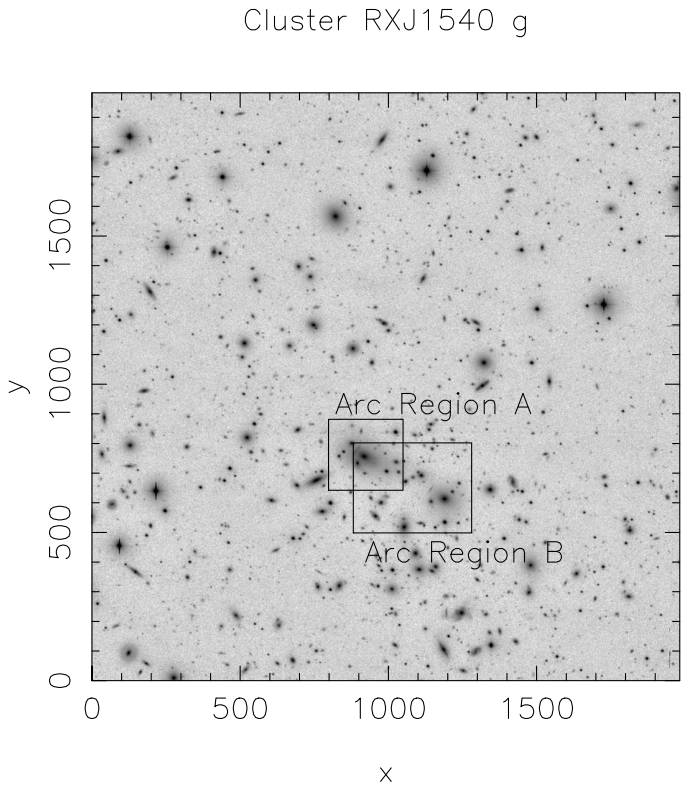


FIGURE E.1: PSZ1 G002.80-39.24 or RXJ 1540.1-0318

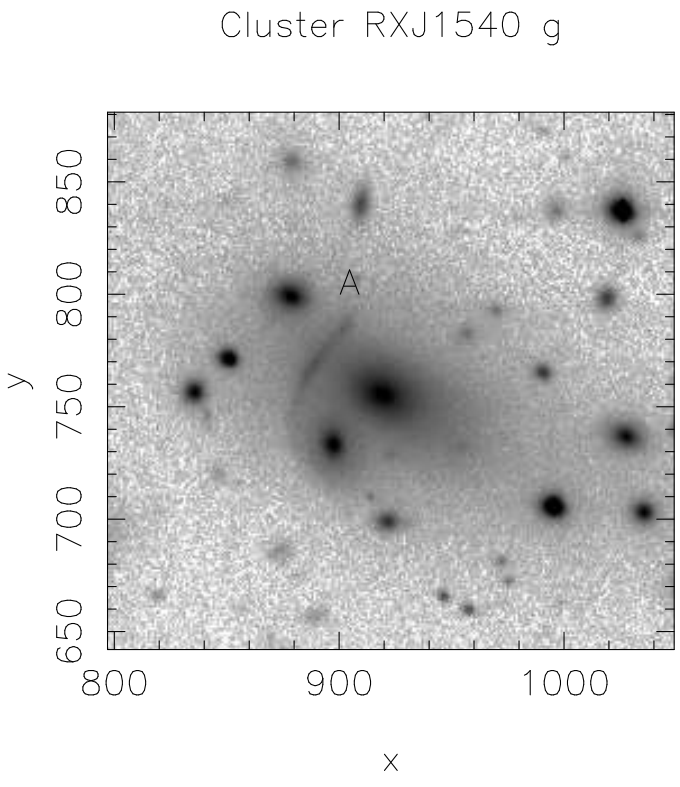


FIGURE E.2: PSZ1 G002.80-39.24 Long tangential arc near BCG

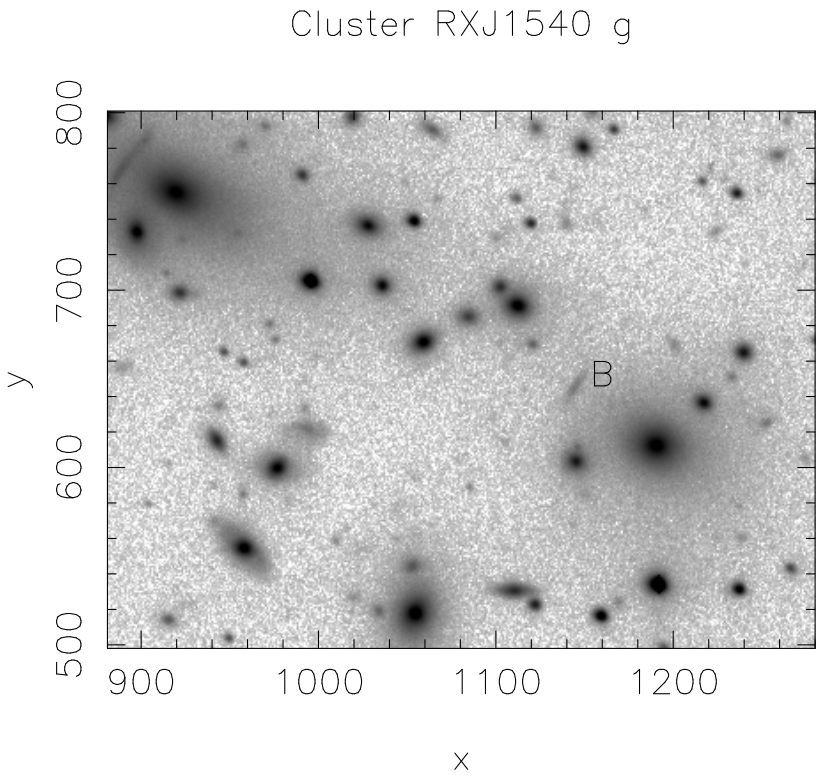


FIGURE E.3: PSZ1 G002.80-39.24. Short tangential arc near separate lensing galaxy.

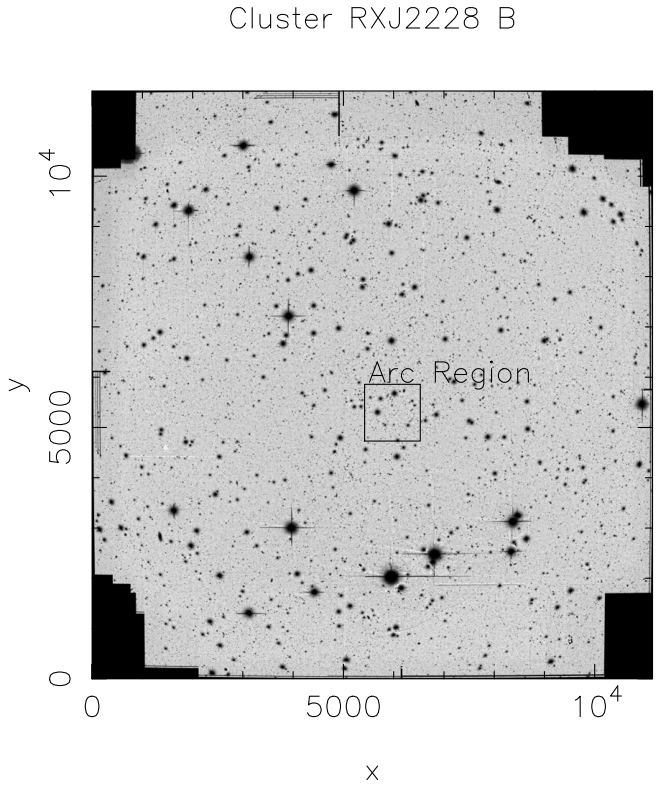


FIGURE E.4: PSZ1 G083.83-31.01 or RXJ 2228.6+2036.

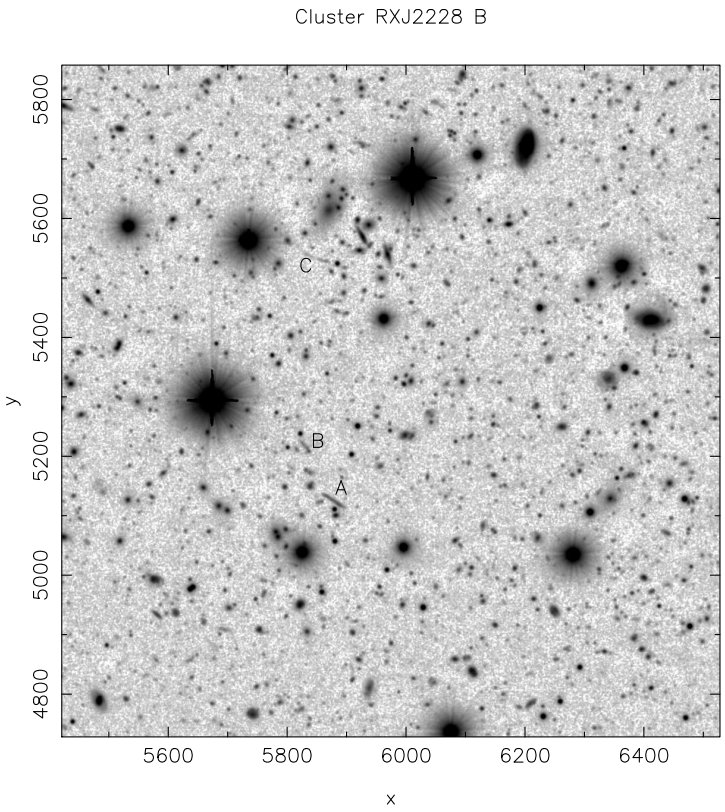


FIGURE E.5: PSZ1 G083.83-31.01 3 tangential arcs

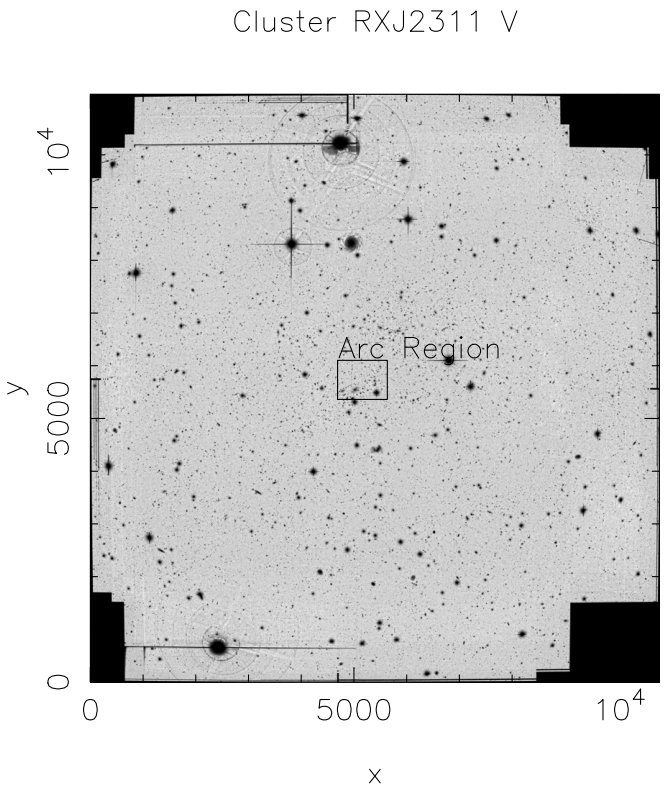


FIGURE E.6: PSZ1 G081.01-50.92 or RXJ 2311.5+0338.

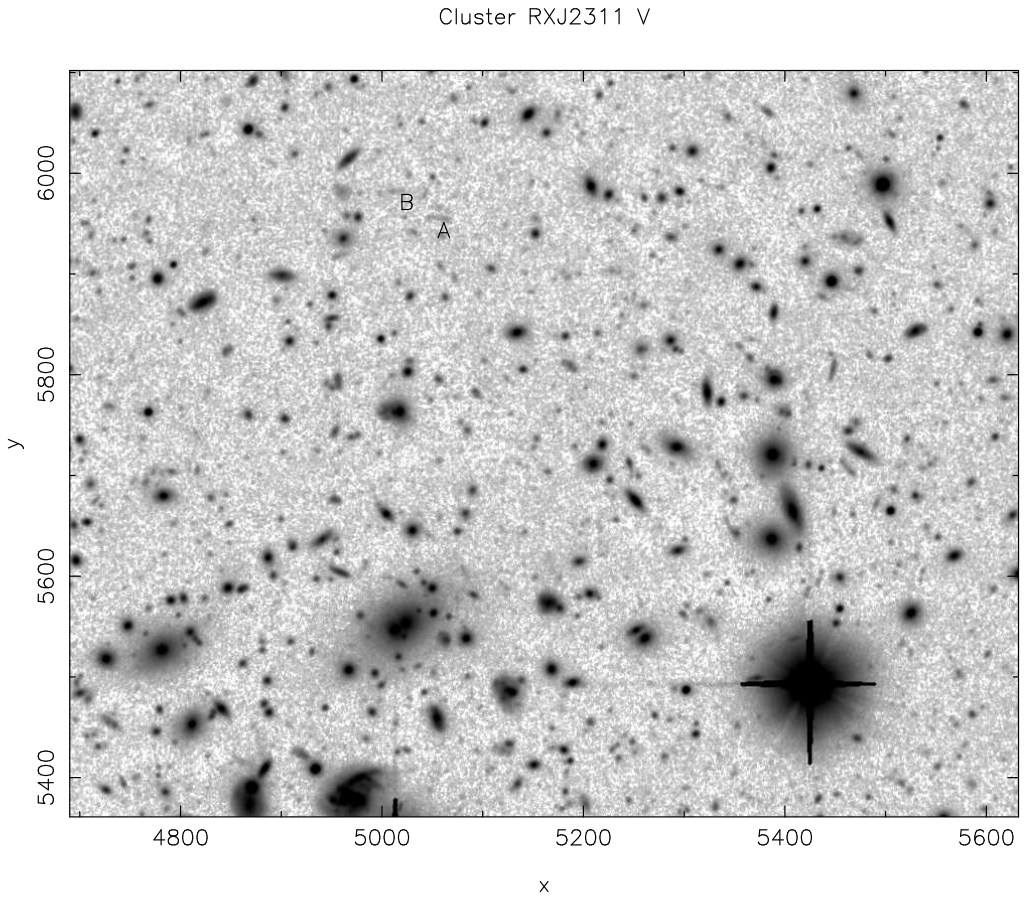


FIGURE E.7: PSZ1 G081.01-50.92 two faint tangential arcs

# Appendix F

# PSF Giant Arc Flux Extraction Algorithm Outline

```
method for extracting flux from arc segments
find a range of x values that contain the segment
1) for each x value in the cropped image find the max
pixel value for y and that defines the center of the arc
2) set each max pixel value = 1 and all others 0 to
define the arc line. Call this image A
3) find a nearby star and develop a psf_gaussian
with a FWHM=1 arcsecond. Need to convert
arcseconds to pixel resolution .24"/pixel. focal
length/ccd(spatial resolution)
4) make a new image that is 12" x 12" with a pixel
value of 1 at the center and 0 everywhere else.
Call this image B
5) convolve both A and B with the PSF. Store images
 A and B separately. Will want to use A and overlap
 the contour.
6) In image B, go to a diameter of 2*FWHM (radius of 1")
and get the pixel value=p_rad. Gaussian is symmetric
so all pixel values along circle are equal.
6b) For each x value in the convolved image A, we can
store the contour lines as an array by finding the pixel
(x,y) where pixel = p_rad. start at pixel on line center
(unconvolved image A)
 , progress up in y or down in y. iterate over increasing
 (decreasing) y until you find when pixel < p_rad. define
  x,y-1 as the contour point.
7) define a mask to make the contour for image A.
Mask(pixels > p_rad = 1) all else = 0.
8) Multiply original cropped image x Mask, which will
then show only the arc segment with pixels > p_rad
9) Go back to image B and find the pixel value at
radius = 6", which will be the value at [x,y] = [6",0]
 or anywhere else along the cirlce.
10) The sum of the pixels within the p_rad circle will
be the flux = Flux_aperture. The sum of the pixels
within the 6" radius will be the total flux = F_tot.
11) F_ap / F_tot = .97 or similar. Divide the total
flux of the masked original image by this number
to approximate the total flux from the arc segment.
12) output: postage stamp with the arc segment
and the corresponding mask and contour. Show
```

```
original line segment with contour overlaid. Record
the total flux for each arc segment.
13) convert the flux value from digital to analog to
compare with other flux magnitudes
crop the fits image to just the area of interest.
Use R band images as the mask for all other bands.
```

# Appendix G

# PSZ1 Derived Lensing Analysis Set All Cluster Candidates

TABLE G.1: Entire LAS including unobserved clusters

| Has Lens | Source ID | PSZ Name | RA | DEC | SNR | M500 | SZ redshift | NOT MOSCA | ID NOT | NOT ALFOSC ID | ALFOSC z | SUP Data | HST Archive | CFHT | Detector-SOURCE |
|---|---|---|---|---|---|---|---|---|---|---|---|---|---|---|---|
| | 315 | PSZ1 G092.10-66.02 | 00 03 05.5 | -06 05 26 | 6.57 | 6.01 | 0.232 | | | | | yes | no | | W-S-I+, W-J-V |
| | 397 | PSZ1 G108.90-52.04 | 00 16 37.6 | +09 52 50 | 6.89 | | | | | | | no | no | | |
| 1 | 408 | PSZ1 G111.60-45.72 | 00 18 34.6 | +16 25 34 | 6.54 | 8.675 | 0.5456 | | | | | - | yes | | WFPC2 |
| 1 | 391 | PSZ1 G107.66-58.31 | 00 19 35.0 | +03 36 37 | 6.49 | 6.354 | 0.267 | yes | 391 | | | no | no | | g,r,i filters |
| | 454 | PSZ1 G124.20-36.47 | 00 55 59.5 | +26 23 20 | 9.18 | 7.205 | 0.1971 | | | | | - | no | | NICMOS, PC, WFPC2 |
| 1 | 558 | PSZ1 G159.81-73.47 | 01 31 53.4 | -13 34 27 | 12.21 | 8.172 | 0.206 | | | | | - | yes | | ACS-WFC |
| | 546 | PSZ1 G155.25-68.42 | 01 37 18.7 | -08 28 42 | 6.43 | 9.05 | 0.566 | | | 463 | 0.567 | yes | no | | W-S-R+ |
| 1 | 475 | PSZ1 G132.49-17.29 | 01 42 55.5 | +44 37 25 | 8.33 | 8.259 | 0.341 | yes | 475 | | | no | no | | g,r,i filters |
| | 522 | PSZ1 G146.00-49.42 | 01 51 34.5 | +10 44 03 | 6.62 | 4.04 | 0.097 | yes | 522 | | | yes | no | | W-J-VR, W-S-R+ and NOT I-filter |
| | 501 | PSZ1 G138.60-10.85 | 02 27 01.5 | +49 04 54 | 8.26 | 9.26 | 0.702 | yes | 501 | | | no | no | | g,r,i filters |
| 1 | 596 | PSZ1 G172.97-53.54 | 02 39 52.3 | -01 33 23 | 6.15 | 7.626 | 0.373 | | | | | - | yes | | ACS-WFC |
| 1 | 602 | PSZ1 G176.25-52.57 | 02 48 13.1 | -02 14 21 | 6.93 | 6.375 | 0.236 | yes | 602 | | | - | no | | PC, WFPC2 and NOT g,r,i filters |
| | 550 | PSZ1 G157.32-26.77 | 03 09 00.0 | +26 45 30 | 8.24 | 10.026 | 0.356 | | | 201 | 0.402 | - | yes | | PC, WFPC2, ACS-WFC |
| | 580 | PSZ1 G167.43-38.04 | 03 09 16.4 | +12 38 39 | 6.11 | | | | | | | no | no | | |
| | 591 | PSZ1 G171.96-40.64 | 03 13 00.3 | +08 22 53 | 12.7 | 11.127 | 0.27 | | | | | no | no | | |
| | 564 | PSZ1 G162.30-26.92 | 03 24 26.5 | +24 00 45 | 6.56 | | | | | | | no | no | | |
| | 641 | PSZ1 G189.82-37.25 | 03 59 41.0 | +00 06 31 | 6.99 | | | | | | | no | no | | |
| | 624 | PSZ1 G185.42-32.03 | 04 07 57.2 | +06 07 00 | 6.15 | | | | | | | no | no | | |
| 1 | 681 | PSZ1 G205.94-39.46 | 04 17 36.2 | -11 54 12 | 11.43 | 11.7 | 0.443 | | | | | - | yes | | PC, WFPC2, WFC3-UVIS |
| 1 | 688 | PSZ1 G208.80-30.67 | 04 54 05.0 | -10 13 35 | 7.07 | 6.904 | 0.2475 | | | | | - | yes | | PC, WFPC2 |
| 1 | 655 | PSZ1 G195.78-24.29 | 04 54 15.9 | +02 57 10 | 8.4 | 7.059 | 0.203 | | | | | - | yes | | |
| 1 | 686 | PSZ1 G208.59-26.00 | 05 10 44.3 | -08 01 12 | 7.9 | 7.363 | 0.2195 | yes | 686 | | | no | no | | g,r,i filters |
| | 684 | PSZ1 G206.64-21.17 | 05 24 48.9 | -04 14 07 | 6.62 | | | | | | | no | no | | |
| 1 | 548 | PSZ1 G156.88+13.48 | 05 45 41.3 | +55 30 40 | 6.19 | | | yes | 548 | 492 | 0.227 | no | no | | g,r,i filters |
| 1 | 588 | PSZ1 G170.22+09.74 | 06 03 21.5 | +42 13 56 | 14.38 | 11.117 | 0.228 | | | 29 | 0.228 | - | yes | | WFC3-UVIS, ACS-WFC |
| 1 | 503 | PSZ1 G139.61+24.20 | 06 22 13.9 | +74 41 39 | 7.94 | 7.094 | 0.267 | yes | 503 | | | no | no | | g,r,i filters |
| | 746 | PSZ1 G224.01-11.14 | 06 31 00.7 | -14 50 06 | 6.13 | 9.085 | 0.62 | | | 505 | 0.559 | no | no | | ALFOSC SPECTROSCOPY |
| | 529 | PSZ1 G148.20+23.49 | 06 37 45.6 | +66 54 24 | 8.4 | 4.393 | 0.11 | yes | 529 | | | no | no | | g,r,i filters |
| | 582 | PSZ1 G167.64+17.63 | 06 38 02.7 | +47 48 33 | 9.71 | 6.518 | 0.174 | yes | 582 | | | no | no | | g,r,i filters |
| 1 | 608 | PSZ1 G180.25+21.03 | 07 17 28.1 | +37 44 36 | 9.88 | 11.238 | 0.546 | | | | | - | yes | | ACS-WFC |
| 1 | 710 | PSZ1 G215.51+06.58 | 07 19 34.4 | +00 42 58 | 8.03 | 7.309 | 0.2197 | yes | 710 | | | no | no | | g,r,i filters |
| 1 | 632 | PSZ1 G187.53+21.92 | 07 32 15.6 | +31 37 34 | 6.05 | 4.867 | 0.171 | | | | | - | yes | | WF3, WF3-FIX |
| | 720 | PSZ1 G217.40+10.88 | 07 38 17.7 | +01 01 37 | 6.26 | 5.355 | 0.189 | yes | 720 | | | no | no | | I-filter |
| | 551 | PSZ1 G157.44+30.34 | 07 49 00.1 | +59 40 50 | 7.54 | 8.621 | 0.45 | yes | 551 | | | no | no | | g,r,i filters |
| 1 | 623 | PSZ1 G184.70+28.92 | 08 01 01.7 | +36 05 06 | 6.06 | 5.851 | 0.288 | | | | | - | yes | | ACS-WFC |
| | 732 | PSZ1 G220.13+22.93 | 08 25 53.1 | +04 17 52 | 6.16 | 5.044 | 0.2248 | | | | | - | no | | PC, WFPC2 |
| | 533 | PSZ1 G149.75+34.68 | 08 30 50.9 | +65 52 01 | 13.74 | 8.233 | 0.1818 | | | | | - | no | | PC |
| | 542 | PSZ1 G153.41+36.58 | 08 42 40.0 | +62 34 31 | 6.85 | | 0.65 | | | | | no | no | | |
| 1 | 628 | PSZ1 G186.37+37.26 | 08 42 59.6 | +36 21 10 | 15.86 | 11.481 | 0.282 | | | | | - | yes | | PC, WFPC2, ACS-HRC, STIS-CCD |
| 1 | 631 | PSZ1 G186.98+38.66 | 08 50 10.3 | +36 04 47 | 6.58 | 7.396 | 0.378 | | | | | - | yes | | PC, WFPC2 |
| 1 | 589 | PSZ1 G171.01+39.44 | 08 50 59.6 | +48 29 29 | 6.68 | 8.6 | 0.553615 | yes | 589 | 465 | 0.553 | no | no | | g,r,i filters |
| 1 | 726 | PSZ1 G218.83+35.49 | 09 09 06.9 | +10 57 45 | 7.94 | 5.535 | 0.1751 | | | | | - | yes | | PC, WFPC2 |
| 1 | 579 | PSZ1 G166.61+42.12 | 09 09 34.1 | +51 33 28 | 6.46 | 5.564 | 0.23225 | yes | 579 | | | - | no | | STIS-CCD and NOT g,r,i filters |
| 1 | 578 | PSZ1 G166.11+43.40 | 09 18 04.5 | +51 42 15 | 10.38 | 7.082 | 0.2172 | | | | | - | yes | | PC, WFPCS, WFC3-IR, ACS-WFC, STIS-CCD |
| | 654 | PSZ1 G195.60+44.03 | 09 20 16.0 | +30 29 56 | 7 | 6.355 | 0.2952 | | | | | - | no | | ACS-WFC |

TABLE G.1: Entire LAS including unobserved clusters

| Has Lens | Source ID | PSZ Name | RA | DEC | SNR | M500 | SZ redshift | NOT MOSCA | ID NOT | NOT ALFOSC ID | ALFOSC z | SUP Data | HST Archive | CFHT | Detector-SOURCE |
|---|---|---|---|---|---|---|---|---|---|---|---|---|---|---|---|
| 1 | 829 | PSZ1 G244.67+32.47 | 09 45 21.7 | -08 38 19 | 7.88 | 5.095 | 0.1535 | | | | | - | yes | | PC, WFPCS2, STIS-CCD, |
| 1 | 485 | PSZ1 G135.03+36.03 | 09 47 00.2 | +76 23 44 | 6.15 | 6.271 | 0.345 | | | | | - | yes | | ACS-WFC, WFC3-IR |
| 1 | 715 | PSZ1 G216.60+47.00 | 09 49 48.5 | +17 08 19 | 8.18 | 8.22 | 0.3826 | | | | | - | yes | | ACS-WFC-HRC |
| | 827 | PSZ1 G244.48+34.06 | 09 49 51.8 | -07 29 28 | 8.14 | | | yes | 827 | | | no | no | | g,r,i filters |
| | 847 | PSZ1 G249.38+33.27 | 09 58 24.6 | -11 03 59 | 6.97 | 5.184 | 0.1669 | | | | | yes | no | | W-J-V, W-J-B.. |
| | 647 | PSZ1 G192.19+56.12 | 10 16 21.8 | +33 39 28 | 6.84 | 3.649 | 0.124 | | | | | no | no | yes | r.MP9601 and g.MP9401 filters. |
| 1 | 617 | PSZ1 G182.55+55.83 | 10 17 03.0 | +39 02 58 | 7.96 | 5.736 | 0.206 | | | | | - | yes | | PC, WFPC2 |
| | 567 | PSZ1 G163.69+53.52 | 10 22 23.4 | +50 07 11 | 8.71 | 4.935 | 0.158 | | | | | - | no | | PC, WFPC2, STIS-CCD |
| | 572 | PSZ1 G165.06+54.13 | 10 23 45.7 | +49 07 58 | 8.76 | 4.633 | 0.144 | | | | | - | no | | PC, WFPC2, ACS-SBC |
| 1 | 535 | PSZ1 G150.56+58.32 | 11 15 10.8 | +53 19 39 | 7.76 | 7.962 | 0.47 | | | | | - | yes | | ACS-WFC-, WFC3-IR |
| 1 | 502 | PSZ1 G139.17+56.37 | 11 42 24.5 | +58 31 41 | 8.68 | 7.142 | 0.322 | | | | | - | yes | | ACS-WFC |
| 1 | 765 | PSZ1 G228.21+75.20 | 11 49 37.4 | +22 23 35 | 6.68 | 8.551 | 0.545 | | | | | - | yes | | ACS-WFC |
| | 971 | PSZ1 G280.21+47.83 | 11 49 53.8 | -12 18 24 | 8.31 | 5.406 | 0.1557 | | | | | yes | no | | W-S-I+, W-J-V |
| | 845 | PSZ1 G249.01+73.75 | 11 56 46.2 | +16 55 44 | 7.14 | | 0.156 | yes | 845 | | | no | no | | g,r,i filters |
| 1 | 610 | PSZ1 G180.56+76.66 | 11 57 19.9 | +33 36 39 | 7.87 | 6.087 | 0.2138 | | | | | - | yes | | ACS-WFC |
| 1 | 513 | PSZ1 G143.28+65.22 | 11 59 15.8 | +49 47 12 | 8.01 | 7.35 | 0.350117 | yes | 513 | | | no | no | | g,r,i filters. |
| 1 | 773 | PSZ1 G229.70+77.97 | 12 01 21.1 | +23 06 31 | 8.95 | 7.736 | 0.269 | yes | 773 | | | no | no | | g,r,i filters |
| 1 | 984 | PSZ1 G284.43+52.44 | 12 06 18.9 | -08 47 50 | 10 | 10.32 | 0.4414 | | | | | - | yes | | ACS-WFC |
| 1 | 685 | PSZ1 G207.87+81.31 | 12 12 21.3 | +27 33 18 | 6.81 | 7.128 | 0.353 | yes | 685 | | | no | no | | g,r,i filters |
| | 477 | PSZ1 G133.56+69.05 | 12 28 58.7 | +47 36 42 | 6.49 | 5.56 | 0.254 | | | | | yes | no | | W-S-G+, W-S-R+ |
| | 988 | PSZ1 G285.63+72.72 | 12 30 49.6 | +10 32 54 | 8.52 | 5.689 | 0.165 | | | | | - | no | | STIS-CCD |
| | 1014 | PSZ1 G289.19+72.19 | 12 34 31.8 | +09 46 23 | 6.99 | 6.036 | 0.229 | | | | | - | yes | | PC,WFPC2, STIS-ccd |
| 1 | 460 | PSZ1 G125.72+53.87 | 12 36 48.9 | +63 10 40 | 7.77 | 5.981 | 0.3019 | | | | | - | yes | | ACS-WFC, WFC3-IR |
| | 1122 | PSZ1 G318.61+83.80 | 12 58 36.5 | +21 09 03 | 6.93 | | | | | | | no | no | | |
| | 442 | PSZ1 G121.09+57.02 | 12 59 28.1 | +60 04 33 | 6.98 | 5.957 | 0.344 | | | | | no | no | | |
| | 277 | PSZ1 G083.62+85.08 | 13 05 55.7 | +30 52 53 | 6.63 | 5.304 | 0.1832 | | | | | yes | no | | W-J-V |
| 1 | 422 | PSZ1 G114.99+70.36 | 13 06 54.9 | +46 31 33 | 8.71 | 6.199 | 0.2259 | | | | | - | yes | | PC, WFPC2, STIS-CCD |
| 1 | 1105 | PSZ1 G313.33+61.13 | 13 11 26.5 | -01 20 11 | 13.06 | 8.856 | 0.1832 | | | | | - | yes | | WFPC2 |
| 1 | 417 | PSZ1 G114.29+64.91 | 13 15 04.6 | +51 48 48 | 7.37 | 5.92 | 0.2836 | | | | | - | yes | | ACS-WFC, NIC3, WFC3-IR |
| 1 | 228 | PSZ1 G068.32+81.81 | 13 22 48.0 | +31 39 06 | 6.97 | 6.633 | 0.3083 | | | | | - | yes | | WFPC2, PC |
| | 1130 | PSZ1 G323.30+63.65 | 13 27 00.7 | +02 12 14 | 7.22 | 7.051 | 0.259 | | | | | no | no | | |
| 1 | 389 | PSZ1 G107.14+65.29 | 13 32 39.5 | +50 32 47 | 12.21 | 7.991 | 0.2799 | | | | | - | yes | | WFPC2 |
| | 1227 | PSZ1 G359.99+78.04 | 13 34 09.6 | +20 14 00 | 6.63 | 4.989 | 0.171 | | | | | no | no | | |
| 1 | 319 | PSZ1 G092.67+73.44 | 13 35 18.1 | +41 00 10 | 13.52 | 8.294 | 0.2279 | | | | | - | yes | | PC, WFPC2, STIS-CCD |
| | 1140 | PSZ1 G326.64+54.79 | 13 45 20.1 | -05 34 46 | 6.61 | | | yes | G326+54 | 285A | 0.54 | no | no | | g,r filters |
| 1 | 1134 | PSZ1 G324.05+48.79 | 13 47 33.5 | -11 45 42 | 8.86 | 10.608 | 0.4516 | | | | | - | yes | | ACS-WFC |
| 1 | 434 | PSZ1 G118.46+39.31 | 13 54 48.7 | +77 15 15 | 6.47 | 6.15 | 0.3967 | | | | | - | yes | | ACS-WFC, WFC3-IR |
| | 1220 | PSZ1 G357.38+69.50 | 13 59 49.1 | +14 14 15 | 6.6 | 5.702 | 0.209 | | | | | - | no | | WFC3-UVIS |
| 1 | 1182 | PSZ1 G340.37+60.57 | 14 01 02.7 | +02 51 56 | 9.73 | 8.46 | 0.2528 | | | | | - | yes | | WFPC2 |
| | 415 | PSZ1 G113.84+44.33 | 14 14 00.3 | +71 18 23 | 8.92 | 5.003 | 0.225 | yes | 415 | | | no | no | | g,r,i filters |
| 1 | 224 | PSZ1 G067.19+67.44 | 14 26 03.9 | +37 49 35 | 12.77 | 6.971 | 0.1712 | | | | | - | yes | | PC, WFPC2, STIS-CCD |
| 1 | 12 | PSZ1 G004.13+56.84 | 14 47 22.4 | +08 28 14 | 6.43 | 7.461 | 0.38 | | | | | - | yes | | ACS-WFC |
| 1 | 337 | PSZ1 G096.87+52.48 | 14 52 56.4 | +58 03 35 | 6.45 | 5.147 | 0.3179 | | | | | - | yes | | PC, WFPC2, ACS-WFC |
| 1 | 1216 | PSZ1 G355.07+46.20 | 15 04 05.4 | -02 47 54 | 7.66 | 6.98 | 0.2153 | | | | | - | yes | | WFC3-UVIS, ACS-SBC |
| 1 | 7 | PSZ1 G002.80+39.24 | 15 40 00.0 | -03 17 34 | 7.04 | 5.912 | 0.1533 | | | | | yes | no | | W-J-V, W-S-I+ |
| 1 | 359 | PSZ1 G100.16+41.66 | 15 56 09.1 | +66 22 36 | 6.28 | 3.854 | 0.2339 | | | | | | yes | | ACS-WFC |
| 1 | 19 | PSZ1 G006.76+30.45 | 16 15 49.2 | -06 09 09 | 27.2 | 16.442 | 0.203 | | | | | | yes | | ACS-WFC |
| | 4 | PSZ1 G001.00+25.71 | 16 18 20.2 | -13 04 12 | 6.04 | | | yes | 4 | | | no | no | | g,r,i filters |
| 1 | 54 | PSZ1 G021.10+33.24 | 16 32 47.8 | +05 35 32 | 14.17 | 7.958 | 0.1514 | | | | | - | yes | | WFPC2 |
| 1 | 341 | PSZ1 G097.72+38.13 | 16 35 52.0 | +66 11 44 | 16.6 | 6.41 | 0.1709 | | | | | - | yes | | ACS-WFC |
| | 49 | PSZ1 G019.12+31.23 | 16 36 29.4 | +03 08 51 | 6.95 | 7.084 | 0.28 | yes | 49 | G019 | 0.274 | no | no | | g,r,i filters |
| 1 | 242 | PSZ1 G072.61+41.47 | 16 40 18.6 | +46 41 55 | 20.04 | 11.009 | 0.228 | | | | | - | yes | | ACS-WFC |
| | 226 | PSZ1 G067.52+34.75 | 17 17 15.6 | +42 27 46 | 6.6 | 4.418 | 0.1754 | | | | | - | yes | | ACS-SBC, PC, WFPC2 |
| 1 | 153 | PSZ1 G049.22+30.84 | 17 20 12.6 | +26 37 23 | 10.76 | 6.344 | 0.1644 | | | | | - | no | | PC, WFPC2 |
| 1 | 174 | PSZ1 G055.58+31.87 | 17 22 21.9 | +32 07 58 | 10.61 | 7.39 | 0.224 | | | | | - | yes | | ACS-WFC |
| | 435 | PSZ1 G118.58+28.57 | 17 25 00.4 | +85 53 41 | 8.06 | 5.479 | 0.178 | | | | | - | yes | | PC, WFPC2, STIS-CCD |
| 1 | 137 | PSZ1 G046.09+27.16 | 17 31 45.4 | +22 51 49 | 7.5 | 7.945 | 0.389 | | | | | - | yes | | PC, WFPC2, WFC3-IR, ACS-WFC |
| | 238 | PSZ1 G071.63+29.78 | 17 47 18.2 | +45 11 24 | 7.7 | 4.393 | 0.1565 | yes | 238 | | | no | no | | g,r,i filters |
| | 235 | PSZ1 G071.21+28.86 | 17 52 03.1 | +44 40 10 | 8.24 | 6.959 | 0.366 | | | | | | yes | | ACS-WFC |
| 1 | 221 | PSZ1 G066.41+27.03 | 17 56 48.2 | +40 07 59 | 6.46 | 7.413 | 0.576 | yes | 221 | I377 | 0.575 | no | no | | g,r,i filters |
| | 102 | PSZ1 G037.67+15.71 | 18 03 14.4 | +11 12 21 | 6.35 | | | yes | 102 | | | yes | no | | r,i filter |
| | 100 | PSZ1 G036.73+14.93 | 18 04 31.1 | +10 03 19 | 8.6 | 5.538 | 0.1525 | yes | 100 | | | no | no | | g,r,i filters |
| | 291 | PSZ1 G085.98+26.69 | 18 19 56.7 | +57 10 17 | 7.12 | 4.222 | 0.179 | yes | 291 | | | no | no | | g,r,i filters |
| 1 | 326 | PSZ1 G094.00+27.41 | 18 22 00.4 | +64 20 34 | 9.35 | 6.311 | 0.3315 | | | | | - | yes | | WFPC2 |
| | 313 | PSZ1 G091.82+26.11 | 18 31 08.2 | +62 14 52 | 7.52 | 7.45 | 0.822 | yes | 313 | G091 | 0.816 | no | no | | g,r,i filters |
| 1 | 330 | PSZ1 G094.69+26.34 | 18 32 33.4 | +64 49 38 | 7.05 | 3.257 | 0.1623 | yes | 330 | | | no | no | | g,r,i filters |
| | 127 | PSZ1 G044.83+10.02 | 18 36 39.4 | +15 04 50 | 7.27 | | | | | | | no | no | | |
| | 201 | PSZ1 G060.12+11.42 | 18 58 47.2 | +29 16 12 | 6.29 | 5.5 | 0.224 | | | | | no | no | | g,r,i filters |
| 1 | 225 | PSZ1 G067.36+10.74 | 19 16 02.3 | +35 24 45 | 9.09 | 6.269 | 0.209 | yes | 225 | | | no | no | | g,r,i filters |
| | 293 | PSZ1 G086.47+15.31 | 19 38 13.0 | +54 10 25 | 14.53 | 7.45 | 0.26 | | | | | no | no | | |

TABLE G.1: Entire LAS including unobserved clusters

| Has Lens | Source ID | PSZ Name | RA | DEC | SNR | M500 | SZ redshift | NOT MOSCA | ID NOT | NOT ALFOSC ID | ALFOSC z | SUP Data | HST Archive | CFHT | Detector-SOURCE |
|---|---|---|---|---|---|---|---|---|---|---|---|---|---|---|---|
| | 88 | PSZ1 G032.15-14.93 | 19 43 30.8 | -07 25 27 | 8.21 | | | | | | | yes | no | | W-C-IC |
| | 283 | PSZ1 G084.47+12.63 | 19 48 18.9 | +51 14 22 | 9.29 | 4.996 | 0.185 | yes | 283 | | | no | no | | g,r,i filters |
| | 78 | PSZ1 G029.79-17.37 | 19 48 26.2 | -10 31 30 | 6.59 | | | yes | 78 | | | no | no | | r,i filter |
| | 179 | PSZ1 G056.76-11.60 | 20 18 54.0 | +15 06 08 | 6.56 | 3.965 | 0.122 | yes | 179 | 371 | 0.122 | no | no | | g,r,i filters |
| 1 | 156 | PSZ1 G049.83-25.22 | 20 51 20.3 | +02 16 40 | 6.03 | 6.127 | 0.3211 | | | | | - | yes | | ACS-WFC |
| | 243 | PSZ1 G072.78-18.70 | 21 22 17.3 | +23 12 08 | 11.97 | 5.914 | 0.143 | | | 45 | 0.143 | no | no | | |
| | 108 | PSZ1 G039.81-39.96 | 21 26 57.5 | -12 11 09 | 8.01 | 5.711 | 0.176 | | | | | - | no | | PC, WFPC2 |
| 1 | 164 | PSZ1 G053.42-36.25 | 21 35 10.1 | -01 03 15 | 7.78 | 7.571 | 0.33 | | | | | - | yes | | ACS-WFC |
| | 177 | PSZ1 G055.95-34.87 | 21 35 13.6 | +01 25 40 | 9.09 | 6.924 | 0.231 | yes | 177 | | | no | no | | g,r,i filters |
| | 282 | PSZ1 G084.41-12.43 | 21 37 51.4 | +35 34 55 | 7.06 | 5.8 | 0.273 | yes | 282 | | | no | no | | g,r,i filters |
| | 250 | PSZ1 G074.75-24.59 | 21 46 08.9 | +20 28 43 | 6.12 | 5.057 | 0.25 | yes | 250 | 359 | 0.31 | no | no | | g,r,i filters |
| | 284 | PSZ1 G084.62-15.86 | 21 49 43.7 | +33 10 24 | 6.01 | 6.62 | 0.3673 | yes | 284 | | | no | no | | g,r,i filters |
| 1 | 248 | PSZ1 G073.98-27.83 | 21 53 44.0 | +17 41 35 | 15.21 | 9.482 | 0.2329 | | | | | - | yes | | WFPC2 |
| | 232 | PSZ1 G070.09-31.79 | 21 55 42.2 | +12 31 13 | 6.07 | 4.808 | 0.192 | | | | | yes | no | | W-J-V, W-S-I+ |
| | 301 | PSZ1 G088.83-12.99 | 21 55 55.9 | +37 59 59 | 7.72 | 7.353 | 0.292 | | | 262 | 0.29 | - | yes | | WFPC2 |
| | 256 | PSZ1 G077.89-26.62 | 22 00 53.2 | +20 57 59 | 9.32 | 5.443 | 0.147 | | | | | - | yes | | PC, WFPC2 |
| | 183 | PSZ1 G057.28-45.37 | 22 11 51.2 | -03 49 19 | 9.56 | 9.201 | 0.397 | | | | | - | yes | | WFC3-UVIS, ACS-WFC |
| 1 | 125 | PSZ1 G044.77-51.30 | 22 15 03.7 | -13 59 16 | 7.3 | 8.461 | 0.5027 | | | | | - | yes | | NIC3, ACS-WFC, ACS-HRC |
| | 336 | PSZ1 G096.44-10.40 | 22 19 35.1 | +44 31 05 | 6.55 | | | yes | 336 | | | no | no | | g,r,i filters |
| 1 | 275 | PSZ1 G083.30-31.01 | 22 28 29.1 | +20 38 22 | 6.94 | 7.82 | 0.412 | | | | | yes | no | | W-C-RC, W-C-IC, W-J-V, W-S-Z+, W-J-B |
| | 239 | PSZ1 G071.64-42.76 | 22 30 51.4 | +05 41 07 | 8.82 | | | yes | 239 | | | no | no | yes | z.MP9801 and r.MP9601 and NOT I-filter |
| | 241 | PSZ1 G072.59-43.25 | 22 34 15.1 | +05 48 39 | 6.08 | 4.401 | 0.159 | yes | 241 | | | no | no | | I-filter |
| 1 | 181 | PSZ1 G056.94-55.06 | 22 43 17.1 | -09 34 50 | 10.81 | 10.074 | 0.447 | | | | | - | yes | | ACS-WFC |
| 1 | 247 | PSZ1 G073.85-54.94 | 23 08 28.1 | -02 12 00 | 6.21 | 6.168 | 0.2966 | | | | | - | yes | | WFPC2 |
| 1 | 268 | PSZ1 G081.01-50.92 | 23 11 36.3 | +03 38 38 | 8.59 | 7.529 | 0.2998 | | | | | yes | no | | W-J-V, W-C-RC, W-J-B, W-S-I+ |
| | 360 | PSZ1 G100.18-29.68 | 23 20 56.4 | +29 09 44 | 6.15 | 7.971 | 0.485 | yes | 360 | | | no | no | | g,r,i filters |
| | 394 | PSZ1 G108.18-11.53 | 23 22 29.7 | +48 46 30 | 6.36 | 7.7 | 0.336 | yes | 394 | 431 | 0.335 | no | no | | G,r,i filters |
| 1 | 267 | PSZ1 G080.66-57.87 | 23 27 33.7 | -02 03 42 | 6.37 | 8.304 | 0.705 | | | | | - | yes | | ACS-WFC |
| | 368 | PSZ1 G102.86-31.07 | 23 33 07.9 | +28 43 52 | 6.12 | 8.25 | 0.5915 | | | | | no | no | | |
| 1 | 297 | PSZ1 G087.03-57.37 | 23 37 43.7 | +00 16 06 | 7.5 | 6.965 | 0.2779 | | | | | - | yes | | PC, WFPC2 |
| | 399 | PSZ1 G109.14-28.02 | 23 53 08.8 | +33 16 48 | 6.51 | 8.094 | 0.457 | yes | 399 | 435 | 0.456 | no | no | | g,r,i filters |
| | 381 | PSZ1 G105.91-38.39 | 23 53 54.1 | +22 34 21 | 7.16 | | | yes | 381 | | | no | no | | g,r,i filters |

# Appendix H

# Bibliography

# References

Abell, G. O., H. G. Corwin Jr., and R. P. Olowin (1989). "A catalog of rich clusters of galaxies". In: ApJS 70, pp. 1–138. DOI: 10.1086/191333.

Ammons, S. M. et al. (2014). "Mapping Compound Cosmic Telescopes Containing Multiple Projected Cluster-scale Halos". In: ApJ 781, 2, p. 2. DOI: 10.1088/0004-637X/781/1/2. arXiv: 1311.2583.

Bayliss, M. B. et al. (2011). "Gemini/GMOS Spectroscopy of 26 Strong-lensing-selected Galaxy Cluster Cores". In: ApJS 193, 8, p. 8. DOI: 10.1088/0067-0049/193/1/8. arXiv: 1010.2714 [astro-ph.CO].

Carlstrom, J. E., G. P. Holder, and E. D. Reese (2002). "Cosmology with the Sunyaev-Zel'dovich Effect". In: ARA&A 40, pp. 643–680. DOI: 10.1146/annurev.astro.40.060401.093803. eprint: astro-ph/0208192.

Coe, D. et al. (2010). "A High-resolution Mass Map of Galaxy Cluster Substructure: LensPerfect Analysis of A1689". In: ApJ 723, pp. 1678–1702. DOI: 10.1088/0004-637X/723/2/1678. arXiv: 1005.0398 [astro-ph.CO].

Cypriano, E. S. et al. (2005). "Gemini and Chandra Observations of Abell 586, A Relaxed Strong-lensing Cluster". In: ApJ 630, pp. 38–49. DOI: 10.1086/430661. eprint: astro-ph/0504036.

Dahle, H. et al. (2002). "Weak Gravitational Lensing by a Sample of X-Ray Luminous Clusters of Galaxies. I. The Data Set". In: ApJS 139, pp. 313–368. DOI: 10.1086/338678.

de Blok, W. J. G. (2010). "The Core-Cusp Problem". In: *Advances in Astronomy* 2010, 789293, p. 789293. DOI: 10.1155/2010/789293. arXiv: 0910.3538.

Ebeling, H., A. C. Edge, and J. P. Henry (2001). "MACS: A Quest for the Most Massive Galaxy Clusters in the Universe". In: ApJ 553, pp. 668–676. DOI: 10.1086/320958. eprint: astro-ph/0009101.

Fedeli, C. et al. (2006). "A fast method for computing strong-lensing cross sections: application to merging clusters". In: A&A 447, pp. 419–430. DOI: 10.1051/0004-6361:20053762. eprint: astro-ph/0507093.

Graham, A. W. and S. P. Driver (2005). "A Concise Reference to (Projected) Sérsic $R^{1/n}$ Quantities, Including Concentration, Profile Slopes, Petrosian Indices, and Kron Magnitudes". In: PASA 22, pp. 118–127. DOI: 10.1071/AS05001. eprint: astro-ph/0503176.

Hoag, A. et al. (2015). "RCS2 J232727.6-020437: An Efficient Cosmic Telescope at z=0.6986". In: ApJ 813, 37, p. 37. DOI: 10.1088/0004-637X/813/1/37. arXiv: 1503.02670.

Hogg, David W. (1999). "Distance measures in cosmology". In: arXiv: astro-ph/9905116 [astro-ph].

Holhjem, K., M. Schirmer, and H. Dahle (2009). "Weak lensing density profiles and mass reconstructions of the galaxy clusters Abell 1351 and Abell 1995". In: A&A 504, pp. 1–13. DOI: 10.1051/0004-6361/20079006. arXiv: 0906.2938.

Kawamata, R. et al. (2016). "Precise Strong Lensing Mass Modeling of Four Hubble Frontier Field Clusters and a Sample of Magnified High-redshift

Galaxies". In: ApJ 819, 114, p. 114. DOI: 10.3847/0004-637X/819/2/114. arXiv: 1510.06400.

Kitching, T. et al. (2010). "Gravitational Lensing Accuracy Testing 2010 (GREAT10) Challenge Handbook". In: *ArXiv e-prints*. arXiv: 1009.0779 [astro-ph.CO].

Kneib, J.-P. and P. Natarajan (2011). "Cluster lenses". In: A&A Rev. 19, 47, p. 47. DOI: 10.1007/s00159-011-0047-3. arXiv: 1202.0185 [astro-ph.CO].

Lachièze-Rey, M., ed. (1999). *Theoretical and observational cosmology*. Vol. 541. NATO Advanced Science Institutes (ASI) Series C.

Limousin, M. et al. (2008). "Strong lensing in Abell 1703: constraints on the slope of the inner dark matter distribution". In: A&A 489, pp. 23–35. DOI: 10.1051/0004-6361:200809646. arXiv: 0802.4292.

Longair, M. S., ed. (1998). *Galaxy formation*.

Meylan, G. et al., eds. (2006). *Gravitational Lensing: Strong, Weak and Micro*. eprint: astro-ph/0407232.

Newman, A. et al. (2013). "The Dark Matter Density Profile in Brightest Cluster Galaxies". In: *Probes of Dark Matter on Galaxy Scales*. Vol. 1.

Oguri, M. et al. (2009). "Subaru Weak Lensing Measurements of Four Strong Lensing Clusters: Are Lensing Clusters Overconcentrated?" In: ApJ 699, pp. 1038–1052. DOI: 10.1088/0004-637X/699/2/1038. arXiv: 0901.4372 [astro-ph.CO].

Oguri, M. et al. (2012). "Combined strong and weak lensing analysis of 28 clusters from the Sloan Giant Arcs Survey". In: MNRAS 420, pp. 3213–3239. DOI: 10.1111/j.1365-2966.2011.20248.x. arXiv: 1109.2594.

Pen, Ue-Li (1996). "Analytical fit to the luminosity distance for flat cosmologies with a cosmological constant: Brief note". In: *Astron. Astrophys. Suppl. Ser.* 120. [Astrophys. J. Suppl.120,49(1999)], p. 49. DOI: 10.1086/313167. arXiv: astro-ph/9904172 [astro-ph].

Planck Collaboration et al. (2015a). "Planck 2013 results. XXXII. The updated Planck catalogue of Sunyaev-Zeldovich sources". In: A&A 581, A14, A14. DOI: 10.1051/0004-6361/201525787. arXiv: 1502.00543.

Planck Collaboration et al. (2015b). "Planck 2015 results. I. Overview of products and scientific results". In: *ArXiv e-prints*. arXiv: 1502.01582.

Planck Collaboration et al. (2015c). "Planck 2015 results. XXIII. The thermal Sunyaev-Zeldovich effect–cosmic infrared background correlation". In: *ArXiv e-prints*. arXiv: 1509.06555.

Planck Collaboration et al. (2015d). "Planck 2015 results. XXVII. The Second Planck Catalogue of Sunyaev-Zeldovich Sources". In: *ArXiv e-prints*. arXiv: 1502.01598.

Postman, M. et al. (2012). "The Cluster Lensing and Supernova Survey with Hubble: An Overview". In: ApJS 199, 25, p. 25. DOI: 10.1088/0067-0049/199/2/25. arXiv: 1106.3328.

Richard, J. et al. (2014). "Mass and magnification maps for the Hubble Space Telescope Frontier Fields clusters: implications for high-redshift studies". In: MNRAS 444, pp. 268–289. DOI: 10.1093/mnras/stu1395. arXiv: 1405.3303.

Sand, D. J. et al. (2005). "A Systematic Search for Gravitationally Lensed Arcs in the Hubble Space Telescope WFPC2 Archive". In: ApJ 627, pp. 32–52. DOI: 10.1086/430298. eprint: astro-ph/0502528.

Sersic, J. L. (1968). *Atlas de galaxias australes*.

Smith, G. P. et al. (2005). "A Hubble Space Telescope lensing survey of X-ray luminous galaxy clusters - IV. Mass, structure and thermodynamics of cluster cores at z= 0.2". In: MNRAS 359, pp. 417–446. DOI: 10.1111/j.1365-2966.2005.08911.x. eprint: astro-ph/0403588.

Sunyaev, R. A. and I. B. Zeldovich (1980). "Microwave background radiation as a probe of the contemporary structure and history of the universe". In: ARA&A 18, pp. 537–560. DOI: 10.1146/annurev.aa.18.090180.002541.

Voges, W. et al. (1999). "The ROSAT all-sky survey bright source catalogue". In: A&A 349, pp. 389–405. eprint: astro-ph/9909315.

Voges, W. et al. (2000). "Rosat All-Sky Survey Faint Source Catalogue". In: IAU Circ. 7432.

Webb, S., ed. (1999). *Measuring the universe : the cosmological distance ladder*.

Wen, Z. L., J. L. Han, and F. S. Liu (2012). "A Catalog of 132,684 Clusters of Galaxies Identified from Sloan Digital Sky Survey III". In: ApJS 199, 34, p. 34. DOI: 10.1088/0067-0049/199/2/34. arXiv: 1202.6424 [astro-ph.CO].

Zaritsky, Dennis and Anthony H. Gonzalez (2003). "On the Incidence of Strong Gravitational Lensing by Clusters in the Las Campanas Distant Cluster Survey". In: *The Astrophysical Journal* 584.2, p. 691. URL: http://stacks.iop.org/0004-637X/584/i=2/a=691.

Zitrin, A. et al. (2015). "Hubble Space Telescope Combined Strong and Weak Lensing Analysis of the CLASH Sample: Mass and Magnification Models and Systematic Uncertainties". In: ApJ 801, 44, p. 44. DOI: 10.1088/0004-637X/801/1/44. arXiv: 1411.1414.